MEDICAL DOSIMETRY AND DOSE DELIVERY FOR PHOTOBIOMODULATION AND PHOTODYNAMIC THERAPY

Dennis Sourvanos

A DISSERTATION

in

Dentistry

Presented to the Faculties of the University of Pennsylvania in Partial Fulfillment of the

Requirements for the Doctor of Science in Dentistry

2023

_____   _____

Joseph P. Fiorellini   Timothy C. Zhu
(Supervisor of Dissertation)   (Co-Supervisor of Dissertation)
Postdoctoral Director of Periodontics,   Professor of Radiation Oncology
Professor of Periodontics   Hospital of the University of
                                                         Pennsylvania

_____

Rodrigo Neiva
(Dissertation Chairperson)
Chair and Clinical Professor of Periodontics
.

Dissertation Committee:
-Andreea Dimofte, Staff Physicist, Department of Radiation Oncology, Hospital of the University of Pennsylvania
-Hector Sarmiento, Clinical Assistant Professor of Periodontics, School of Dental Medicine
-Dr. Praveen Arany, Assistant Professor, Department of Oral Biology, School of Dental Medicine, University at Buffalo

DEDICATION

To my beloved parents.

This dissertation is dedicated to my parents, Gerassimos & Marianthi Sourvanos. This work is the result of your courage, sacrifices, and belief in the power of education. Your journey began with a dream. One where you could provide your children a future that was rich in opportunities beyond your reach.

You have taught me that a formalized education is not just about academic learning. That education will help me understand my place in this world. It will guide me through the darkness, prompting me to reflect, as I grow through the adversity of life. Despite not having had the same opportunity, you understood that an education would help me connect with others as an authentic human being.

Dad, I wish I could thank you again, one last time, for teaching me the value of discipline, focus, and hard work. I grew up watching you work tirelessly to provide for our family. This became your passion and your purpose. Your commitment has helped me discover a similar passion in my professional pursuits. This work ethic has provided a significant advantage in my life and has been pivotal in helping me accomplish my goals. I am appreciative of this lesson and will continue to carry it forward in my journey.

I am thankful to both of you for teaching me the values of perseverance and empathy. You have always said that education is the one privilege in life that must be earned and, subsequently, can never be taken away. This dissertation is the culmination of eighteen humbling years of formal education in the highest echelons of academia.

With all my love,

Dennis Sourvanos

ACKNOWLEDGEMENTS

- **Student Presentation Travel Grant.** Osteology Foundation International Meeting Barcelona, (April 2023).

- **Education Grant.** Osteology Foundation, Research Academy Vienna. (Nov. 2022).

- **Student Travel Grant.** International Society for Optics and Photonics. (Sep. 2022).

- **Urbach Travel Student Award.** American Society for Photobiology. (Sep. 2022).

- **CiPD Scientific Image Award.** Inaugural CiPD Symposium. (Jun 2022).

- **T-90 Postdoctoral Fellow.** Center for Innovation and Precision Dentistry. (Jan. 2022).

- **T90DE030854.** National Institute of Dental and Craniofacial Research. (Jan. 2022).

- **Junior Investigator AADR Travel Award.** Penn Dental Medicine Research Day Oral Competition. (May 2021).

- **William B. Clark Fellowship.** American Association Dental Oral Craniofacial Research. (May 2021).

- **TL1TR001880.** National Center for Advanced Translational Sciences of the National Institutes of Health. (Apr. 2021).

- **Doctor of Science in Dentistry Scholarship.** Penn Dental Medicine. (Aug. 2020).

- **Nobel Biocare Student Member Annual Meeting Scholarship.** American Academy of Periodontology. (Nov. 2019).

ABSTRACT

MEDICAL DOSIMETRY AND DOSE DELIVERY FOR PHOTOBIOMODULATION AND PHOTODYNAMIC THERAPY

Dennis Sourvanos

Joseph P. Fiorellini

Timothy C. Zhu

The successful application of Photobiomodulation (PBM) and Photodynamic Therapy (PDT) in clinical settings is challenging due to the complex tissue boundaries and intricate 3-dimensional geometries of the targeted anatomical site. There are no known advanced medical dosimetry protocols that incorporate the tissue optical properties of bone, soft tissue, dentin, and enamel. To address this issue of calculating dosage for tissue boundaries of the head and neck region, this thesis aims to investigate dosimetry in the traditional silicone phantom model, a novel 3-dimensional model of the human maxilla, and the mandibular tissues of the porcine cadaver.

The medical dosimetry system utilized throughout this thesis incorporates a dual-motor continuous wave transmittance spectroscopy technique to measure tissue optical properties. The system has been successfully used in human clinical PDT treatment and calibrated with a new series of silicone phantom models in both traditional and novel 3-D shapes. The phantom optical properties were extended to include a broader spectrum of human dental-oral craniofacial tissues. Multiple translational preclinical porcine mandible cadaver experiments were conducted to investigate light transmission through complex tissue boundaries at different power outputs and wavelengths.

The optical properties of all silicon phantom models and porcine cadavers were validated through dual-catheter, interstitial, and semi-infinite light transmission measurements. Statistical assessments

revealed significant variations across all silicon phantom model types, the impact of light transmissions through the optical properties of complex geometries, and that significant variabilities of the 3D shape could lead to inaccuracies when modeling complex anatomical structures.

The porcine mandible cadaver system demonstrated that transmission is modified as it passes through boundaries with different optical properties. Significant findings revealed consistencies for soft tissue light transmission irrespective of power, the correlation of light transmission, distance, and different tissues. Significance was determined between the 661nm and 810nm wavelengths and for the semi-infinite light dosimetry protocol to recognize homogenous and mixed tissue groups.

The research conducted seeks to enhance medical dosimetry protocols in the head and neck region with eventual translation to human clinical care.

TABLE OF CONTENTS

LIST OF TABLES

LIST OF FIGURES

1 INTRODUCTION

Photodynamic Therapy (PDT) and Photobiomodulation (PBM) utilize similar red and near-infrared wavelengths in the 400-1,000nm range. Both are utilized in medicine and dentistry based on treatment indications. (1-9) Despite a substantial amount of literature publications for various head and neck applications in both fields, protocols are still needed to evaluate and improve light dosimetry for this region.

1.1 Photodynamic Therapy (PDT)

PDT involves the production of a photochemical interaction between light, a photosensitizer, and oxygen. (10-13) Mechanisms of PDT affect the generation of reactive oxygen species (ROS), including cell death, vascular damage, and immune response. (14) Conventional PDT utilizes the visible electromagnetic spectrum between 400-750nm and a light-sensitive photosensitizer (e.g., Photofrin). This chemical is administered systemically, absorbed, and then irradiated. (15, 16) The photosensitizer's interaction with light to generate singlet oxygen is critical to this reaction, which results in a shift of oxygen distribution, alteration, and consumption. (13) This gives rise to ROS, which in turn oxidizes intracellular molecules. (16) PDT treatment can be offered as either a standalone or adjunct therapy, depending on the overall treatment approach and required endpoints.

Clinical PDT is predominantly recognized in radiation oncology with lesser-known applications in dentistry. According to the National Cancer Institute, the FDA has approved PDT to treat actinic keratosis, advanced cutaneous T-cell lymphoma, Barrett esophagus, basal cell skin cancer, esophageal cancer, non-small cell lung cancer, and squamous cell skin cancer (Stage 1). (17) Other investigational applications for PDT in radiation oncology include the prostate, bladder, pleural cavity, spinal metastases, and various head and neck indications. (18-22) Although PDT has not received regulatory approvals for the intra-oral region, dental applications of PDT do address periodontal disease, peri-implant disease, endodontic therapy,

cariogenic bacteria, candidiasis, alveolar osteitis, and post-extraction pain. (23-27) Calibrating for an optimal PDT dose requires precise light fluence, photosensitizer concentration, and tissue oxygenation levels. (28, 29) A common challenge of PDT occurs where an inadequate dose might leave remnants of disease, and an excessive dose may cause damage to surrounding healthy sites. (29)

1.2   Photobiomodulation (PBM)

Photobiomodulation is the minimally invasive delivery of light with the potential to improve wound healing, dampen the inflammatory cascade, and provide an overall sense of analgesia to an intended site. (30-47) The molecular mechanisms of PBM are organized into three groups that are defined as intracellular membrane complexes, cell membrane receptors, and extracellular complexes. (34, 48-50) Each group has unique biomolecular targets that engage when a specific laser wavelength activates a threshold. (34) The intracellular mechanisms are understood to involve an interplay of cytochrome c oxidase (CcO), which is contained in the respiratory chain located within the mitochondria. (51) It is theorized that the absorption of PBM light energy causes photodissociation of inhibitory nitrous oxide (NO) from CcO, (52, 53) leading to enhancement of enzyme activity, (54) electron transport, (55) mitochondrial respiration, and ATP production. (51, 56) By altering the cellular redox state, PBM can induce activation of numerous intracellular signaling pathways and alter the affinity of transcription factors concerned with cell proliferation. (51, 55) Resulting in applications for PBM to improve cellular metabolism, mitochondrial function, and ATP production. (57-63)

The theorized cell membrane receptor mechanisms can modulate photosensitive ions on the membrane receptors of Opsins 2-4, TRPV1, AHR, and P2X6. (64-67) The extracellular mechanisms include the redox-mediated activation of latent TGF-β1, a pluripotent family of cytokines significantly

2

involved as multifunctional growth factors for re-epithelialization, inflammation, angiogenesis, and granulation tissue formation during wound healing. (30, 35, 37-41, 47, 68-70)

1.3 Clinical and Translational Science

PBM and PDT applications are shared across several clinical disciplines. (1, 4, 33, 43, 64, 71-75) Although PBM devices produce a similar fluence rate to PDT, PBM will utilize lower rates than ablative or coagulative systems operating on the same wavelengths. The FDA has granted limited marketing clearance for qualified PBM devices. FDA marketing approval is for temporary relief from minor muscle and joint pain, stiffness, minor arthritis pain, muscle spasms, and a temporary increase in local blood circulation. Numerous PBM protocols are documented in medicine and dentistry to improve soft tissue wound healing, reduce inflammation, increase blood flow, and provide analgesia to an intended site. (3, 4, 64, 73, 76-96)

Translational dental research has been directed toward PBM to reduce the healing time and improve the potential for bone regeneration in preparation for implant placement. (97) PBM has been documented to decrease post-operative pain and swelling. (98, 99) Thus, supporting the hypothesis that it may positively contribute to implant osseointegration and stability. (59, 97)

There is great potential to adopt PBM in dentistry to improve the overall standard of care. Despite several promising human studies, there are limited validated postoperative protocols for applying PBM in dental alveolar ridge preservation before implant placement. (60, 76, 100-102) The application of PBM in clinical practice has yet to fully develop due to misinterpreted light dosimetry measurements, inconsistent variations in light dose, and inconsistent irradiation parameters in human tissues. (101, 103-106) Accurate light dosimetry is critical for predicting the efficacy of PBM.

It is well known that tissue optical properties of absorption and scattering can vary from person to person and between species. (107) This will result in varying delivery of light dose in these tissues due to

these absorption and scattering properties. The minimum irradiation parameters for the desired treatment areas (intraoral or extraoral) include wavelength (nm), laser power (W), treatment time (sec), and energy dose (J). Others that should be considered include the number of contact points (per dose), beam area spot size of the device (cm^2), power density (W/cm^2), fluence (J/cm^2), and irradiance (mW/cm^2). The accurate quantification of light dose and irradiance should help optimize the parameters for PBM therapy.

1.4   Thesis Outline

Throughout this thesis dissertation, I present a range of translational science applications for medical dosimetry and fluence calculations that are currently under investigation for photodynamic therapy (PDT) and photobiomodulation (PBM). I provide a detailed description of the comprehensive set of data analytics that will support the calibration of a medical dosimetry system and enable the phase of translation that is required for pre-clinical research into human clinical care.

In this work, I explore the progression of the traditional cylinder silicone phantom model (Chapter 2, section 2.4) to a novel 3-dimensional model (Chapter 2, section 2.5) and the porcine mandible cadaver (Chapter 3). In Chapter 4, I will describe a protocol to improve light-fluence delivery by digitally acquiring the surface area of complex geometric shapes indicative of the lung pleural cavity. The presented set of analytics and methods provides a robust framework for real-time medical dosimetry applications in the clinical setting to improve patient outcomes.

This medical dosimetry system described throughout this thesis has been utilized in human clinical care for over fifteen years. In Chapter One, I will describe the fundamental translational science of PDT and PBM. In Chapter Two, section 2.2, I will comprehensively describe the fabrication process for phantom models. To calibrate the medical dosimetry system to a broader spectrum of known tissue optical properties, I have developed an updated silicone phantom modeling system that will be discussed in detail in sections

2.2 – 2.4. These findings will be correlated with an alternative type of light delivery described as a semi-infinite approach in section 2.5. This approach is particularly useful in investigating light transmission in 3-dimensional boundaries that involve convex and concave shapes.

Chapter 3 of this thesis focuses on a comprehensive investigation of a novel porcine mandible cadaver modeling system. Section 3.3 presents a proof-of-concept investigation of 661nm light transmission at the complex boundaries of bone, soft tissue, dentin, and enamel. Subsequently, section 3.4 investigates 661nm light transmission through various soft tissue regions across five porcine specimens. This investigation is further expanded to compare the light transmission variations of the same regions between the 661nm and the 810nm wavelengths in section 3.5.

The semi-infinite light delivery method is applied to all five porcine cadaver specimens across twenty-two regions of interest in section 3.6. This approach will investigate the differences between homogenous soft tissue and mixed tissue regions consisting of bone, soft tissue, dentin, and enamel. Section 3.7 explores histology to provide a microscopic understanding of the porcine soft tissue regions of interest. Section 3.8 will acquire bone tissue optical properties with the calibrated medical dosimetry system to provide an in-depth analysis of the bone tissue characteristics available.

Chapter 4 will summarize this thesis and future work.

2   SILICONE PHANTOM MODELS

2.1   Innovation of Potential Findings

The research conducted in this dosimetry study is driven by the need to develop better treatment guidelines for the application of PDT and PBM therapies. In the field of dentistry, there is a great purpose for both techniques as an adjunct for improving post-operatory outcomes of alveolar bone and tissue healing. (33, 43)

Through this research compellation, multiple pre-clinical phantom modeling systems will introduce concepts that are unique to the heterogeneous tissues of human clinical application. This is the first body of research to investigate PBM/PDT dosimetry using a traditional silicone and novel 3Dimensional phantom model. This will be accompanied by an equally unique translational component that will investigate the tissue heterogeneities across multiple regions of interest in the porcine cadaver specimen. The objective is to develop novel treatment parameters to guide clinical care.

Findings from these pre-clinical models will then eventually be applied to clinical delivery protocols to maximize efficacy and safety potential. Outcomes from the phantom modeling systems will be used to develop a database of external beams and imaging co-registrations. These values will be validated to create a mathematic predictive modeling tool that will adequately classify irradiation parameters and determine the spectrum of dosing in simulated alveolar bone and supporting structures in a human study.

2.2   Cylinder & 3-Dimensional Shape

The efficacy of light delivery in photobiomodulation and photodynamic therapy is determined by the amount of light delivered to the intended target. Adjusting dosage for the various coefficients of absorption (μa) and scattering (μs) is critical to achieving the desired effect. The primary tool developed in this

laboratory group is the silicone phantom model, which can test the capabilities and calibrate the medical dosimetry system for therapeutic applications. (108-111) This medical dosimetry system comprises a dual-motor continuous wave transmittance spectroscopy system designed to measure optical properties specifically.

The phantom models from this dosimetry group are fabricated from a silicone vulcanizing medium, allowing for high predictability and reproducibility. Nonetheless, these silicone phantom concepts are designed to have optical property light coefficients like human biological tissues. Introducing absorption and scattering light coefficients into this phantom modeling system is significant for PDT calibration and testing because it allows adjusting each coefficient's quantity. This can test the capability of the system to calibrate towards this amount during therapy accurately. Absorption determines how much light is absorbed and delivered to an intended target. If the absorption value is a lower coefficient, less light must be delivered to achieve the desired effect. If the chromophores are considered to have high absorption coefficients, then more light would need to be delivered. Scattering coefficients can provide insight into the spread of light. A high scattering measurement would mean less light is spread out through the same quantity of tissue versus a lower scattering measurement. Thus, the reason why a low scattering value would require a higher dose of light delivery.

In this modeling system, carbon black is utilized in precise ratios as an absorption medium to help understand how much light the tissue absorbs. Titanium Dioxide (TiO2) is used in defined ratios as a scattering medium to understand the propensity that light is scattered as it is redirected through the tissue. This allows for theoretical adjustments to the dose to stimulate a biological effect in photobiomodulation and intentionally kill harmful cancerous cells during photodynamic therapy.

Although light can be delivered through several mediums, the preferred application for this group is transmittance spectroscopy. This system is common in clinical settings. Measurements quantify the

amount of light that passes through the phantom model (or tissue) evaluated against the amount of light passing through the same model before light activation. The algorithms developed by this group have created an ongoing long-term study that can quantify how much light is absorbed or scattered by the target (tissue or phantom). This is critical to understanding how to adjust the dose during active treatment.

The protocol and algorithms developed by this lab acquire data on how much light is absorbed or scattered by the tissue, which is critical to dose adjustment during therapy. This involves the placement of two catheters interstitially into the phantom to take optical property measurements internally at the intended site. The advantage of interstitial catheters is having real-time feedback of the unique optical properties of the tissues at that location. Measurements are accurately tracked by a dual motor platform that can precisely control and modify the position of the light source and detector sitting within the interstitial catheter. This type of system can quantify the intricate variations in a homogenous phantom model. This allows light delivery adjustment, ensuring the therapeutic dose is delivered while achieving the intended effect.

2.2.1   Silicone Phantom Model Fabrication

The protocol for this silicone phantom modeling system is built upon the research of preceding personnel affiliated with the Tim Zhu Laboratory group, spanning back to 2005. (10, 13, 21, 22, 28, 29, 107-115) In 2019, a prior Postdoctoral Fellow with this lab published results of the latest version of this phantom modeling system consisting of 9 different ratios of absorption (0.09-0.45 cm^-1) and scattering (4.2-16.9 cm^-1) properties for known human tissue optical properties. (29) This phantom modeling project expanded these ratios of absorption (0.1-1 cm^-1) and scattering (5-20 cm^-1). (See Table 1)

Expected Optical Properties (cm^-1)				
	Original Ratios (29)		New Ratios	
Phantom	Absorption coefficient μa (cm^-1)	Reduced Scattering coefficient μs' (cm^-1)	Absorption coefficient μa (cm^-1)	Reduced Scattering coefficient μs' (cm^-1)
1	0.09	4.2	0.1	5
2	0.09	8.5	0.1	10
3	0.09	16.9	0.1	20
4	0.25	4.2	0.5	5
5	0.25	8.5	0.5	10
6	0.25	16.9	0.5	20
7	0.45	4.2	1	5
8	0.45	8.5	1	10
9	0.45	16.9	1	20

Table 1. Silicone Phantom. Expected optical property ratios of the current silicone phantom modeling system (right) expanded from prior values (left).

After several versions of the original modeling system were attempted, two phantom silicone models were fabricated. Several state-of-the-art methodologies and pouring techniques from dentistry were implemented to build upon prior generations of this phantom modeling platform. The first is the traditional "flat-planar" shape in a cylindrical structure. (29) The second is a new novel concept attempting to replicate the three-dimensional shape, volume, and configuration of a real-size anatomy of the human maxilla. (See Figure 1)
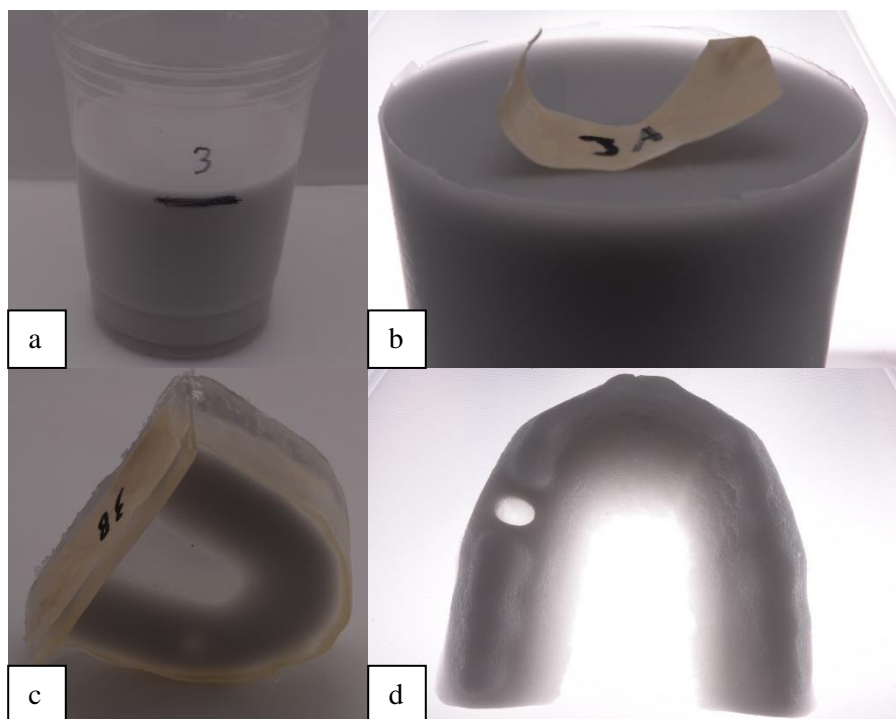
Figure 1. Phantom Model Series #3. a) traditional cylinder-shaped phantom model in container mold. b) Traditional shaped phantom model after curing/processing. c) 3-dimensional phantom model in custom printed mold, d) 3-dimensional phantom model after processing.

For this study, we utilized 27 solid silicone phantoms. Nine were cylindrical in shape, as reported by prior group members. Additional models were fabricated in the 3-dimensional shape, with one set (n=9) as a backup if a 3-D model was damaged. Precise methodologies were followed for the solution preparation, which ensured consistency in the optical properties across each series of models.

The silicone catalyst mixture comprised a two-part formulation manufactured by Momentive Performance LLC. The silicone rubber base compound (RTV 12A) and the silicone catalyst mixture curing agent (RTV 12C). RTV 12A and 12C carried either Category 1, 2, 3, and 4 (or some combination) hazard identifications. RTV 12A contained the following chemicals in its' mixture: solvent naphtha, gamma-aminopropyltriethoxysilane, silicic acid, ethyl ester, tetraethyl silicate, dibutyl tinoxide. RTV 12C contained Toluene.

Both absorption and light scattering ratio calculations were based on prior work from affiliates of this lab. (29, 115) Absorption was defined by carbon ratios, and light scattering parameters were determined by titanium dioxide ratios. The carbon was a general-purpose adsorbent manufactured by Supelco (14028-U) with no relevant hazardous identifications. This was selected in a powdered form with a molecular weight of 12.01 g/mol. (See Figure 1-2). Titanium dioxide was a reagent manufactured by Spectrum (T1085) with a category 2 hazard statement and was manufactured in a solid white powder state. (See Figure 2)

Figure 2. Measurement of Carbon to mimic human tissue optical properties of absorption.

The amount of carbon black adsorbent and titanium dioxide powder was based on the following formulations. (See Figure 3), (29, 115)

$$\text{Carbon required (mg)} = \frac{\mu a(\text{cm}^{-1}) + 0.00685(\text{cm}^{-1})}{0.0203(\text{cm}^{-1} \times mg^{-1})} \times \frac{total\ volume\ (ml)}{1650(ml)}$$

$$\text{Titanium Dioxide required (mg)} = 3.6(g) \times \frac{\mu's(\text{cm}^{-1})}{7.5(\text{cm}^{-1})} \times \frac{total\ volume\ (ml)}{1650(ml)}$$

Figure 3. Absorber and Scatterer formulations were used to determine the ratios of carbon and TiO2.

This experiment consisted of a series of 9 different ratios of carbon and titanium dioxide based on the desired optical properties. The absorption coefficient ranged from 0.1 – 1 cm^-1. The scattering coefficient ranged from 5 – 20 cm^-1. Additional calculations were made considering the mean free path (cm) and the minimum distance for optical characterization necessary for transmittance spectroscopy. (See Table 2.
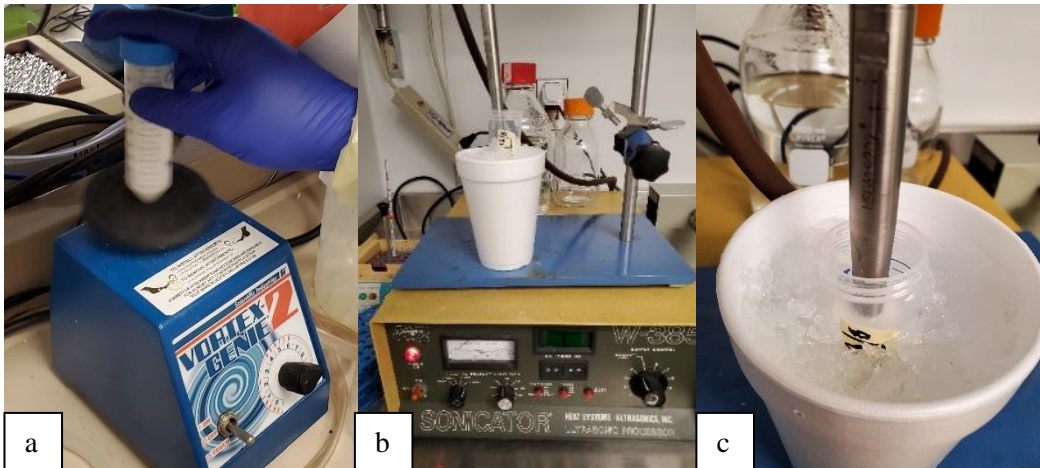
Figure 4. Absorber and Scatterer Concentration Preparation. a) Vortexing of titanium dioxide solution at full speed, b) Sonicator system, c) Scatterer solution being sonicated inside of ice bath.

Series	Carbon (mL) (1mg/mL)	TiO2 (mL) (0.1g/mL)	RTV 12C (mL)	Absorption μa (cm^-1)	Scattering μ's (cm^-1)	Mean-free-path (cm)	Min. distance for optic characterization
1	1.084	4.945	24.88	0.1	5	0.816496581	2.449489743
2	1.084	9.891	19.934	0.1	10	0.577350269	1.732050808
3	1.084	19.782	10.04	0.1	20	0.40824829	1.224744871
4	5.144	4.945	20.819	0.5	5	0.365148372	1.0985445115
5	5.144	9.891	15.873	0.5	10	0.25819889	0.774596669
6	5.144	19.782	5.983	0.5	20	0.182574186	0.547722558
7	10.22	4.945	15.744	1	5	0.25819889	0.774596669
8	10.22	9.891	10.798	1	10	0.182574186	0.547722558
9	10.22	19.782	0.907	1	20	0.129099445	0.387298335

Table 2. Carbon and Titanium Dioxide concentrations per series (1-9). Based on pre-determined absorption and scattering coefficients of human tissue optical properties. Ratios based on the amount to be formulated into RTV12C curing agent.

A ratio of 10:1 was used for RTV 12A: RTV 12C to increase the curing rate of the silicone matrix, as described by Yi-Hong et al., 2019. (29) Both carbon and titanium dioxide were calculated into the RTV 12C curing agent while maintaining the appropriate ratio of RTV 12C needed to complement each series RTV 12A. Adjusted amounts of RTV 12C are listed in Table 1-3. To prepare the absorber, 10mg of black carbon powder was dissolved in 10 mL of an RTV 12C carbon ink solution. Subsequently, 10g of titanium dioxide powder was dissolved in 100 mL of RTV 12C to make the necessary scatterer solution at 0.1g/mL. Both solutions were independently vortexed for 30 seconds at full speed, then placed in an ice batch and sonicated for 1 hour to break down the particles. The ice bath was necessary due to the low flashpoint of RTV 12C. (See Figure 4)

Once the appropriate amount of absorber and scatterer was calculated for each series, the appropriate amounts of each were combined, and the required quantity of curing agent was substituted to ensure the appropriate ratio of RTV 12C: RTV 12A was proportionate. It was advised that an issue experienced in prior versions of this experiment was with the silicone substrate adhering to the plastic container. With anticipation, three different lubricants were applied to coat the internal aspect of each mold. The first lubricant was Vaseline Pure Ultra White Petroleum Jelly (Manufactured by Covidien) and Trader Joe's Organic Extra Virgin Olive Oil Spray. The third lubricant was Ease Release 200, an industrial-strength aerosol clear mold release spray (Manufactured by Mann Release Technologies). Both components of this silicone compound were combined in a fume hood, hand-mixed with a metal spatula for 5 minutes, and then poured into their respective containers. The molds were then placed into a desiccator connected to a vacuum pump (remained between 25-30 inHG) to cure for 72 hours. (29) (See Figure 5)
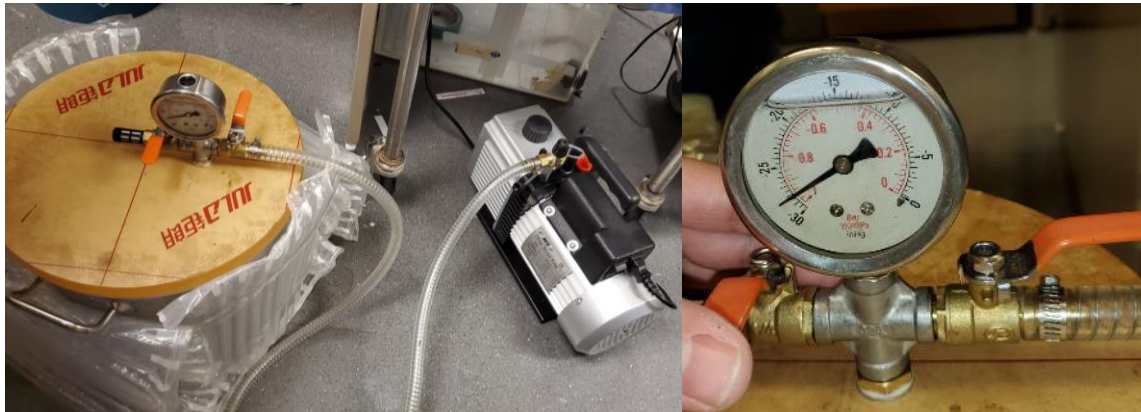
Figure 5. A) Desiccation system connected to vacuum pump. B) Dessication system remaining between 25-30 inHG after 72 hours of curing.

Of the three models, only the specimen coated with Ease Release 200 was extracted without tearing the sides of the silicone or destroying the mold. Upon removal, several trapped air bubbles were discovered. (See Figure 6)
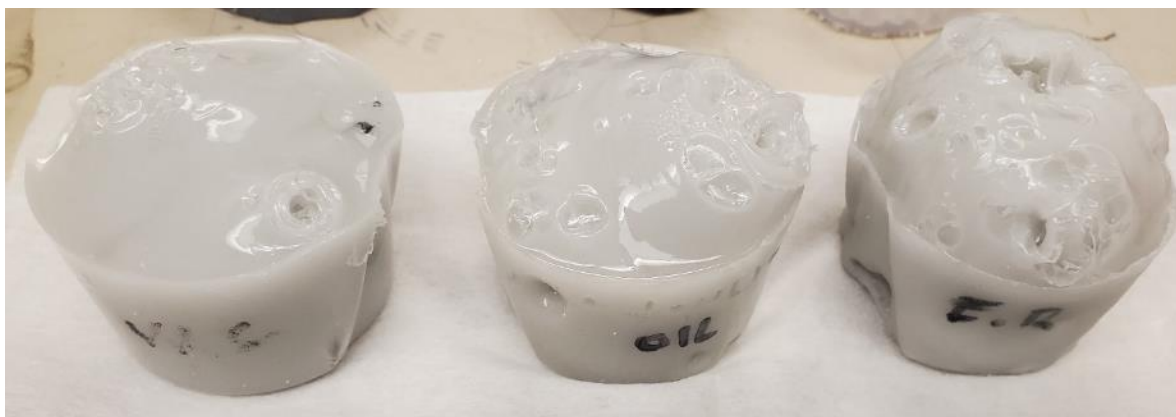
Figure 6. Specimens retrieved highlighting issue of trapped air bubbles. From Left to Right are the specimens coated with Vaseline, cooking spray, and ease release.

To address the trapped air bubble developing within the cured silicone compound, it was determined that a series of intermediary steps could be implemented to improve the final product. A tabletop dental vibrating device (Vibrator Variable Speed 115v Ea, Manufactured by Ray Foster Dental Supply-DV34) that is typically used in dental labs to remove trapped air bubbles from the intraoral cast molding before curing. The tabletop unit was first at the lowest speed, then gradually transitioned to the highest intensity for 2 minutes. This was to ensure that vibrations were gently introduced without splattering the material.

For the next phase of testing the silicone phantom mold, the first step would include a) 2 minutes of vibration + 5 minutes of desiccation, round b) vibration + desiccation, and then vibration. The molds were allowed to cure on the tabletop for 36 hours. After curing, it was discovered that no air bubbles were trapped in the cured silicone models. (See Figure 7)
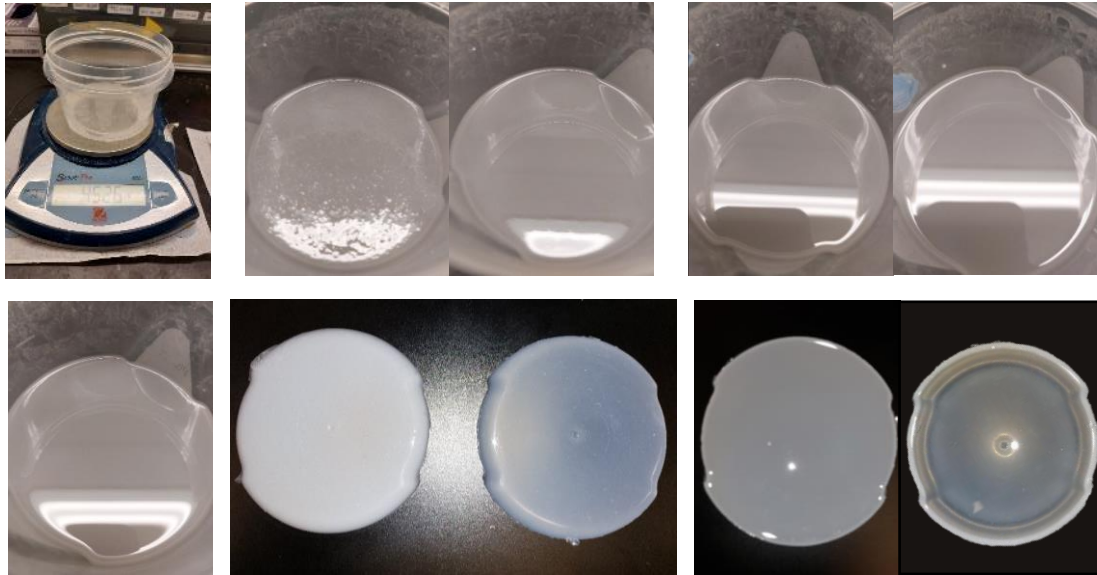
Figure 7. Silicone phantom mold testing phase. Multiple stages of vibration and desiccation that remove trapped air particles (top row). Final products as solid homogenous structures (bottom row).

A dental typodont with removable teeth (Manufacturer Kilgore Nissin 200) was utilized for this novel simulation of an actual-sized human anatomy. The typodont model was selected to standardize an actual human intraoral scan. The upper right maxillary second premolar (#4) was removed and would serve as the hypothetical tooth extraction socket for this novel phantom modeling system. A polyvinylsiloxane impression of the typodont was captured and then scanned with a desktop intraoral scanner and converted to a stereolithography digital file (.stl) for image manipulation in Autodesk Meshmixer (2017. Autodesk, INC). The digital image file was smoothened and adjusted to conform to printing requirements as advised by the Biotech Common 3-Dimensionl Printing Core at the University of Pennsylvania. (See Figure 8)
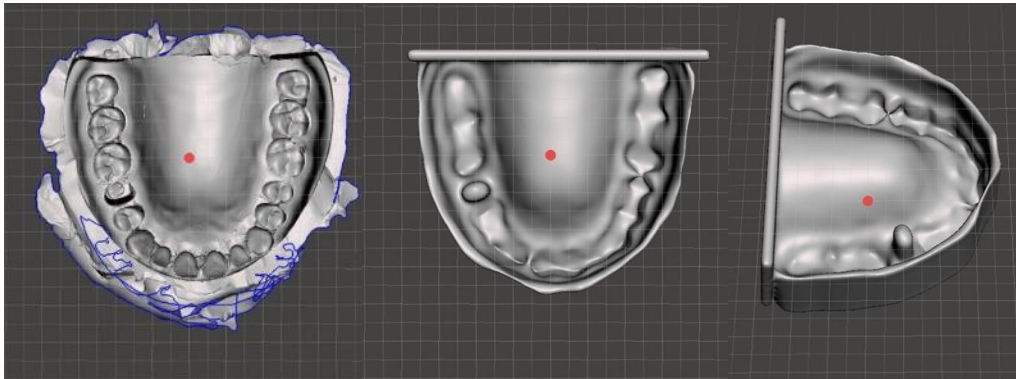
Figure 8. 3D file image manipulation in Autodesk Meshmixer software. 1) Initial scanned impression of maxilla and tooth extraction site, b) smoothening of relevant anatomies to allow for printing in resin material, c) lateral view showing inverted extraction site.

After the design of the printed mold was finalized, it was discovered that printing it in a standard resin material would not be feasible. The tear strength of the cured silicone compound was high and could not be extracted in the desired form without tearing it apart. Additional test molds were also printed in photopolymer resin materials manufactured by Formlabs in "Flexible" (#FLFLGR02) and "Elastic" (#FLELCL01). Both the flexible and elastic resins produced the desired shape and phantom model with the extraction socket completely intact when hand-torn apart and elevated using dental composite instruments. The process for removing each model from the flexible mold was between 2-3 hours, whereas the model housed in the elastic resin could be safely removed in 2 hours. (See Figure 9)

Figure 9. 3D Dental Model. a) top is traditional grey resin, left is "Flexible", right is "Elastic, b) Silicon material poured in all 3 resin materials, c) removal of phantom molds from each model (L-R traditional resin, flexible, and elastic).

In moving forward with the Formlabs elastic resin, 18 molds were fabricated using the Formlabs Printer (Formlabs 3L resin printer, Formlabs, Somerville, MA) in the Biotech Commons 3D printing core facility. Molds were printed in two sets, totaling over fifteen hours of processing and post-production time for each group. (See Figure 10)
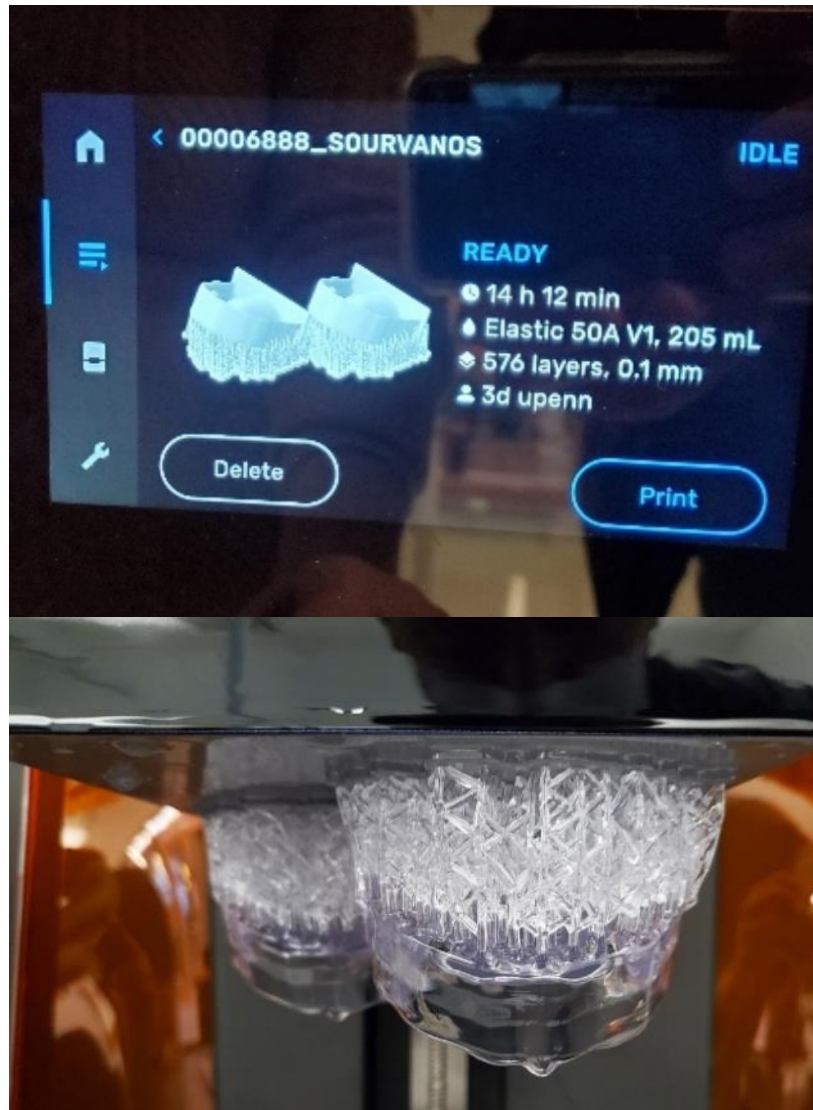
Figure 10. Processing information for each set prints in Formlabs 3D printer. b) Example of 2 prints before post-processing as recommended by manufacturer.

Implementing the additional steps of distributing each batch of silicone (based on optical properties by series 1-9) between 3 molds (traditional cylinder, dental mold 1, dental mold 2) proved several challenges. The first was that a larger volume of solution was needed, the second was that more air bubbles

would be entrapped in the compound, and the third was that all three molds needed to be perfectly homogenous and of the same concentration. After several test rounds to determine the optimal post-mixture processing sequence and instrumentation to fill a single cylinder (traditional phantom. 260mL) and two dental molds (novel 3-dimensional phantom, 40mL each). While in the large container (340mL total, the silicone compound was hand-stirred in a counterclockwise direction to prevent the introduction of trapped air while on the vibrating plate. (See Figure 11 – 12)

Figure 11. Due to the high tear-ability of the silicone phantom in its cured form, removing the extraction socket should be the last portion and the most difficult. a) resin remaining in the extraction socket. B) extraction socket exposed without resin.
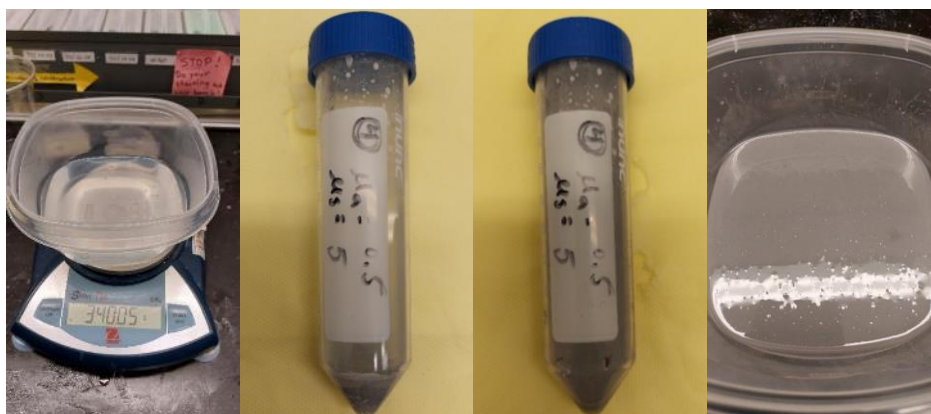
Figure 12. Initial Mixing Sequence of RTV Silicone Compound. a) RTV 12A silicone compound, b) RTV 12C Series 4 absorption and scattering ratios pre vortex. Note TiO2 at bottom of container. c) RTV 12C after vortexing showing equal distribution, d) RTV 12C & 12A.

This final processing sequence was replicated nine times and included the following steps (See Table 3):

Step	Container	Processing Description	
Step 1	Large Container (1)	Stirring & Vibrating 2 mins (3 levels). 5 Minutes Desiccation.	
Step 2	Large Container (2)	Stirring & Vibrating 2 mins (3 levels). 5 Minutes Desiccation.	
Step 3	Large Container (3)	Stirring & Vibrating 2 mins (3 levels). 5 Minutes Desiccation.	

Step 4	Pour into Cylinder mold.		
Step 5	Cylinder Mold (1)	Stirring & Vibrating 2 mins (3 levels). 5 Minutes Desiccation.	
Step 6	Cylinder Mold (2)	Stirring & Vibrating 2 mins (3 levels). 5 Minutes Desiccation.	
Step 7	Pour into Dental Molds (x2). Processed simultaneously.		
Step 8	Dental Mold #1a (1)	Stirring & Vibrating 2 mins (3 levels). 5 Minutes Desiccation.	
Step 9	Dental Mold #1a (2)	Stirring & Vibrating 2 mins (3 levels). 5 Minutes Desiccation.	
Step 10	Dental Mold #1b (1)	Stirring & Vibrating 2 mins (3 levels). 5 Minutes Desiccation.	
Step 11	Dental Mold #1b (2)	Stirring & Vibrating 2 mins (3 levels). 5 Minutes Desiccation.	

Table 3. Final Processing Sequence for Phantom Fabrication

2.2.1.1 Discussion

The development of cylindrical and 3-dimensional phantom models required a rigorous and continuous refinement of the manufacturing protocol. (See Table 3). The goal was to create a phantom series that was entirely homogeneous, free from any air bubbles or inconsistencies. Each series was required to have the same optical property ratios in both cylinder and 3-dimensional shapes. Achieving this required multiple batches and the incorporation of additional desiccation/vibration steps into the protocol. The timing was

imperative as the silicone material would begin to set at about fifty-five minutes. With a systematic and thorough approach, phantom models that met the standards of quality and reliability in the field of scientific research for the Zhu lab. The resulting phantom models have proven to be invaluable tools in the advancement of various scientific studies and have contributed significantly to the understanding of complex light transmission phenomena.

2.2.1.2 Results

A total of 9 Phantoms groups were created in both cylindrical and 3-dimensional shapes according to the pre-determined ratios of carbon and titanium oxide. (See table 1-3). This resulted in 9 total cylindrical phantoms with duplicate 3-dimensional dental molds (n=18). (See Figure 1-12).
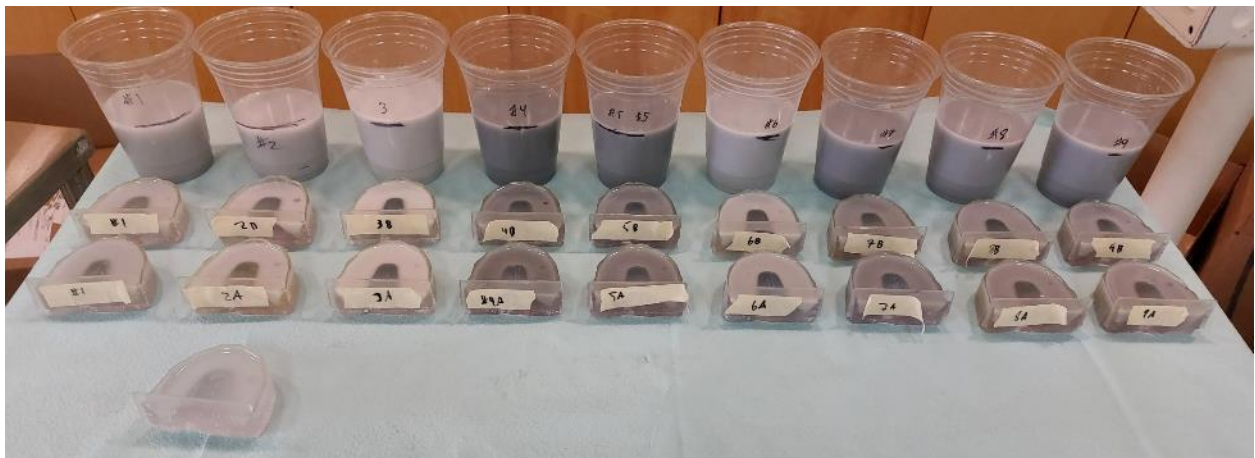
Figure 13. Phantom Model Groups 1-9 in both cylinder (back row) and 3-dimensional dental mold (front) configurations. N=27.

2.3   Medical Dosimetry System

The Zhu lab group developed a standardized methodology to validate the optical properties of the nine phantom model cylinders. (21, 29, 108, 109, 112, 115, 116) Power measurements were standardized and acquired inside an integrating sphere (See Figure 14), and isotropic detectors were calibrated with an LED calibration sphere. (See Figure 15)
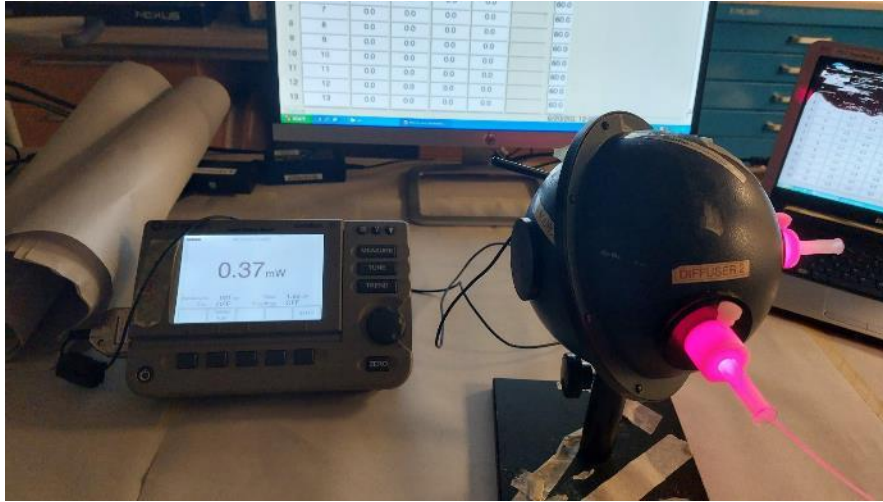
Figure 14. Power Measurements conducted with point light source entering a diffuser integrating sphere (right). Which is directly connected to a power meter reading output mW (left).
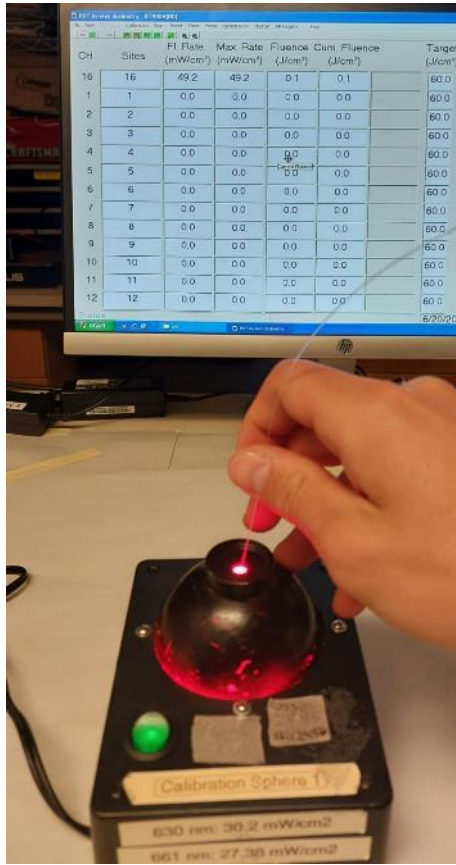
Figure 15. Isotropic detector placed directly inside of LED Calibration Sphere with output measurements reading directly into dosimetry system.

A dual catheter motorized dosimetry system paired with wavelength-based algorithms acquired and analyzed data and calibrated to known tissue optical properties from the nine series of cylindrical phantom models. (See Figure 16 - 17). A customized Matlab® software analyzed the measured data to determine tissue optical properties, including absorption (µa), reduced scattering (µ's) coefficients, and the effective attenuation coefficient (µeff). (See Figure 16 - 18)
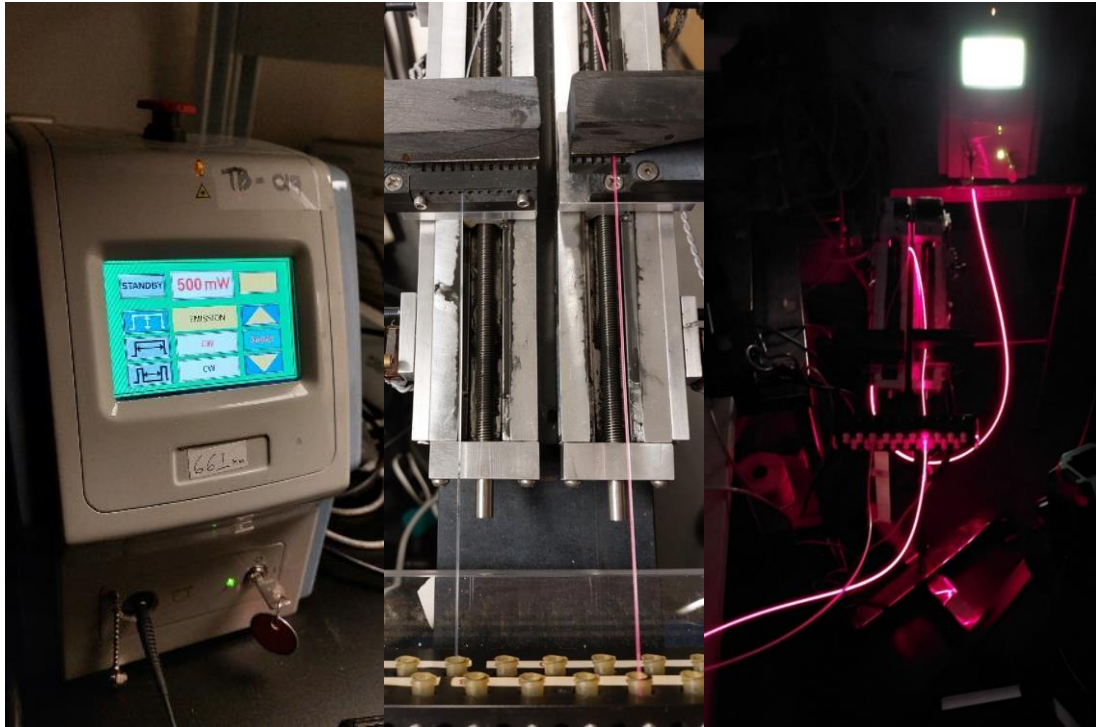
Figure 16. a) 661nm laser console, b) dual motorized dosimetry system. c) Laser Activation of fibers from 661 laser unit through dual motor system.
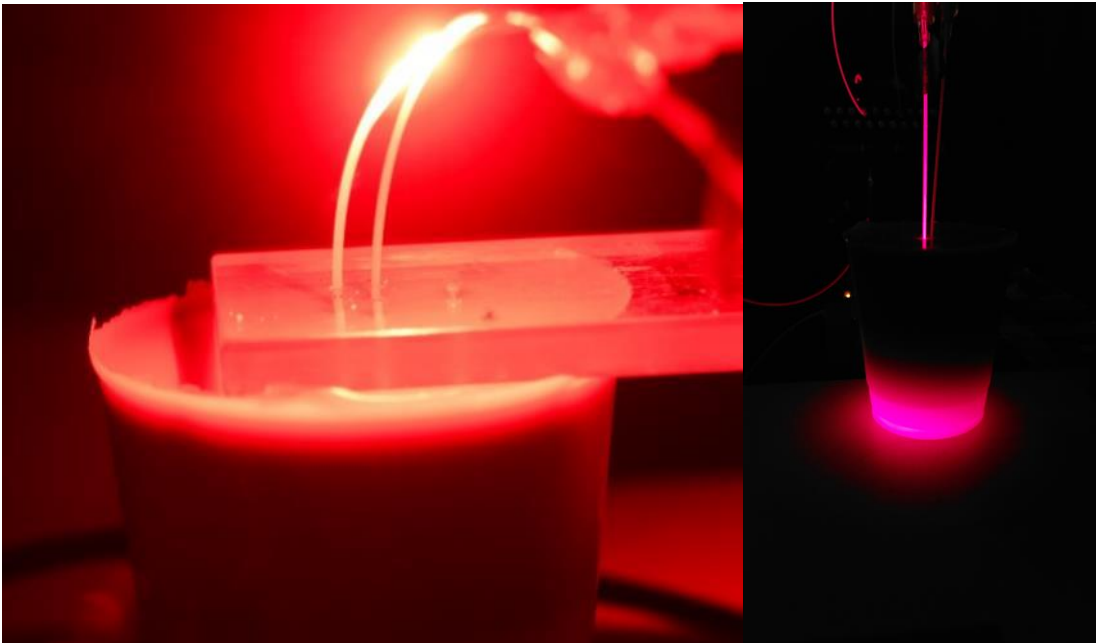
Figure 17. Standard cylindrical silicone phantom model. Catheters containing light source (left) and isotropic detector (right) are guided through a custom fabricated jig that will ensure equal distance placement amongst all models.
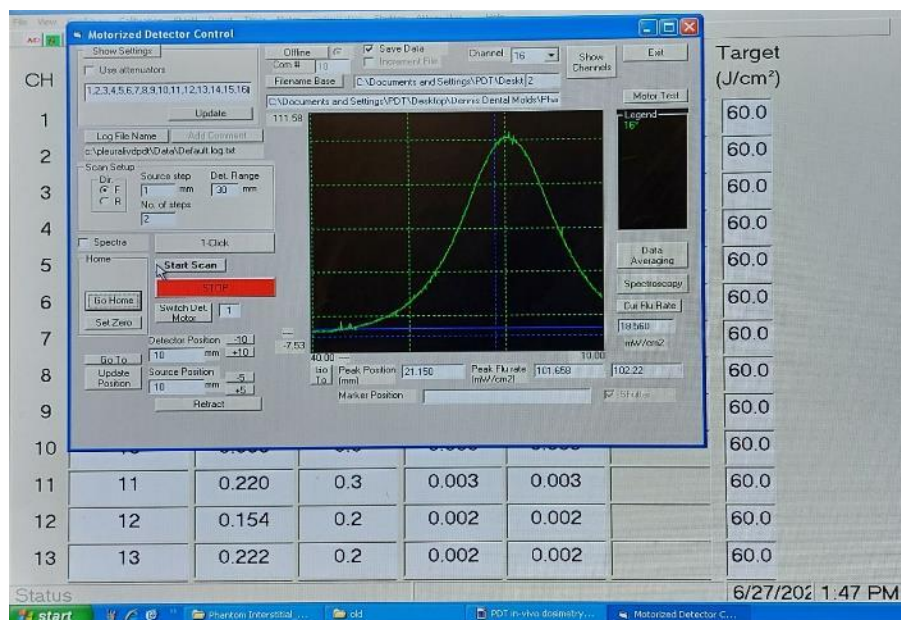
Figure 18. Medical Dosimetry System during acquisition of data from cylindrical model.
Data is prior to processing through algorithms.

This "system automatically records and plots the light fluence rate per unit source power as a function of position." (109) This system consisted of 2 transparent 1.86mm catheters (Flexineedle 18G 20cm with Luer Lock, Manufactured by Best Medical Int.) that were connected to a 665nm laser system (B&W Tek, Newark DE) and one channel of a custom sixteen channel medical dosimetry system. A 0.8mm isotropic detector (IP85, Manufactured by Medlight S.A.) and a custom 2.0mm point light source (#7035-01 Rev 2; Manufactured by Pioneer Optics) were placed inside of the catheters and connected to a computer-controlled dual-motor platform (Velmex, Inc. East Bloomfield, NY). During activation, the position of the light source was fixed, and the detector acquired data at 0.05mm intervals. (See Figure 19)

To Light Dosimetry System. Isotropic Detector

From 661nm Laser System. Point Light Source.

Vertical Distance Between Point Source and Detector

Horizontal Distance Between Point Source and Detector
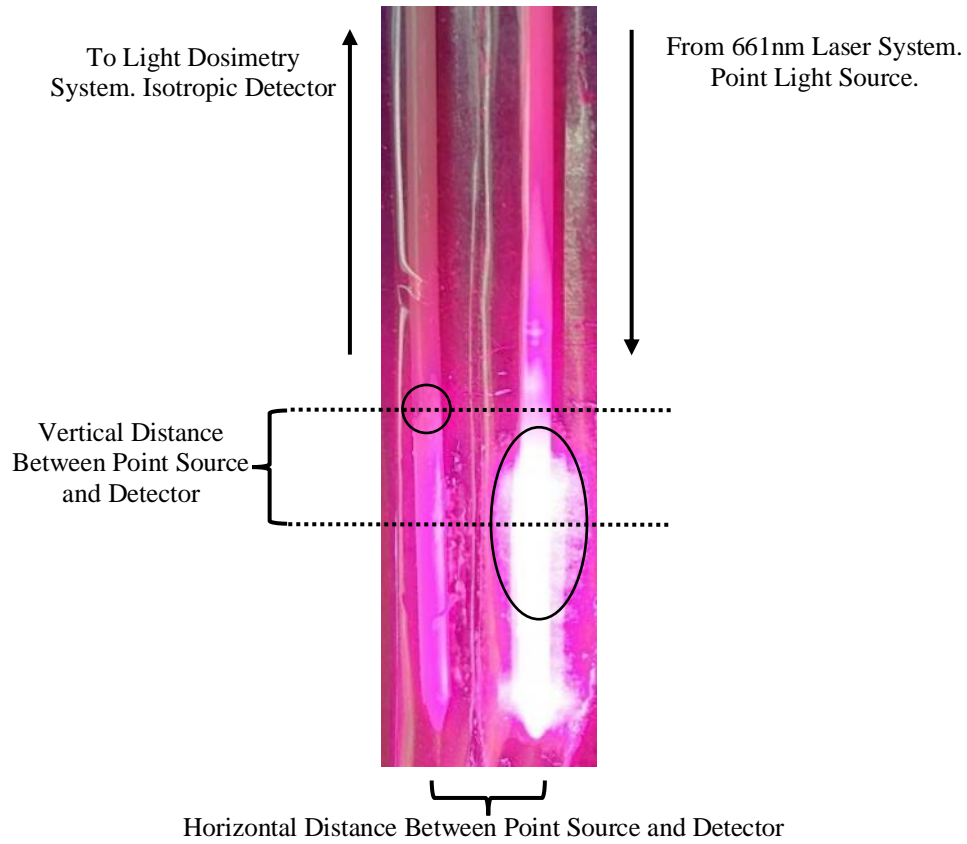
Figure 19. Schematic of dosimetry system with two parallel catheters containing 0.5mm isotropic detector (left) and an activated 2mm point light source (right).

The diffusion approximation method was utilized to determine how light propagates through a scattering medium like the phantom model simulating human tissue. Although light fluence rate φ measurements at two different distances can be used to calculate absorption and scattering coefficients, this methodology involves acquiring over 800 measurements at varying depths. (29) Per Ong and colleagues (29), the light fluence rate φ per source power S at a distance r from a point source can be expressed as the following formula:

28

$$\frac{\varphi}{S} = \frac{\mu^2 eff}{4\pi r}e^{-\mu_{efff}r} = \frac{3\mu_s'}{4\pi r}e^{-\mu_{efff}r}$$

Further details about the distance calculations, differential evolution algorithms, wavelength fitting algorithms, and system configurations can be found in prior work published by this laboratory group. (21, 29, 108, 109, 112, 115)

2.4 Interstitial Light Delivery (Cylinder Phantom)

A dual motor continuous wave medical dosimetry system was engaged for each cylindrical phantom mold in triplicate. (See Figure 20) This system is optimized by a continuous wave transmittance spectroscopy system. The primary function of this medical dosimetry system is to quantify the optical properties of absorption and reduced scattering within the regions of interest.
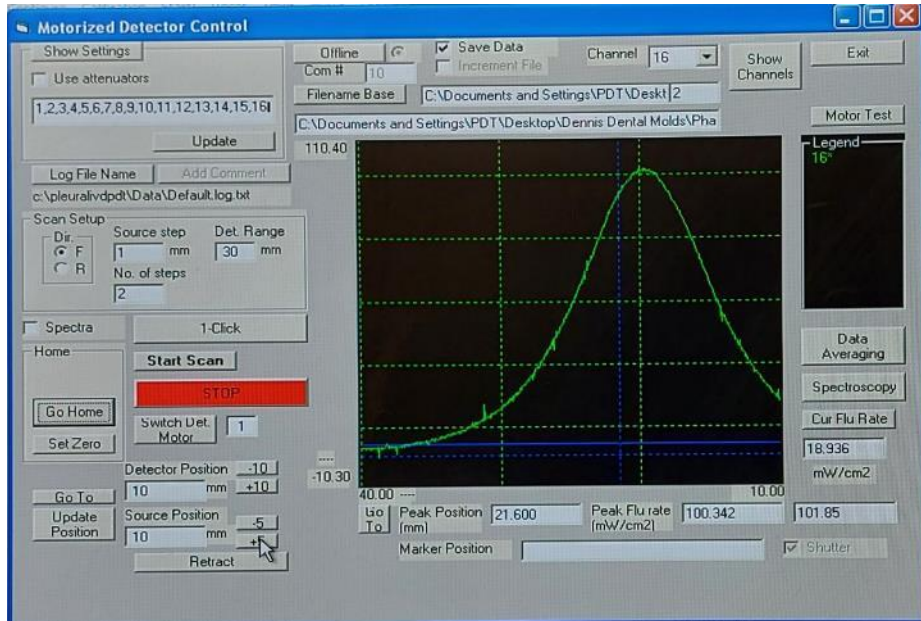
Figure 20. Medical Dosimetry system software with scan setup and wavelength visualization.

The initial detector and source positions were set at 10mm from the bottom of the catheters to allow for enough distance from the most inferior boundary of the mold. The source step was established at 1mm, the range at 30mm, with a total of 2 steps per dosimetry calculation. (See Figure 21)
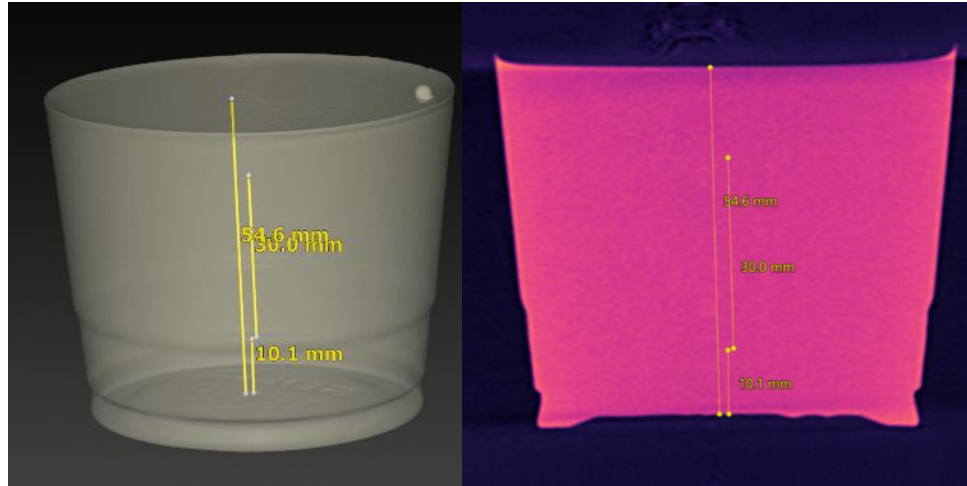
Figure 21. CBCT visualization of cylinder phantom #1. Digital measurements are visualized on the internal aspect, representing the range of measurements scanned with the dual motor dosimetry system.

A total of nine silicone phantoms were fabricated to predetermined optical properties. (See table 1-3). To ensure the accuracy and reliability of results, each phantom was scanned a total of three times without adjusting the catheters. This resulted in a total of nine scans per phantom, providing a robust dataset of 81 absorption measurements and 81 reduced scattering measurements for detailed analysis. The histogram was standardized to the "fit range" from -0.9 to 0.9 readings. (See Figure 22)

Figure 22. Matlab software with standardized settings for analysis.

2.4.1 Statistical Analysis & Discussion

2.4.1.1 Data Distribution

-Methods and Materials: Data was analyzed using IBM SPSS Statistic (version 29.0.1.0 (1711). Initial tests for normality were conducted using both the Kolmogorov-Smirnov (K-S) and Shapiro-Wilk (S-W) Tests.

-Results: The absorption and scattering properties of all nine phantoms were subjected to analysis using the K-S and S-W tests. The K-S test produced a statistic of .390 (P<.001) and 0.357 (P<.001) for absorption and scattering, respectively. The S-W test reported a corresponding statistic of 0.193 (p<.001) and 0.545 (p<.001) for absorption and scattering, respectively. The results indicate that both the measured absorption and scattering data for all nine phantoms significantly deviated from a normal distribution (p<.001 for both tests. (See Figure 23)

Tests of Normality

	Kolmogorov-Smirnov[a]			Shapiro-Wilk		
	Statistic	df	Sig.	Statistic	df	Sig.
Measured Absorption	.390	81	<.001	.193	81	<.001
Measured Scattering	.357	81	<.001	.545	81	<.001

a. Lilliefors Significance Correction

Figure 23. SPSS software output for 9 phantoms (81 absorption, 81 scattering).

-Discussion: A deviation from normality should be expected given that all phantoms were fabricated with pre-determined absorption and scattering coefficients that are not related. The significant deviation from normality suggests that each phantom can contribute to a diverse range of readings which are attributed to the dosimetry systems ability to recognize differences in optical coefficients.

2.4.1.2 Absorption and Reduced Scattering Coefficients

-Primary Objective: To determine if there is a significant difference in quantified absorption and reduced scattering coefficients between the nine phantoms.

-AIM: This analysis aims to determine if the nine silicone phantoms with predetermined optical properties exhibit significant differences in their absorption and scattering properties.

-Materials and Methods: Data was analyzed using IBM SPSS Statistic (version 29.0.1.0 (1711). A non-normal distribution was established for this dataset, resulting in the non-parametric Kruskal-Wallis (K-W) H test being utilized to detect differences among the nine phantoms for absorption and reduced scattering coefficients. The post hoc comparison Mann-Whitney (M-W) U test was utilized for pairwise comparisons to determine which specific pairs differ. Thirty-six pairs were conducted for absorption and scattering optical properties with a Bonferroni correction (.001389).

-Results: The K-W test reported statistically significant differences among the phantoms for absorption (H= 63.4587, p<.001) and scattering (H=61.321, p<.001). (See Figure 24, Table 4)

Test Statistics[a,b]

	Measured Absorption
Kruskal-Wallis H	63.458
df	8
Asymp. Sig.	<.001

a. Kruskal Wallis Test
b. Grouping Variable: Phantom ID

Test Statistics[a,b]

	Measured Scattering
Kruskal-Wallis H	61.321
df	8
Asymp. Sig.	<.001

a. Kruskal Wallis Test
b. Grouping Variable: Phantom ID

Figure 24. SPSS software output Kruskal-Wallis test.

Pairwise Comparisons		
	(Absorption)	(Scattering)
Phantom 1 vs 2:	U = 31.500, p = .420	U = 9.00, p = .005
Phantom 1 vs 3:	U = 0.000, p = <.001*	U = 0.000, p = <.001*
Phantom 1 vs 4:	U = 0.000, p = <.001*	U = 36.000, p = .691
Phantom 1 vs 5:	U = 18.000, p = .045	U = 0.000, p = <.001*
Phantom 1 vs 6:	U = 36.000, p = .689	U = 0.000, p = <.001*
Phantom 1 vs 7:	U = 0.000, p = <.001*	U = 16.000, p = .030
Phantom 1 vs 8:	U = 0.000, p = <.001*	U = 7.000, p = .003
Phantom 1 vs 9:	U = 0.000, p = <.001*	U = 27.000, p = .233
Phantom 2 vs 3:	U = 0.000, p = <.001*	U = 0.000, p = <.001*
Phantom 2 vs 4:	U = 0.000, p = <.001*	U = 26.000, p = .200
Phantom 2 vs 5:	U = 18.000, p = .047	U = 0.000, p = <.001*
Phantom 2 vs 6:	U = 36.000, p = .690	U = 0.000, p = <.001*
Phantom 2 vs 7:	U = 0.000, p = <.001*	U = 6.000, p = .002
Phantom 2 vs 8:	U = 0.000, p = <.001*	U = 40.000, p = .965
Phantom 2 vs 9:	U = 0.000, p = <.001*	U = 30.000, p = .354
Phantom 3 vs 4:	U = 0.000, p = <.001*	U = 0.000, p = <.001*
Phantom 3 vs 5:	U = 18.000, p = .046	U = 9.000, p = .005
Phantom 3 vs 6:	U = 36.000, p = .690	U = 1.000, p = <.001*
Phantom 3 vs 7:	U = 0.000, p = <.001*	U = 0.000, p = <.001*
Phantom 3 vs 8:	U = 0.000, p = <.001*	U = 0.000, p = <.001*
Phantom 3 vs 9:	U = 0.000, p = <.001*	U = 0.000, p = <.001*
Phantom 4 vs 5:	U = 2.000, p = <.001*	U = 2.000, p = <.001*
Phantom 4 vs 6:	U = 0.000, p = <.001*	U = 0.000, p = <.001*
Phantom 4 vs 7:	U = 6.000, p = .002	U = 40.000, p = .965
Phantom 4 vs 8:	U = 9.000, p = .005	U = 26.000, p = .200
Phantom 4 vs 9:	U = 26.000, p = .200	U = 38.000, p = .825
Phantom 5 vs 6:	U = 36.500, p = .723	U = 32.000, p = .439
Phantom 5 vs 7:	U = 9.000, p = .005	U = 0.000, p = <.001*
Phantom 5 vs 8:	U = 9.000, p = .005	U = 0.000, p = <.001*
Phantom 5 vs 9:	U = 5.000, p = .002	U = 1.000, p = <.001*
Phantom 6 vs 7:	U = 0.000, p = <.001*	U = 0.000, p = <.001*
Phantom 6 vs 8:	U = 0.000, p = <.001*	U = 0.000, p = <.001*
Phantom 6 vs 9:	U = 0.000, p = <.001*	U = 0.000, p = <.001*
Phantom 7 vs 8:	U = 12.000, p = .012	U = 2.000, p = <.001*
Phantom 7 vs 9:	U = 0.000, p = <.001*	U = 24.000, p = .145
Phantom 8 vs 9:	U = 5.500, p = .002	U = 31.000, p = .402
*Significant with Bonferroni Correction Factor (0.05/36 = 0.00138)		

Table 4. Results from Mann-Whitney pairwise comparison with Bonferroni adjustment.

-Discussion: The K-W test provided evidence of the differences in absorption and reduced scattering coefficients between the nine phantoms. The M-W test and correction reported variability in significance across all the phantoms.

-Conclusion: The findings of this analysis emphasize the significant variations in the optical properties observed among the nine phantoms. This heterogeneity is expected due to the pre-determined ratios, with some models being more similar than others. It is worth noting that several of the pairwise comparisons exhibited similarities. (See table 1-4). This supports the notion that the reduced scattering coefficient will have a direct dosimetric effect on absorption and vice versa. These observations highlight the complexity between varying optical properties in a phantom and the considerations needed for real-time dosimetry adjustment during therapy.

2.4.1.3   Variations Within Each Phantom Group

-Primary Objective: To determine the consistency of triplicate measurements within each phantom group.

-Aim: This analysis aims to evaluate the consistency of triplicate measurements for each phantom and to investigate if there are any statistical variations between these triplicate measurements.

-Materials and Methods: Data was analyzed using IBM SPSS Statistic (version 29.0.1.0 (1711). The Friedman's test with Bonferroni correction for repeated measures was selected due to non-normality.

-Results: Friedman's Test Pair Comparison with correction is detailed in Table 5. (See Figure

Friedman's Test Pair Comparisons				
	(Absorption)		(Scattering)	
Sample 1-Sample 2	*Sig.*	*Adj. Sig.[a]*	*Sig.*	*Adj. Sig.[a]*
Run 1 Sample 1-Run 1 Sample 3	0.83	1	0.282	1
Run 1 Sample 1-Run 1 Sample 2	0.576	1	0.182	1
Run 1 Sample 1-Run 2 Sample 1	0.302	1	0.121	1
Run 1 Sample 1-Run 3 Sample 3	0.168	1	0.028	1
Run 1 Sample 1-Run 2 Sample 2	0.078	1	0.01	0.354
Run 1 Sample 1-Run 2 Sample 3	0.02	0.725	0.005	0.186
Run 1 Sample 1-Run 3 Sample 1	0.006	0.212	<.001	0.024
Run 1 Sample 1-Run 3 Sample 2	0.002	0.061	<.001	0.009
Run 1 Sample 3-Run 1 Sample 2	0.731	1	0.796	1
Run 1 Sample 3-Run 2 Sample 1	0.414	1	0.636	1
Run 1 Sample 3-Run 3 Sample 3	0.245	1	0.263	1
Run 1 Sample 3-Run 2 Sample 2	0.121	1	0.132	1
Run 1 Sample 3-Run 2 Sample 3	0.035	1	0.085	1
Run 1 Sample 3-Run 3 Sample 1	0.011	0.4	0.02	0.725
Run 1 Sample 3-Run 3 Sample 2	0.003	0.124	0.01	0.354
Run 1 Sample 2-Run 2 Sample 1	0.636	1	0.83	1
Run 1 Sample 2-Run 3 Sample 3	0.414	1	0.389	1
Run 1 Sample 2-Run 2 Sample 2	0.228	1	0.212	1
Run 1 Sample 2-Run 2 Sample 3	0.078	1	0.143	1
Run 1 Sample 2-Run 3 Sample 1	0.028	1	0.039	1
Run 1 Sample 2-Run 3 Sample 2	0.01	0.354	0.02	0.725
Run 2 Sample 1-Run 3 Sample 3	0.731	1	0.519	1
Run 2 Sample 1-Run 2 Sample 2	0.464	1	0.302	1
Run 2 Sample 1-Run 2 Sample 3	0.197	1	0.212	1
Run 2 Sample 1-Run 3 Sample 1	0.085	1	0.064	1
Run 2 Sample 1-Run 3 Sample 2	0.035	1	0.035	1
Run 3 Sample 3-Run 2 Sample 2	0.699	1	0.699	1
Run 3 Sample 3-Run 2 Sample 3	0.344	1	0.547	1
Run 3 Sample 3-Run 3 Sample 1	0.168	1	0.228	1
Run 3 Sample 3-Run 3 Sample 2	0.078	1	0.143	1
Run 2 Sample 2-Run 2 Sample 3	0.576	1	0.83	1
Run 2 Sample 2-Run 3 Sample 1	0.322	1	0.414	1
Run 2 Sample 2-Run 3 Sample 2	0.168	1	0.282	1
Run 2 Sample 3-Run 3 Sample 1	0.667	1	0.547	1
Run 2 Sample 3-Run 3 Sample 2	0.414	1	0.389	1
Run 3 Sample 1-Run 3 Sample 2	0.699	1	0.796	1
Bonferroni Correction (0.05/36= .00138)				

Table 5. Results from Friedman's

test pair comparison with Bonferroni adjustment.
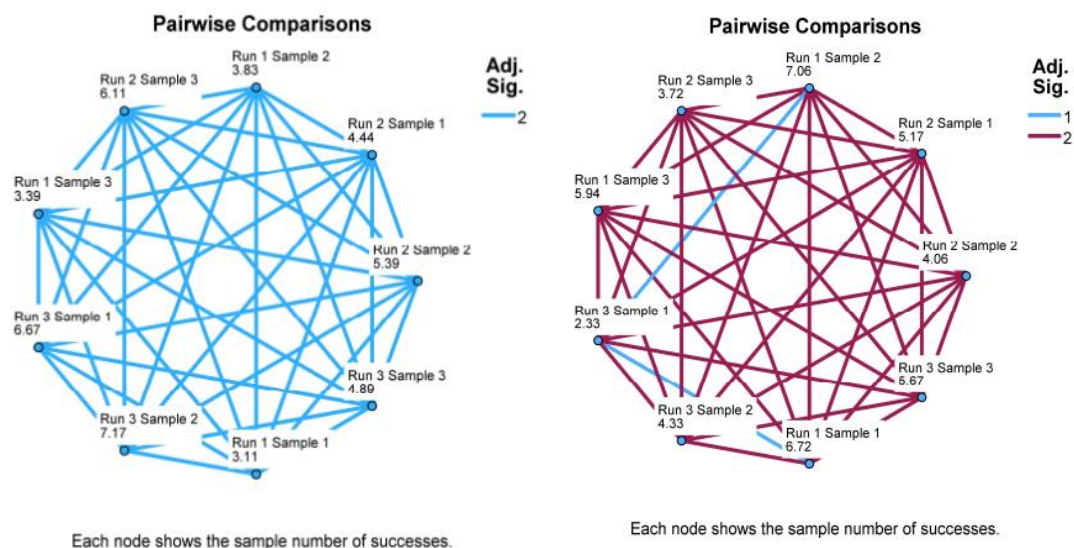
Table 6. SPSS software output Pairwise Comparisons for Absorption (left), Scattering (right).

-Discussion: The results of comparing all the phantoms indicate that the measurements are consistent across each phantom. (See Figure 1-25). After adjusting the p-value with the appropriate correction factor, none of the differences remained significant. (See table 1-5)

-Conclusion: The results obtained from the triplicate measurements of all nine phantoms have demonstrated a high level of consistency and reliability with this dosimetry system. These results support the repeatability and stability of this study's measurement techniques. Therefore, this experimental model is highly sensitive, making it a reliable tooth for assessing absorption and scattering in phantom model applications.

2.4.1.4 Relationship to predetermined absorption and scattering

-Primary Objective: To assess whether there is a relationship between the predetermined absorption or reduced scattering coefficients and the measurements obtained from the medical dosimetry system.

-Aim: This analysis aims to quantify the relationship between the predetermined absorption and scattering coefficients and the measurements obtained from the medical dosimetry system.

-Materials and Methods: Data was analyzed using IBM SPSS Statistic (version 29.0.1.0 (1711). The Spearman's rank order correlation was selected to measure directionality, given the data did not meet the normality assumption.

-Results: A significant correlation coefficient of .594 for absorption was found between the measured and predetermined absorption p<.001. A significant correlation coefficient of .582 was determined between measured and predetermined scattering p<.001. (See Figure 25)

Correlations

			Measured Absorption	Predetermined Absorption
Spearman's rho	Measured Absorption	Correlation Coefficient	1.000	.594[**]
		Sig. (2-tailed)	.	<.001
		N	81	81
	Predetermined Absorption	Correlation Coefficient	.594[**]	1.000
		Sig. (2-tailed)	<.001	.
		N	81	81

**. Correlation is significant at the 0.01 level (2-tailed).

Correlations

			Measured Scattering	Predetermined Scattering
Spearman's rho	Measured Scattering	Correlation Coefficient	1.000	.582[**]
		Sig. (2-tailed)	.	<.001
		N	81	81
	Predetermined Scattering	Correlation Coefficient	.582[**]	1.000
		Sig. (2-tailed)	<.001	.
		N	81	81

**. Correlation is significant at the 0.01 level (2-tailed).

Figure 25. SPSS software output for Spearman's Correlation for Absorption (top), Scattering (bottom).

-Discussion: The correlation coefficient for absorption (0.594) indicates a positive relationship between the predetermined absorption measurements and those acquired from the dosimetry system. This suggests that medical dosimetry measurements are reliably associated with the predetermined values (p<.001). The observed correlation coefficient for scattering (.582) indicates a similar relationship between predetermined scattering and acquired dosimetry measurements. As both sets of predetermine measurements begin to increase, so do the measurements obtained from the dosimetry system. (See Figure 25)

-Conclusion: The results of this experiment demonstrate a statistically significant correlation between predetermined absorption and scattering coefficients and the corresponding measurements obtained from the medical dosimetry system.

2.5   Semi-infinite Light Delivery (Cylinder and 3-dimensional Shape)

2.5.1   Methods

The success of light-based therapy depends on the amount of light transmitted (Max fluence rate = mW/cm^2) to the target site or region of interest. Based on prior work from Andreea Dimofte et al., (21) a calibrated 0.5mm isotropic detector (MEDLIGHT) and a 2mm isotropic point light source (Pioneer optics) were placed inside two catheters (Flexineedle). The catheters were secured at a distance of 3m by a prefabricated acrylic jig and secured with clear transparent adhesive tape on the front and dark-colored adhesive tape on the posterior. (See Figure 26). The isotropic detector was connected to a 16-channel receiver and to a medical dosimetry system with the potential to measure the effective attenuation coefficient (μ-eff), absorption (μ-a), and scattering (μ's). The light source was connected to a 661nm laser system.
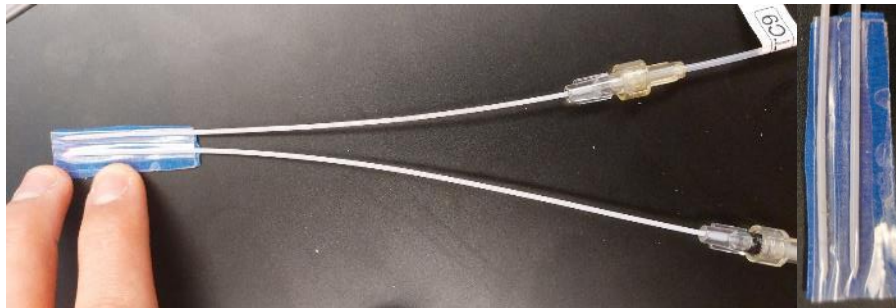
Figure 26. a) dual catheter placement inside of catheters containing detector and light source at fixed distance. b) closeup of secured portion.
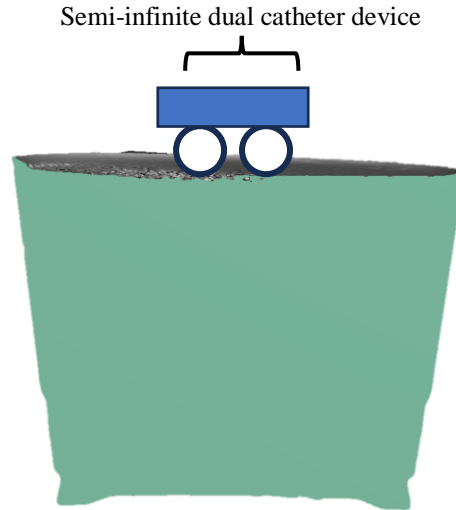
Figure 27. Semi-infinite dual catheter device schematic placed on top of a cylindrical dental mold. Note that both catheters are directly in contact with the target area region of interest.

All surface-based measurements were acquired using the same protocol. The portion of the catheters covered with clear transparent adhesive tape was placed directly in contact with the surface. The surface with dark-colored adhesive paper was facing away from the surface. (See Figure 27). Each experimental series consisted of 10 measurements. The data capture was acquired in 10-second intervals triggered by an internal automatic camera timer. A camera and tripod were standardized to capture the values directly from the dosimetry system.

Figure 29. Semi-infinite device placed on 3-Dimensional phantom simulating human maxilla with extraction socket. a) lateral view. b) superior view showing that semi-infinite device is fully in contact with target surface.
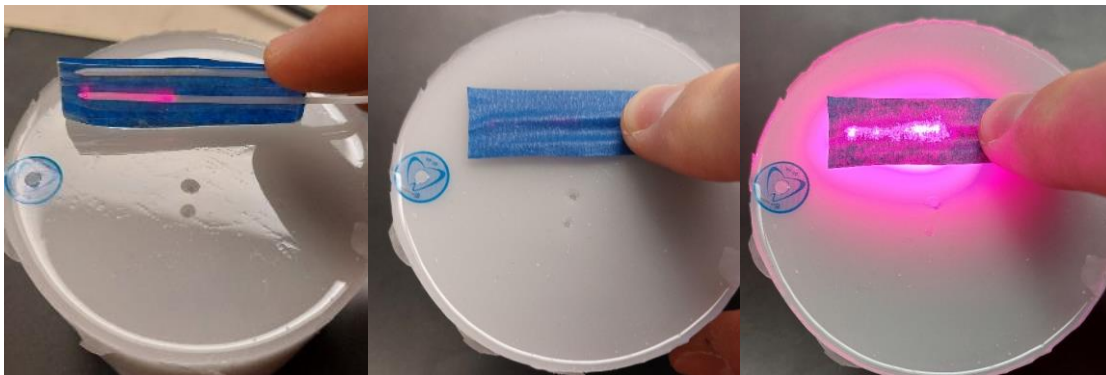
Figure 28. A semi-infinite device placed on the flat surface of cylindrical tissue phantom #1. a) Semi-infinite device facing up with light source activated 10mm away from tip. b) Dark-colored adhesive paper portion facing away from the target surface, c) activation of semi-infinite light delivery with 661nm laser device.

Semi-infinite reflectance measurements were acquired from the cylindrical phantoms and both sets of 3-dimensional dental phantoms (n=27). (See Figure 28 – 29). Ten randomized measurements were taken in each region of interest by a photographic camera timer in 10-second intervals. Amongst the varying optical properties, there were several regions of interest, including convex, concave, extraction socket hole, and other random volumetric shapes. Each phantom cylinder's innermost top flat planar segment was considered the placebo for each series 1-9. Different non-flat planar components were assessed. (See Figure 30 and 31)

Figure 31. Phantom Model shapes used for Semi-Infinite experiments. a) cylindrical, b) 3-dimensional phantom with regions of interest (red highlight), c) 3-dimensional phantom with complex geometries of interest, green (left) extraction socket.

Figure 30. a) Semi-infinite device with 661nm light source activated, b) 3-Dimensional dental phantom with buccal region of interest, c) cylindrical phantom with top outer region of interest.

The cylindrical phantoms had multiple regions of interest. (See Figure 30) This included the flat planar top portion (inner/middle), full (outer), Side 1 (leading edge), Side 2 (center), Side 3 (bottom edge), Bottom (middle), and Bottom (outer edge). (See Figure 31)
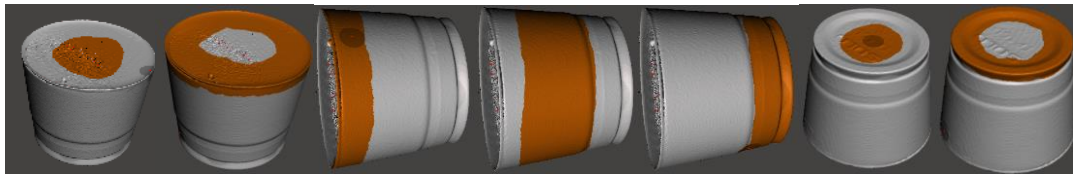
Figure 32. Cylindrical Phantom regions of interest. a) top center (placebo), b) top outer, c) side 1 top edge, d) side 2 middle, e) side 3 bottom, f) bottom middle, g) bottom outer edge.

The 3-Dimensional dental arches included only non-flat planar surfaces and consisted of the posterior buccal (extraction socket), posterior palatal (extraction socket), anterior (buccal), anterior (lingual), posterior (buccal), and posterior (lingual). (See Figure 32)
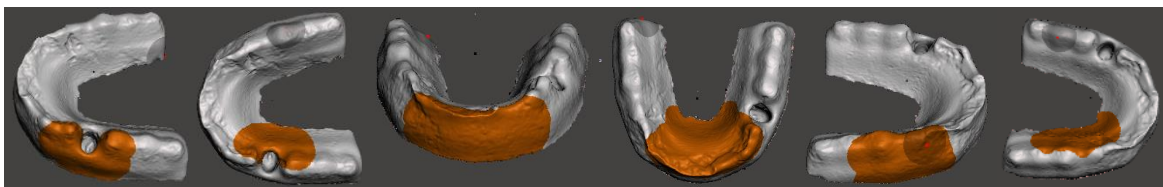
Figure 33. 3-Dimensional non-flat planar surfaces and regions of interest: a) posterior buccal (extraction socket), b) posterior palatal (extraction socket), c) anterior (buccal), d) anterior (lingual), e) posterior (buccal), f) and posterior (lingual).

All cylindrical and 3-dimensional dental models were digitized utilizing a cone-beam computerized tomography (CBCT) machine (3D Accuitomo XYZ Slice View Tomograph, Norita, Japan). This was to validate that all models were free of voids (no microbubbles) and to quantify shape and acquire

44

measurements where necessary. (117-123) The settings for all image acquisitions were as follows: field of view 170 x 120, tube voltage 90kV, tube current 5.0mA, Imaging D140 x 100 Hi-Fi. All CBCT images were converted to DICOM files with proprietary software provided by Norita and Stereolithography (STL) files by InVesalius 3.1 (Center for Information Technology Renato Archer, Brazil). The data in the DICOM file allows us to view the internal regions of interest, whereas the STL files allow us to assess the outer surface-based topographies. CBCT images were viewed and assessed by the DTX Studio Implant Software (Version 3.6.6.1, Nobel Biocare, Goteborg, Sweden). (See Figure 34)

Figure 34. Semi-infinite, phantom model, CBCT assessment.

2.5.2   Results

A novel phantom modeling system was developed to simulate various tissue optical properties for photodynamic therapy applications in radiation oncology. A total of nine unique phantom groups with varying concentrations of titanium dioxide and carbon were created in both flat planar (cylinder) and non-flat (3-dimensional) geometric shapes. Pre-measured quantities of titanium dioxide acted as a reduced scattering agent and carbon as an absorption agent.

A semi-infinite dosimetry technique was utilized to evaluate the light transmission of both the 3-dimensional and cylinder phantoms. The evaluation was conducted by taking semi-infinite transmission

measurements at 18 designated sections for each phantom group (1 cylinder + 2 dental molds). To ensure accuracy and repeatability of the results, 10 measurements were taken at each of the 18 locations.

2.5.3   Statistical Analysis & Discussion

2.5.3.1   Data Distribution

-Methods and Materials: Data was analyzed using IBM SPSS Statistic (version 29.0.1.0 (1711). Initial tests for normality were conducted using both the Kolmogorov-Smirnov (K-S) and Shapiro-Wilk (S-W) Tests.

-Results: Per the K-S test, several phantoms reported significant p values 4 & 9 (< .001). Phantoms 1, 6, and 7 have significant values (.006, .009, and .004, respectively). Phantom groups 2, 3, 5, and 8 reported non-significant values. All phantom groups have significant p-values (<.05) per the S-W test for normal distribution. (See Figure 35 & 36)

-Discussion: The reported statistically significant variations in data from the K-S and S-W tests reject the notion that data is normally distributed in all groups.

Tests of Normality

| | Phantom ID | Kolmogorov-Smirnov[a] | | | Shapiro-Wilk | |
		Statistic	df	Sig.	Statistic	df
Transmission Value (mW/cm^2)	1	.079	190	.006	.964	190
	2	.064	190	.053	.957	190
	3	.070	189	.025	.973	189
	4	.090	190	<.001	.955	190
	5	.053	190	.200*	.984	190
	6	.076	190	.009	.978	190
	7	.081	190	.004	.952	190
	8	.057	190	.200*	.985	190
	9	.149	190	<.001	.851	190

Tests of Normality

	Phantom ID	Shapiro-... Sig.
Transmission Value (mW/cm^2)	1	<.001
	2	<.001
	3	<.001
	4	<.001
	5	.028
	6	.004
	7	<.001
	8	.037
	9	<.001

*. This is a lower bound of the true significance.

a. Lilliefors Significance Correction

Figure 36. SPSS software output Semi-Infinite Transmission per data distribution assessment.
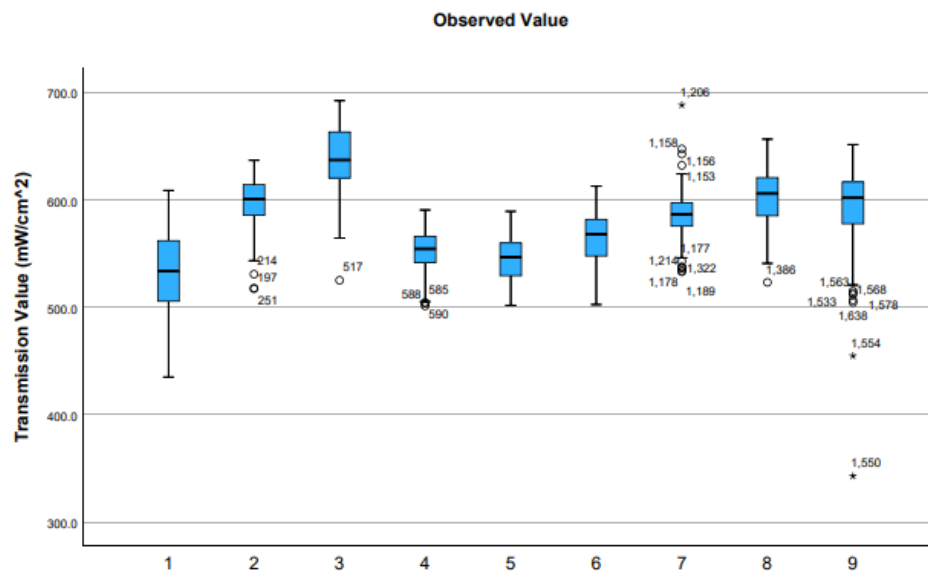
Figure 35. Semi-infinite box plot analysis of transmission values in phantoms 1-9.

47

2.5.3.2 Optical Property Variations (Absorption and Scattering).

-Primary Objective: To determine if the variations of optical property absorption and scattering influence light transmission in phantom groups 1-9 in both types of geometric models.

-Aim: This study AIMS to investigate the effect of predetermined optical properties μa and μ's with the light transmission optical properties collected from the semi-infinite method of dosimetry.

-Materials and Methods: Data was analyzed using IBM SPSS Statistic (version 29.0.1.0 (1711). Given the non-normal distribution of data, the Kruskal-Wallis test was used to assess for differences across phantoms categorized by μa and μ's, followed by Dunn's test with Bonferroni correction post-hoc analysis for multiple corrections. A Spearmen's correlation analysis was utilized to measure the association between optical properties and transmission values.

-Results: The Kruskal-Wallis test determined significance in transmission values across all μ's relationships (H=279.899, p<0.001). (See Figure 1-38). Pairwise comparisons revealed significant differences between all groups μ's=5 vs. μ's=10 (Standard Test Statistic = -10.829, Adj. Sig. < 0.001), μ's=5 vs. μ's=20 (Standard Test Statistic = -16.458, Adj. Sig. < 0.001), and μ's =10 vs. μ's =20 (Standard Test Statistic = -5.633, Adj. Sig. < 0.001), with all p-values remaining significant after Bonferroni adjustment. (See Figure 1-39). The Spearman's correlation analysis revealed a coefficient of 0.056 between the absorption coefficient and the transmission values as statistically significant (p= 0.021). (See Figure 37 - 39).

Independent-Samples Kruskal-Wallis Test Summary

Total N	1709
Test Statistic	279.899[a]
Degree Of Freedom	2
Asymptotic Sig.(2-sided test)	<.001

a. The test statistic is adjusted for ties.
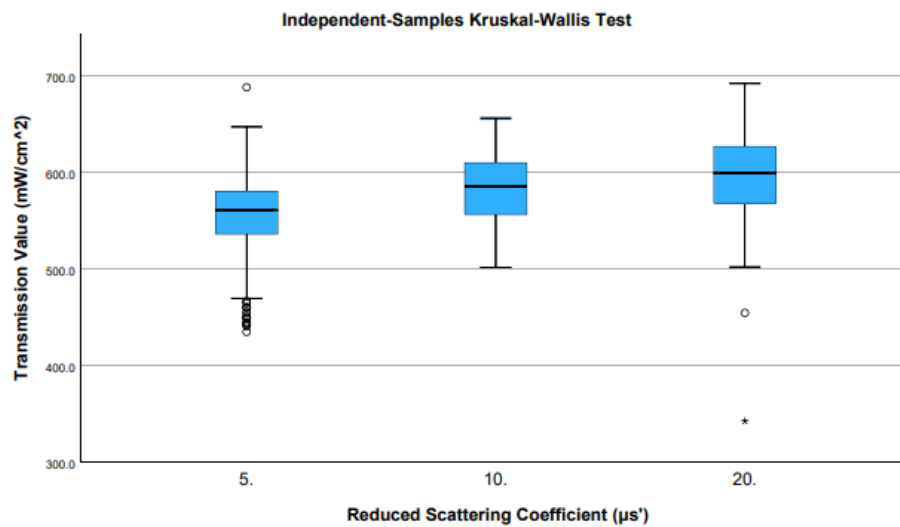
Figure 37. Kruskal-Wallis test summary (top) reduced scattering coefficient descriptive statistics (bottom).

Pairwise Comparisons of Reduced Scattering Coefficient (µs')

Sample 1-Sample 2	Test Statistic	Std. Error	Std. Test Statistic	Sig.	Adj. Sig.[a]
5-10	-316.561	29.232	-10.829	<.001	.000
5-20	-481.303	29.245	-16.458	<.001	.000
10-20	-164.742	29.245	-5.633	<.001	.000

Each row tests the null hypothesis that the Sample 1 and Sample 2 distributions are the same.

Asymptotic significances (2-sided tests) are displayed. The significance level is .050.

a. Significance values have been adjusted by the Bonferroni correction for multiple tests.

Figure 38. Semi-infinite light transmission pairwise comparisons for reduced scattering.

49

Nonparametric Correlations

Correlations

			Absorption Coefficient (µa)	Transmission Value (mW/cm^2)
Spearman's rho	Absorption Coefficient (µa)	Correlation Coefficient	1.000	.056*
		Sig. (2-tailed)	.	.021
		N	1710	1709
	Transmission Value (mW/cm^2)	Correlation Coefficient	.056*	1.000
		Sig. (2-tailed)	.021	.
		N	1709	1709

*. Correlation is significant at the 0.05 level (2-tailed).

Figure 39. Semi-infinite light transmission Spearman's correlation for absorption.

-Discussion: The Kruskal-Wallis test revealed significant variation in transmission values that were inversely related to the levels of scattering. The positive Spearman's correlation coefficient indicated that as the absorption coefficient increases, there is a corresponding slight increase in the transmission values.

2.5.3.3 Influence of Phantom Shape

-Primary Objective: To determine whether the phantom shape (cylinder vs. 3-dimensional dental mold) will affect light transmission.

-Aim: The primary AIM of this study is to evaluate the impact of phantom shape (cylinder vs. 3-Dimentional) on light transmission values.

-Materials and Methods: Transmission measurements (mW/cm^2) were taken from seven distinct regions on each cylinder and 6 sections for the dental molds. Data was analyzed using IBM SPSS Statistic (version

29.0.1.0 (1711). The Wilcoxon Signed Rank test assessed transmission values for each phantom group between each mold and cylinder and between both corresponding 3D dental molds.

-Results: The Wilcoxon Signed Rank Tests revealed statistically significant differences in light transmission values between the 3D dental molds (Z=-5.077, p<0.001) and between each dental mold and the cylinder (3D Dental Mold 1 vs. Cylinder: Z = -6.591, p < 0.001; 3D Dental Mold 2 vs. Cylinder: Z = -10.335, p < 0.001). (See Figure 40 - 43)

Test Statistics[a]

	3D Dental Mold 2 - 3D Dental Mold 1	3D Dental Mold 1 - Cylinder	3D Dental Mold 2 - Cylinder
Z	-5.077[b]	-6.591[b]	-10.335[b]
Asymp. Sig. (2-tailed)	<.001	<.001	<.001

a. Wilcoxon Signed Ranks Test

b. Based on negative ranks.

Figure 40. Semi-infinite transmission, Wilcoxon signed rank test.
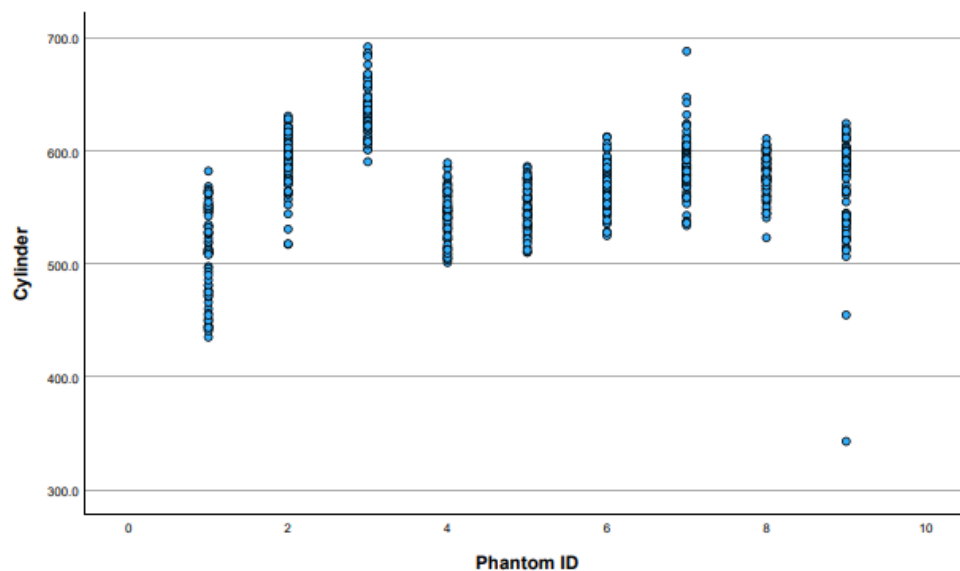
Figure 41. Semi-infinite Scatterplot for Cylinder.
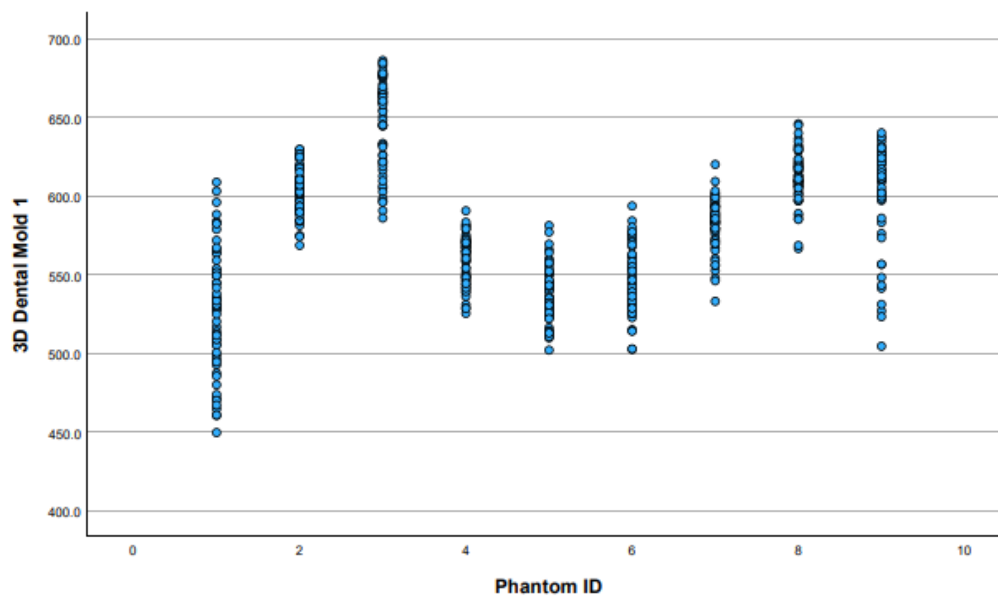
Figure 42. Semi-infinite Scatterplot for Dental Mold 1.

Graph
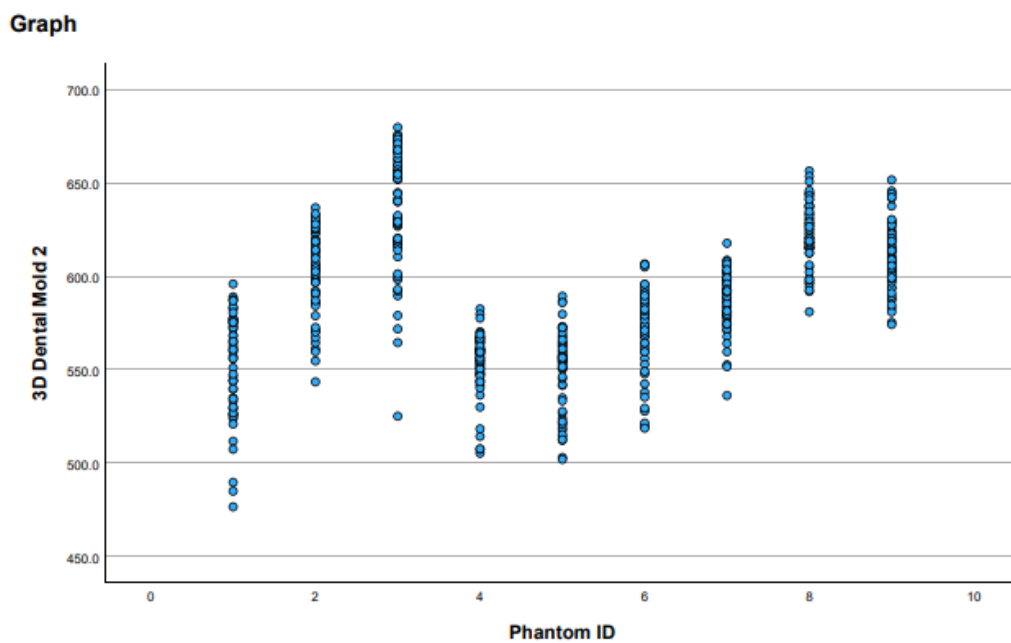
Figure 43. Semi-infinite Scatterplot for Dental Mold 2.

-Discussion: The differences between the transmission values of the cylinder and the 3D dental molds suggest that there is an impact on how light transmission is affected by geometry for this model. This could be a limitation of the 3-dimensional dental model due to the increased path length for measuring titanium and carbon materials. It could also be a result of light transmission through complex 3D shapes, convexities, and concavities, which could introduce further effects on optical properties not measured by this system. There were also statistically significant differences between both groups of dental molds, which could result from inconsistencies in the phantom fabrication process.

2.5.3.4 Between Cylinders and Dental Moldes

-Primary Objective: To determine if there are differences in light transmission values between the two 3D dental molds and the cylinder within each phantom group.

-Aim: This research aims to comprehensively evaluate the light transmission within each phantom group of cylindrical phantoms and 3D dental molds.

-Materials and Methods: Data was analyzed using IBM SPSS Statistic (version 29.0.1.0 (1711). The Wilcoxon Signed Rank Test was utilized to compare transmission values for each group between the cylinder and both 3D dental molds.

-Results: Transmission values and statistical significance are detailed in Figure 44.

Test Statistics[a]

	1-3D Dental Mold 1 - 1-Cylinder	1-3D Dental Mold 2 - 1-Cylinder	1-3D Dental Mold 2 - 1-3D Dental Mold 1	2-3D Dental Mold 1 - 2-Cylinder
Z	-2.985[b]	-6.427[b]	-4.726[b]	-3.640[b]
Asymp. Sig. (2-tailed)	.003	<.001	<.001	<.001

Test Statistics[a]

	2-3D Dental Mold 2 - 2-Cylinder	2-3D Dental Mold 2 - 2-3D Dental Mold 1	3-3D Dental Mold 1 - 3-Cylinder	3-3D Dental Mold 2 - 3-Cylinder
Z	-2.886[b]	-.456[c]	-3.253[b]	-.785[b]
Asymp. Sig. (2-tailed)	.004	.648	.001	.432

Test Statistics[a]

	3-3D Dental Mold 2 - 3-3D Dental Mold 1	4-3D Dental Mold 1 - 4-Cylinder	4-3D Dental Mold 2 - 4-Cylinder	4-3D Dental Mold 2 - 4-3D Dental Mold 1
Z	-2.757[c]	-3.489[b]	-2.304[b]	-2.367[c]
Asymp. Sig. (2-tailed)	.006	<.001	.021	.018

Test Statistics[a]

	5-3D Dental Mold 1 - 5-Cylinder	5-3D Dental Mold 2 - 5-Cylinder	5-3D Dental Mold 2 - 5-3D Dental Mold 1	6-3D Dental Mold 1 - 6-Cylinder
Z	-3.048[c]	-.670[b]	-3.051[b]	-4.943[c]
Asymp. Sig. (2-tailed)	.002	.503	.002	<.001

Test Statistics[a]

	6-3D Dental Mold 2 - 6-Cylinder	6-3D Dental Mold 2 - 6-3D Dental Mold 1	7-3D Dental Mold 1 - 7-Cylinder	7-3D Dental Mold 2 - 7-Cylinder
Z	-.449[b]	-5.672[b]	-.611[c]	-.777[b]
Asymp. Sig. (2-tailed)	.653	<.001	.541	.437

Test Statistics[a]

	7-3D Dental Mold 2 - 7-3D Dental Mold 1	8-3D Dental Mold 1 - 8-Cylinder	8-3D Dental Mold 2 - 8-Cylinder	8-3D Dental Mold 2 - 8-3D Dental Mold 1
Z	-1.528[b]	-6.655[b]	-6.633[b]	-3.302[b]
Asymp. Sig. (2-tailed)	.127	<.001	<.001	<.001

Test Statistics[a]

	9-3D Dental Mold 1 - 9-Cylinder	9-3D Dental Mold 2 - 9-Cylinder	9-3D Dental Mold 2 - 9-3D Dental Mold 1
Z	-5.900[b]	-6.352[b]	-.784[b]
Asymp. Sig. (2-tailed)	<.001	<.001	.433

a. Wilcoxon Signed Ranks Test

b. Based on negative ranks.

c. Based on positive ranks.

Figure 44. Semi-Infinite transmission, Wilcoxon Signed Rank Test.

-Discussion: The transmission values realized from this assessment indicate that 3D shapes can introduce additional complexity for calculating light transmission with this dosimetry system. There is an indication that the cylinder molds are either more uniform or that this specific combination of absorption and scattering properties allowed for more consistent light transmission

-Conclusion: This assessment has successfully demonstrated that the light transmission values can vary significantly between cylindrical phantoms and 3D dental molds. This highlights the importance of shape consideration and the ability of this medical dosimetry system to calibrate these differences.

2.5.3.5   Control Group Analysis- Variance by Shape

-Primary Objective: To determine how transmission values at the placebo/control (top middle of each cylinder) compare with other sections within the same phantom groups.

-Aim: This assessment aims to determine if there are statistically significant differences across different geometric locations of cylindrical and 3D models for each phantom group.

-Materials and Methods: Transmission measurements (mW/cm^2) were taken from seven distinct regions on each cylinder and 6 sections for the dental molds. The top (middle) section of each cylinder served as the control.

Data was analyzed using IBM SPSS Statistic (version 29.0.1.0 (1711). A Friedman two-way analysis of variance was conducted to assess the consistency of measurements across multiple related samples. Semi-infinite light transmission determined if there were statistically significant differences in rankings across these measurements for each subject under nineteen different conditions. Pairwise

comparison and Wilcoxon Signed-Rank Test were utilized for each pair of samples with Bonferroni correction applied to adjust for significance values for multiple tests.

Phantom 1

-Results: Friedman's test yielded a test statistic of 144.387. The asymptomatic significance level for the two-sided test (p<0.001) indicated statistical significance. The pairwise comparison revealed a range of test statistics and significance levels when compared to the control. (See Figure 45 & 46, Table 7)

Related-Samples Friedman's Two-Way Analysis of Variance by Ranks Summary

Total N	10
Test Statistic	144.387
Degree Of Freedom	18
Asymptotic Sig.(2-sided test)	<.001

Figure 45. Semi-Infinite, Phantom 1. Friedmans Analysis.

Section	Test Statistic	Sig.	Adj. Sig.	Section	Test Statistic	Sig.	Adj. Sig.
1Top (Middle) vs. 2Top (Outer):	-0.700	.781	1.000	**1Top (Middle) vs. 11Anterior Lingual**	-10.600	<.001*	0.004
1Top (Middle) vs. 3Side (top edge):	-4.300	.088	1.000	**1Top (Middle) vs. 12Posterior Buccal**	-15.900	<.001*	0.000000453**
1Top (Middle) vs. 4Side (middle):	-10.600	<.001*	0.004	**1Top (Middle) vs. 13Posterior Lingual**	-3.500	.164	1.000
1Top (Middle) vs. 5Side (bottom edge):	-7.600	.003*	0.432	**1Top (Middle) vs. 14Posterior Buccal (Osteotomy):**	-5.300	.035*	1.000
1Top (Middle) vs. 6Bottom (middle):	-11.000	<.001*	0.002	**1Top (Middle) vs. 15Posterior Palatal (Osteotomy):**	-13.900	<.001*	0.000005689**
1Top (Middle) vs. 7Bottom (outer edge):	-8.100	.001*	0.220	**1Top (Middle) vs. 16Anterior Buccal**	-7.500	.003*	0.493
1Top (Middle) vs. 8Posterior Buccal (Osteotomy):	-2.100	.404	1.000	**1Top (Middle) vs. 17Anterior Lingual**	-14.050	<.001*	0.000004045**
1Top (Middle) vs. 9Posterior Palatal (Osteotomy	-10.100	<.001*	0.010	**1Top (Middle) vs. 18Posterior Buccal**	-15.000	<.001*	0.000000430**
1Top (Middle) vs. 10Anterior Buccal	-5.900	.019*	1.000	**1Top (Middle) vs. 19Posterior Lingual**	-15.350	<.001*	0.000000182**

Each row tests the null hypothesis that sample 1 and sample 2 distributions are the same.
*Asymptomatic significances (2-sided tests) are displayed. The significance level is .050.
**Significance values have been adjusted by Bonferroni correction for multiple tests. (0.05/171) = .000292

Table 7. Semi-Infinite, Phantom 1. Pairwise Comparison.
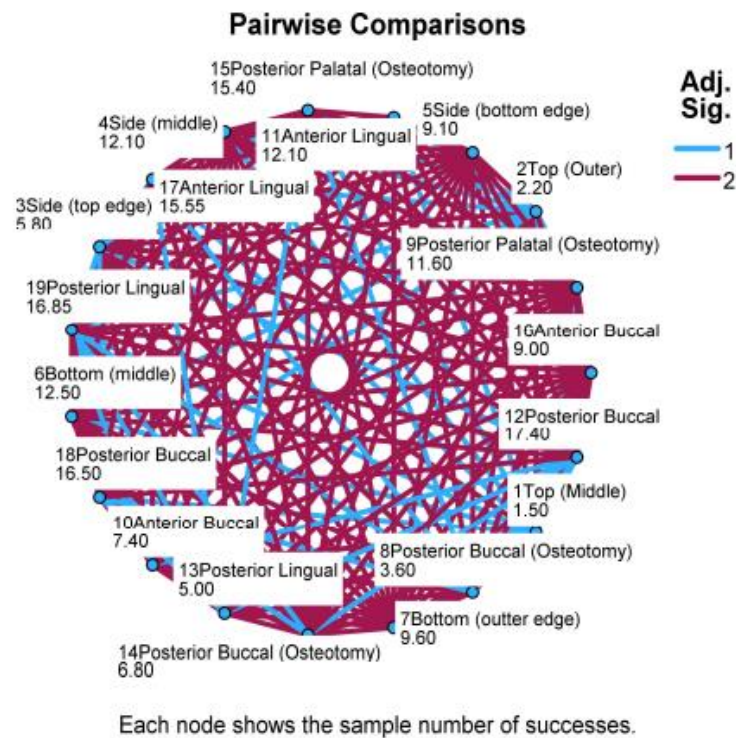
Figure 46. Semi-Infinite, Phantom 1. Pairwise Comparison.

-Discussion: The statistically significant results of Friedman's test suggest that at least one of the conditions produced a different effect compared to the others. The degree of certainty (P<0.001) is evidence that this variance is not due to randomness. For Phantom 1, a total of fourteen groups recorded significant results prior to correction, with five groups in the 3D molds having significance after Bonferroni correction.

Phantom 2

-Results: Friedman's test yielded a test statistic of 76.470. The asymptomatic significance level for the two-sided test (p<0.001) indicated statistical significance. The pairwise comparison revealed a range of test statistics and significance levels when compared to the control. (See Figure 47 & 48, Table 8).

Related-Samples Friedman's Two-Way Analysis of Variance by Ranks Summary

Total N	10
Test Statistic	76.470
Degree Of Freedom	18
Asymptotic Sig.(2-sided test)	<.001

Figure 47. Semi-Infinite, Phantom 2. Friedman analysis.

Section	Test Statistic	Sig.	Adj. Sig.	Section	Test Statistic	Sig.	Adj. Sig.
1Top (Middle) vs. 2Top (Outer):	1.150	.648	1.000	1Top (Middle) vs. 11Anterior Lingual	-3.450	.170	1.000
1Top (Middle) vs. 3Side (top edge):	1.850	.462	1.000	1Top (Middle) vs. 12Posterior Buccal	-0.650	.796	1.000
1Top (Middle) vs. 4Side (middle):	1.350	.592	1.000	1Top (Middle) vs. 13Posterior Lingual	-6.400	.011	1.000
1Top (Middle) vs. 5Side (bottom edge):	3.150	.211	1.000	1Top (Middle) vs. 14Posterior Buccal (Osteotomy):	5.950	.018*	1.000
1Top (Middle) vs. 6Bottom (middle):	0.000	1.000	1.000	1Top (Middle) vs. 15Posterior Palatal (Osteotomy):	-4.4450	.077	1.000
1Top (Middle) vs. 7Bottom (outer edge):	2.850	.257	1.000	1Top (Middle) vs. 16Anterior Buccal	3.250	.197	1.000
1Top (Middle) vs. 8Posterior Buccal (Osteotomy):	0.850	.736	1.000	1Top (Middle) vs. 17Anterior Lingual	-8.450	<.001*	0.134
1Top (Middle) vs. 9Posterior Palatal (Osteotomy	-3.850	.126	1.000	1Top (Middle) vs. 18Posterior Buccal	-2.550	.311	1.000
1Top (Middle) vs. 10Anterior Buccal	0.600	.812	1.000	1Top (Middle) vs. 19Posterior Lingual	-3.550	.158	1.000
Each row tests the null hypothesis that sample 1 and sample 2 distributions are the same. *Asymptomatic significances (2-sided tests) are displayed. The significance level is .050. **Significance values have been adjusted by Bonferroni correction for multiple tests. (0.05/171) = .000292							

Table 8. Semi-Infinite, Phantom 2. Pairwise comparison.
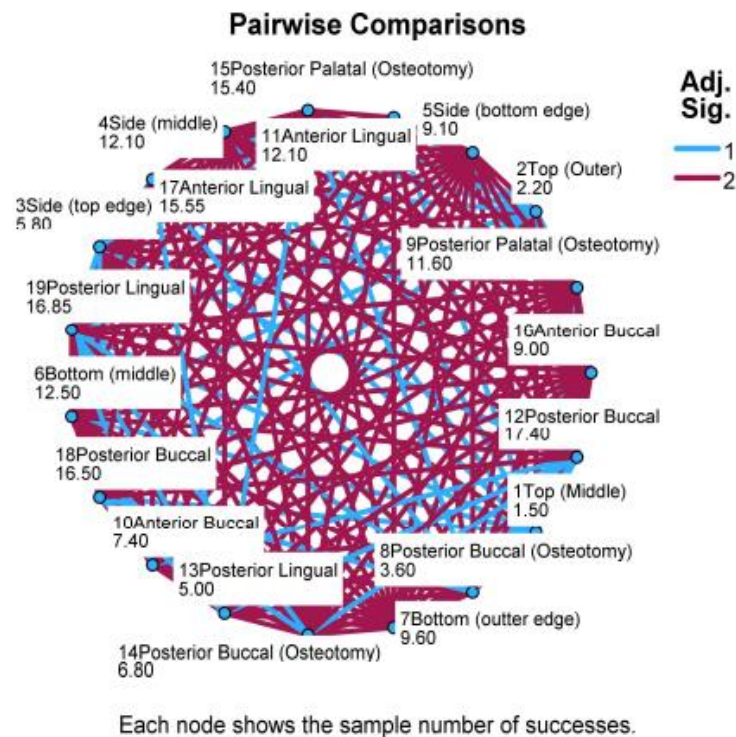
Figure 48. Semi-Infinite, Phantom 2. Pairwise Comparison.

-Discussion: The results obtained from the application of Friedman's test revealed variability in light transmission across the different geometric phantom sections. Particularly, this phantom group displayed significant differences between both types of models when compared to the control group. There were no sections in the cylindrical and 3D dental models that showed any statistical significance after the Bonferroni correction.

Phantom 3

-Results: Friedman's test produced a test statistic of 116.964. The results of the test revealed that there was a statistically significant difference between the samples. This was indicated by the asymptomatic significance level for the two-sided test (p<0.001). The pairwise comparison revealed a range of test statistics and significance levels when compared to the control. These findings strongly suggest that significant differences exist between the geometric models regardless of the conservative correction, therefore supporting the validity of the test results. (See Figure 49-50, Table 9)

Related-Samples Friedman's Two-Way Analysis of Variance by Ranks Summary

Total N	10
Test Statistic	116.964
Degree Of Freedom	18
Asymptotic Sig.(2-sided test)	<.001

Figure 49. Semi-Infinite, Phantom 3. Friedman analysis.

Section	Test Statistic	Sig.	Adj. Sig.	Section	Test Statistic	Sig.	Adj. Sig.
1Top (Middle) vs. 2Top (Outer):	-5.050	.045*	2.517	1Top (Middle) vs. 11Anterior Lingual	-11.150	<.001*	0.002
1Top (Middle) vs. 3Side (top edge):	-5.750	.022*	1.000	1Top (Middle) vs. 12Posterior Buccal	-8.550	<.001*	0.116
1Top (Middle) vs. 4Side (middle):	-2.850	.257	1.000	1Top (Middle) vs. 13Posterior Lingual	-10.750	<.001*	0.003
1Top (Middle) vs. 5Side (bottom edge):	-4.050	.108	1.000	1Top (Middle) vs. 14Posterior Buccal (Osteotomy):	1.950	.438	1.000
1Top (Middle) vs. 6Bottom (middle):	-9.750	<.001*	0.18	1Top (Middle) vs. 15Posterior Palatal (Osteotomy):	-10.150	<.001*	0.009
1Top (Middle) vs. 7Bottom (outer edge):	-5.950	.018*	1.000	1Top (Middle) vs. 16Anterior Buccal	-6.250	.013*	1.000
1Top (Middle) vs. 8Posterior Buccal (Osteotomy):	2.050	.415	1.000	1Top (Middle) vs. 17Anterior Lingual	-5.950	.018*	1.000
1Top (Middle) vs. 9Posterior Palatal (Osteotomy	-12.950	<.001*	0.002	1Top (Middle) vs. 18Posterior Buccal	-10.350	<.001*	0.007
1Top (Middle) vs. 10Anterior Buccal	-3.400	.177	1.000	1Top (Middle) vs. 19Posterior Lingual	-0.350	.889	1.000
Each row tests the null hypothesis that sample 1 and sample 2 distributions are the same.							
*Asymptomatic significances (2-sided tests) are displayed. The significance level is .050.							
**Significance values have been adjusted by Bonferroni correction for multiple tests. (0.05/171) = .000292							

Table 9. Semi-Infinite, Phantom 3. Pairwise Comparison

Pairwise Comparisons

15Posterior Palatal (Osteotomy)
14.40

4Side (middle)
7.10

5Side (bottom edge)
8.30

11Anterior Lingual
15.40

2Top (Outer)
9.30

17Anterior Lingual

3Side (top edge) 10.20
10.00

9Posterior Palatal (Osteotomy)
17.20

19Posterior Lingual
4.60

16Anterior Buccal
10.50

6Bottom (middle)
14.00

12Posterior Buccal
12.80

18Posterior Buccal
14.60

1Top (Middle)
4.25

10Anterior Buccal
7.65

8Posterior Buccal (Osteotomy)
2.20

13Posterior Lingual
15.00

7Bottom (outter edge)
10.20

14Posterior Buccal (Osteotomy)
2.30

Adj.
Sig.

—— 1
—— 2

Each node shows the sample number of successes.

Figure 50. Semi-Infinite, Phantom 3. Pairwise Comparison.

-Discussion: The results of Phantom 3 the Friedman's test are significant and indicate that at least one of the conditions has produced a distinctive light transmission effect in comparison to the others. The degree of certainty (P<.001) supports that these findings are not due to chance alone. The pairwise comparison for Phantom 3 revealed that 12 sections were statistically significant when compared to the control. After applying the Bonferroni correction factor, none of the groups reported any significant findings.

<u>Phantom 4</u>

-Results: Friedman's test was performed on Phantom group 4 to assess differences among multiple related sections between the cylinder and dual 3D dental molds of the same optical properties. The results yielded a test statistic of 84.264 with an asymptomatic significance level for the two-sided test (p<0.001). Further analysis using pairwise comparisons demonstrated 5 statistically significant results when compared to the control. There were no groups reporting significance after correction was applied. (See Figure 51 &52, Table 10)

Related-Samples Friedman's Two-Way Analysis of Variance by Ranks Summary

Total N	10
Test Statistic	84.264
Degree Of Freedom	18
Asymptotic Sig.(2-sided test)	<.001

Figure 51. Semi-Infinite, Phantom 4. Friedman analysis.

Section	Test Statistic	Sig.	Adj. Sig.	Section	Test Statistic	Sig.	Adj. Sig.
1Top (Middle) vs. 2Top (Outer):	6.550	.009*	1.000	1Top (Middle) vs. 11Anterior Lingual	-7.150	.004*	.769
1Top (Middle) vs. 3Side (top edge):	3.050	.226	1.000	1Top (Middle) vs. 12Posterior Buccal	-5.100	.043*	1.000
1Top (Middle) vs. 4Side (middle):	-5.350	.034*	1.000	1Top (Middle) vs. 13Posterior Lingual	1.750	.487	1.000
1Top (Middle) vs. 5Side (bottom edge):	-2.250	.371	1.000	1Top (Middle) vs. 14Posterior Buccal (Osteotomy):	3.500	.164	1.000
1Top (Middle) vs. 6Bottom (middle):	3.550	.158	1.000	1Top (Middle) vs. 15Posterior Palatal (Osteotomy):	-1.850	.462	1.000
1Top (Middle) vs. 7Bottom (outer edge):	5.350	.034*	1.000	1Top (Middle) vs. 16Anterior Buccal	0.550	.827	1.000
1Top (Middle) vs. 8Posterior Buccal (Osteotomy):	-1.950	.438	1.000	1Top (Middle) vs. 17Anterior Lingual	-3.750	.136	1.000
1Top (Middle) vs. 9Posterior Palatal (Osteotomy	-4.200	.136	1.000	1Top (Middle) vs. 18Posterior Buccal	-2.650	.292	1.000
1Top (Middle) vs. 10Anterior Buccal	-1.050	.677	1.000	1Top (Middle) vs. 19Posterior Lingual	-3.250	.197	1.000
Each row tests the null hypothesis that sample 1 and sample 2 distributions are the same. *Asymptomatic significances (2-sided tests) are displayed. The significance level is .050. **Significance values have been adjusted by Bonferroni correction for multiple tests. (0.05/171) = .000292							

Table 10. Semi-Infinite, Phantom 4. Pairwise comparisons.

Pairwise Comparisons

15Posterior Palatal (Osteotomy)
11.10

5Side (bottom edge)
11.50

4Side (middle)
14.60

11Anterior Lingual
16.40

2Top (Outer)
2.70

17Anterior Lingual
13.00

3Side (top edge)
6.20

9Posterior Palatal (Osteotomy)
13.45

19Posterior Lingual
12.50

16Anterior Buccal
8.70

6Bottom (middle)
5.70

12Posterior Buccal
14.35

18Posterior Buccal
11.90

1Top (Middle)
9.25

10Anterior Buccal
10.30

8Posterior Buccal (Osteotomy)
11.20

13Posterior Lingual
7.50

7Bottom (outter edge)
3.90

14Posterior Buccal (Osteotomy)
5.75

Adj. Sig.

— 1
— 2

Each node shows the sample number of successes.

Figure 52. Semi-Infinite, Phantom 4. Pairwise comparisons.

-Discussion: The results obtained from the Friedman's test for phantom group 4 show that there is a significant difference in the effect produced by at least one of the phantom sections when compared to the other geometric configurations. The degree of certainty ($P<0.001$) is evidence that this variance is not due to randomness. Within each group of geometric sections, five comparisons revealed statistical significance when compared to the control. None reported significance after applying the Bonferroni correction. These findings provide robust evidence for the presence of an effect due to geometric shape.

Phantom 5

-Results: Friedman's test yielded a test statistic of 96.420. The asymptomatic significance level for the two-sided test (p<0.001). The pairwise comparison of all geometric sections with the control revealed seven groups reporting statistical significance. None of the groups resulted in significance after the Bonferroni correction. (See Figure 53 & 44, Table 11)

Related-Samples Friedman's Two-Way Analysis of Variance by Ranks Summary

Total N	10
Test Statistic	106.204
Degree Of Freedom	18
Asymptotic Sig.(2-sided test)	<.001

Figure 53. Semi-Infinite, Phantom 5. Friedman analysis.

Section	Test Statistic	Sig.	Adj. Sig.	Section	Test Statistic	Sig.	Adj. Sig.
1Top (Middle) vs. 2Top (Outer):	6.700	.008*	1.000	1Top (Middle) vs. 11Anterior Lingual	1.100	.662	1.000
1Top (Middle) vs. 3Side (top edge):	-5.300	.035*	1.000	1Top (Middle) vs. 12Posterior Buccal	7.050	.005*	.870
1Top (Middle) vs. 4Side (middle):	-4.300	.088	1.000	1Top (Middle) vs. 13Posterior Lingual	7.050	.005*	.870
1Top (Middle) vs. 5Side (bottom edge):	1.900	.450	1.000	1Top (Middle) vs. 14Posterior Buccal (Osteotomy):	3.100	.218	1.000
1Top (Middle) vs. 6Bottom (middle):	.500	.843	1.000	1Top (Middle) vs. 15Posterior Palatal (Osteotomy):	-.650	.796	1.000
1Top (Middle) vs. 7Bottom (outer edge):	-3.000	.233	1.000	1Top (Middle) vs. 16Anterior Buccal	5.100	.043*	1.000
1Top (Middle) vs. 8Posterior Buccal (Osteotomy):	.500	.843	1.000	1Top (Middle) vs. 17Anterior Lingual	-4.200	.095	1.000
1Top (Middle) vs. 9Posterior Palatal (Osteotomy	6.100	.015*	1.000	1Top (Middle) vs. 18Posterior Buccal	-.650	.796	1.000
1Top (Middle) vs. 10Anterior Buccal	3.600	.153	1.000	1Top (Middle) vs. 19Posterior Lingual	-6.200	.014*	1.000
Each row tests the null hypothesis that sample 1 and sample 2 distributions are the same. *Asymptomatic significances (2-sided tests) are displayed. The significance level is .050. **Significance values have been adjusted by Bonferroni correction for multiple tests. (0.05/171) = .000292							

Table 11. Semi-Infinite, Phantom 5. Pairwise comparisons.

Pairwise Comparisons

15Posterior Palatal (Osteotomy)
12.85

4Side (middle)
15.20

11Anterior Lingual
9.80

5Side (bottom edge)
9.00

17Anterior Lingual 15.10

2Top (Outer)
4.20

3Side (top edge)
16.20

9Posterior Palatal (Osteotomy)
4.80

19Posterior Lingual
17.10

16Anterior Buccal
5.80

6Bottom (middle)
10.40

12Posterior Buccal
3.85

18Posterior Buccal
11.55

1Top (Middle)
10.90

10Anterior Buccal
7.30

8Posterior Buccal (Osteotomy)
10.40

13Posterior Lingual
3.85

7Bottom (outter edge)
13.90

14Posterior Buccal (Osteotomy)
7.80

Adj. Sig.
— 1
— 2

Each node shows the sample number of successes.

Figure 54. Semi-Infinite, Phantom 5. Pairwise comparisons.

-Discussion: The findings from Friedman's phantom group 5 suggest that at least one of the geometric conditions produced a different effect compared to the others. Per phantom 5, seven groups reported significance, with none resulting in significance after the Bonferroni correlation.

Phantom 6

-Results: The results of Friedman's test for phantom group 6 showed a test statistic of 82.445. The asymptomatic significance level for the two-sided test (p<0.001) indicated statistical significance. Further analysis through pairwise comparison against the control revealed four groups with statistical significance. None resulted in significance after Bonferroni's correction. (See Figure 55 & 56, Table 12)

Related-Samples Friedman's Two-Way Analysis of Variance by Ranks Summary

Total N	10
Test Statistic	82.445
Degree Of Freedom	18
Asymptotic Sig.(2-sided test)	<.001

Figure 55. Semi-Infinite, Phantom 6. Friedman analysis.

Section	Test Statistic	Sig.	Adj. Sig.	Section	Test Statistic	Sig.	Adj. Sig.
1Top (Middle) vs. 2Top (Outer):	-1.000	.691	1.000	1Top (Middle) vs. 11Anterior Lingual	4.300	.088	1.000
1Top (Middle) vs. 3Side (top edge):	3.400	.177	1.000	1Top (Middle) vs. 12Posterior Buccal	4.600	.068	1.000
1Top (Middle) vs. 4Side (middle):	-2.850	.257	1.000	1Top (Middle) vs. 13Posterior Lingual	6.850	.006*	1.000
1Top (Middle) vs. 5Side (bottom edge):	-0.100	.968	1.000	1Top (Middle) vs. 14Posterior Buccal (Osteotomy):	7.150	.004*	0.769
1Top (Middle) vs. 6Bottom (middle):	.850	.736	1.000	1Top (Middle) vs. 15Posterior Palatal (Osteotomy):	-2.900	.249	1.000
1Top (Middle) vs. 7Bottom (outer edge):	4.050	.108	1.000	1Top (Middle) vs. 16Anterior Buccal	-0.800	.751	1.000
1Top (Middle) vs. 8Posterior Buccal (Osteotomy):	8.900	<.001*	0.069	1Top (Middle) vs. 17Anterior Lingual	.500	.843	2.517
1Top (Middle) vs. 9Posterior Palatal (Osteotomy	2.000	.427	1.000	1Top (Middle) vs. 18Posterior Buccal	-1.700	.499	1.000
1Top (Middle) vs. 10Anterior Buccal	6.650	.008*	1.000	1Top (Middle) vs. 19Posterior Lingual	-3.800	.131	1.000
Each row tests the null hypothesis that sample 1 and sample 2 distributions are the same. *Asymptomatic significances (2-sided tests) are displayed. The significance level is .050. **Significance values have been adjusted by Bonferroni correction for multiple tests. (0.05/171) = .000292							

Table 12. Semi-Infinite, Phantom 6. Pairwise comparison.

\

Pairwise Comparisons

15Posterior Palatal (Osteotomy) 14.80

4Side (middle) 14.75

11Anterior Lingual 7.60

5Side (bottom edge) 12.00

2Top (Outer) 12.90

17Anterior Lingual 11.40

3Side (top edge) 8.50

9Posterior Palatal (Osteotomy) 9.90

19Posterior Lingual 15.70

16Anterior Buccal 12.70

6Bottom (middle) 11.05

12Posterior Buccal 7.30

18Posterior Buccal 13.60

1Top (Middle) 11.90

10Anterior Buccal 5.25

8Posterior Buccal (Osteotomy) 3.00

13Posterior Lingual 5.05

7Bottom (outter edge) 7.85

14Posterior Buccal (Osteotomy) 4.75

Adj. Sig.
— 1
— 2

Each node shows the sample number of successes.

Figure 56. Semi-Infinite, Phantom 6. Pairwise comparison.

-Discussion: The statistically significant results of Friedman's test for phantom group 6 indicate that at least one of the geometric conditions produced a significant effect when compared to the others. The degree of certainty ($P<0.001$) is evidence that this variance is not due to randomness. The pairwise comparison to the control revealed that four groups reported significance prior to adjustment, with none resulting in significance after Bonferroni correction. These findings provide robust evidence of the differences observed through the light transmission effects.

Phantom 7

-Results: Friedman's test for phantom group 7 produced a test statistic of 73.194. The asymptomatic significance level for the two-sided test (p<0.001) indicated statistical significance. The pairwise comparison with the control revealed four significant regions when compared to the control. (See Figure 75 & 58, Table 13)

Related-Samples Friedman's Two-Way Analysis of Variance by Ranks Summary

Total N	10
Test Statistic	73.194
Degree Of Freedom	18
Asymptotic Sig.(2-sided test)	<.001

Figure 57. Semi-Infinite, Phantom 7. Friedman analysis.

| Section	Test Statistic	Sig.	Adj. Sig.	Section	Test Statistic	Sig.	Adj. Sig.
1Top (Middle) vs. 2Top (Outer):	-6.000	.017*	1.000	1Top (Middle) vs. 11Anterior Lingual	-.500	.843	1.000
1Top (Middle) vs. 3Side (top edge):	.600	.812	1.000	1Top (Middle) vs. 12Posterior Buccal	6.500	.010*	1.000
1Top (Middle) vs. 4Side (middle):	10.000	<.001*	.012	1Top (Middle) vs. 13Posterior Lingual	-.200	.937	1.000
1Top (Middle) vs. 5Side (bottom edge):	5.600	.026*	1.000	1Top (Middle) vs. 14Posterior Buccal (Osteotomy):	-2.200	.382	1.000
1Top (Middle) vs. 6Bottom (middle):	-1.300	.605	1.000	1Top (Middle) vs. 15Posterior Palatal (Osteotomy):	3.500	.164	1.000
1Top (Middle) vs. 7Bottom (outer edge):	-.900	.721	1.000	1Top (Middle) vs. 16Anterior Buccal	-1.900	.450	1.000
1Top (Middle) vs. 8Posterior Buccal (Osteotomy):	-.400	.937	1.000	1Top (Middle) vs. 17Anterior Lingual	-1.200	.633	1.000
1Top (Middle) vs. 9Posterior Palatal (Osteotomy	2.900	.249	2.517	1Top (Middle) vs. 18Posterior Buccal	1.100	.662	1.000
1Top (Middle) vs. 10Anterior Buccal	1.300	.605	1.000	1Top (Middle) vs. 19Posterior Lingual	2.100	.404	1.000
Each row tests the null hypothesis that sample 1 and sample 2 distributions are the same. *Asymptomatic significances (2-sided tests) are displayed. The significance level is .050. **Significance values have been adjusted by Bonferroni correction for multiple tests. (0.05/171) = .000292							

Table 13. Semi-Infinite, Phantom 7. Pairwise comparison.

Pairwise Comparisons

15Posterior Palatal (Osteotomy)
7.50

4Side (middle)
1.00

11Anterior Lingual
11.50

5Side (bottom edge)
5.40

17Anterior Lingual

2Top (Outer)
17.00

3Side (top edge) 12.20
10.40

9Posterior Palatal (Osteotomy)
8.10

19Posterior Lingual
8.90

16Anterior Buccal
12.90

6Bottom (middle)
12.30

12Posterior Buccal
4.50

18Posterior Buccal
9.90

1Top (Middle)
11.00

10Anterior Buccal
9.70

8Posterior Buccal (Osteotomy)
11.40

13Posterior Lingual
11.20

7Bottom (outter edge)
11.90

14Posterior Buccal (Osteotomy)
13.20

Adj.
Sig.
— 1
— 2

Each node shows the sample number of successes.

Figure 58. Semi-Infinite, Phantom 7. Pairwise comparison.

-Discussion: Friedman's test for phantom group 7 suggests that at least one of the geometric conditions produced a different effect compared to the others. The degree of certainty ($P<0.001$) is evidence that this level of significance is not due to randomness. The pairwise comparison of all regions in phantom group 7 to the control reported significance in four groups prior to adjustment. None of the groups resulted in significance after the Bonferroni correction.

Phantom 8

-Results: Friedman's test for phantom group 8 yielded a test statistic of 135.325, with an asymptomatic significance level for the two-sided test (p<0.001), indicating statistical significance. The pairwise comparison revealed 10 groups having statistical significance when compared to the control. None reported significance after the Bonferroni correction. (See Figure 59 & 60, Table 14)

Related-Samples Friedman's Two-Way Analysis of Variance by Ranks Summary

Total N	10
Test Statistic	135.325
Degree Of Freedom	18
Asymptotic Sig.(2-sided test)	<.001

Figure 59. Semi-Infinite, Phantom 8. Friedman analysis.

| Section	Test Statistic	Sig.	Adj. Sig.	Section	Test Statistic	Sig.	Adj. Sig.
1Top (Middle) vs. 2Top (Outer):	3.700	.141	1.000	1Top (Middle) vs. 11Anterior Lingual	-8.550	<.001*	.116
1Top (Middle) vs. 3Side (top edge):	2.100	.404	1.000	1Top (Middle) vs. 12Posterior Buccal	-7.150	.004*	.769
1Top (Middle) vs. 4Side (middle):	4.400	.080	1.000	1Top (Middle) vs. 13Posterior Lingual	-1.200	.633	1.000
1Top (Middle) vs. 5Side (bottom edge):	.800	.751	1.000	1Top (Middle) vs. 14Posterior Buccal (Osteotomy):	-7.300	.004*	.637
1Top (Middle) vs. 6Bottom (middle):	2.200	.382	1.000	1Top (Middle) vs. 15Posterior Palatal (Osteotomy):	-10.600	<.001*	.004
1Top (Middle) vs. 7Bottom (outer edge):	-.400	.874	1.000	1Top (Middle) vs. 16Anterior Buccal	-8.700	<.001*	.093
1Top (Middle) vs. 8Posterior Buccal (Osteotomy):	-4.100	.103	1.000	1Top (Middle) vs. 17Anterior Lingual	-10.700	<.001*	.004
1Top (Middle) vs. 9Posterior Palatal (Osteotomy	-5.300	.035*	1.000	1Top (Middle) vs. 18Posterior Buccal	-5.400	.032*	1.000
1Top (Middle) vs. 10Anterior Buccal	-7.000	.005*	.925	1Top (Middle) vs. 19Posterior Lingual	-5.200	.039*	1.000
Each row tests the null hypothesis that sample 1 and sample 2 distributions are the same. *Asymptomatic significances (2-sided tests) are displayed. The significance level is .050. **Significance values have been adjusted by Bonferroni correction for multiple tests. (0.05/171) = .000292							

Table 14. Semi-Infinite, Phantom 8. Pairwise comparison.
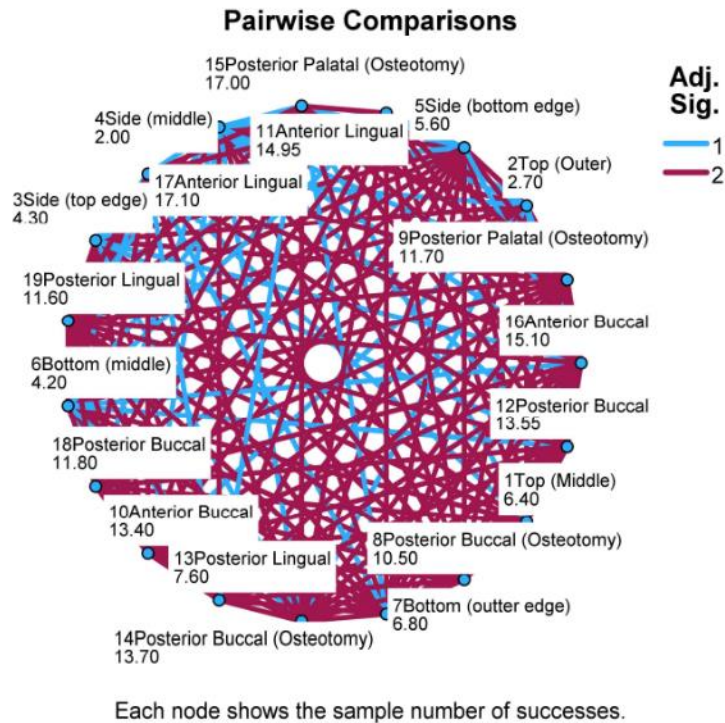
Figure 60. Semi-Infinite, Phantom 8. Pairwise comparison.

-Discussion: The results from the phantom group 8 Friedman's test are indicative of the presence of a significant difference between geometric sections. The degree of certainty (P<0.001) is evidence that this variance is not due to randomness. Ten groups in phantom 8 reported significance when compared to the control, with none resulting in significance after correction was applied. These findings provide robust scientific evidence of the effects of comparing different geometric conditions within the same group of optical properties.

Phantom 9

-Results: Friedman's test for phantom group 9 reported a test statistic of 94.930. The asymptomatic significance level for the two-sided test (p<0.001) indicated statistical significance. The pairwise comparison of all geometric sections to the control revealed seven groups reporting significant levels. None resulted in significance after the Bonferroni correction. (See Figures 61 & 62, Table 15)

Related-Samples Friedman's Two-Way Analysis of Variance by Ranks Summary

Total N	10
Test Statistic	94.930
Degree Of Freedom	18
Asymptotic Sig.(2-sided test)	<.001

Figure 61. Semi-Infinite, Phantom 9. Friedman analysis.

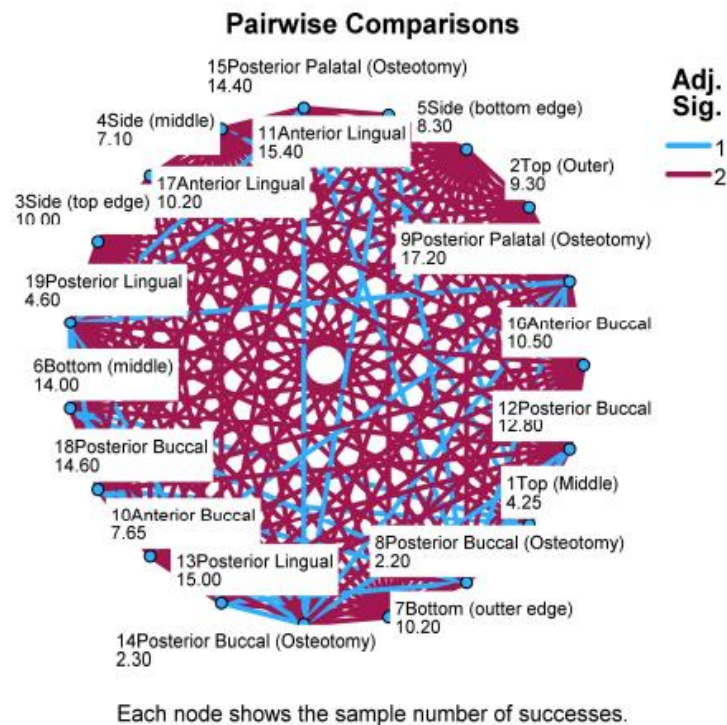| Section	Test Statistic	Sig.	Adj. Sig.	Section	Test Statistic	Sig.	Adj. Sig.
1Top (Middle) vs. 2Top (Outer):	5.350	.034*	1.000	**1Top (Middle) vs. 11Anterior Lingual**	-6.250	.013*	1.000
1Top (Middle) vs. 3Side (top edge):	-1.950	.438	1.000	**1Top (Middle) vs. 12Posterior Buccal**	1.950	.438	1.000
1Top (Middle) vs. 4Side (middle):	1.250	.619	1.000	**1Top (Middle) vs. 13Posterior Lingual**	-2.150	.393	1.000
1Top (Middle) vs. 5Side (bottom edge):	6.250	.013*	1.000	**1Top (Middle) vs. 14Posterior Buccal (Osteotomy):**	-2.400	.390	1.000
1Top (Middle) vs. 6Bottom (middle):	3.050	.226	1.000	**1Top (Middle) vs. 15Posterior Palatal (Osteotomy):**	-2.150	.393	1.000
1Top (Middle) vs. 7Bottom (outer edge):	1.700	.499	1.000	**1Top (Middle) vs. 16Anterior Buccal**	-6.050	.016*	1.000
1Top (Middle) vs. 8Posterior Buccal (Osteotomy):	-7.050	.005*	.870	**1Top (Middle) vs. 17Anterior Lingual**	-5.350	.034*	1.000
1Top (Middle) vs. 9Posterior Palatal (Osteotomy	-4.850	.054	1.000	**1Top (Middle) vs. 18Posterior Buccal**	-3.150	.211	1.000
1Top (Middle) vs. 10Anterior Buccal	-4.800	.056	1.000	**1Top (Middle) vs. 19Posterior Lingual**	-6.650	.008*	1.000
Each row tests the null hypothesis that sample 1 and sample 2 distributions are the same. *Asymptomatic significances (2-sided tests) are displayed. The significance level is .050. **Significance values have been adjusted by Bonferroni correction for multiple tests. (0.05/171) = .000292							

Table 15. Semi-Infinite, Phantom 9. Pairwise comparison.

Pairwise Comparisons

15Posterior Palatal (Osteotomy) 10.40

4Side (middle) 7.00

11Anterior Lingual 14.50

5Side (bottom edge) 2.00

2Top (Outer) 2.90

17Anterior Lingual 13.60

3Side (top edge) 10.20

9Posterior Palatal (Osteotomy) 13.10

19Posterior Lingual 14.90

16Anterior Buccal 14.30

6Bottom (middle) 5.20

12Posterior Buccal 6.30

18Posterior Buccal 11.40

1Top (Middle) 8.25

10Anterior Buccal 13.05

8Posterior Buccal (Osteotomy) 15.30

13Posterior Lingual 10.40

7Bottom (outter edge) 6.55

14Posterior Buccal (Osteotomy) 10.65

Adj. Sig.

— 1
— 2

Each node shows the sample number of successes.

Figure 62. Semi-Infinite, Phantom 9. Pairwise comparison.

-Discussion: The results of Friedman's test for phantom group 9 have demonstrated statistical significance. The degree of certainty (P<0.001) is evidence that this variance is not due to randomness. The pairwise comparison for phantom group 9 reported seven groups with significance prior to adjustment, with none resulting in significance after Bonferroni correction.

2.6   Conclusion

This body of research developed a new cohort of silicone phantom models and has demonstrated a notable expansion of the optical property calibration for the medical dosimetry system in the Tim Zhu laboratory. The results of this series indicate that this medical dosimetry system can differentiate similar optical properties for complex three-dimensional shapes that resemble the human maxilla with precision, accuracy, and repeatability.

Several investigations were conducted through this series of assessments in the phantom models. This includes an analysis of optical property variations, the influence of geometric shapes, a comparison of cylinder and dental models, and an extensive placebo-control analysis of light transmission.

The assessment investigating the optical property variation across nine different phantom models revealed that the medical dosimetry system can recognize significant variations across all the phantom types. This observation is attributed to the predetermined ratios of titanium dioxide (scattering) and carbon (absorption). The analyses demonstrate that scattering is inversely related to light transmission, while an increase in absorption is related to an increase in light transmission.

The assessment evaluating the impact of the phantom shape indicates that the shape has an impact on how light transmits through the optical properties of complex geometries. However, the analysis also identified inconsistent light transmission between the dental molds, which could be a limitation of the fabrication process. Despite this discrepancy, this finding provides a more robust calibration metric of the medical dosimetry system. The comparison between cylindrical phantoms and 3D dental models also validated these results, reinforcing the significant differences between the two types of phantoms.

A placebo control standardized the investigation of light transmission variance in geometric shapes. The results of Friedman's assessments for phantom groups 1-9 revealed significant differences in comparisons between different geometries. All groups reported asymptomatic significance levels <.001, which indicates that these results are not due to chance alone. This rejects the idea that light transmission values are identical regardless of different phantom shapes.

The pairwise comparisons provide valuable insight into the consistency of light transmission across different sections when compared to the control (1Top(Middle)). This reveals that certain geometries can cause non-uniform transmission when compared to control. This suggests that the phantom's geometry and unique combination of absorption and scattering properties affect light transmission.

Additionally, it was determined that the cylindrical phantoms (control) provide predictable and consistent light transmission values across all the different combinations of optical properties in groups 1-9. The complex geometry of the 3D dental molds introduces variability that could lead to inaccuracies when modeling complex anatomical structures. These findings highlight the need for advanced computational models that can account for complex geometries and guide real-time dosimetry protocols for patient-specific treatments. This study emphasizes the significance of considering phantom shapes in dosimetry modeling, especially for patient-specific approaches that are 3-dimensional.

The present series highlights the importance of incorporating phantom shapes, absorption, and scattering profiles when modeling complex anatomic structures. The outcomes of this research provide insights that guide the development of advanced computational models for patient-specific treatment planning, with the potential to improve the accuracy and efficacy of medical dosimetry applications.

3   THE PORCINE MODEL

3.1   Innovation of Potential Findings

The porcine mandible cadaver model represents a significant step forward to optimizing dosing protocols for PDT and PBM in translational science. This preclinical model provides researchers with a valuable tool to explore anatomic variations, understand tissue heterogeneities, and refine dosing protocols to better align with translational research requirements for human clinical care. As the demands for PDT and PBM continue to evolve, researchers can adapt the porcine model to accommodate the ethical and methodological requirements of the field and pave the way toward scientific advancement.

The remarkable similarities between intraoral porcine and human tissues have established the porcine model as an invaluable tool for gaining insight into the complex details of PDT and PBM delivery. (124-135) This model provides an opportunity to analyze the intricacies of tissue responses. This can be expanded to in-vivo simulations to expand dose-escalation trial formats with new dosimetry investigations. (131, 136-138) This approach holds immense potential for providing a deeper understanding of mechanistic approaches, which can eventually lead to more effective treatment strategies.

3.2   Tissue Modeling for Light Transmission

The porcine cadaver provides a newly developed modeling system for investigating light penetration and dosimetry across diverse tissue boundaries. This model has a unique advantage due to its close anatomical and histological resemblance to human tissues. Porcine experiment models are commonly utilized to simulate human oral and maxillofacial surgery due to the similarities in musculoskeletal and nervous

systems. (129, 139) Contrary to small animal models like rats and mice, the porcine model offers a substantial depth from the skin through adipose and facial layers to reach underlying structures. While there are certain differences in muscle thickness and the number of the foramen, the other similarities make the porcine model a viable choice for a range of head and neck translational research disciplines, including nerve regeneration, immunology, bone biology, and titanium osseointegration. (129, 139-146) The porcine mandible cadaver model provides a model for the comprehensive assessment of dosimetry, optical property characterizations, computed tomography (CT) analysis, and histology. (125, 126, 132)

The red visible wavelengths of the electromagnetic spectrum range between 625nm-740nm and have unique nonionizing capabilities to elicit phototherapeutic effects in biological mediums. (10, 19, 48, 49, 53, 147-149) Red wavelengths are commonly utilized in Photodynamic Therapy (PDT) and Photobiomodulation (PBM), which have broad clinical applicability in medicine and dentistry. (28, 106, 150-152) PDT incorporates non-toxic photosensitizers to eliminate disease pathologies, while PBM is a minimally invasive application to reduce pain and improve wound healing. (11, 13-16, 64-67) Although wavelength is a critical parameter in dosimetry, other factors related to the propagation of light through host biological tissue mediums significantly influence therapeutic efficacy. Understanding how the heterogeneous properties of different soft tissues affect maximum light fluence (mW/CM^2) and optical property characterization (μa, μs') is essential.

PDT and PBM are two distinct modalities that utilize light to treat a variety of medical conditions. (6, 7, 10, 107, 113, 153-159) While PDT utilizes visible electromagnetic spectrum from 400-750nm, PBM utilizes red and near-infrared (NIR) wavelengths ranging from 600-1,000nm. (10, 15, 33, 43, 148, 160-162) A higher wavelength on the electromagnetic spectrum generally correlates with a deeper penetration depth. (124, 147, 160, 163) However, the overall exposure time of light delivery can increase signal penetration regardless of that wavelength. (164) It should be emphasized that transmission depth is dependent on morphological characteristics rather than an increase or decrease in optical power. (156, 160, 165-171).

The ability to accurately predict the desired biological effect is critical in light dosimetry calculations. This involves the precise calculation of dosimetry quantities absorbed at the intended site to deliver fluence and irradiance dosage. This can be accomplished through pre-planning, real-time monitoring, treatment adaptation, and outcome assessment. (14)

The porcine modeling system provides a robust environment for translational insight and facilitation of new PDT and PBM dosimetry therapeutic strategies. This model enables an innovative framework to study variables, including light transmission, depth of penetration, and tissue optical properties. The primary focus of this proof-of-concept investigational study is to assess interstitial 661nm light transmission at various tissue junctions in the porcine mandible cadaver. Core outcome measures include the parameters of light penetration, three-dimensional surface acquisition of targeted tissues, and Cone Beam Computed Tomography (CBCT) analyses. This investigational study aims to demonstrate that light transmission values are influenced by the anatomical relationships and distances between irradiated tissues of the head and neck regions, thus providing critical data for dosimetry optimization for PDT and PBM.

3.3   Proof-of-Concept Porcine Investigation

3.3.1   Methods

The study was conducted using a single fully intact Yorkshire pig mandible that was obtained from a slaughterhouse (Animal Technologies, Tyler, Texas). The specimen was transported in a frozen, unfixed state and was fully thawed prior to analysis. The mandible included the complete intra and extraoral regions, consisting of a variety of tissue types such as bone (cancellous and cortical), adipose, muscle, dentin,

enamel, dermis, and external hair. (See Figure 63). The investigation was standardized and focused on specific anatomic regions, including the condyles, posterior quadrants, and anterior segments.
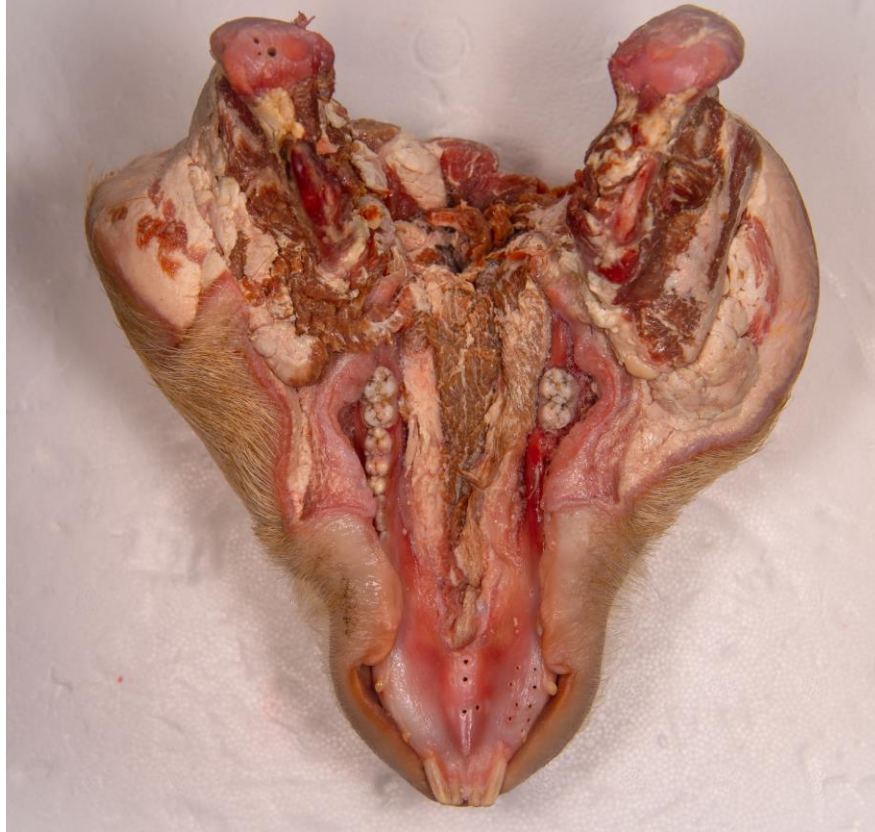
Figure 63. Regions of anatomical interest in the porcine mandible.

To standardize anatomical references at regions of interest, a dental surgical drill was utilized to prepare 2mm osteotomies with the V35 electric handpiece, dental motor (Buffalo Dental Manufacturing Co. Inc, Syosset, NY), and Versah osseodensification drills (Versah LLC, Jackson, MI). These osteotomies were then used as primary reference points for light transmission measurements and were randomized in both soft tissue and bone at fixed distances ranging from 2-8mm. This approach ensured accuracy and consistency in the data collection process, providing a reliable basis for the subsequent analysis.

The acquisition of 661nm light fluence rate measurements (mW/cm^2) was conducted using an interstitial dual-catheter medical dosimetry system. These measurements were performed at various distances from a point source with known light power emission. The point source power measurements and calibration were made using an integrating sphere calibrated at a wavelength of 661 nm. (21, 108, 109, 112). The dual-catheter configuration, coupled with a wavelength-specific algorithm, enabled data acquisition and analysis across all regions of interest.

Light fluence rate transmission was measured with an isotropic detector that was calibrated with an LED calibration sphere. This dual-catheter configuration and wavelength-specific algorithm allows data acquisition and analysis across all anatomical regions of interest. A 0.8mm diameter spherical isotropic detector (IP85, Medlight S.A.) was connected to one channel of a 16-channel light dosimetry system. A customized Matlab® software analyzed the measured data to determine tissue optical properties, including absorption (μ_a), scattering (μ'_s), and the effective attenuation coefficient (μ_{eff}). A 2.0mm long linear source (#7035-01 Rev 2; Pioneer Optics) was used as an approximate point source while allowing adequate power to be tolerated and was connected to a 661nm laser system (B&W Tek, Newark, DE). (See Figure 64)
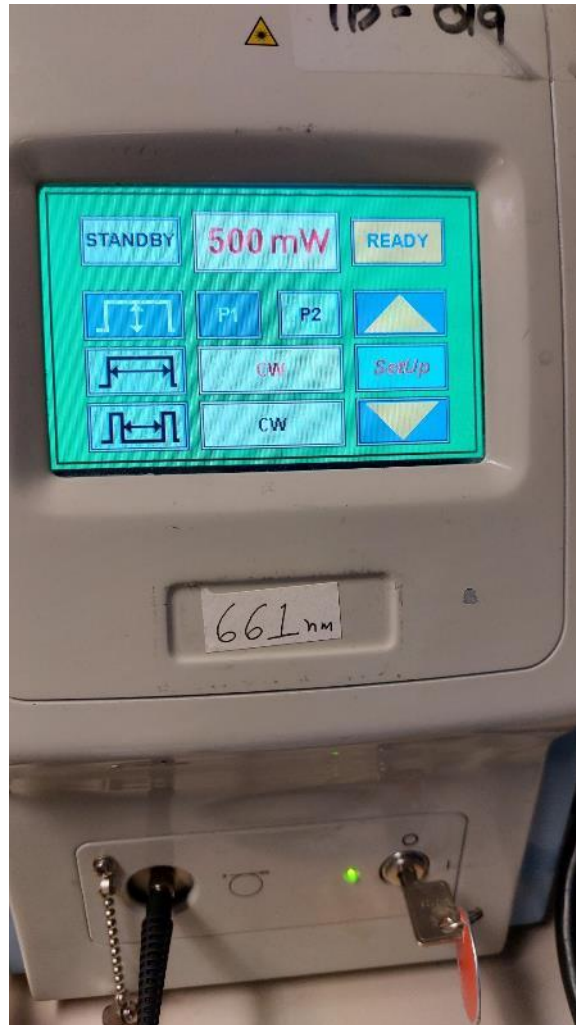
Figure 64. 661nm laser system (B&W Tek, Newark, DE).

The light source and detector were securely positioned within 1.86mm catheters (Flexineedle 18G, Best Medical Inc., USA) to ensure data integrity. This process was standardized for data acquisition at all anatomical regions and measurements. The light source and detectors were configured in statict positions to enhance the system's analytical accuracy.

To establish a comparative baseline with the dual catheter system, an "in-air" placebo experiment was designed and implemented. The experiment involved capturing measurements at fixed distances ranging from 2-10mm between the isotropic detector and the light source using a custom 3D-printed jig.

This approach aimed to gain a deeper understanding of the behavior of 661nm light transmission and to offer a point of reference when evaluating its transmission through different anatomical regions of the porcine model. All measurements were standardized with other protocols performed throughout this study, ensuring accurate and reliable results.

This study utilized cone-beam computed tomography (CBCT) to image all specimen sites digitally. A standardized protocol was followed using the CS 9300 Carestream CBCT machine (Carestream Dental LLC): field of view 17 x 11, voxel size 250, tube voltage 80kV, tube current 4.0mA, and dose length product 650 mGy.Cm^2. The resulting images were preserved in a DICOM format and converted to stereolithography (STL) with the software application InVesalius 3.1 (Center for Information Technology Renato Archer, Brazil).

To assess variables such as tissue type, distance, density, radiopacity, and radiolucency, two separate CBCT scans were acquired of the anterior and posterior segments. The scans were then imported into Blue Sky Plan Software (Blue Sky Plan, Version 4.8.38) for further analysis. Data obtained was correlated with fluence rate values (mW/cm^2) from the medical dosimetry system.

The anatomic regions of interest were scanned using the Medit 700i (MEDIT CORP.) surface topography optical imaging acquisition device. This device incorporates a highly functioning proprietary software suite that enables the integration of the STL file of the Porcine mandible as a base outline for the precise acquisition of surface topography of the external surface layer with accuracy and repeatability. This combined approach allowed for precise surface topography while building the external surface layer with accuracy and repeatability. This protocol allowed the preservation of catheter placement during data collection for improved accuracy.

3.3.2 Results

This proof-of-concept investigation of the porcine mandible cadaver compared light fluence transmission rates across several types of tissue boundaries and junctions. These anatomic regions of interest are identified as the following right condyle (featuring thick cortical bone), left condyle (consisting of thick cortical bone), right condylar ramus (characterized by thick cortical bone), right posterior quadrant (comprised of bone & root), left posterior quadrant (characterized by bone & root), left posterior middle segment (featuring half bone & half soft tissue), right anterior segment (consisting of cancellous bone & root), left anterior segment (characterized by a combination of cancellous bone & root).

Data points were collected for each region considering combinations of soft tissue, bone, and the presence or absence of dentin and enamel. Measurements in the porcine cadaver mandible were taken across distances ranging from 2mm to 10mm. Additionally, placebo (in air) light transmission was analyzed within the same range of distances (2mm to 10mm) to provide a comprehensive understanding of tissue and light interactions within these anatomical regions. (See Figures 65 - 72)
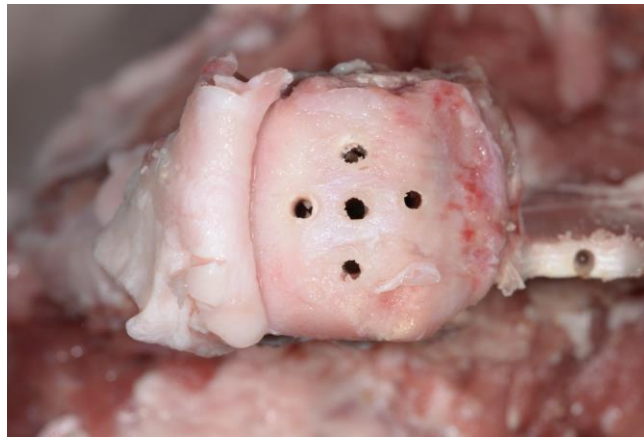
Figure 65. Proof-of-concept porcine investigation. Right Condyle.

Figure 67. Proof-of-concept porcine investigation. Right Condylar Ramus.
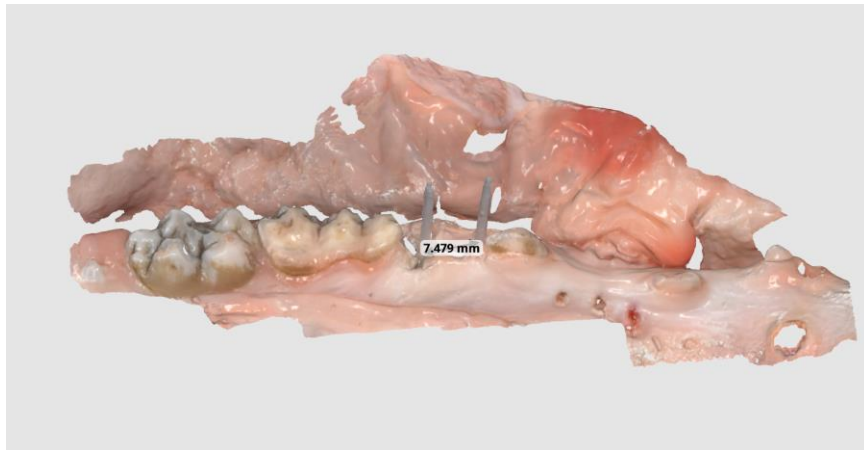
Figure 66. Proof-of-concept porcine investigation. Left Posterior Quadrant.

Figure 69. Proof-of-concept porcine investigation. Left Condyle.
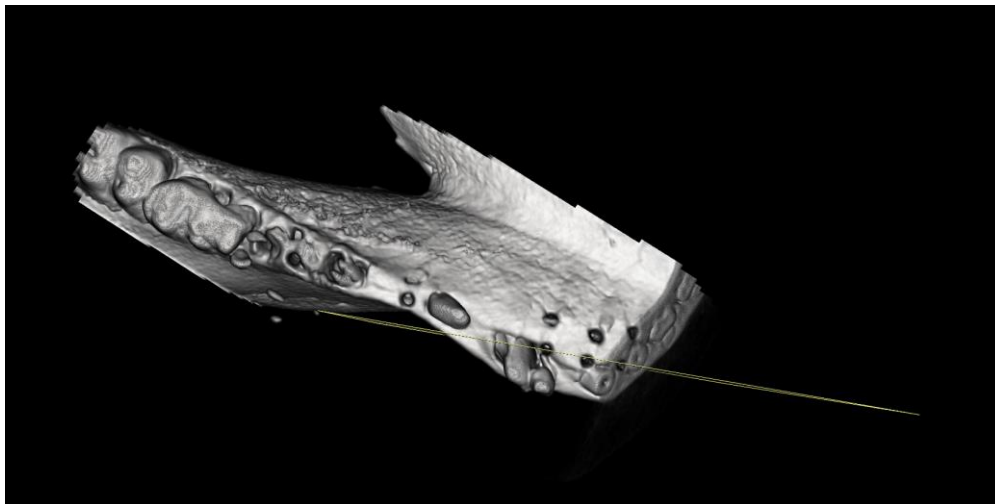
Figure 68. Proof-of-concept porcine investigation. Right Anterior Segment.

Figure 71. Proof-of-concept porcine investigation. Right Posterior Quadrant.
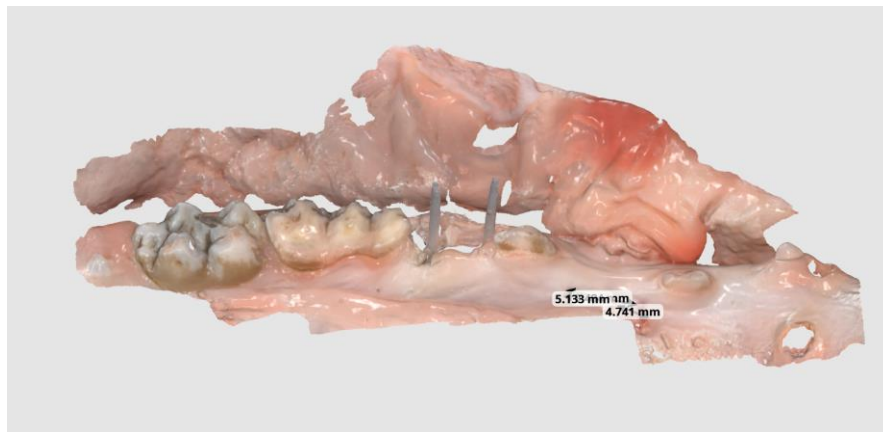
Figure 70. Proof-of-concept porcine investigation. Left Posterior Middle Segment.
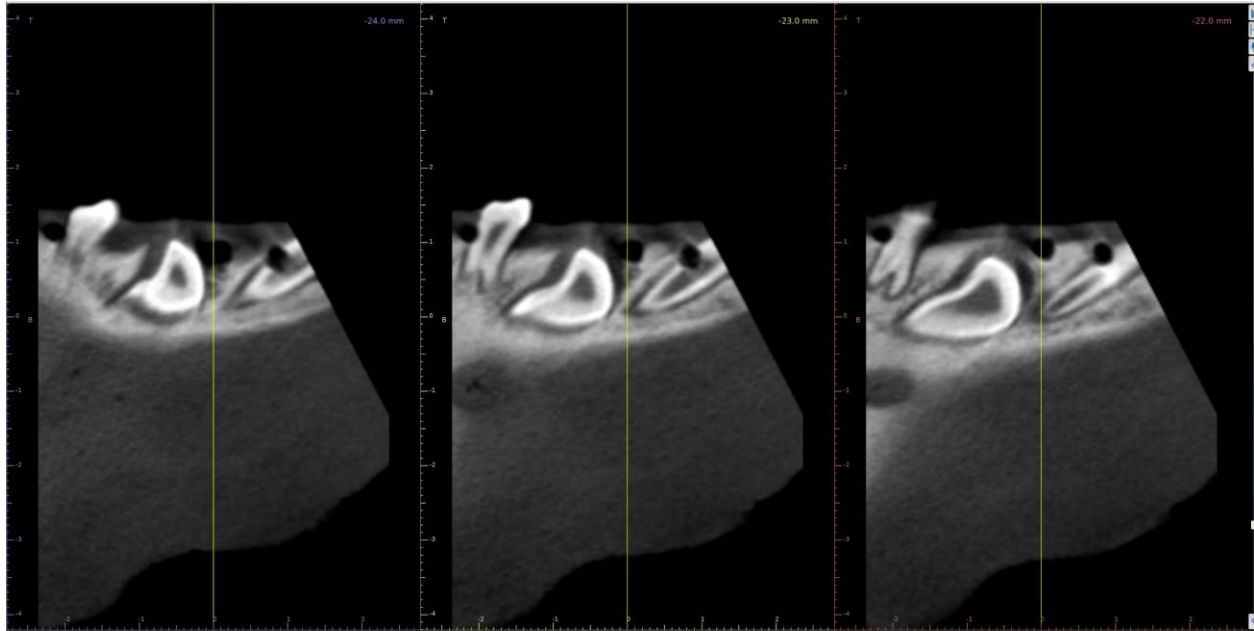
Figure 72. Proof-of-concept porcine investigation. Left Anterior Segment.

The placebo-control (in air) 661nm light transmission recorded values for distances of 2mm-10mm. The following intervals were observed: 2mm (265.18mW/cm^2), 4mm (73.75mw/cm^2), 6mm (34.01 mw/cm^2), 8mm (19.52 mw/cm^2), 10mm (12.48 mw/cm^2). These light transmission measurements indicate a decrease as the distance from the light source increases. This suggests an inverse relationship between distance and the source of light transmission. (See Figure 73 - 74)
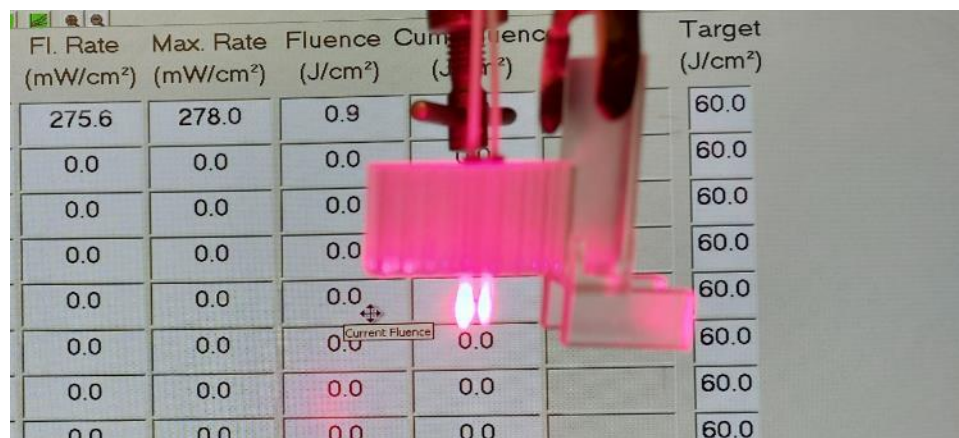
Figure 73. Placebo-control (in air) light transmission measurement with dual catheter approach and customized 3-D printed jig.
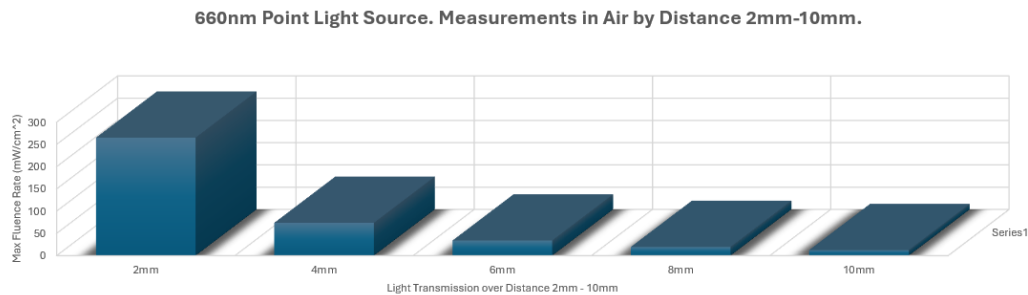
Figure 74. Results for Placebo-Control.

A consistent trend of decreasing fluence rate (mW/cm^2) with increasing separation from the light source was noted for this investigation. Regions characterized by dentin/enamel consistently exhibited diminished light transmission compared to regions composed solely of bone. The highest recorded fluence rate was 203.1 mW/cm^2 (bone + dental root + soft tissue), while the lowest transmission recorded was 5.7 mW/cm^2 (bone alone). These findings are supported by a detailed and expanded graphical representation of the light transmission rates of a 661nm wavelength across all anatomical regions investigated. (See Figure 75)
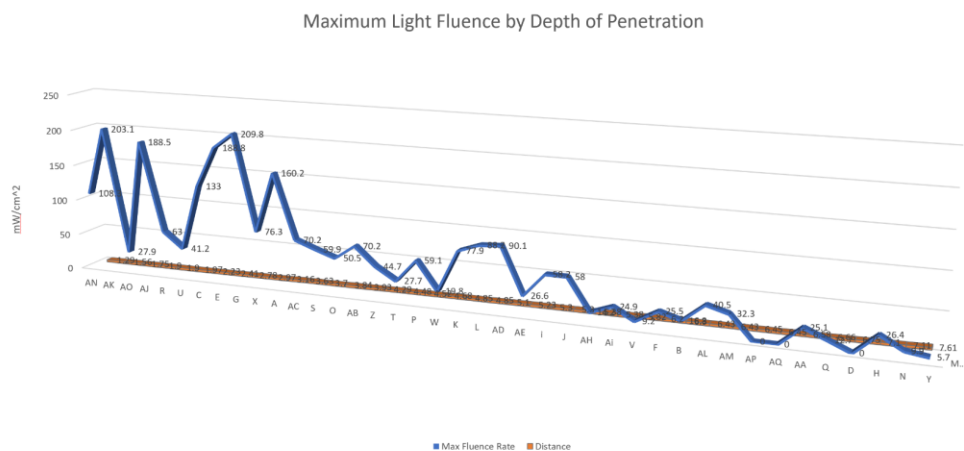
Figure 75. Porcine Light Transmission Through Bone. Area Map depicting fluence transmission rates (mW/cm^2) for 661nm point laser light source through porcine bone.

89

The analysis assessing light transmission through tissue boundaries resulted in noticeable patterns of fluence valuations. These patterns were categorized into groups of 1) bone and soft tissue, and 2) those incorporating both dentin and enamel. The light fluence rate value in thick cortical bone was found to be lower than in other regions at the following distances: 2mm (76.3 mW/cm^2), 4mm (61.7 mW/cm^2), 6mm (42.3 mW/cm^2), 8mm (16.05 mW/cm^2)). Fluence rates in bone and soft tissue were recorded as 2mm (195.8 mW/cm^2) and 6mm (36.4 mW/cm^2). Fluence rate in regions characterized by cancellous bone and the presence of dentin/enamel: 2mm (52.1 mW/cm^2), 4mm (43.4 mW/cm^2), 6mm (10.95 mW/cm^2), 8mm (9.9 mW/cm^2). The fluence rate in bone, dentin/enamel, and soft tissue regions was recorded at 2mm from the point source (68.1 mW/cm^2).

The impact of tissue type on 661nm light transmission was investigated by comparing regions with dentin/enamel of only bone and soft tissue. Fluence rates (mW/cm^2) were based on available data and assessed at 2mm and 6mm. Fluence rate values at 2mm from the point source were recorded for the following: bone, root, and soft tissue only (68 mW/cm^2), Thick Cortical Bone (76.3 mW/cm^2), Cancellous Bone + Root (52.1 mW/cm^2), and Bone and Soft Tissue (195.8 mW/cm^2). Similar values at 6mm included cancellous bone + root (10.95 mW/cm^2), thick cortical bone (16.05 mW/cm^2), bone, and soft tissue (36.04 mW/cm^2).

Specific reductions were observed when focusing on the presence of dentin and enamel. These reductions were assessed at 2mm and 6mm from the point source. At the 2mm interval, 661nm transmission was reduced by 31.72% for bone alone and 65.22% for a combination of bone and soft tissue. Sites at 6mm were reduced by 31.78%.

3.3.3   Discussion

The results from the porcine mandible cadaver preliminary investigation have established light transmission characteristics. It is now understood that light transmission is altered when transitioning across distinct tissue boundaries at interfaces with differing optical properties. This specifically includes bone, soft tissue, bone, dentin, and enamel. Dosing adjustments should be considered to accommodate the varying optical characteristics, absorption, and scattering profiles. This is particularly relevant in vascular-rich regions of soft tissue and cancellous medullary bone with improved access to hemoglobin-based chromophores for absorption.

The results of this study have indicated that areas containing dentin/enamel exhibit reduced light transmission when directly irradiated through these properties. This trend was also consistent in the presence of dentin/enamel. On the other hand, soft tissue regions reported increased rates when compared to those without soft tissue. Although further investigation is needed to quantify these preliminary results, these phenomena are likely driven by the complex anatomical structures of each tissue type.

PDT and PBM dosage significantly depend on the anatomical features and light optical properties at the site of light delivery. Given the anatomical similarities between human intraoral tissues and the porcine mandible, this study establishes a foundational platform for future investigations to improve medical dosimetry and light delivery. The research on light delivery therapies involves complex models to simulate the intricate pathophysiology of the head and neck region. The current dose-escalation models have limitations that need to be addressed for PDT and PBM. This is driven by ethical considerations, economic viability, and direct translation to human clinical care.

3.4 Light Transmission (661nm), 500mW vs. 1W, Porcine Soft Tissues

The efficacy of PDT and PBM are significantly influenced by irradiation parameters and the anatomical characteristics of the target site. PDT involves the use of non-toxic photosensitizers to eliminate disease pathologies, while PBM is a minimally invasive application that helps reduce pain and improve wound healing. (11, 13-16, 64-67) Variations of wavelength, power, fluence, irradiance, and beam area spot size of the device are all factors that contribute to dosing.

PDT and PBM are two therapeutic approaches that utilize different portions of the electromagnetic spectrum to achieve their therapeutic effects. PDT works within the visible electromagnetic spectrum (400-750nm) and PBM will utilize both red and near-infrared (NIR) wavelengths 600-1,000nm). (10, 15, 33, 43, 148, 160-162) Wavelength characterizations vary with higher wavelengths typically correlating to a deeper penetration depth. (124, 147, 160, 163) Regardless of wavelength, the signal penetration will decrease as the distance that light will travel increases. (164)

3.4.1 Theory, Dosimetry

The red visible region of the electromagnetic spectrum (625nm-740nm) has unique nonionizing capabilities in biological mediums. (10, 19, 48, 49, 53, 147-149) These wavelengths are extensively used with broad clinical applicability in medicine and dentistry. (28, 106, 150-152) Although wavelength is a parameter in dosimetry, other factors related to light propagation through host biological tissue mediums significantly influence therapeutic efficacy. Therefore, it is essential to understand how the heterogeneous properties of different soft tissues affect the transmission of light fluence (mW/CM^2).

It is important to note that transmission depth is influenced by tissue morphology rather than an increase or decrease in optical power. (156, 160, 165-171) Making real-time dosimetry adjustments can help predict the desired biological effect. This involves the precise calculation of dosimetric quantities absorbed at the intended site to deliver the appropriate dosage of fluence and irradiance. This can be

achieved through various techniques such as pre-planning, real-time monitoring, treatment adaptation, and outcome assessment. (14)

In photochemistry, fluence is the flux of radiation particles or energy delivered within a specific time interval. (172, 173) It is defined as the radiant energy Q at a given point in space that is incident on a small sphere from all directions divided by the cross-sectional area of that sphere (J m^{-2}). (173, 174) The energy fluence determines the laser energy delivered and is expressed in joules/cm^2. (175) Fluence is calculated as $Fluence \left[\frac{J}{cm^2}\right] = \frac{energy \ [J]}{beam \ area \ spot \ size \ [cm^2]}$. (176)

Irradiance is the *radiant power* of all wavelength's incident from an upward direction on a small element of the surface containing the point under consideration divided by the area of the element (W m^{-2} or mW/cm^2). (173, 175, 177) The necessary dose is specified by the energy or amount of photons absorbed per unit area or unit volume by an irradiated object. Irradiance is calculated using the formula $Irradiance \left[\frac{W}{cm^2}\right] = \frac{output \ power \ [W]}{beam \ area \ spot \ size \ [cm^2]}$. (176)

The optical properties of soft tissues are heterogeneous, and they have a significant impact on light propagation and dosimetry. The distribution of light through a turbid medium is dependent on the characteristics of the light source and the optical properties of the medium. (10) In therapeutic applications, red wavelength light follows a complex path through tissue, and its distribution and energy deposition are critical. (124) Chromophores, such as water, oxyhemoglobin, deoxyhemoglobin, melanin, and cytochromes all play a role in affecting light absorption and scattering in tissues. (16, 178) (See Figure 76 – 79)

REFLECTION
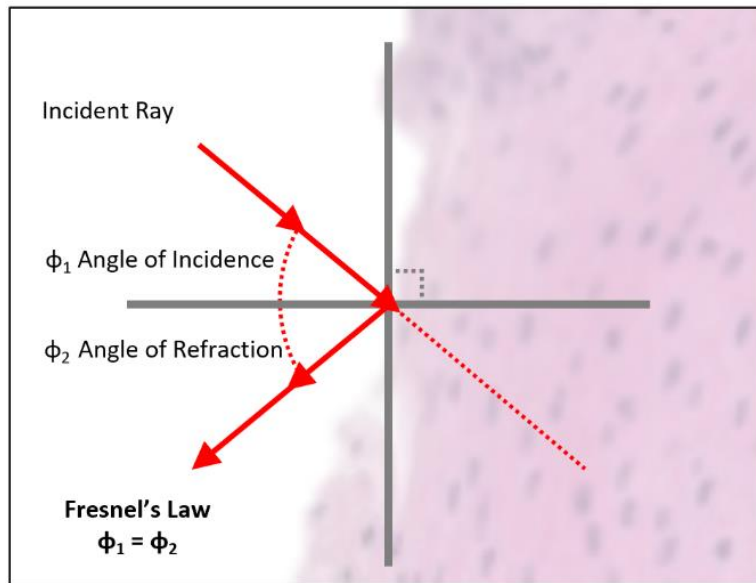
Figure 76. Reflection Diagram with depiction of Fresnel's Law.

REFRACTION
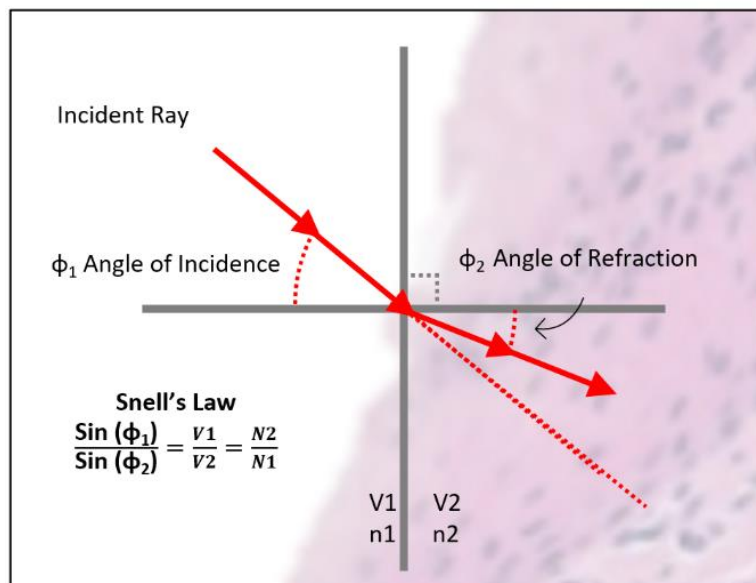
Figure 77. Refraction Diagram with depiction of Snell's Law.

ABSORPTION

Figure 79. Absorption diagram depicting Lambert-Beer's Law.

SCATTERING
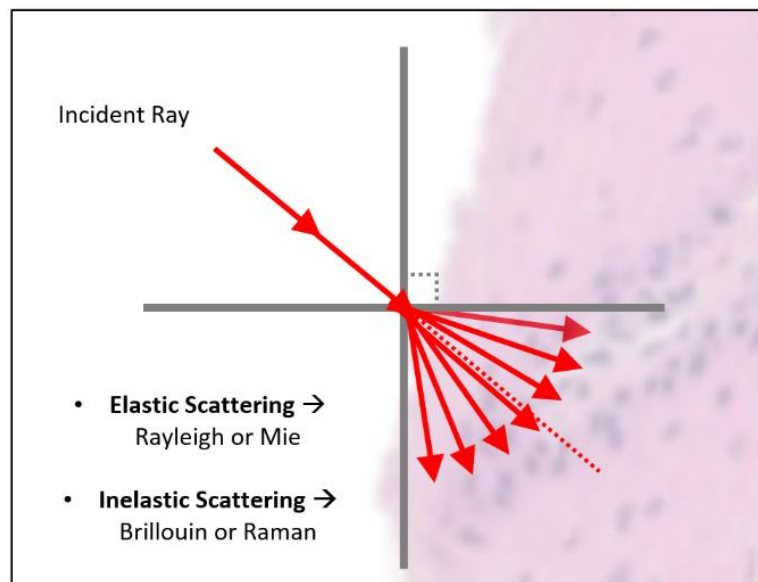
Figure 78. Scattering diagram depicting elastic and inelastic scattering.

The interaction of light with a target is a fundamental aspect of optics that is characterized by reflection, refraction, absorption, and scattering coefficients. (16) The reflection and refraction of light are governed by Fresnel's and Snell's laws. (179-181) Both of these are directly proportional to the angle of incidence and can be adjusted by manipulating the light beam's angulation. (16, 179-182)

Snell's law is calculated by the formula: (16, 180, 181)

$$\frac{\sin(\varphi_1)}{\sin(\varphi_2)} = \frac{v_1}{v_2} = \frac{n_2}{n_1}.$$

Fresnel's law is calculated using the formula: (16, 180, 181)

$$\varphi_1 = \varphi_2.$$

The medium of light absorption is defined by the coefficient μa (cm^-1), which represents the fraction of incident light absorbed per incremental pathlength or travel within the medium. *(124)* The absorption coefficient is given by $\mu_a = \sum_{n=1}^{n} c_n \varepsilon_n(\lambda)$. (180) Absorption is the sum of contributions from all absorbing chromophores within the tissue and is a reduction in light energy proportional to penetration depth as defined by Lambert-Beer's Law. (16, 124, 180, 181, 183)

The Lambert-Beer's law is calculated by the formula: (16, 180, 181)

$$I_x = I_o e^{-a_{abs}*x}$$

The optical properties of biological tissue are a function of various factors such as blood, water, melanin, and adipose cell concentrations. (16, 183) These constituents significantly impact the absorption coefficient of light. Hemoglobin and melanin have been identified as the dominant absorbers of light in the visible range. (124, 183) The scattering of light in tissue is defined by the coefficient $\mu s'$ (cm^-1) and the

probability of scatter per unit length of photon travel. (184, 185) The scattering coefficient is defined by $\mu_s = p\sigma_s$. (180) This interaction of particles with differing optical properties from their surrounding medium directly affects light intensity due to scattering. (16, 183) The forward scattering of tissue photons is defined by Rayleigh and Mie's theories, which play a role in determining the direction of the scattered beam. (16, 124)

3.4.2   Methods

The mandibles of five Yorkshire pigs were obtained from a slaughterhouse (Animal Technologies, Tyler, Texas). All specimens were transported frozen, unfixed, and fully thawed before analysis. Both males and females were of different weights and ages to show conditions variability within the same animal model. Each specimen consisted of the entire mandible, condylar structures, and intact intra and extraoral tissues for this respective anatomy. This feature was requested that the tongue was removed to provide access to the underlying tissues and structures.

Soft Tissue measurements were acquired in the same regions of interest across all models. This included G1) genioglossus muscle, G2) masseter muscle, G3) sternohyoid muscle, G4) buccinator muscle, G5) cutaneous fascia, G6) vestibular tissue. (See Figure 80)

LEGEND

G1: Genioglossus Muscle

G2: Masseter Muscle

G3: Sternohyoid Muscle

G4: Buccinator Muscle

G5: Cutaneous Fascia

G6: Vestibule
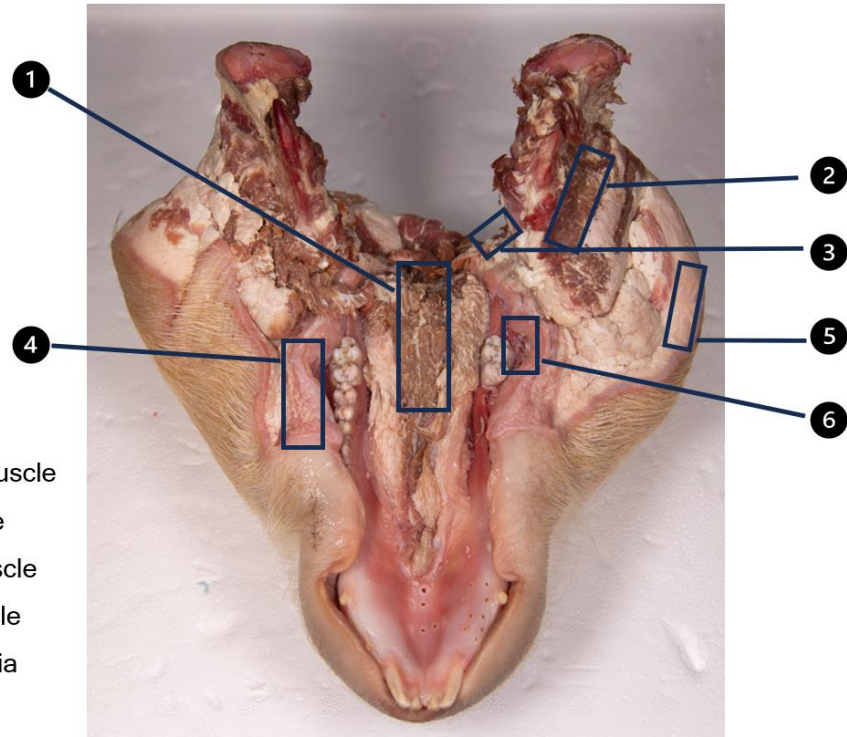
LEGEND

G1: Genioglossus Muscle

G2: Masseter Muscle

G5: Cutaneous Fascia
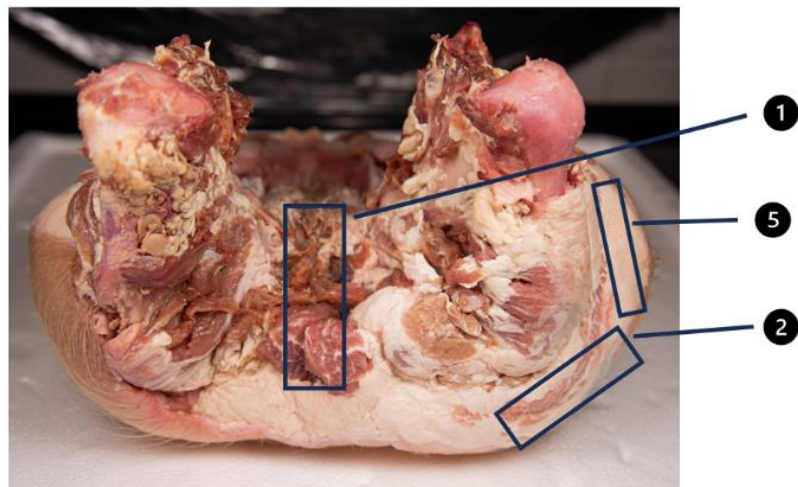
Figure 80. Porcine Light Transmission (661), Soft Tissue, Regions of Interest.

98

An interstitial dual-catheter medical dosimetry system, a light source, and a detector acquired interstitial 661nm light transmission measurements (mW/cm^2). (21, 29, 108, 109, 112, 115, 116) The power measurements were standardized inside an integrating sphere, and the isotropic detector was calibrated using an LED calibration sphere. This dual-catheter configuration was connected to a customized medical dosimetry system programmed with a wavelength-specific algorithm to acquire and analyze data across all anatomical regions of interest.

The experimental setup consisted of two primary electronic components, namely an isotropic detector and a light source. The 0.8mm isotropic detector (IP85, Medlight S.A.) was connected to a 16-channel receiver and a medical dosimetry system. This system is designed to quantify optical light coefficients during in vivo dosimetry calculations, including absorption (μ-a), scattering (μ's), and the effective attenuation coefficient (μ-eff). A custom 2.0mm point light source (#7035-01 Rev 2; Pioneer Optics) was coupled to a 661nm laser system (B&W Tek, Newark, DE) and the same medical dosimetry system arrangement. (See Figure 81)
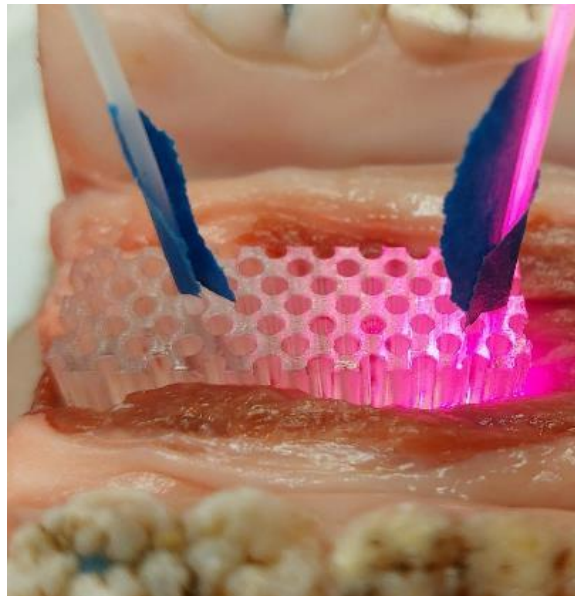
Figure 81. Dosimetry system catheters placed interstitially for light transmission measurement through the genioglossus muscle.

The light source and detector were securely positioned within 1.86mm catheters (Flexineedle 17G 20cm with Luer Lock, Best Medical Int.). The data acquisition process was standardized for all measurements and anatomical regions with data measurements at fixed distances of 2-14mm. The light source and detectors were secured at constant positions to optimize the system's analytical accuracy. Further details about distance calculations, differential evolution algorithms, wavelength fitting algorithms, and system configurations can be found in prior work published by the Zhu laboratory group. (21, 29, 108, 109, 112, 115)

The diffusion approximation method was utilized to determine light propagation through a scattering medium like porcine cadaver tissue. Although light fluence rate φ measurements at two different distances can be used to calculate absorption and scattering coefficients. Per Ong and colleagues (29), the light fluence rate φ per source power S at a distance r from a point source can be expressed as the following formula:

$$\frac{\varphi}{S} = \frac{\mu^2 eff}{4\pi r} e^{-\mu_{efff}r} = \frac{3\mu'_s}{4\pi r} e^{-\mu_{efff}r}$$

A custom-designed three-dimensional jig was designed in the Meshmixer software package (Autodesk) with 2mm holes separated at distances of 2mm in a linear direction. The design was then printed in clear acrylic resin (Formlabs). This design enabled the replication of measurements across multiple specimen samples, thereby facilitating the measurements of the maximum fluence rate at precise intervals of 2mm, 4mm, 6mm, 8mm, 10mm, 12mm, and 14mm. This provided a systematic approach to producing results with accuracy and precision. (See Figure 82 & 83)
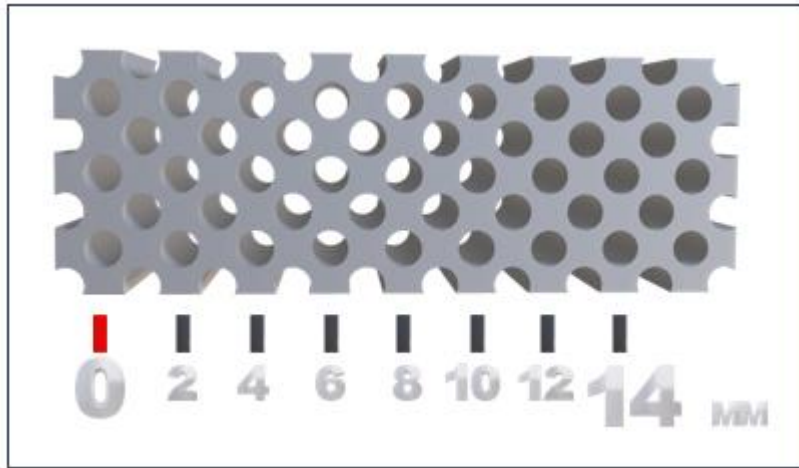
Figure 82. Rendering of custom 3D printed resin jig allowing catheter placement at fixed distances from 0-14mm.
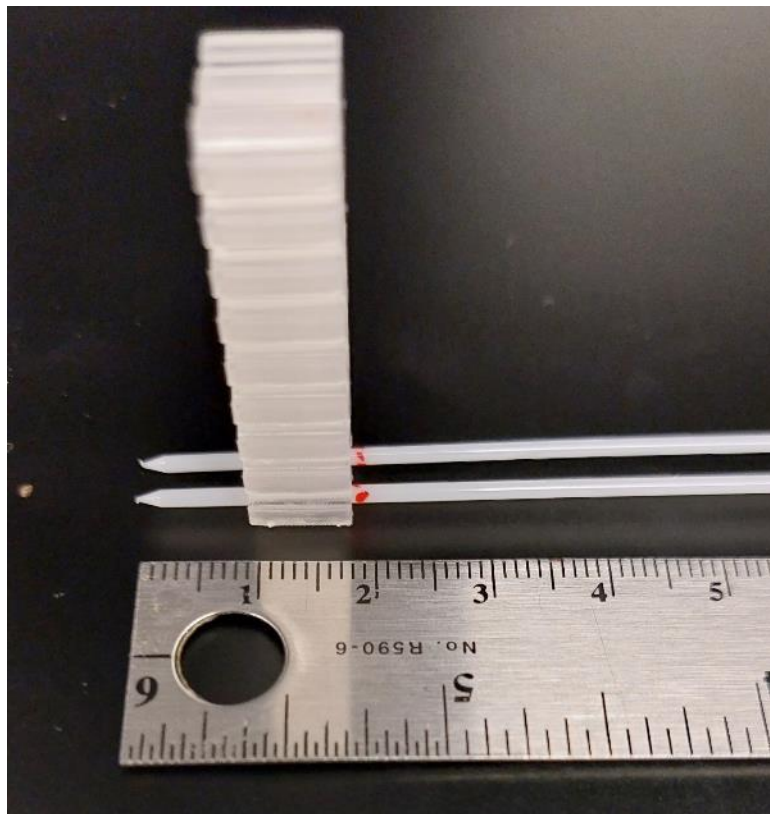
Figure 83. Measured placement of both catheters through the custom 3D printed jig to ensure that at least 10mm of each catheter is interstitially inserted at each region of interest.

A standardized jig and catheter placement methodology was adopted for all regions of interest across all specimens. After locating the anatomical reference, the 0.5mm detector and catheter were interstitially placed through the jig at 0mm. This was immediately followed by the interstitial placement of the 2mm point light source and catheter. The first placement was at 2mm, then followed by 4mm, and so on. This protocol did not cause rotation of the 0.5mm isotropic detector receiving the light signal. (See Figure 84)
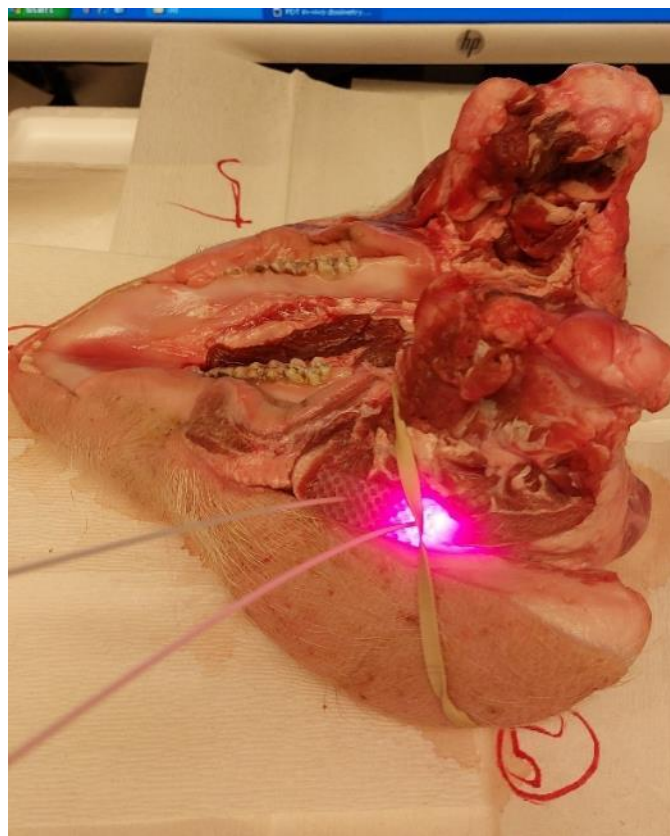
Figure 84. Region of interest is the masseter muscle lateral to the base of condyle.

An elevated camera and tripod were standardized to capture the values directly from the dosimetry system. The data capture was acquired in 10-second intervals triggered by an internal automatic camera

timer. Five 5 data points were taken per region of interest (per specimen) to ensure the accuracy and reliability of the results.

Each porcine mandible specimen was digitized utilizing a cone-beam computerized tomography machine (3D Accuitomo XYZ Slice View Tomograph, Norita, Japan) to conduct assessments in all regions of interest based on the work of other groups. (117-123) The settings for all image acquisitions were as follows: field of view 170 x 120, tube voltage 90kV, tube current 5.0mA, Imaging D140 x 100 Hi-Fi. All CBCT images were converted to DICOM files with proprietary software provided by Norita and Stereolithography (STL) files by InVesalius 3.1 (Center for Information Technology Renato Archer, Brazil). The data in the DICOM file allows us to view the internal regions of interest, whereas the STL files allow us to assess the outer surface-based topographies. CBCT images were viewed and assessed by the DTX Studio Implant Software (Version 3.6.6.1, Nobel Biocare, Goteborg, Sweden). (See Figure 85 - 87)

Figure 85. Porcine Cadaver CBCT Assessment in HU. a) standardization for image acquisition of anterior mandible. b) re-positioning to acquire image of condyles.
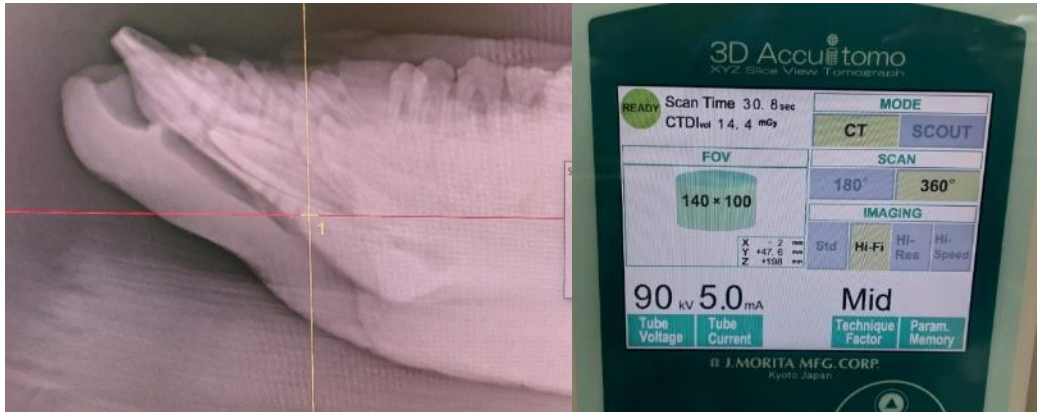
Figure 86. Porcine cadaver CBCT image acquisition. Image rendering from Norita software (left). CBCT device settings (right).
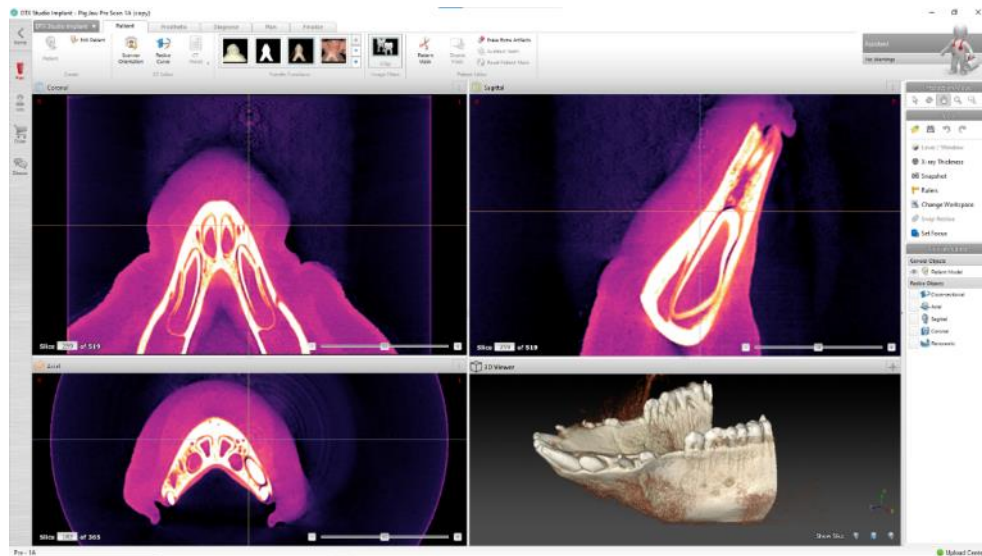
Figure 87. Porcine cadaver CBCT Assessment in the DTX software package.

3.4.3 Results

Light transmission values were obtained from five porcine mandible cadaver specimens across six anatomic regions (G1 to G6). Measurements were captured at varying distances (2mm – 14mm) within each region and repeated five times. This procedure was conducted for two power output levels: 500mW and 1W. This ensured a true power comparison for each reference point, eliminating any variables and micromovements that could impact results. Five data points were collected for each series, ranging from 2mm to 14mm. This resulted in 70 data points in each of the six anatomical regions of the five specimens. For this analysis, 350 data points were prepared for each region in both power configurations.

3.4.4 Statistical Analysis & Discussion

3.4.4.1 Data Distribution

-Methods and Materials: Data was analyzed using IBM SPSS Statistic (version 29.0.1.0 (1711). The distribution characteristics of light transmission were screened for all combinations of factors (anatomic regions, specimens, distances, and power outputs) using the Shapiro-Wilk test. Following significant deviations from normal distributions, the non-parametric Friedman's test was employed to explore relationships between light transmission values and the examined factors.

-Results: The Shapiro-Wilk test revealed significant deviations from normal distribution across all examined factor combinations: combinations of light transmission values with specimens ($P<0.001$), power outputs ($p<0.001$), anatomic regions ($p<0.001$), and distances ($p<0.0001$). Friedman's test determined statistical significance in light transmission across specimens ($p<0.001$) and across all anatomic regions ($P<0.001$). There was no significant difference in light transmission across different distances ($p=0.264$). (See Figure 87-96).

Tests of Normality

	Specimen	Kolmogorov-Smirnov[a]			Shapiro-Wilk		
		Statistic	df	Sig.	Statistic	df	Sig.
MFR	1	.323	420	<.001	.513	420	<.001
	2	.322	420	<.001	.523	420	<.001
	3	.333	420	<.001	.485	420	<.001
	4	.344	420	<.001	.448	420	<.001
	5	.342	420	<.001	.456	420	<.001

a. Lilliefors Significance Correction

Figure 88. Light Transmission (661nm), Porcine Soft Tissue Regions. Shapiro-Wilk Normality test for all five specimens.

Figure 89. Light Transmission (661nm), Porcine Soft Tissue Regions. Descriptive Statistics, Box Plot Light Distribution for all five specimens.

106

Tests of Normality

	Group	Kolmogorov-Smirnov[a]			Shapiro-Wilk		
		Statistic	df	Sig.	Statistic	df	Sig.
MFR	1	.362	350	<.001	.492	350	<.001
	2	.333	350	<.001	.500	350	<.001
	3	.322	350	<.001	.505	350	<.001
	4	.329	350	<.001	.504	350	<.001
	5	.280	350	<.001	.625	350	<.001
	6	.344	350	<.001	.483	350	<.001

a. Lilliefors Significance Correction

Figure 90. Light Transmission (661nm), Porcine Soft Tissue Regions. Shapiro-Wilk Normality test for all six anatomic regions of interest.

'
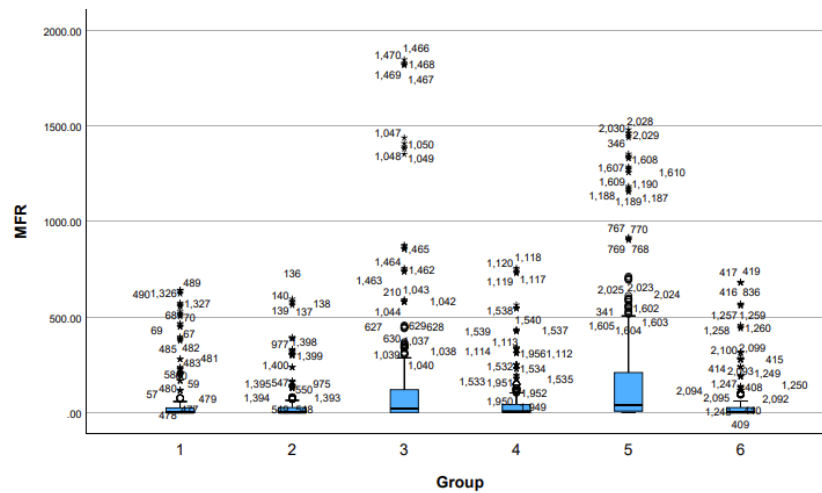
Figure 91. Light Transmission (661nm), Porcine Soft Tissue Regions. Descriptive Statistics, Box Plot Light Distribution for all six anatomic regions of interest.

Tests of Normality

	Power	Kolmogorov-Smirnov[a]			Shapiro-Wilk		
		Statistic	df	Sig.	Statistic	df	Sig.
MFR	1W	.322	1050	<.001	.524	1050	<.001
	500mW	.322	1050	<.001	.528	1050	<.001

a. Lilliefors Significance Correction

Figure 92. Light Transmission (661nm), Porcine Soft Tissue Regions. Shapiro-Wilk Normality test for power output 1W and 500mW.
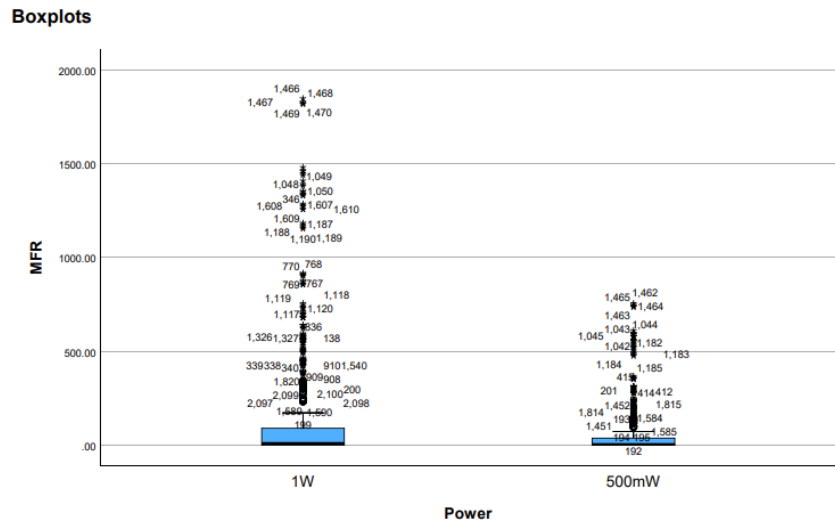
Boxplots

Figure 93. Light Transmission (661nm), Porcine Soft Tissue Regions. Descriptive Statistics, Box Plot Light Distribution for power output 1W and 500mW.

Tests of Normality

	Distance ???	Kolmogorov-Smirnov[a]			Shapiro-Wilk		
		Statistic	df	Sig.	Statistic	df	Sig.
MFR	2	.170	300	<.001	.805	300	<.001
	4	.217	300	<.001	.725	300	<.001
	6	.240	300	<.001	.712	300	<.001
	8	.260	300	<.001	.700	300	<.001
	10	.383	300	<.001	.637	300	<.001
	12	.499	300	<.001	.463	300	<.001
	14	.540	300	<.001	.208	300	<.001

a. Lilliefors Significance Correction

Figure 94. Light Transmission (661nm), Porcine Soft Tissue Regions. Shapiro-Wilk Normality test for distance 2mm - 14mm.
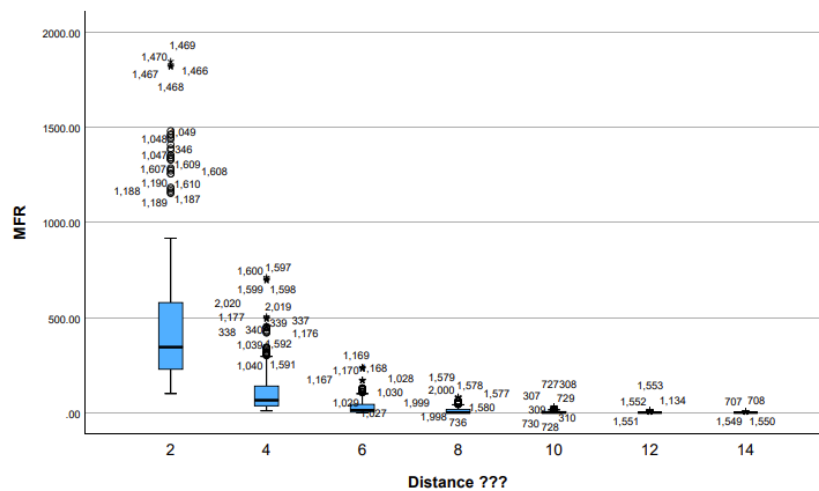
Figure 95. Light Transmission (661nm), Porcine Soft Tissue Regions. Descriptive Statistics, Box Plot Light Distribution for distance 2mm - 14mm.

109

NPar Tests

Friedman Test

Ranks	
	Mean Rank
Specimen	1.44
MFR	1.56

Ranks	
	Mean Rank
MFR	1.56
Group	1.44

Ranks	
	Mean Rank
MFR	1.49
Distance ???	1.51

Test Statistics[a]	
N	2100
Chi-Square	29.288
df	1
Asymp. Sig.	<.001

a. Friedman Test

Test Statistics[a]	
N	2169
Chi-Square	34.361
df	1
Asymp. Sig.	<.001

a. Friedman Test

Test Statistics[a]	
N	2169
Chi-Square	1.247
df	1
Asymp. Sig.	.264

a. Friedman Test

Figure 96. Light Transmission (661nm), Porcine Soft Tissue Regions of Interest, Friedman Test.

-Discussion: The reported significance of the Shapiro-Wilk series for all combinations highlights the intricacies of performing light dosimetry within heterogeneous tissues of similar origin. Friedman's test determined significant differences in light transmission across all specimens, which emphasizes the variations that exist among the same biological species. The significant results reported between the six regions of interest highlight the variation in anatomical structure for each region of interest. The non-significance reported for distance suggests that the depth of measurement may not significantly influence the light transmission in this context.

110

3.4.4.2 Light Transmission Between Anatomic Regions

-Primary Objective: To determine how the power output of 500mW vs. 1W can affect light transmission across various anatomical regions of all porcine cadaver specimens.

-Aim: The primary AIM of this assessment is to analyze the effects of 500mW and 1W power output on light transmission (mW/cm^2).

-Materials and Methods: Data was analyzed using IBM SPSS Statistic (version 29.0.1.0 (1711). The Wilcoxon Signed Ranks test was utilized to analyze the differences in light transmission for 500mW and then 1W power output. Comparisons were made for 10 different pairings of specimens 1-5 with a Bonferroni correction (0.05 / 10 = 0.005).

-Results: The Wilcoxon Signed Rank test reported statistical significance for Specimens 1 & 2 after correction in both 500mW and 1W cohorts. (See Figure 97 - 98)

Test Statistics[a]

	Median S2 - Median S1	Median S3 - Median S1	Median S4 - Median S1	Median S5 - Median S1
Z	-3.437[b]	-.029[c]	-.040[c]	-1.023[b]
Asymp. Sig. (2-tailed)	<.001	.977	.968	.306

Test Statistics[a]

	Median S3 - Median S2	Median S4 - Median S2	Median S5 - Median S2	Median S4 - Median S3
Z	-1.737[c]	-1.472[c]	-.452[c]	-.852[c]
Asymp. Sig. (2-tailed)	.082	.141	.651	.394

Test Statistics[a]

	Median S5 - Median S3	Median S5 - Median S4
Z	-1.354[b]	-2.236[b]
Asymp. Sig. (2-tailed)	.176	.025

a. Wilcoxon Signed Ranks Test

b. Based on positive ranks.

c. Based on negative ranks.

Figure 97. Light Transmission (661nm), Porcine Soft Tissue Regions. Wilcoxon Signed Rank Test. 500mW.

Test Statistics[a]

	Median S2 - Median S1	Median S3 - Median S1	Median S4 - Median S1	Median S5 - Median S1
Z	-3.871[b]	-.285[b]	-.054[c]	-1.418[b]
Asymp. Sig. (2-tailed)	<.001	.776	.957	.156

Test Statistics[a]

	Median S3 - Median S2	Median S4 - Median S2	Median S5 - Median S2	Median S4 - Median S3
Z	-1.802[c]	-1.742[c]	-.216[c]	-1.105[c]
Asymp. Sig. (2-tailed)	.072	.081	.829	.269

Test Statistics[a]

	Median S5 - Median S3	Median S5 - Median S4
Z	-1.413[b]	-2.595[b]
Asymp. Sig. (2-tailed)	.158	.009

a. Wilcoxon Signed Ranks Test

b. Based on positive ranks.

c. Based on negative ranks.

Figure 98. Light Transmission (661nm), Porcine Soft Tissue Regions. Wilcoxon Signed Rank Test. 1W.

-Discussion: A statistically significant difference in light transmission was reported between specimens 1 and 2 between both power outputs. This suggests that while laser power may influence the intensity of light transmission, the differences between all the sample pairings remain consistent. This finding supports the notion that the underlying tissue optical properties are more likely to influence light transmission rather than power output.

3.4.4.3 Light Transmission Relationship for a Particular Region Between All Specimens

-Primary Objective: To determine the variation in distance and anatomical region of interest.

-Aim: The primary AIM of this analysis is to determine the relationship between light transmission, distance, and anatomical region of interest.

-Materials and Methods: Data was analyzed using IBM SPSS Statistic (version 29.0.1.0 (1711). Due to the non-normal distribution of data, A Pearson correlation analysis was utilized to assess the relationships between light transmission, distance, and anatomical region of interest.

-Results: There was a significant negative correlation (-.552, $p<.001$) reported between light transmission and distance. A significant positive correlation (.75, $p<.001$) was detected between light transmission and the anatomical regions. (See Figure 99)

Correlations

		MFR	Distance ???	Group
MFR	Pearson Correlation	1	-.552**	.075**
	Sig. (2-tailed)		<.001	<.001
	N	2169	2169	2169
Distance ???	Pearson Correlation	-.552**	1	.000
	Sig. (2-tailed)	<.001		1.000
	N	2169	2170	2170
Group	Pearson Correlation	.075**	.000	1
	Sig. (2-tailed)	<.001	1.000	
	N	2169	2170	2170

**. Correlation is significant at the 0.01 level (2-tailed).

Figure 99. Light Transmission (661nm), Porcine Soft Tissue Regions. Pearson Correlation.

-Discussion: The negative correlation reported between light transmission and distance implies that there was a consistent decline in light transmission as distance away from the light source increased. The significant positive correlation reported between light transmission and anatomical regions indicates that certain anatomical regions resulted in higher transmission rates than others.

113

3.5 661nm vs. 810nm Light Transmission, Porcine Soft Tissue Regions.

3.5.1 Methods

The same methodology was conducted for the comparison of the 661nm and 810nm wavelengths in the porcine mandible cadaver as per the porcine experiments described prior. In addition to the 661nm wavelength laser system, an 810nm wavelength device was utilized as a comparison (Arroyo Instruments, 6300 Series Dual Range Laser Driver + Temperature Controller, San Luis Obispo, Ca).

Light transmission values were obtained from five porcine mandible cadaver specimens across six anatomic regions (G1 to G6). Measurements were captured at varying distances (2mm – 14mm) within each region and repeated five times. This procedure was conducted for both 661nm and 810nm wavelengths at a power output level of 500mW. This investigation was standardized to ensure a true wavelength comparison for each reference point, eliminating any variables and micromovements that could impact results. Ten data points were collected for each series, ranging from 2mm to 14mm. This resulted in 140 data points in each of the six anatomical regions of the five specimens. For this analysis, 350 data points were prepared for each region in both wavelength configurations. The total amount of data points acquired were n=4,200.

3.5.2 Results

In summary, five Yorkshire pigs were prepared for investigation of interstitial soft tissue measurements in 6 regions of interest: G1) genioglossus muscle, G2) masseter muscle, G3) sternohyoid muscle, G4) buccinator muscle, G5) cutaneous fascia, G6) vestibular tissue. An interstitial dual-catheter medical dosimetry system, a light source, and a detector acquired 661nm and 810nm light transmission measurements (mW/cm^2). (21, 29, 108, 109, 112, 115, 116). This dual-catheter configuration was

connected to a customized medical dosimetry system programmed with a wavelength-specific algorithm to acquire and analyze data across all anatomical regions of interest. The 0.8mm isotropic detector (IP85, Medlight S.A.) was connected to a 16-channel receiver and a medical dosimetry system. A custom 2.0mm point light source (#7035-01 Rev 2; Pioneer Optics) was independently coupled to both a 661nm and 810nm and the same medical dosimetry system arrangement. (See Figure 100 - 102)
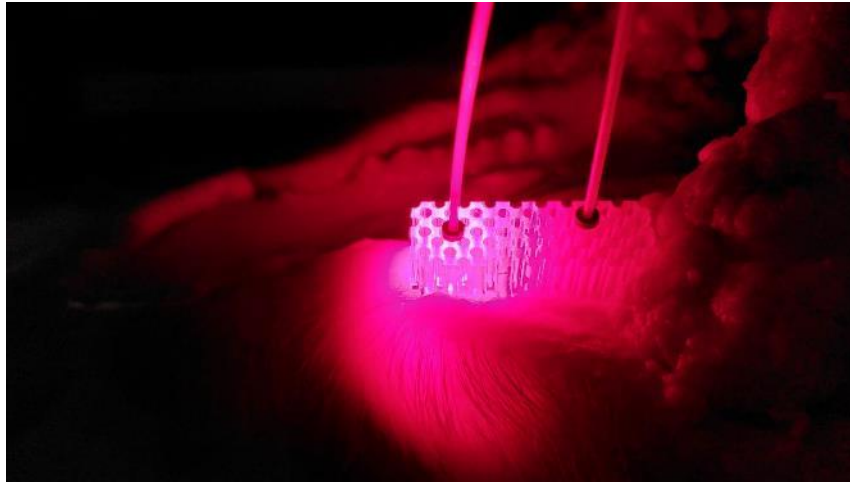
Figure 100. Light Transmission 661nm vs. 810nm. Light Transmission of 661nm laser on buccinator muscles of the porcine specimen.
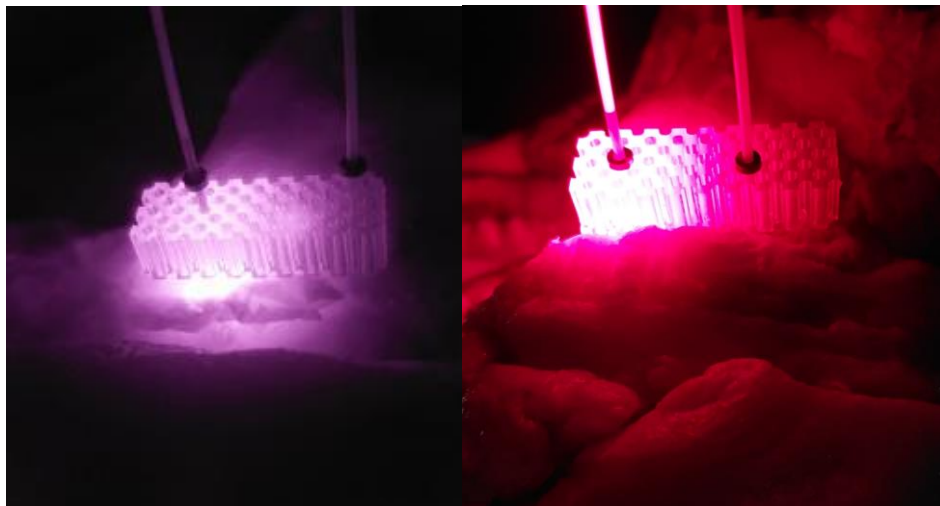
Figure 101. Light Transmission 661nm vs. 810nm. Light Transmission engaged through point light source in custom 3D printed jig 810nm (left), 661nm (right).
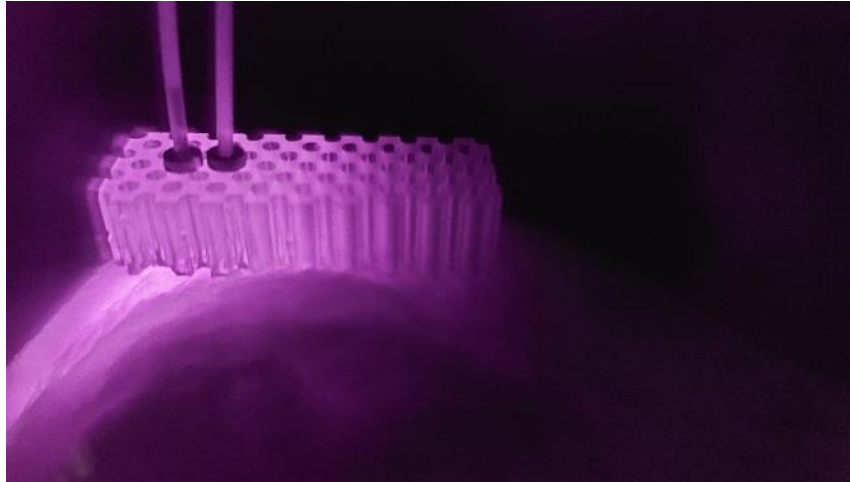
Figure 102. Light Transmission 661nm vs. 810nm. Light Transmission of 810nm laser on buccinator muscles of the porcine specimen.

3.5.3 Statistical Analysis & Discussion

3.5.3.1 Data Distribution

-Methods and Materials: Data was analyzed using IBM SPSS Statistic (version 29.0.1.0 (1711). The distribution light transmission values at various depths (2mm to 14mm) were evaluated using the Kolmogorov-Smirnov (K-S) and Shapiro-Wilk tests (S-W).

-Results: Light transmission values were assessed for 661nm and 810nm wavelengths at all depths 2-14mm. The K-S and S-W tests reported significance (p<0.001) for all groups, indicating deviation from normality. (See Figure 104 – 109)

Tests of Normality

	Distance	Kolmogorov-Smirnov[a]			Shapiro-Wilk		
		Statistic	df	Sig.	Statistic	df	Sig.
Transmission 660	2	.172	300	<.001	.749	300	<.001
	4	.177	300	<.001	.834	300	<.001
	6	.209	300	<.001	.816	300	<.001
	8	.348	300	<.001	.753	300	<.001
	10	.464	300	<.001	.586	300	<.001
	12	.540	300	<.001	.172	300	<.001
	14	.	300	.	.	300	.
Transmission 810	2	.153	300	<.001	.914	300	<.001
	4	.218	300	<.001	.853	300	<.001
	6	.214	300	<.001	.877	300	<.001
	8	.214	300	<.001	.872	300	<.001
	10	.193	300	<.001	.885	300	<.001
	12	.162	300	<.001	.890	300	<.001
	14	.162	300	<.001	.868	300	<.001

a. Lilliefors Significance Correction

Figure 104. Light Transmission (661nm vs 810nm), Porcine Soft Tissue Regions. Normality test for all distances.
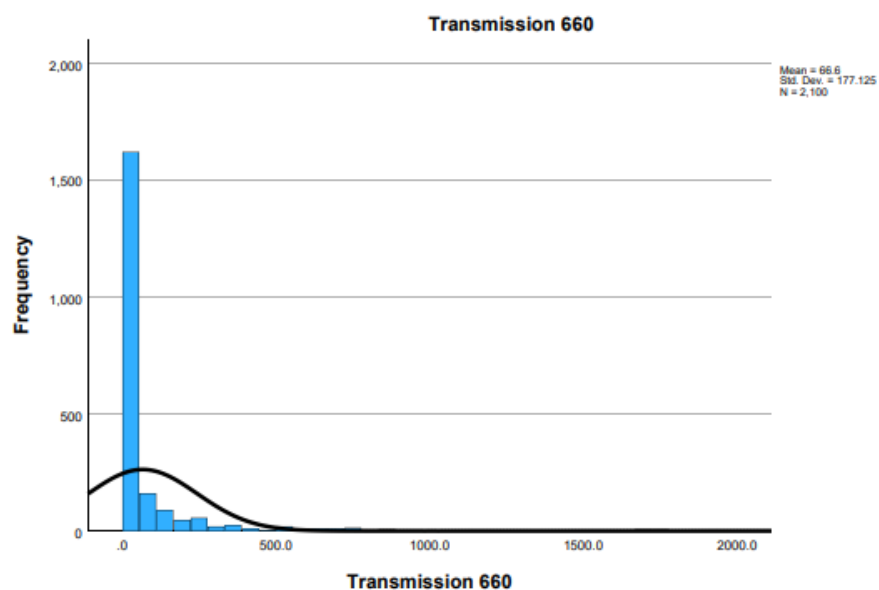
Figure 103. Light Transmission (661nm vs 810nm), Porcine Soft Tissue Regions. Histogram for transmission at 661nm.
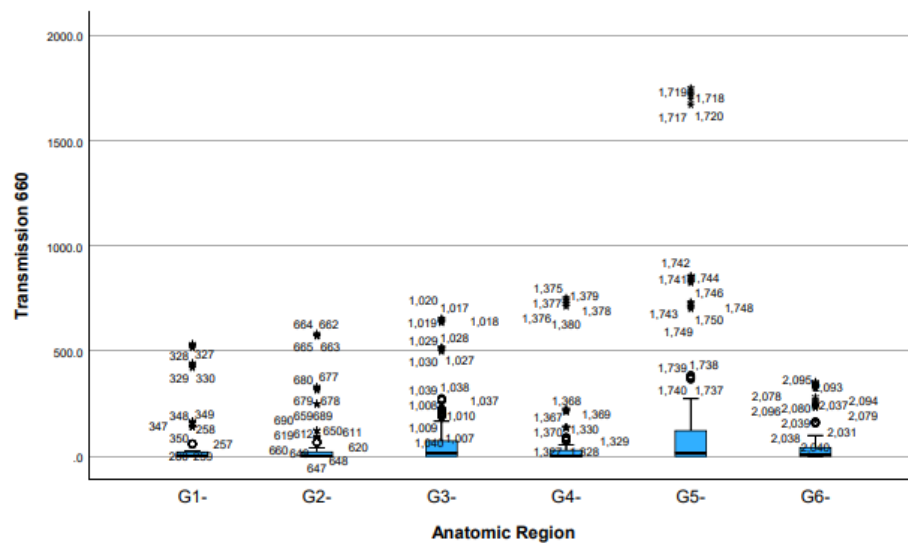
Figure 105. Light Transmission (661nm vs 810nm), Porcine Soft Tissue Regions. Box Plot for in each anatomic region at 661nm.
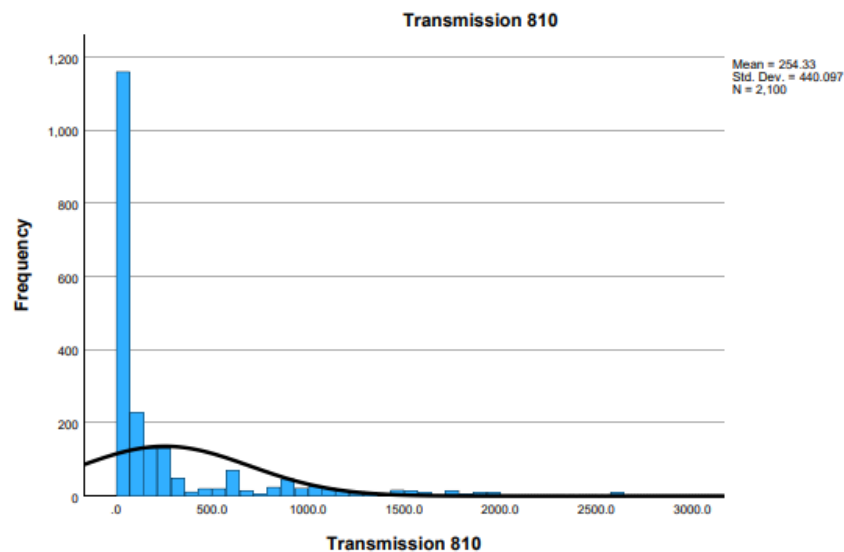
Figure 106. Light Transmission (661nm vs 810nm), Porcine Soft Tissue Regions. Histogram for transmission at 810nm.

118

Figure 107. Light Transmission (661nm vs 810nm), Porcine Soft Tissue Regions. Box Plot for in each anatomic region at 810nm.

Figure 108. Light Transmission (661nm vs 810nm), Porcine Soft Tissue Regions. Box Plot of light transmission by distance from light source for 661nm.

119
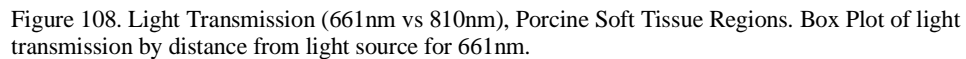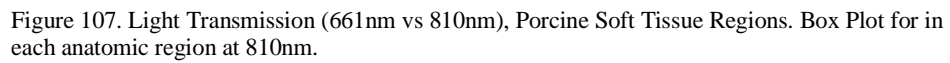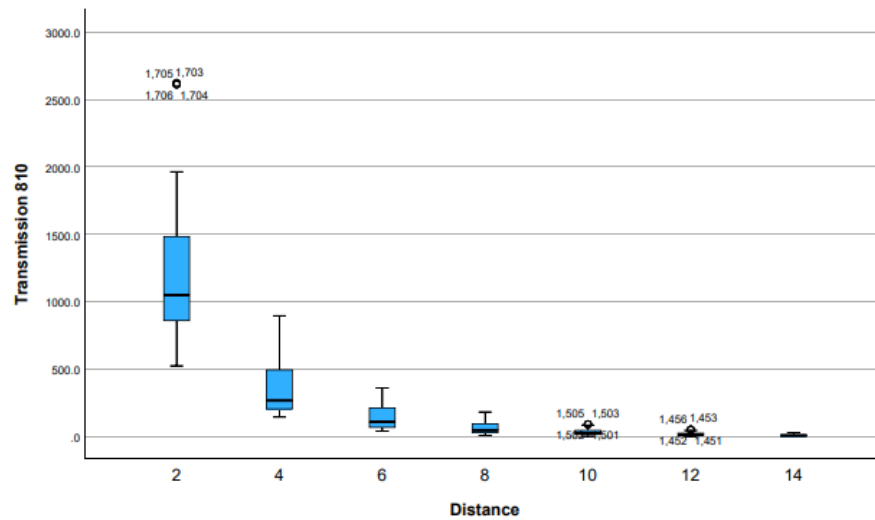
Figure 109. Light Transmission (661nm vs 810nm), Porcine Soft Tissue Regions. Box Plot of light transmission by distance from the light source for 810nm.

-Discussion: The results of both the K-S and S-W tests reveal non-normal distributions at all depths for both wavelengths, indicating that the light transmission properties of the various anatomic regions are not uniformly distributed. This suggests that light transmission is affected by differences in tissue structure at varying depths.

3.5.3.2 Light Transmission Between Anatomic Regions G1-G6

-Primary Objective: To determine how light transmitted between the 661nm and 810nm wavelengths would vary between six standardized anatomical regions of interest.

-Aim: The primary aim of this assessment is to quantify the light transmission values (661nm and 810) across different anatomic regions at fixed distances and to identify any region-specific properties.

-Materials and Methods: Data was analyzed using IBM SPSS Statistic (version 29.0.1.0 (1711). A prior analysis determined this dataset to deviate from a normal distribution. The Kruskal-Wallis test was utilized to examine differences in light transmission across six anatomic regions of porcine mandible tissues at 661nm and 810nm wavelengths. The Mann-Whitney test with Bonferroni correction (0.05/15 = .0033).

-Results: The Kruskal-Wallis H test revealed significant differences in light transmission at 661nm (H= 109.079, $p < 0.001$) and 810nm (H= 179.334, $p < 0.001$) wavelengths across the anatomic regions. The mean ranks for light transmission at 661nm varied from 891.91 in region G1 to 1226.90 in region G5. The mean ranks for light transmission at 810nm ranged from 859.87 in region G1 to 1356.84 in region G5. The application of the Mann-Whitney test with correction resulted in nine groups reporting significance for the 661nm transmission and 12 groups reporting significance for the 810nm transmission. (See Figure 110, Table 16 & 17).

Kruskal-Wallis Test

Ranks

	Anatomic Region	N	Mean Rank
Transmission 810	1	350	859.87
	2	350	891.36
	3	350	1207.02
	4	350	962.70
	5	350	1356.84
	6	350	1025.22
	Total	2100	
Transmission 660	1	350	891.91
	2	350	936.05
	3	350	1208.86
	4	350	979.59
	5	350	1226.90
	6	350	1059.69
	Total	2100	

Test Statistics[a,b]

	Transmission 810	Transmission 660
Kruskal-Wallis H	179.334	109.079
df	5	5
Asymp. Sig.	<.001	<.001

a. Kruskal Wallis Test

b. Grouping Variable: Anatomic Region

Figure 110. Light Transmission (661nm vs 810nm), Porcine Soft Tissue Regions. Kruskal Wallis Test for 661nm and 810nm.

661nm Transmission

	Mann-Whitney U	Wilcoxon W	Z	Asymp. Sig. (2-tailed)
G1 vs. G2	59112.5	120537.5	-0.932	0.351
G1 vs. G3	42619	104044	-7.493	<.001*
G1 vs. G4	55513	116938	-2.422	0.015
G1 vs. G5	42200	103625	-7.661	<.001*
G1 vs. G6	51300	112725	-4.114	<.001*
G2 vs. G3	45630.5	107055.5	-6.242	<.001*
G2 vs. G4	58672	120097	-1.078	0.281
G2 vs. G5	44612	106037	-6.649	<.001*
G2 vs. G6	53891	115316	-3.018	0.003
G3 vs. G4	47991	109416	-5.212	<.001*
G3 vs. G5	59902	121327	-0.517	0.605
G3 vs. G6	51985.5	113410.5	-3.604	<.001*
G4 vs. G5	46751	108176	-5.699	<.001*
G4 vs. G6	55873.5	117298.5	-2.158	0.031
G5 vs. G6	51044	112469	-3.97	<.001*
*Bonferroni Correction (.05/15= .0033)				

Table 16. Light Transmission (661nm vs 810nm), Porcine Soft Tissue Regions. Pairwise comparisons for 661nm.

810nm Transmission

	Mann-Whitney U	Wilcoxon W	Z	Asymp. Sig. (2-tailed)
G1 vs. G2	59119.5	120544.5	-.798 .425	0.425
G1 vs. G3	40501	101926	-7.759	<.001*
G1 vs. G4	55229.5	116654.500 -	2.252	0.024*
G1 vs. G5	33780	95205	-10.272	<.001*
G1 vs. G6	50900	112325	-3.87	<.001*
G2 vs. G3	43235.5	104661.5	-6.735	<.001*
G2 vs. G4	56427.5	117852.5	1.803	0.071
G2 vs. G5	34698.5	96123.5	-9.927	<.001*
G2 vs. G6	52808.5	114233.5	-3.156	.002*
G3 vs. G4	46951	108376	-5.345	<.001*
G3 vs. G5	51464.5	112889.5	-3.658	<.001*
G3 vs. G6	49746.5	111171.5	-4.3	<.001*
G4 vs. G5	38499	99924	-8.505	<.001*
G4 vs. G6	56726.5	118151.5	-1.691	0.091
G5 vs. G6	40590	102015	-7.723	<.001*
*Bonferroni Correction (.05/15= .0033)				

Table 17. Light Transmission (661nm vs 810nm), Porcine Soft Tissue Regions. Pairwise comparisons for 810nm.

-Discussion: The significance reported in the Kruskal-Wallis test indicates that there are differences in the light transmission values across all anatomic regions of interest for both 661nm and 810nm. The highest rank was observed in region 5, which correlates with the highest transmission values for this dataset. The lowest rank was found in region 1. The results of the pairwise comparison support the notion that light transmission values vary significantly across the 6 anatomic regions of interest. The absence of significant differences in the other region indicates similarities in tissue type or structure. Although G3-G5 reported significance for 810nm, this pairing did not result in significant differences for the 661nm wavelength. Note that this is a between wavelength and not inter-wavelength comparison. These findings support the idea that there are wavelength-dependent characteristics in transmission that must be accounted for when delivering light in biological tissues.

3.5.3.3 Light Transmission Between 661nm and 810nm Wavelengths.

-Primary Objective: To determine if there is a significant difference in light transmission through porcine mandible soft tissues between two wavelengths (661nm and 810nm).

-Aim: This assessment aims to compare light transmission at 661nm and 810nm wavelengths to determine if there are significant wavelength-dependent differences in tissue interaction.

-Materials and Methods: Data was analyzed using IBM SPSS Statistic (version 29.0.1.0 (1711). Given the non-normal distribution of data, the Wilcoxon Signed-Rank Test was utilized to compare the light transmission values at two wavelengths (661nm and 810nm) across all regions of interest.

-Results: The results of the Wilcoxon Signed-Rank Test reported a significant difference in the light transmission values between the two wavelengths ($Z = -38.532$, $p < 0.000$). The analysis reported that out of the total pairs, 1977 showed higher transmission values for the 810nm wavelength compared to the 661nm wavelength (mean rank of 991.89). There were only 3 examples where the 661nm wavelength had higher transmission than the 810nm wavelength. Additionally, 120 pairs demonstrated tied transmission values for both wavelengths. (See Figure 111 & 112).

Wilcoxon Signed Ranks Test

Ranks

		N	Mean Rank	Sum of Ranks
Transmission 810 - Transmission 660	Negative Ranks	3[a]	71.67	215.00
	Positive Ranks	1977[b]	991.89	1960975.00
	Ties	120[c]		
	Total	2100		

a. Transmission 810 < Transmission 660
b. Transmission 810 > Transmission 660
c. Transmission 810 = Transmission 660

Test Statistics[a]

	Transmission 810 - Transmission 660
Z	-38.532[b]
Asymp. Sig. (2-tailed)	<.001

a. Wilcoxon Signed Ranks Test
b. Based on negative ranks.

Figure 112. Light Transmission (661nm vs 810nm), Porcine Soft Tissue Regions. Wilcoxon Signed Ranks Test.

Descriptive Statistics

	N	Mean	Std. Deviation	Minimum	Maximum	Percentiles 25th
Transmission 660	2100	66.596	177.1248	.0	1751.3	.000
Transmission 810	2100	254.335	440.0967	.0	2623.2	14.000

Descriptive Statistics

	Percentiles 50th (Median)	75th
Transmission 660	.000	41.075
Transmission 810	50.900	249.000

Figure 111. Light Transmission (661nm vs 810nm), Porcine Soft Tissue Regions. Wilcoxon Signed Ranks Test. Descriptive Statistics.

-Discussion: The results of this study reported significant wavelength-dependent differences in light transmission through various regions of interest. That light transmission in soft tissue at the same distance is consistently higher for 810nm when compared to the 661nm. This finding may reflect differences in the optical properties of the tissues that are related to their absorption and scattering characteristics respective for each wavelength.

3.5.3.4 Tissue Depth (2-14mm), Light Transmission (661nm vs. 810nm), Soft Tissue

-Primary Objective: To determine the relationship between tissue depth (2mm to 14mm) and light transmission (661nm vs. 810nm) in porcine mandible soft tissues.

-Aim: The assessment aims to analyze the depth-dependent relationship of light transmission porcine mandible soft tissues for the 661nm and 810nm wavelengths.

-Materials and Methods: Data was analyzed using IBM SPSS Statistic (version 29.0.1.0 (1711). Given the non-normal distribution of the data, Spearman's rho correlation analysis was utilized to investigate the association between tissue depth and light transmission. The Locally Weighted Scatterplot Smoothing (LOWESS) was utilized to visualize the trend of the data.

-Results: Spearman's rho correlation indicated a negative relationship between tissue depth and light transmission for both wavelengths: -0.849 for 661nm and -0.928 for 810nm (p<0.001). The LOWESS visualization demonstrated an initial decline in light transmission as tissue depth increased, which was followed by a plateau. (See Figure 113 – 116).

Nonparametric Correlations

Correlations

			Distance	Transmission 660
Spearman's rho	Distance	Correlation Coefficient	1.000	-.849[**]
		Sig. (2-tailed)	.	<.001
		N	2100	2100
	Transmission 660	Correlation Coefficient	-.849[**]	1.000
		Sig. (2-tailed)	<.001	.
		N	2100	2100

**. Correlation is significant at the 0.01 level (2-tailed).

Figure 113. Light Transmission (661nm vs 810nm), Porcine Soft Tissue Regions. Wilcoxon Signed Ranks Test. Spearman's rho, 661nm.

Nonparametric Correlations

Correlations

			Distance	Transmission 810
Spearman's rho	Distance	Correlation Coefficient	1.000	-.928**
		Sig. (2-tailed)	.	<.001
		N	2100	2100
	Transmission 810	Correlation Coefficient	-.928**	1.000
		Sig. (2-tailed)	<.001	.
		N	2100	2100

**. Correlation is significant at the 0.01 level (2-tailed).

Figure 114. Light Transmission (661nm vs 810nm), Porcine Soft Tissue Regions. Wilcoxon Signed Ranks Test. Spearman's rho, 810nm.

Graph
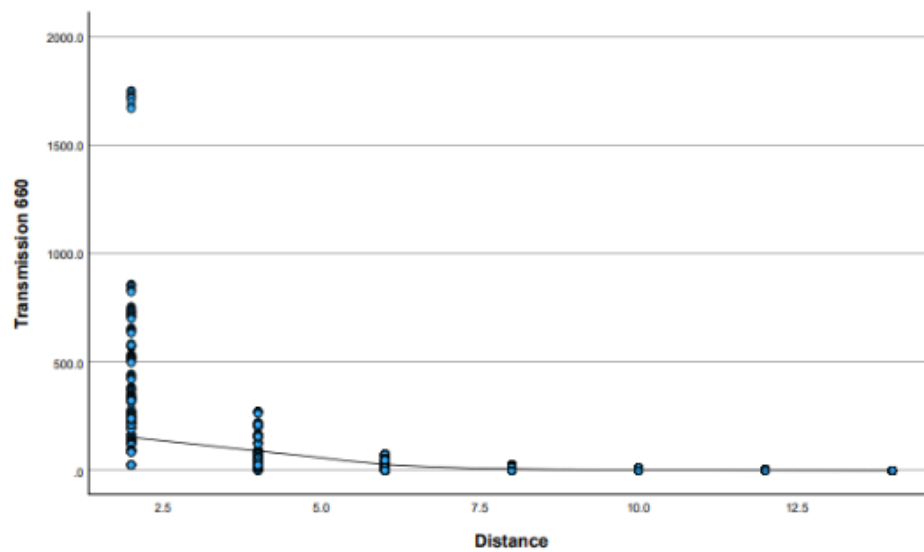
Figure 115. Light Transmission (661nm vs 810nm), Porcine Soft Tissue Regions. Wilcoxon Signed Ranks Test. LOWESS plot visualization, 661nm.
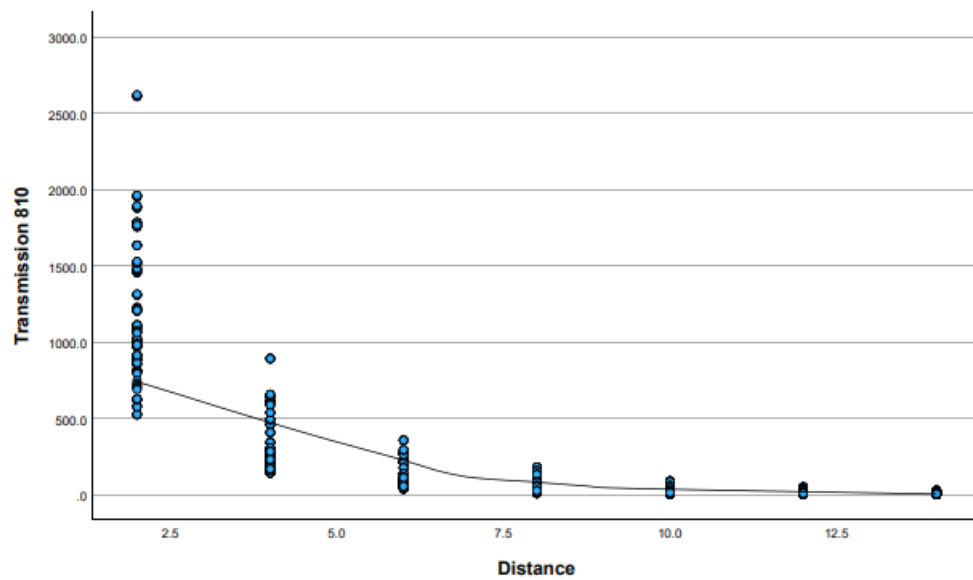
Figure 116. Light Transmission (661nm vs 810nm), Porcine Soft Tissue Regions. Wilcoxon Signed Ranks Test. LOWESS plot visualization, 810nm.

-Discussion: The findings of this study determined that the 661nm and 810nm wavelengths reported an inverse relationship between tissue depth and light transmission in porcine mandible tissues. The analysis revealed that the 810nm wavelength showed a stronger correlation, suggesting that the 810nm is absorbed or scattered more effectively than the 661nm wavelength. The LOWESS analysis provided a visualization of the depth-dependent relationship within the first 5mm, which sharply decreases as the distance from the light source increases.

3.6 **Semi-Infinite Light Transmission (661nm), Porcine Mandible**

3.6.1 **Method**

This semi-infinite light transmission study was conducted using five Yorkshire pigs mandibles that were obtained from a slaughterhouse (Animal Technologies, Tyler, Texas). All specimens were transported frozen, unfixed, and fully thawed before analysis. Both males and females were of different weights and ages to show conditions variability within the same animal model. Each specimen consisted of the entire mandible, condylar structures, and intact intra and extraoral tissues for this respective anatomy. This feature was requested that the tongue was removed to provide access to the underlying tissues and structures.

This investigation incorporated multiple dosimetry techniques that were configured to capture semi-infinite light transmission values representative of max fluence rate (mW/cm^2) across multiple porcine specimens and regions of interest. (10, 13, 21, 22, 29, 107-109, 111, 112, 115, 116, 159, 186-188) Based on prior work from Andreea Dimofte et al., (21) a calibrated 0.8mm isotropic detector (MEDLIGHT) and a 2mm isotropic point light source (Pioneer optics) were placed inside two catheters (Flexineedle). A calibrated 0.5mm isotropic detector (MEDLIGHT) and a 2mm isotropic point light source (Pioneer optics) were placed inside two catheters (Flexineedle). The catheters were secured at a distance of 3mm by a prefabricated acrylic jig and secured with clear transparent adhesive tape on the front and dark-colored adhesive tape on the posterior. The isotropic detector was connected to a 16-channel receiver and to a medical dosimetry system with the potential to measure the effective attenuation coefficient (μ-eff), absorption (μ-a), and scattering (μ's). The light source was connected to a 661nm laser system. (See Figure 117)
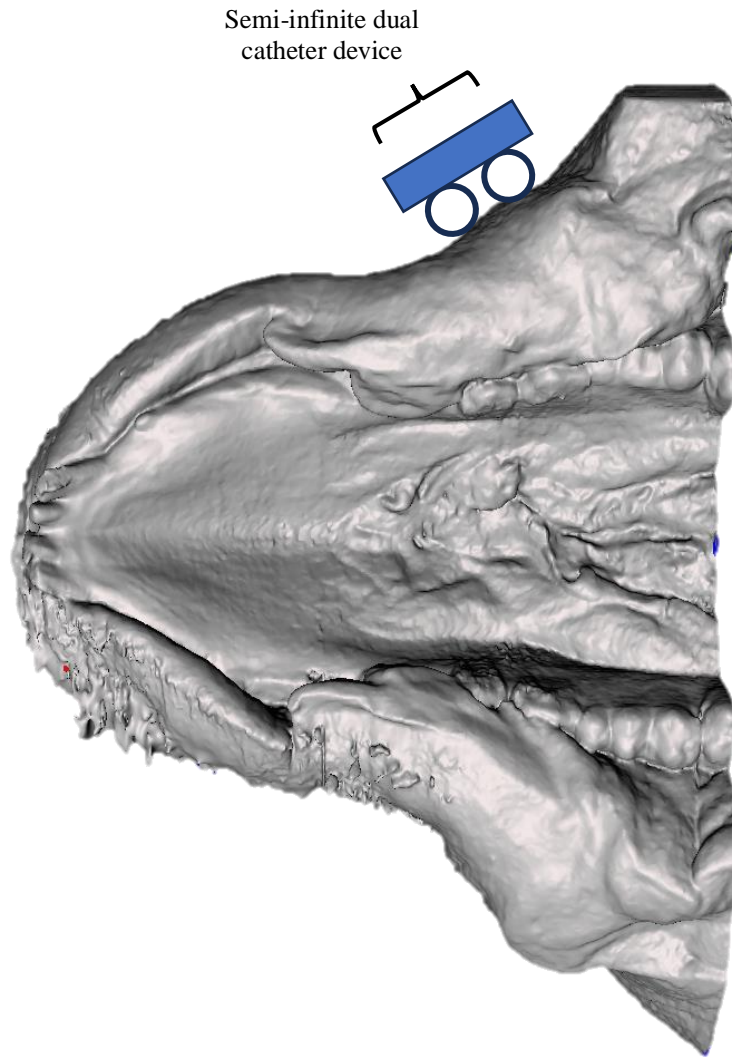
Figure 117. Schematic of semi-infinite dual catheter device adjacent to porcine cadaver region of interest. Not illustrated to scale.

Semi-infinite data was acquired in mW/cm^2 and was standardized across all specimens. The portion of the catheters covered with clear transparent adhesive tape was placed directly in contact with the surface. The surface with dark-colored adhesive paper was facing away from the surface. Ten randomized measurements were taken in each region of interest by a photographic camera timer in 10-second intervals. The regions of interest were standardized across all specimens, including the genioglossus, masseter, sternohyoid, buccinator, cutaneous fascia, vestibular tissue, and several other regions of combinations of

bone, soft tissue, dentin, and enamel. All data values were taken at the power output of 500mW for each

region of interest. (See Figure 118)
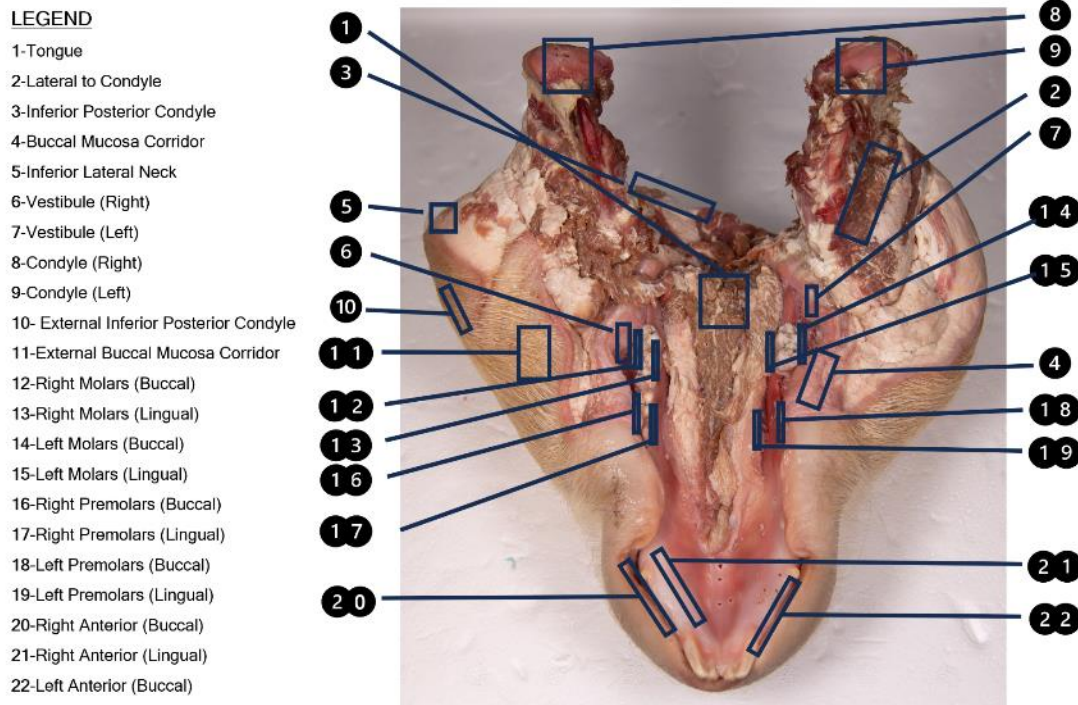
Figure 118. Semi-infinite light transmission. Regions of Interest.

This study standardized five porcine cadaver specimens to investigate 22 distinct regions of interest

that represented multiple combinations of soft tissue, hard tissue, dentin, and enamel. The semi-infinite

light transmission method was incorporated across all specimens, acquiring ten light fluence measurements

(mW/cm^2) for each region at the 661nm wavelength and a power output of 500mW. 10 data points were

acquired in each section across five specimens. Total data amount of data points acquired were n= 1,100.

(See Figure 119 – 122)
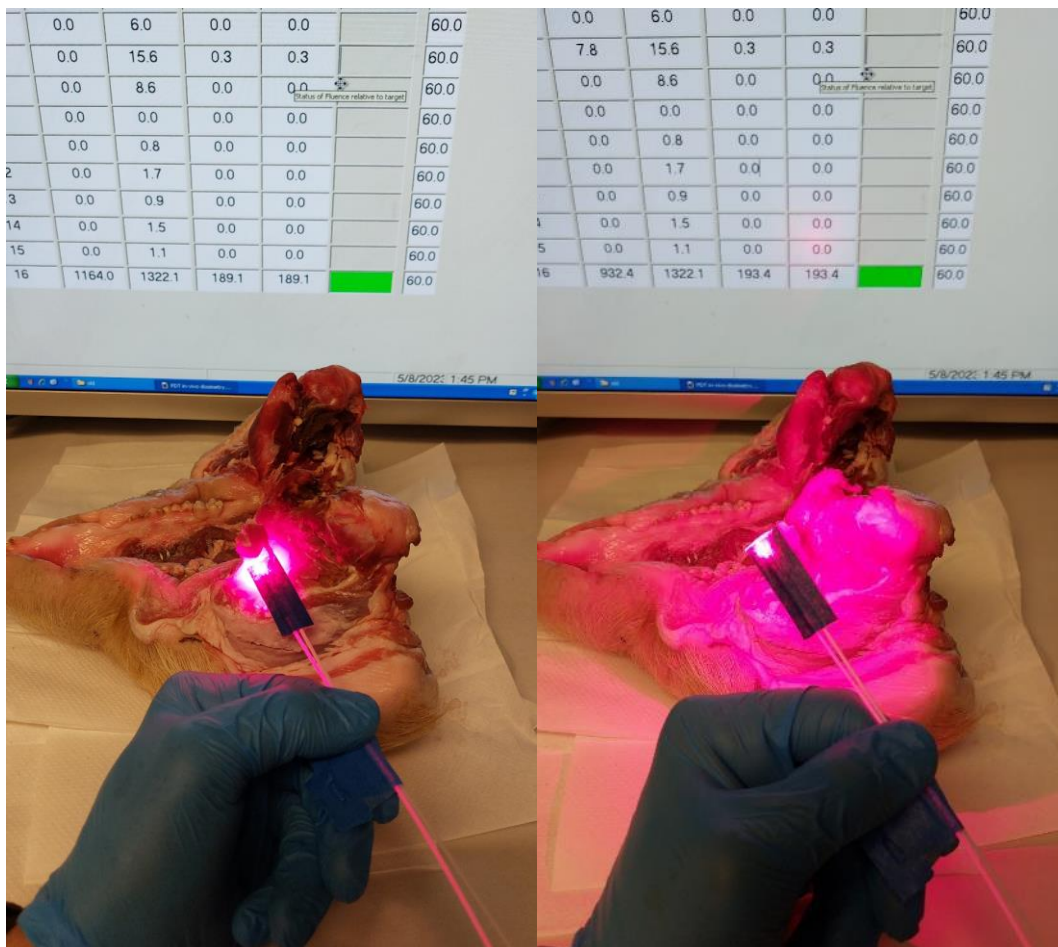
Figure 119. Semi-infinite light transmission. Placement of semi-infinite device on the Group 4 Buccal Mucosal Corridor with direct placement on masseter muscle lateral to base of the condyle.

Figure 120. Semi-infinite light transmission of tissue junctions. Region of interest pictured is Group 10 Exterior Posterior Condyle with placement is directly on the external aspect of hair skin onto cutaneous fascia.
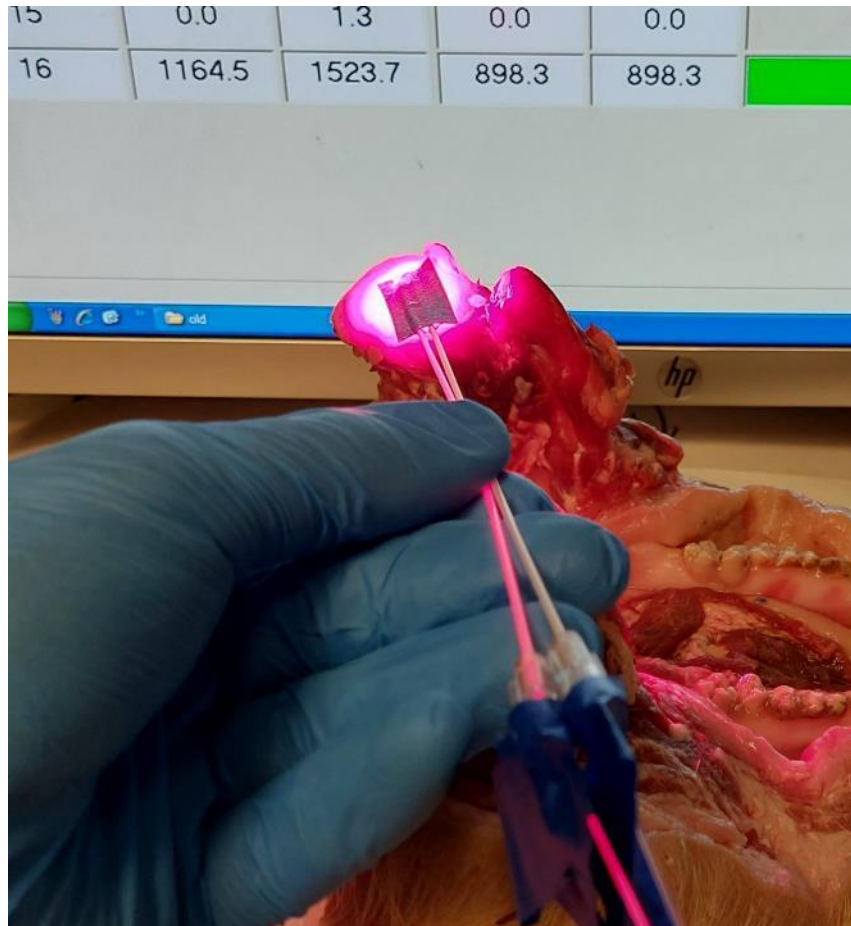
Figure 121. Placement of semi-infinite device on the Group 9 left condyle (bone tissue).
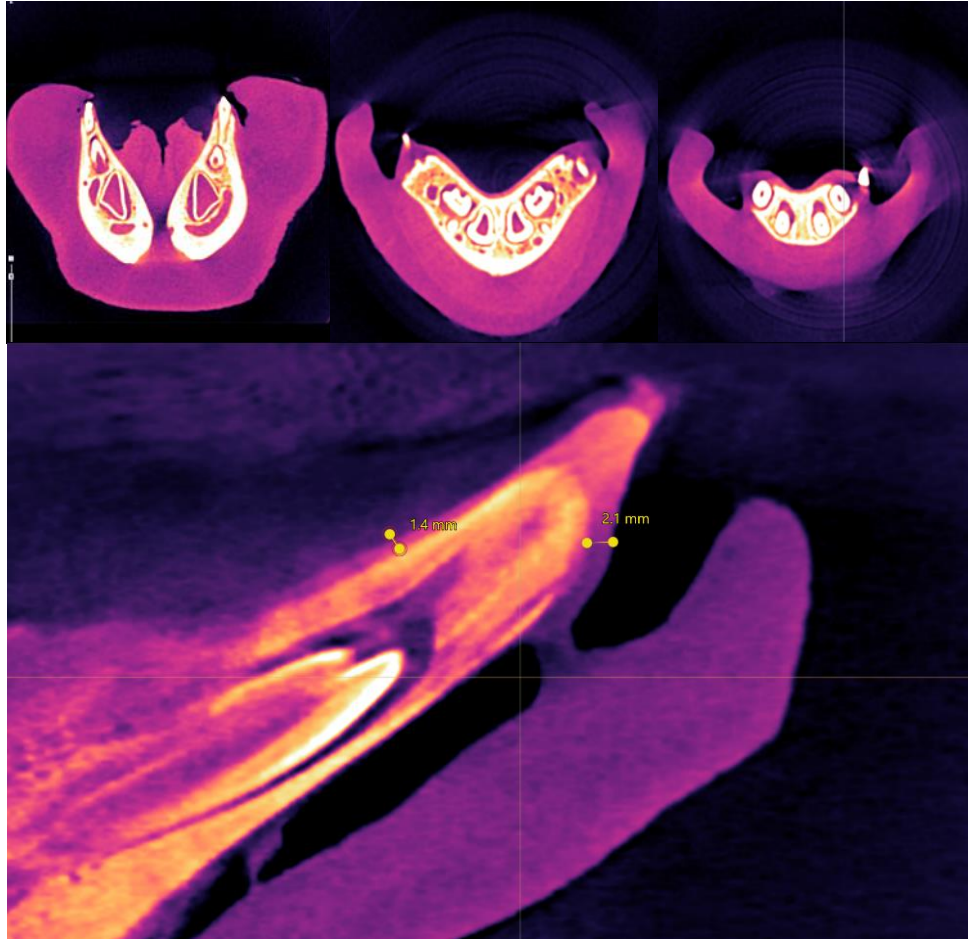
Figure 122. Semi-infinite light transmission of tissue junctions. CBCT image depicting tissue junction of bone, soft tissue, dentin, and enamel. Soft Tissue thickness range of 1.4-2.1mm in anterior sections (bottom).

3.6.2 Statistical Analysis & Discussion

3.6.2.1 Data Distribution

-Materials and Methods: Data was analyzed using IBM SPSS Statistic (version 29.0.1.0 (1711). Data distribution was assessed for normality using the Kolmogorov-Smirnov (K-S) and Shapiro-Wilk (S-W) tests. Descriptive Statistics examined the entire range of semi-infinite light transmission that resulted from this investigation.

-Results: The K-S and S-W tests indicate that light fluence measurements generally did not result in a normal distribution of data. (See Figure 123 – 125)

Tests of Normality

	Tissue Type	Kolmogorov-Smirnov[a]			Shapiro-Wilk		
		Statistic	df	Sig.	Statistic	df	Sig.
Fluence	10Extern	.130	50	.035	.931	50	.006
	11Extern	.180	50	<.001	.895	50	<.001
	12RT mol	.094	50	.200*	.973	50	.296
	13RT mol	.211	50	<.001	.837	50	<.001
	14LT Mol	.223	50	<.001	.843	50	<.001
	15LT Mol	.122	50	.060	.927	50	.004
	16RT PRE	.219	50	<.001	.906	50	<.001
	17RT PRE	.133	50	.027	.922	50	.003
	18LT PRE	.246	50	<.001	.807	50	<.001
	19LT PRE	.112	50	.164	.935	50	.009
	1Tongue	.083	50	.200*	.981	50	.576
	20RT Ant	.125	50	.048	.916	50	.002
	21RT Ant	.178	50	<.001	.905	50	<.001
	22LT Ant	.195	50	<.001	.900	50	<.001
	2Lateral	.174	50	<.001	.883	50	<.001
	3Inferio	.156	50	.004	.927	50	.004
	4Buccal	.094	50	.200*	.961	50	.103
	5Inferio	.145	50	.010	.941	50	.015
	6Vestibu	.210	50	<.001	.847	50	<.001
	7Vestibu	.192	50	<.001	.878	50	<.001
	8Condyle	.133	50	.028	.938	50	.011
	9Condyle	.111	50	.171	.958	50	.076

*. This is a lower bound of the true significance.

a. Lilliefors Significance Correction

Figure 123. Semi-infinite light transmission. Data Distribution, Tests of Normality.
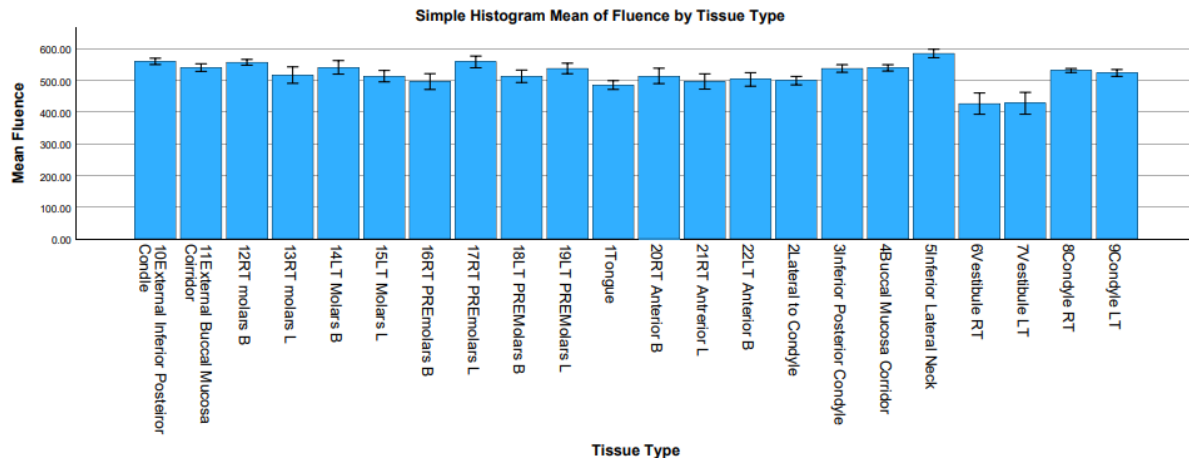
Figure 124. Semi-infinite light transmission. Histogram Mean Fluence by Tissue Region of Interest.

Descriptives

Tissue Type			Statistic	Std. Error
9Condyle	Mean		523.1740	5.34952
	95% Confidence Interval for Mean	Lower Bound	512.4237	
		Upper Bound	533.9243	
	5% Trimmed Mean		523.8178	
	Median		526.7500	
	Variance		1430.867	
	Std. Deviation		37.82680	
	Minimum		448.10	
	Maximum		591.50	
	Range		143.40	
	Interquartile Range		55.15	
	Skewness		-.407	.337
	Kurtosis		-.340	.662

Figure 125. Semi-infinite light transmission. Descriptive Statistics.

-Discussion: Given that K-S and S-W tests did not result in significance for all the groups, it was determined that this dataset deviated from normality. The descriptive statistics from this data set successfully quantified light fluence measurements in all regions, standardizing the semi-infinite light transmission method used for data collection. It is visualized that there is variability between the regions of interest, emphasizing tissue-specific light interactions.

137

3.6.2.2 Variability of Same Tissue Region Across Specimens

-Primary Objective: To determine the semi-infinite light fluence variability across different tissue types in five porcine mandible specimens.

-Aim: This assessment aims to analyze the variability of light measurements across twenty-two different regions of interest in five porcine mandible specimens.

-Materials and Methods: Data was analyzed using IBM SPSS Statistic (version 29.0.1.0 (1711). Semi-infinite light fluence descriptive statistics (mean, standard deviation) were conducted across twenty-two anatomic regions of interest in five specimens.

-Results: The descriptive analysis included light transmission values from 22 tissue types in five porcine mandible specimens. There were 50 measurements for each group with means ranging from 426.46 mw/cm^2 (6Vestibule RT) to 584.76 mw/cm^2 (5Inferior Lateral Neck). The standard deviation varied from 22.48 mw/cm^2 (8Condyle RT), indicating low variability, to 122.21 mw/cm^2 (7Vestibule LT), indicating high variability. (See Figure 126 -127)
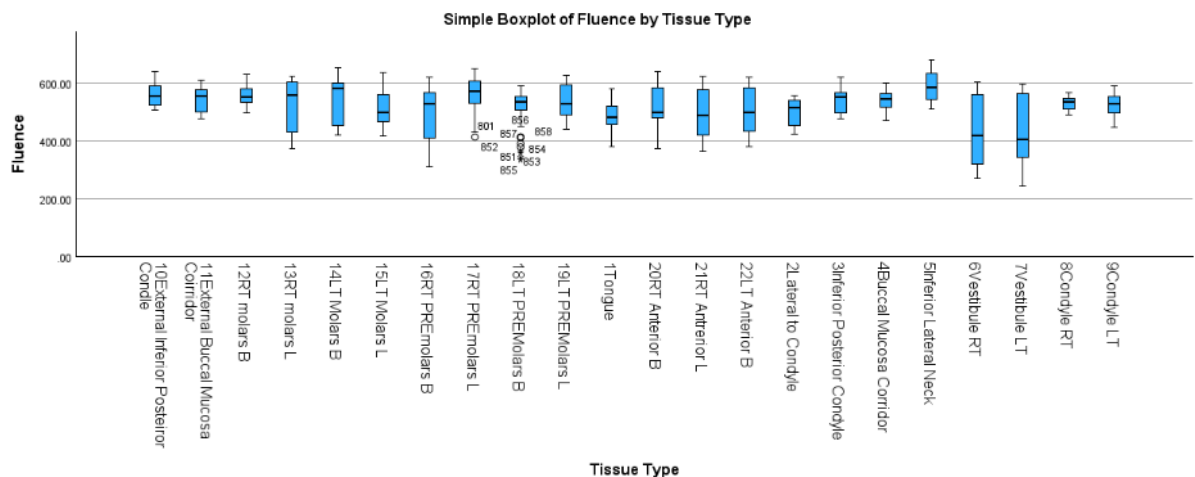
Figure 126. Semi-infinite light transmission. Boxplot Visualization by Region of Interest.

Descriptive Statistics

Dependent Variable: Fluence

Tissue Type	Mean	Std. Deviation	N
10External Inferior Posteiror Condle	559.5540	35.17831	50
11External Buccal Mucosa Coirridor	540.2780	42.39298	50
12RT molars B	556.8140	31.92333	50
13RT molars L	516.3880	91.77305	50
14LT Molars B	540.8680	75.44226	50
15LT Molars L	513.0560	63.57239	50
16RT PREmolars B	496.0440	88.53496	50
17RT PREmolars L	558.1880	65.67789	50
18LT PREMolars B	512.8440	69.43316	50
19LT PREMolars L	537.3560	58.44505	50
1Tongue	485.0248	48.83523	50
20RT Anterior B	513.9160	85.21165	50
21RT Antrerior L	496.4900	85.65787	50
22LT Anterior B	502.9900	75.65523	50
2Lateral to Condyle	499.0620	46.95022	50
3Inferior Posterior Condyle	537.5020	42.14338	50
4Buccal Mucosa Corridor	539.4700	34.85190	50
5Inferior Lateral Neck	584.7600	47.13211	50
6Vestibule RT	426.4600	118.62711	50
7Vestibule LT	427.6120	122.21481	50
8Condyle RT	531.1280	22.48022	50
9Condyle LT	523.1740	37.82680	50
Total	518.1354	77.66147	1100

Figure 127. Semi-infinite light transmission. Descriptive Statistics by anatomic region of interest.

-Discussion: This analysis of descriptive statistics indicates that there is notable light fluence variability across the different regions of interest. The most prominent variation occurred in the vestibular regions, with reported means of 426.4600 mW/cm^2 and 427.6120 mW/cm^2. The standard deviations reported were 118.62711 and 122.21481, respectively. These findings indicate variations in the tissue optical properties of the vestibular region due to underlying anatomic features like tissue type and mucosal glands of this model.

139

3.6.2.3   Variance Across Tissue Types

-Primary Objective: To determine if there are significant differences in light fluence measurements between the anatomical regions of interest.

-Aim: This study aims to assess if there are significant differences in light fluence measurements between the anatomical regions of interest.

-Materials and Methods: Data was analyzed using IBM SPSS Statistic (version 29.0.1.0 (1711). Data was determined to have a non-normal distribution, and the Kruskal-Wallis test analyzed the distribution of light fluence measurements across various tissue types. Pairwise comparisons, Mann-Whitney U test, and Bonferroni correction (.05/231=0.000216) evaluated the difference between each. 1100 measurements were analyzed across 22 groups.

-Results: The Kruskal-Wallis test statistic is 1.81.786 (p <.001). After Bonferroni correction (0.000216), 24 comparisons resulted in statistical significance. It is relevant to note that significance resulted from comparisons of soft tissue groups with a group that contained a combination of soft tissue, bone, dentin, and enamel. This included the following soft tissue groups: #6 Vestibule (Right), #5 Inferior Lateral Neck, #7 Vestibule (Left), #1 Tongue, #10 External Inferior Posterior Condyle, and #2 Lateral to Condyle. Out of 231 pairwise comparisons, the following groups reported statistically significant results. (See Figure 128 – 130, Table 18)

140

Independent-Samples Kruskal-Wallis Test Summary

Total N	1100
Test Statistic	181.786[a]
Degree Of Freedom	21
Asymptotic Sig.(2-sided test)	<.001

a. The test statistic is adjusted for ties.

Figure 128. Semi-infinite light transmission. Kruskal-Wallis test.

Sample 1 - Sample 2	Test Statistic	Sig.	Adj. Sig
6 Vestibule - 14 LT Molars (Buccal)	332.4	<.001	0.000039
6 Vestibule - 12 RT Molars (Buccal)	380.42	<.001	0.00000049
6 Vestibule- 10 External Inferior Posterior Condyle	398.68	<.001	0.000000081
6 Vestibule- 17 RT Premolars (Lingual)	404.36	<.001	0.000000045
6 Vestibule- 5 Inferior Lateral Neck	510.82	<.001	2.05E-13
7 Vestibule (Left)- 14 LT Molars (Buccal)	324.78	<.001	0.0000738
7 Vestibule (Left)- 12 RT Molars (Buccal)	372.8	<.001	0.000001023
7 Vestibule (Left)- 10 External Inferior Posterior Condyle	391.06	<.001	0.000000174
7 Vestibule (Left) - 17 RT Premolars (Lingual)	396.74	<.001	0.000000098
7 Vestibule (Left)- 5 Inferior Lateral Neck	503.2	<.001	5.13E-13
1 Tongue- 12 RT Molars (Buccal)	346.97	<.001	0.000010944
1 Tongue- 10 External Inferior Posterior Condyle	365.23	<.001	2.0827E-06
1 Tongue- 17RT Premolars (Lingual)	370.91	<.001	1.2228E-06
1 Tongue- 5 Inferior Lateral Neck	-477.37	<.001	1E-11
2 Lateral to Condyle - 10 External Inferior Posterior Condyle	305.74	<.001	0.000345224
2 Lateral to Condyle- 17 RT Premolars (Lingual)	311.42	<.001	0.000219845
2 Lateral to Condyle- 5 Inferior Lateral Neck	-417.88	<.001	1.109E-08
21 RT Anterior (Lingual)- 5 Inferior Lateral Neck	-358.41	<.001	3.9069E-06
16 RT Premolars (Buccal)- 5 Inferior Lateral Neck	-350.09	<.001	0.00000829
15 LT Molars (Lingual)- 5 Inferior Lateral Neck	-346.76	<.001	0.00001115
22 LT Anterior (Buccal)- 5 Inferior Lateral Neck	-346.75	<.001	0.00001116
9 Condyle LT- 5 Inferior Lateral Neck	314.14	<.001	0.00017664
18 LT Premolars (Buccal)- 5 Inferior Lateral Neck	-311.58	<.001	0.000217
20 RT Anterior (Buccal)- 5 Inferior Lateral Neck	-307.38	<.001	0.0003033

Table 18. Semi-infinite light transmission. Pairwise Comparisons, Mann Whitney U, Bonferroni Correction.

Pairwise Comparisons of Tissue Type
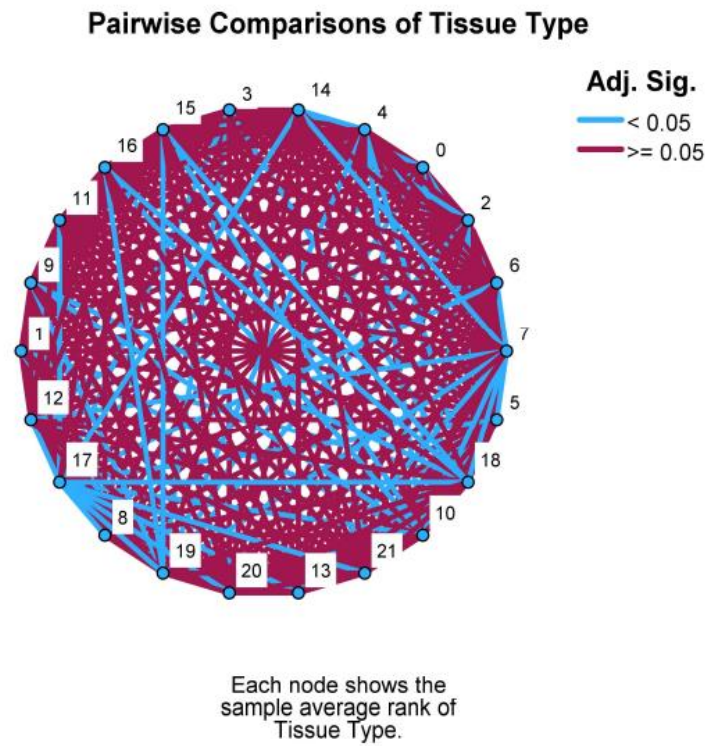
Figure 130. Semi-infinite light transmission. Pairwise Comparison Visualization.
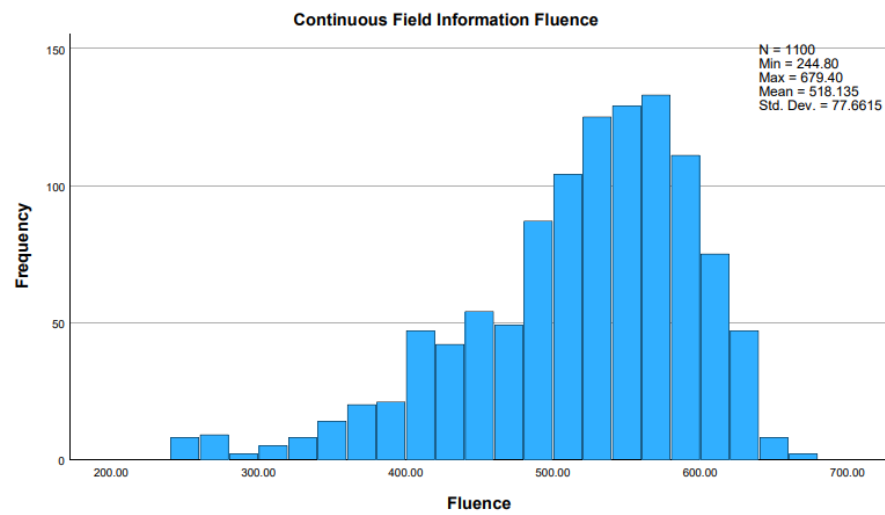
Figure 129. Semi-infinite light transmission. Continuous Field Visualization of Light Transmission Values (Fluence).

142

-Discussion: The results of the Kruskal-Wallis assessment reported significant differences in light transmission (mW/cm^2) for all regions. These findings emphasized soft tissue groups after conducting the necessary adjustments. By understanding which regions significantly differ in light fluence, clinical delivery protocols can be adjusted to reach treatment endpoints. The findings from this assessment validate that the medical dosimetry system can provide semi-infinite dosimetry measurements across a similar tissue type in multiple specimens that are of statistical significance.

3.6.2.4 Homogenous vs. Mixed Tissue Regions of Interest.

-Primary Objective: To determine how semi-influence light fluence differs between homogeneous tissue regions and mixed tissue regions.

-Aims: This study aims to analyze the differences in light fluence measurements between homogenous tissue regions and mixed-tissue regions.

-Material and Methods: Data was analyzed using IBM SPSS Statistic (version 29.0.1.0 (1711). Light fluence measurements collected from all five specimens were assigned to two groups: 1) homogenous tissues (n=450) and 2) mixed tissues (n=650). After determining non-normal distribution, the Mann-Whitney test, Wilcoxon W statistics, Z scores, and descriptive statistics were utilized to compare data between these groups.

-Results: There were a total of 1100 light fluence measurements distributed in two groups. The homogenous tissue group (n=450) had a mean rank of 502.91, whereas the mixed tissue group (n=650) was 583.45. The test statistics of fluence for Mann-Whitney were 124835.500, Wilcoxon W 226310.500, a Z score of -4.1341, and Asymp. Sig. of <.001. (See Figure 131 – 132)

NPar Tests

Descriptive Statistics

	N	Mean	Std. Deviation	Minimum	Maximum	Percentiles 25th	Percentiles 50th (Median)
Fluence	1100	518.1354	77.66147	244.80	679.40	477.9250	533.1000
Region	1100	1.59	.492	1	2	1.00	2.00

Descriptive Statistics

	Percentiles 75th
Fluence	572.5750
Region	2.00

Mann-Whitney Test

Ranks

	Region	N	Mean Rank	Sum of Ranks
Fluence	1	450	502.91	226310.50
	2	650	583.45	379239.50
	Total	1100		

Test Statistics[a]

	Fluence
Mann-Whitney U	124835.500
Wilcoxon W	226310.500
Z	-4.134
Asymp. Sig. (2-tailed)	<.001

a. Grouping Variable: Region

Figure 131. Semi-infinite light transmission. Homogenous vs. Mixed Tissue Regions. Wann-Whitney U, Wilcoxon, Descriptive Statistics.
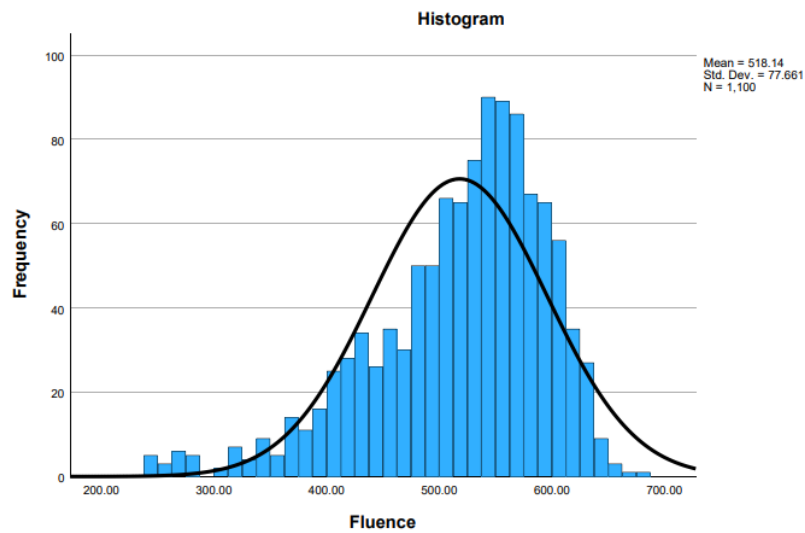
Figure 132. Semi-infinite light transmission. Homogenous vs. Mixed Tissue Regions. Histogram.

145

-Discussion: These results demonstrate that semi-infinite light transmission behaves differently in homogeneous tissues when compared to mixed tissue regions of interest. These findings emphasize the notion that underlying structural anatomies and related optical properties (absorption and scattering) influence their interaction with semi-infinite light fluence transmission (mW/CM^2). The difference in mean rank between the groups suggests that light fluence variability is related to differences between groups and their tissue structure. The asymptomatic significance of $<.001$ observed between both groups indicates that the probability of these differences occurring due to chance is extremely low. The descriptive analysis emphasizes the variability in semi-infinite light fluence measurements.

3.7 Histology of Porcine Mandible Soft Tissues

3.7.1 Methods

A fresh, unfixed Yorkshire pig mandible was obtained from a slaughterhouse (Animal Technologies, Tyler, Texas). The gender and weight of the specimen was unknown. Anatomical features consisted of the entire mandible, condylar structures, and intact intra and extraoral tissues for this respective anatomy. Soft tissue specimen samples were excised with a 3mm biopsy punch (Seamless Disposable Biopsy Punch, Premier Medical Products, Plymouth Meeting PA), surgical forceps, and a scalpel blade. Samples were designated from 6 distinct regions of interest to better understand the architecture of each tissue type. The 6 types of soft tissue collected included the genioglossus muscle, masseter muscle, sternohyoid muscle, buccinator muscle, cutaneous fascia, and vestibular tissue. (See Figure 133).
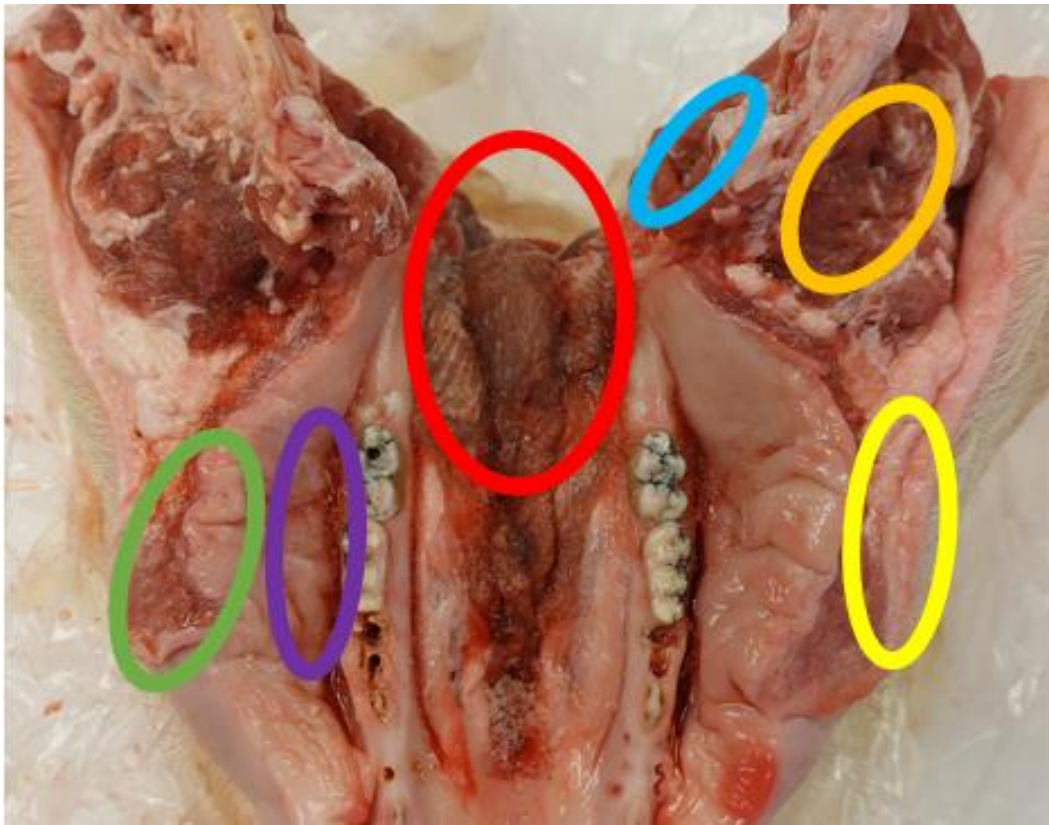
Figure 133. Histology. Regions of interest: genioglossus muscle (red), masseter (orange), sternohyoid (blue), buccinator (green), cutaneous fascia (yellow), vestibule (purple).

Specimen samples were processed with the assistance of members from the Kang Ko Lab. Harvested samples were fixed in 10% formalin at 4°C for 24 hours and washed 2x in dH$_2$0 at 4°C on a shaker (30 minutes each). Tissues were dehydrated with EtOH (70%, 80%, 95&, 100%) and processed with paraffin embedding. Paraffin sections were prepared at 5µm thickness, rehydrated, and stained for H&E per the manufacturer's protocol (Azer Scientific). (189) (See Figure 134 - 135)

Figure 134. Histology. Materials used for paraffin sample dehydration in EtOH.
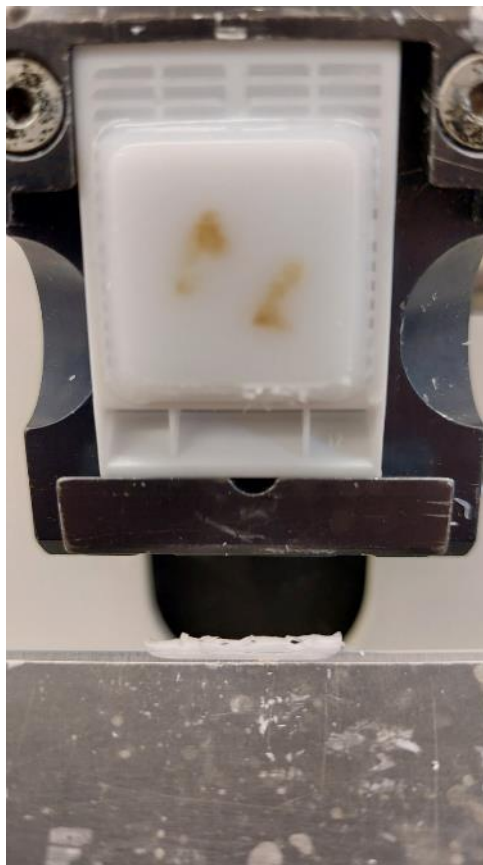
Figure 135. Histology. Sectioning of paraffin-embedded tissue sample on microtome.

Histologic images were captured by the Keyence BZ-X800 Microscope (Keyence Corporation of America, Itasca, Illinois) and processed by the BZ-X800 analyzer software (Keyence Corporation of America, Itasca, Illinois). ImageJ software was utilized to count percent connective tissue cells vs. adipose tissue cells, and Microsoft Excel was used to create bar graph visualizations.

3.7.2 Results

Histology was completed for the following anatomic regions of the porcine mandible cadaver: G1) Genioglossus Muscle, G2) Masseter Muscle, G3) Sternohyoid Muscle, G4) Buccinator Muscle, G5) Cutaneous Fascia, G6) Vestibule. ImageJ muscle tissue evaluations were reported in the mean area: G1) 245.491, G2) 250.218, G3) 155.013, G4) 233.471, G5) 87.481, G6) 207.89. Subsequently, adipose tissue was reported: G1) 55.326, G2) 50.27, G3) 145.139, G4) 66.545, G5) 212.647, G6) 92.652. (See Figure 137 – 143)
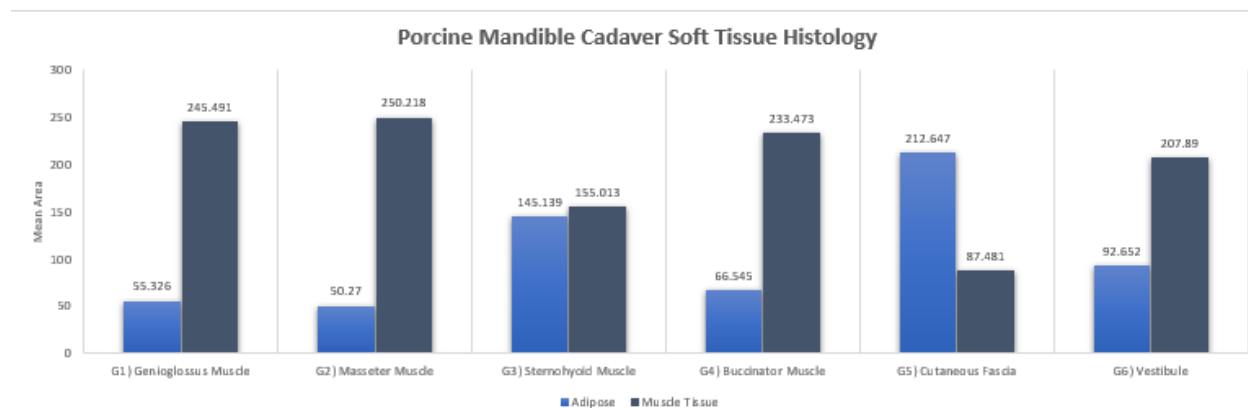
Figure 136. Histology assessment of muscle (top) and adipose tissues (bottom).
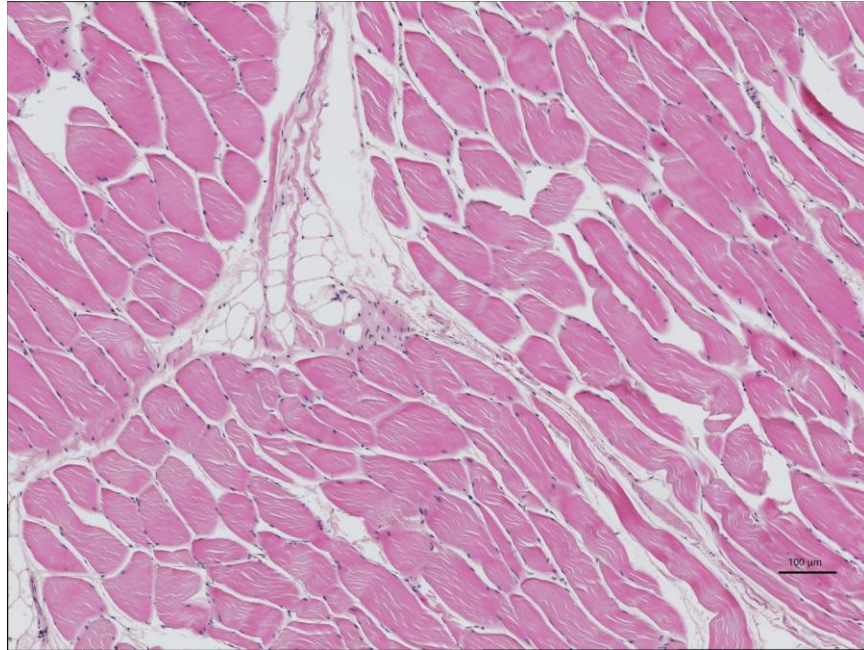
Figure 138. Histology. Group 1 Genioglossus Muscle.
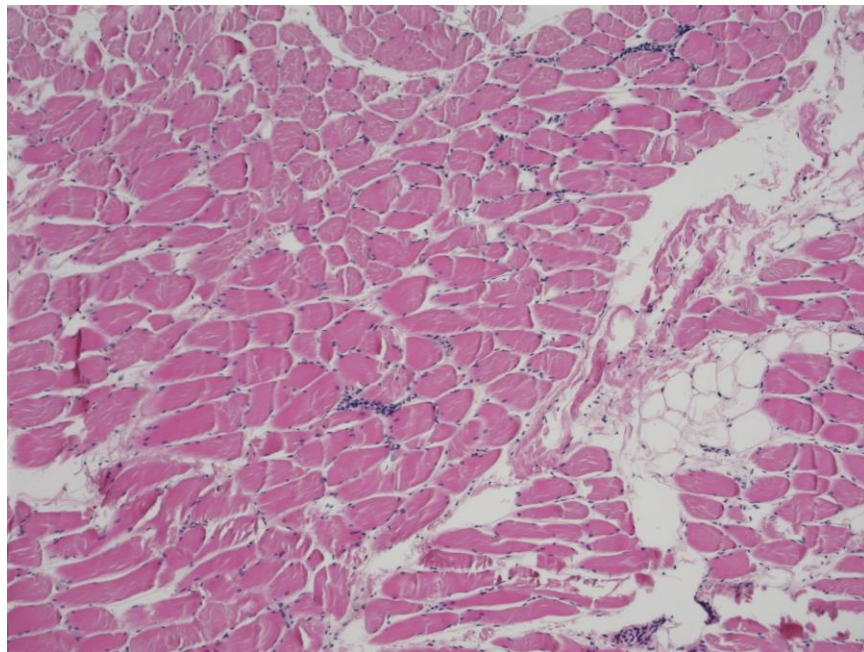
Figure 137. Histology. Group 2 Masseter Muscle.
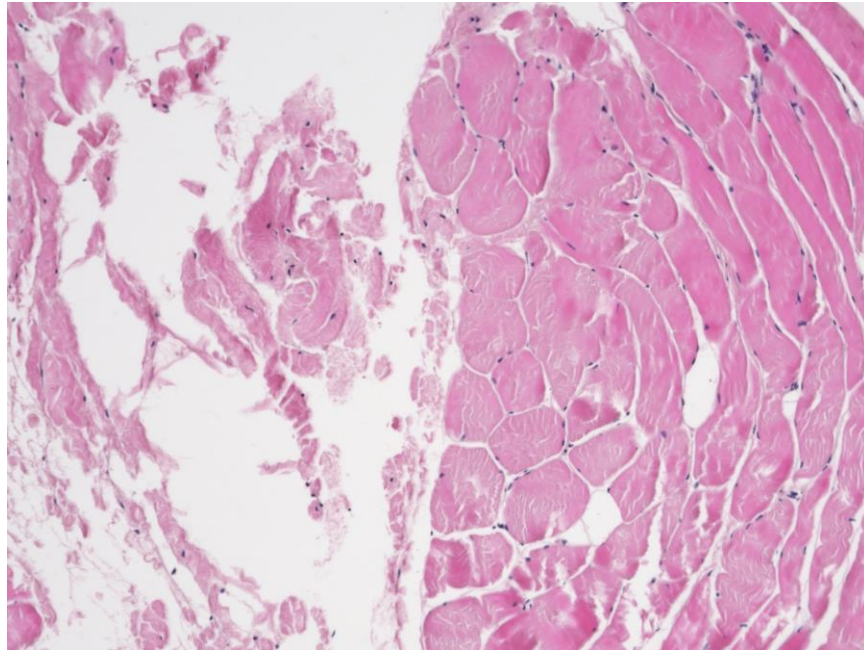
Figure 140. Histology. Group 3 Sternohyoid Muscle.
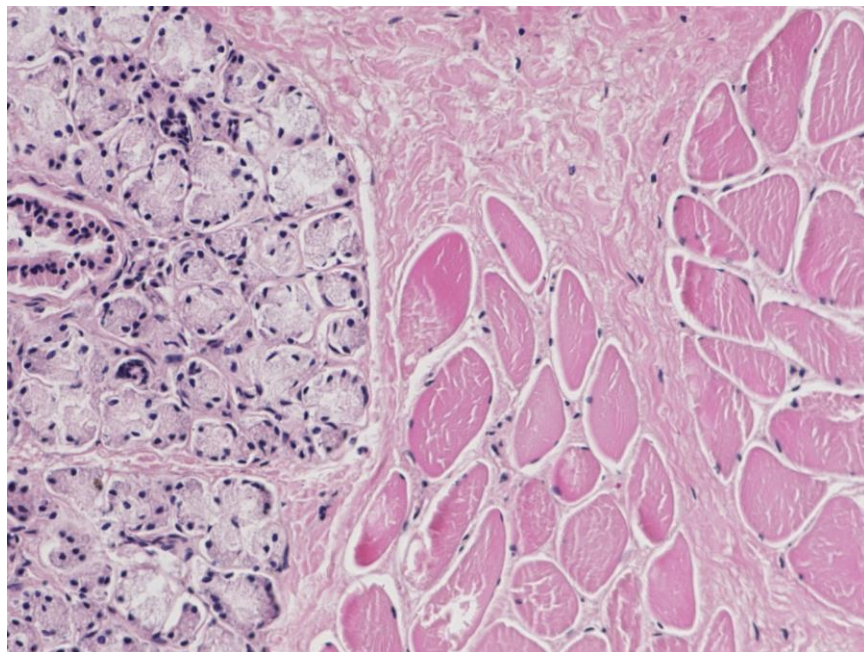
Figure 139. Histology. Group 4 Buccinator Muscle.
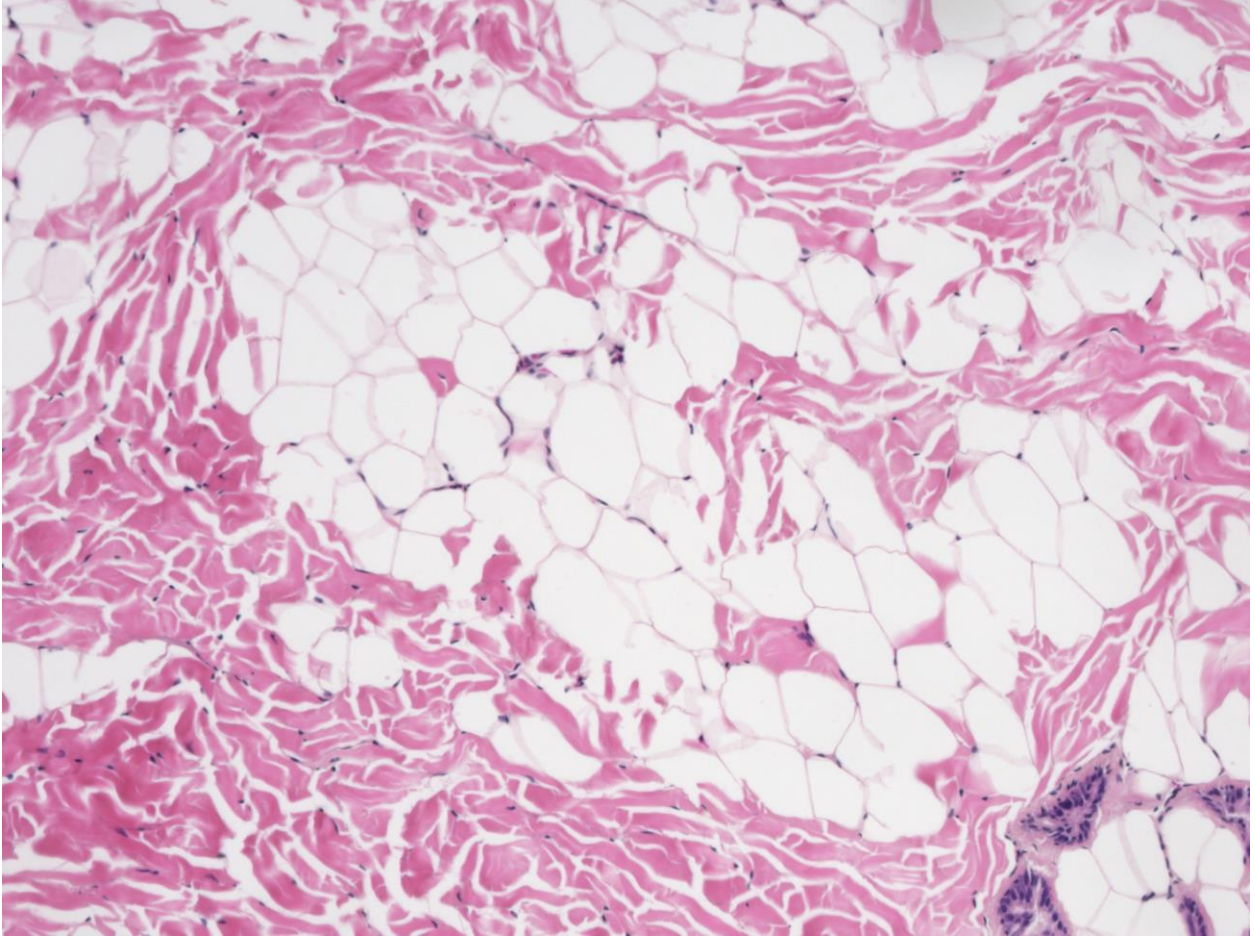
Figure 141. Histology. Group 5 Cutaneous Fascia.
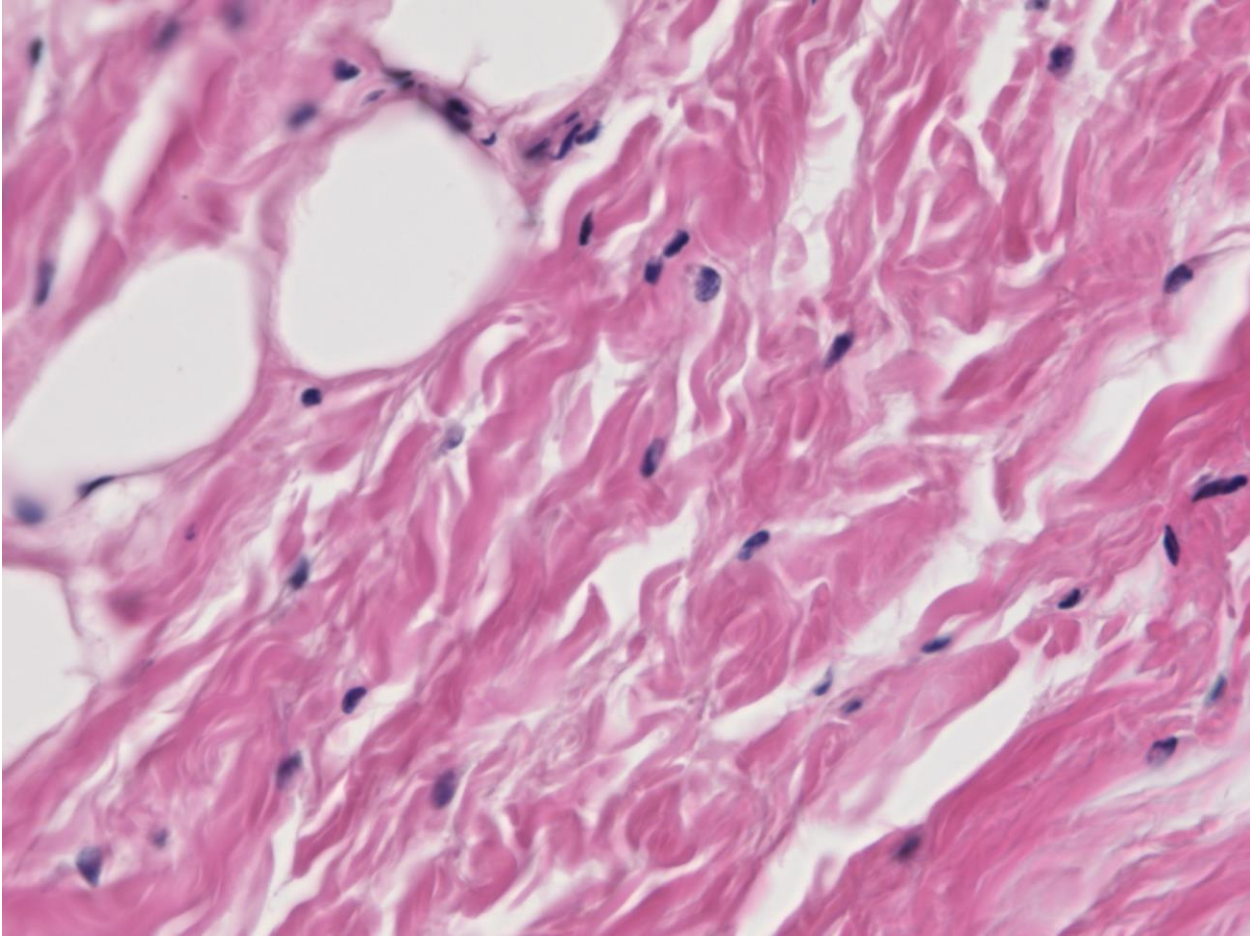
Figure 142. Histology. Group 6 Vestibule.
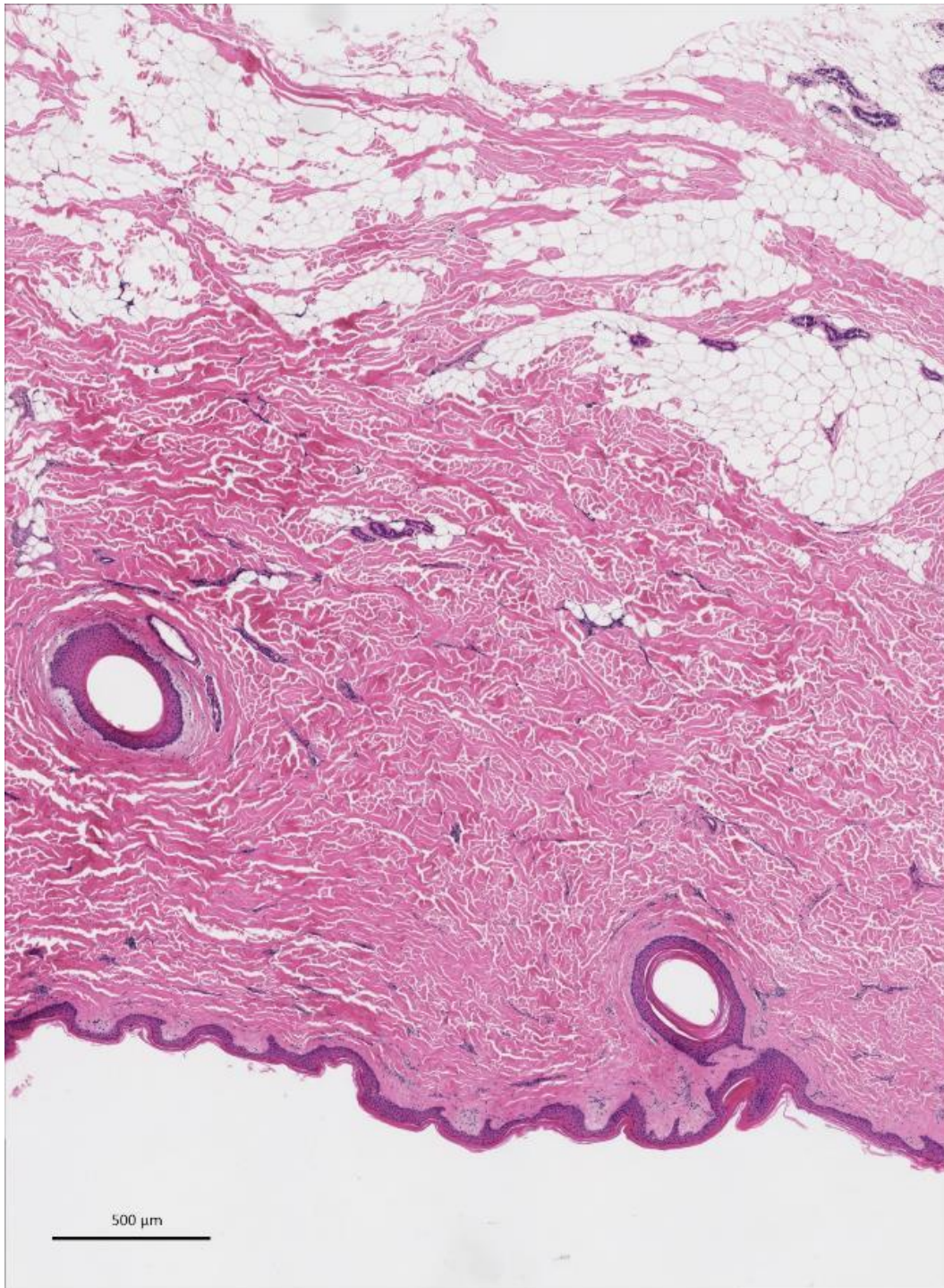
Figure 143. Histology. External to cutaneous fascia region.

3.7.3 Discussion

The findings of this histology assessment characterize muscle and adipose tissue ratios across six anatomic regions (G1 through G6) of interest in the porcine mandible. The results demonstrate that the mean area of muscle tissue exhibits variations across all anatomic regions. The masseter muscle (G2) and genioglossus muscle (G1) presented the highest values, which is indicative of the density of muscle fiber tissue in those regions. The cutaneous fascia (G5) reported the lower mean area for muscle tissue.

In the assessment of adipose tissue, the Sternohyoid muscle (G3) and cutaneous fascia (G5) reported higher means in comparison to the other groups. The genioglossus muscle (G2) and the masseter muscle (G1) displayed the lowest mean areas for adipose tissue. The sternohyoid muscle finding is relevant due to the anatomical size (thin and long, inferior section of the neck) for size and proximity to the fascia at the site where the sample was prepared.

The preliminary results suggest that the soft tissue regions of interest that were sampled from the porcine mandible exhibit notable regional differences in muscle and adipose tissue. These findings are relevant for understanding light distribution, light dosimetry, and treatment planning for various PBM and PDT therapies in soft tissue.

3.8   Bone Tissue Optical Property Characterization and Validation

3.8.1   Methods

The mandibles of five Yorkshire pigs were obtained from a slaughterhouse (Animal Technologies, Tyler, Texas). All specimens were transported frozen, unfixed, and fully thawed before analysis. Both males and females were of different weights and ages to show conditions variability within the same animal model. Each specimen consisted of the entire mandible, condylar structures, and intact intra and extraoral tissues for this respective anatomy.

The regions of interest for the bone tissue optical property characterization were standardized as the right condyle across all specimens. (See Figure 144)

Figure 144. Bone Tissue Optical Property Characterization.
Region of Interest. Right Condyle.

Osteotomies were prepared at all bone tissue sites with the V35 electric handpiece and dental motor (Buffalo Dental Manufacturing Co. Inc, Syosset, NY). The following Versah osseodensification instruments (Versah LLC, Jackson MI) were used to prepare various bone tissue sites: #VPLTT, #ZPLTT-90, VT1525, VT1828, ZT-1525-90, ZT2030-90. (See Figure 145 – 146)

157

Figure 146. Bone tissue optical property characterization. Region of interest right condyle. Osteotomy Preparation.
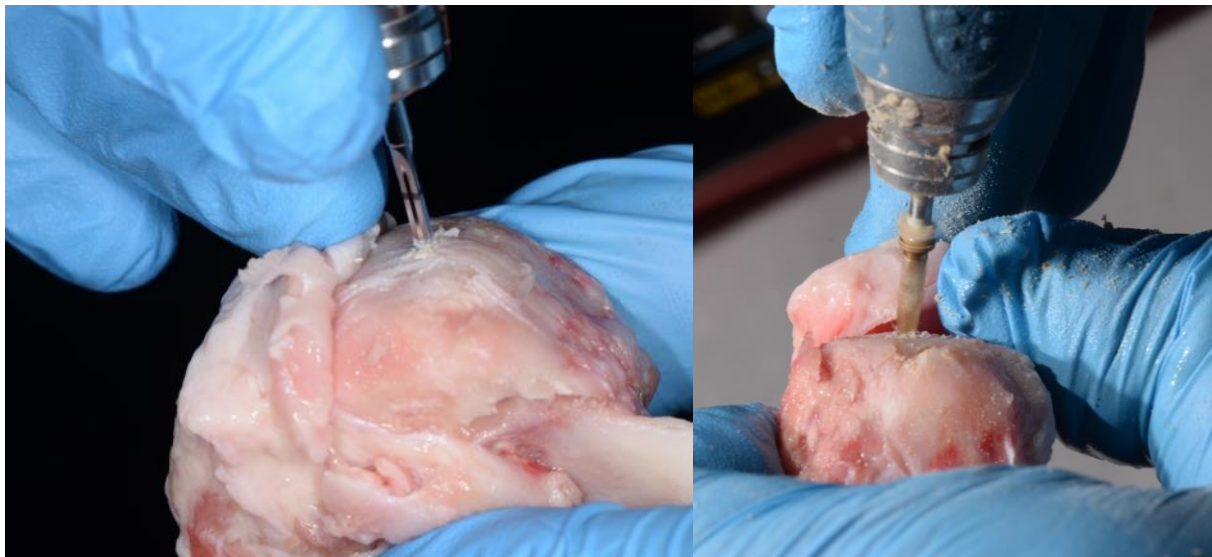
Figure 145. Bone tissue optical property characterization. Region of interest right condyle. Osteotomy Preparation.

After osteotomy preparation, a standardized protocol was developed to validate osteotomy distance and parallelism in all five samples utilizing a cone-beam computerized tomography machine (3D Accuitomo XYZ Slice View Tomograph, Norita, Japan). (117-123) The settings for all image acquisitions were as follows: field of view 170 x 120, tube voltage 90kV, tube current 5.0mA, Imaging D140 x 100 Hi-Fi. All CBCT images were converted to DICOM files with proprietary software provided by Norita and reviewed in the DTX Studio Implant Software (Version 3.6.6.1, Nobel Biocare, Goteborg, Sweden). (See Figure 147- 148)
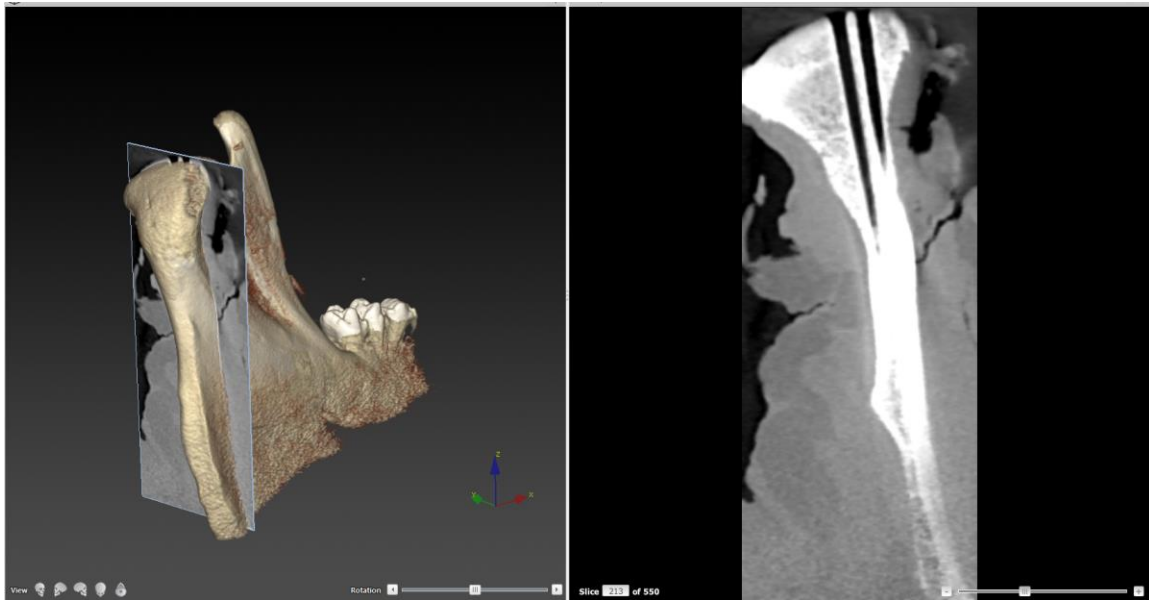
Figure 147. Bone tissue optical property characterization. CBCT imaging of osteotomies in DTX software package.
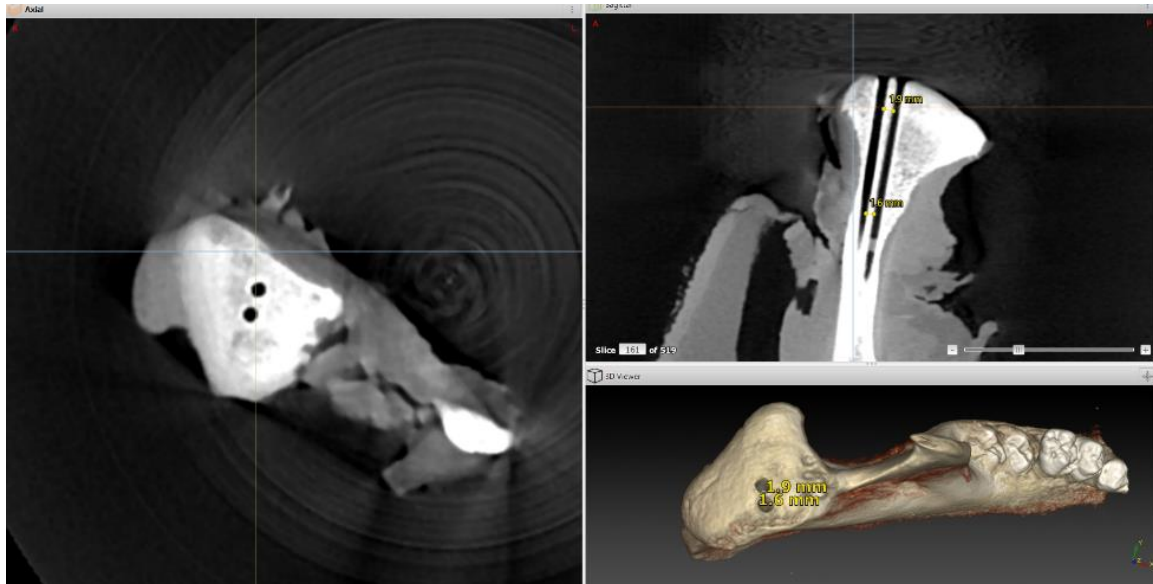
Figure 148. Bone tissue optical property characterization. CBCT imaging of osteotomies in DTX software package.

A standardized methodology developed by the Zhu lab group was adjusted to validate bone tissue optical properties for the series of 5 porcine cadaver mandibles. (21, 29, 108, 109, 112, 115, 116) Power measurements were standardized and acquired inside an integrating sphere, and isotropic detectors were calibrated with an LED calibration sphere. (See Figure 148)

Figure 149. Bone Tissue Optical Properties. Power measurements of
661nm isotropic light source inside of integrating sphere.

A dual catheter motorized dosimetry system paired with wavelength-based algorithms was utilized

for acquiring and analyzing data and calibrating bone tissue optical properties from the five porcine cadaver

models. This "system automatically records and plots the light fluence rate per unit source power as a

function of position." (109). This system consisted of 2 transparent 1.86mm catheters (Flexineedle 17G

20cm with Luer Lock, Manufactured by Best Medical Int.) that were connected to a 665nm laser system

(B&W Tek, Newark DE) and a custom medical dosimetry system. A 0.8mm isotropic detector (IP85,

Manufactured by Medlight S.A.) and a custom 2.0mm point light source (#7035-01 Rev 2; Manufactured

by Pioneer Optics) were placed inside of the catheters and connected to a computer-controlled dual-motor

platform (Velmex, Inc. East Bloomfield, NY). (See Figure 150)
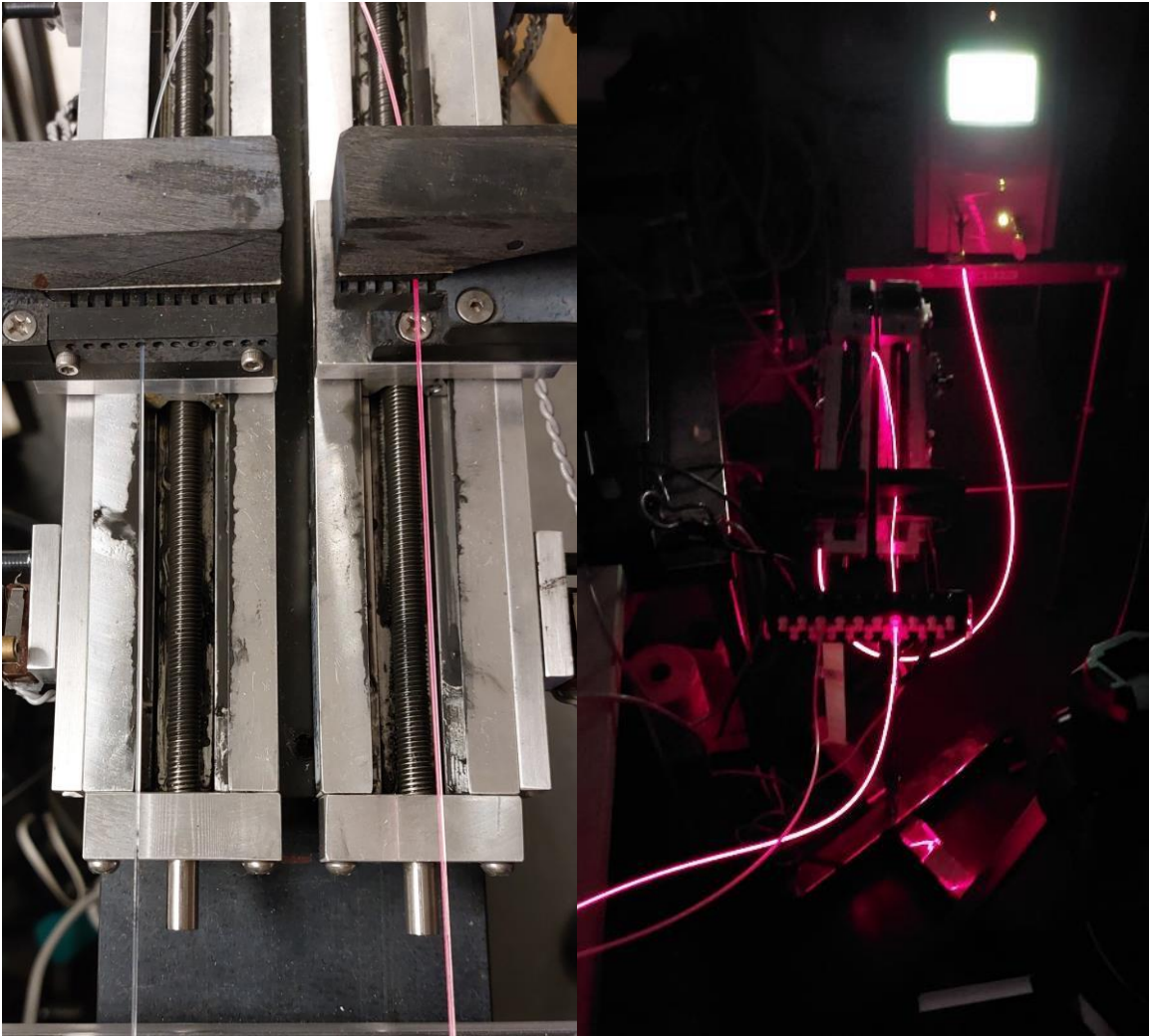
Figure 150. Bone Tissue Optical Properties. Dual Motor Dosimetry System.

The initial detector and source positions were set at 10mm from the bottom of the catheters to allow for enough distance from the most inferior boundary of the mold. The source step was established at 1mm, the range at 20mm, with a total of 2 steps per dosimetry calculation. During activation, the position of the light source was fixed, and the detector acquired data at 0.05mm intervals. This methodology involves acquiring over 800 measurements at varying depths. (29) Details about distance calculations, differential evolution algorithms, wavelength fitting algorithms, and system configurations can be found in prior work published by the Zhu laboratory group. (21, 29, 108, 109, 112, 115)

3.8.2 Results

Five porcine bone tissue specimens were scanned three times without adjusting the catheters to ensure the accuracy and reliability of the results. This resulted in a total of twelve scans per phantom, providing a robust dataset of 60 absorption measurements and 60 reduced scattering measurements for detailed analysis. The histogram was standardized to the "fit range" from -0.1 to 0.9 readings. (See Figure 151)
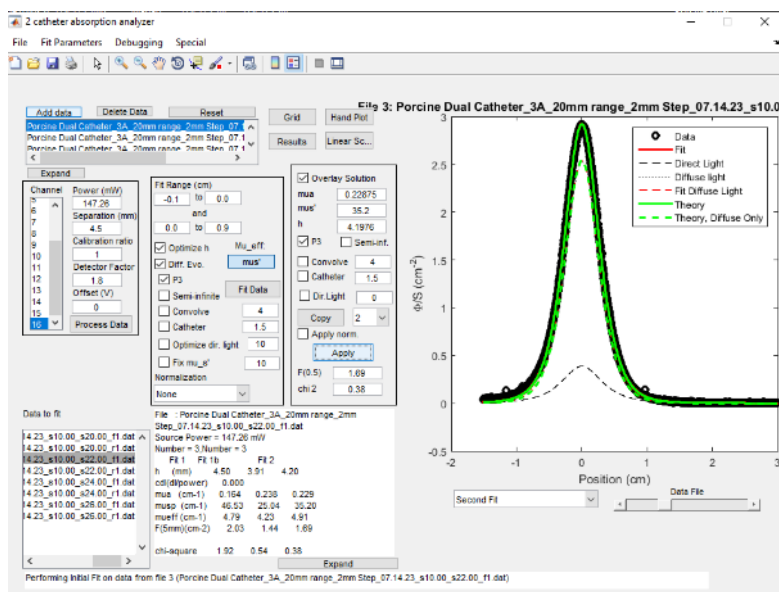
Figure 151. Bone Tissue Optical Properties. Dosimetry Output.

3.8.3   Statistical Analysis & Discussion

3.8.3.1   Data Distribution

-Material and Methods: This experiment involved the use of five porcine cadaver models to determine the optical characteristics of cortical bone tissue in the condyle. Absorption and scattering coefficients were acquired through a dual-motor continuous wave transmittance spectroscopy system connected to a 661nm light source and an isotropic detector. The experiment was performed in triplicate for each specimen, resulting in 60 absorption and 60 reduced scattering measurements.

Data was analyzed using IBM SPSS Statistic (version 29.0.1.0 (1711). Data distribution of absorption and scattering coefficients were assessed using the Kolmogorov-Smirnov (K-S) and Shapiro-Wilk (S-W) tests.

-Results: The bone tissue absorption and scattering properties of all five porcine specimens were subjected to analysis using the K-S and S-W tests. The K-S test reported an absorption statistic of .509 (p<.001) for specimen 3 and .342 (p<.001) for specimen 5. Similarly, the S-W test for absorption reported .365 (p<.001) and .644 (p<.001) for specimens 3 and 5, respectively. However, the K-S test for scattering coefficient reported a test statistic of .351 (p<.001) for specimen 2 and .365 (p<.001) for specimen 5. The S-W test reported a scattering statistic of .653 (p<.001) for specimen 2 and .642 (p<.001) for specimen 5. (See Figure 153 - 154)

Tests of Normality

	Porcine	Kolmogorov-Smirnov[a]			Shapiro-Wilk		
		Statistic	df	Sig.	Statistic	df	Sig.
Absorption	1	.184	12	.200[*]	.883	12	.095
	2	.196	12	.200[*]	.882	12	.093
	3	.509	12	<.001	.365	12	<.001
	4	.235	12	.066	.882	12	.093
	5	.342	12	<.001	.644	12	<.001

*. This is a lower bound of the true significance.

a. Lilliefors Significance Correction

Tests of Normality

	Porcine	Kolmogorov-Smirnov[a]			Shapiro-Wilk		
		Statistic	df	Sig.	Statistic	df	Sig.
Scattering	1	.177	12	.200[*]	.920	12	.282
	2	.351	12	<.001	.653	12	<.001
	3	.240	12	.054	.847	12	.033
	4	.365	12	<.001	.743	12	.002
	5	.271	12	.015	.642	12	<.001

*. This is a lower bound of the true significance.

a. Lilliefors Significance Correction

Figure 153. Bone Tissue Optical Property. Data Distribution Analysis for Normality.
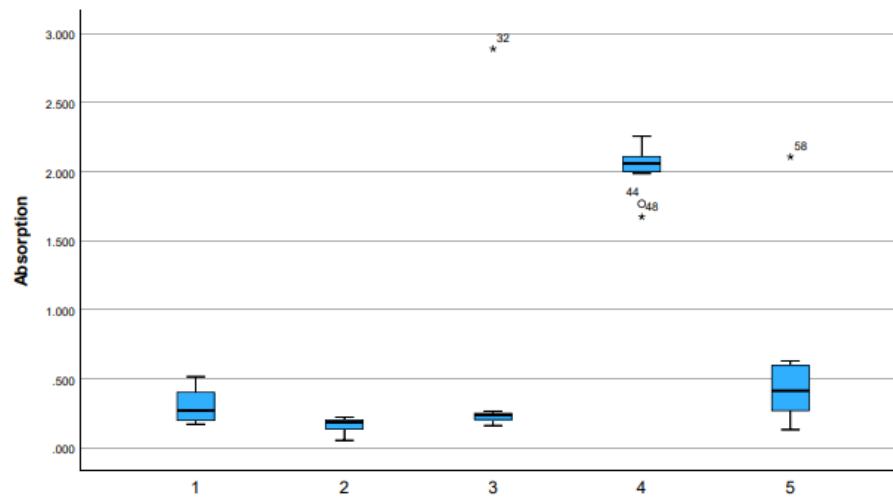
Figure 152. Bone Tissue Optical Property. Box Plot Visualization for Absorption.
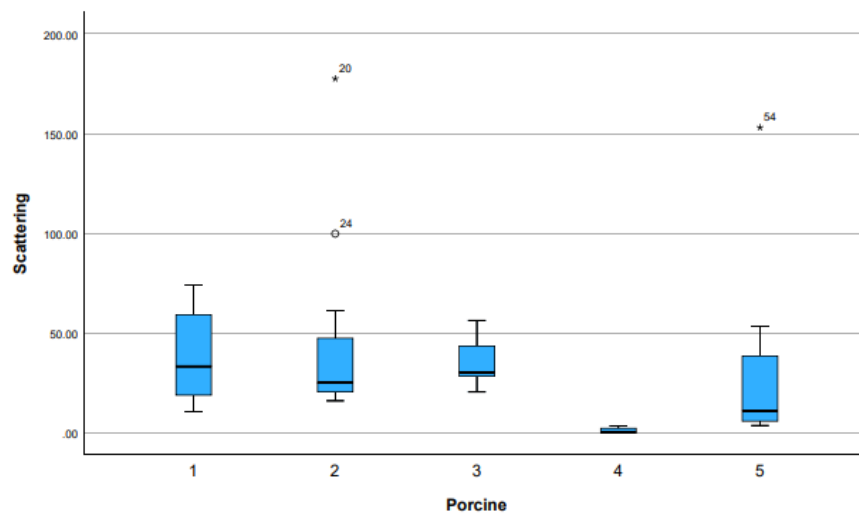
Figure 154. Bone Tissue Optical Property. Box Plot Visualization for Scattering.

-Discussion: The K-S and S-W normality assessments for absorption and scattering coefficients have provided insight into the distribution characteristics in the same region between five specimens. These discrepancies may be due to variations in tissue density, the proximity of each osteotomy to the edge of cortical bone, or sample size limitations. There is an indication of reliability with the absorption metrics for this model, given the agreement between K-S and S-W tests.

3.8.3.2 Variability of Absorption Between Specimens.

-Primary Objective: To determine the variability of the absorption coefficient recorded in bone tissue between the five porcine specimens.

-Aims: This study aims to assess the variability of absorption between five porcine specimens.

-Material and Methods: Data was analyzed using IBM SPSS Statistic (version 29.0.1.0 (1711). Given the non-normal distribution of data, the Friedman test, pairwise comparison with the Wilcoxon Signed Rank Test, and Bonferroni correction (.05/10= .005) were applied.

-Results: The Friedman test reported a chi-square value of 10.400 and a significant difference (p= .034). The pairwise correction with the Wilcoxon Signed Rank test reported a statistic of -1.604 and Asymp. Sig. of .109. There was no statistical significance after the Bonferroni correction. (See Figure 155 - 156)

Friedman Test

Ranks

	Mean Rank
Porcine 1 Absorption	2.67
Porcine 2 Absorption	1.00
Porcine 3 Absorption	2.67
Porcine 4 Absorption	5.00
Porcine 5 Absorption	3.67

Test Statistics[a]

N	3
Chi-Square	10.400
df	4
Asymp. Sig.	.034

a. Friedman Test

Figure 155. Bone Tissue Optical
Properties. Friedmans Test. Absorption.

Test Statistics[a]

	Porcine 2 Absorption - Porcine 1 Absorption	Porcine 3 Absorption - Porcine 1 Absorption	Porcine 4 Absorption - Porcine 1 Absorption	Porcine 5 Absorption - Porcine 1 Absorption	Porcine 3 Absorption - Porcine 2 Absorption	Porcine 4 Absorption - Porcine 2 Absorption	Porcine 5 Absorption - Porcine 2 Absorption	Porcine 4 Absorption - Porcine 3 Absorption	Porcine 5 Absorption - Porcine 3 Absorption	Porcine 5 Absorption - Porcine 4 Absorption
Z	-1.604[b]	.000[c]	-1.604[d]	-1.604[d]	-1.604[d]	-1.604[d]	-1.604[d]	-1.604[d]	-.535[d]	-1.604[b]
Asymp. Sig. (2-tailed)	.109	1.000	.109	.109	.109	.109	.109	.109	.593	.109

a. Wilcoxon Signed Ranks Test
b. Based on positive ranks.
c. The sum of negative ranks equals the sum of positive ranks.
d. Based on negative ranks.

Figure 156. Bone Tissue Optical Properties. Pairwise Comparison, Wilcoxon Signed Rank Tests. Absorption.

-Discussion: The Friedman's test indicated significant variability for absorption across all the trials. This suggests that each specimen may have differences in optical properties. The pairwise comparison with correction suggests that there are no significant differences between the specimens. This can be due to inconsistency or being underpowered.

168

3.8.3.3 Variability of Scattering Between Specimens.

-Primary Objective: To determine the variability of the scattering coefficient recorded in bone tissue between the five porcine specimens.

-Aims: This study aims to assess the variability of absorption between five porcine specimens.

-Material and Methods: Data was analyzed using IBM SPSS Statistic (version 29.0.1.0 (1711). Given the non-normal distribution of data, the Friedman test, pairwise comparison with the Wilcoxon Signed Rank Test, and Bonferroni correction (.05/10= .005) were applied.

-Results: The Friedman test reported a chi-square value of 7.733 (p= .102). The pairwise correction with Wilcoxon Signed Rank and Bonferroni correction did not report statistical significance. (See Figure 157 – 158)

Ranks

	Mean Rank
Porcine 1 Scattering	3.67
Porcine 2 Scattering	4.33
Porcine 3 Scattering	3.33
Porcine 4 Scattering	1.00
Porcine 5 Scattering	2.67

Test Statistics[a]

N	3
Chi-Square	7.733
df	4
Asymp. Sig.	.102

a. Friedman Test

Figure 157. Bone Tissue Optical
Properties. Friedmans Test. Scattering.

Test Statistics[a]

	Porcine 2 Scattering - Porcine 1 Scattering	Porcine 3 Scattering - Porcine 1 Scattering	Porcine 4 Scattering - Porcine 1 Scattering	Porcine 5 Scattering - Porcine 1 Scattering	Porcine 3 Scattering - Porcine 2 Scattering	Porcine 4 Scattering - Porcine 2 Scattering	Porcine 5 Scattering - Porcine 2 Scattering	Porcine 4 Scattering - Porcine 3 Scattering	Porcine 5 Scattering - Porcine 3 Scattering	Porcine 5 Scattering - Porcine 4 Scattering
Z	-.535[b]	-1.069[c]	-1.604[c]	-.535[c]	-1.069[c]	-1.604[c]	-1.604[c]	-1.604[c]	.000[d]	-1.604[b]
Asymp. Sig. (2-tailed)	.593	.285	.109	.593	.285	.109	.109	.109	1.000	.109

a. Wilcoxon Signed Ranks Test
b. Based on negative ranks.
c. Based on positive ranks.
d. The sum of negative ranks equals the sum of positive ranks.

Figure 158. Bone Tissue Optical Properties. Pairwise Comparison, Wilcoxon Signed Rank Tests. Scattering.

-Discussion: The Friedman's test did not indicate significance for scattering across all the trials. The pairwise comparison with correction suggests that there are no significant differences between the specimens. This can be due to inconsistency or being underpowered.

170

3.9 Conclusion

Improving the standard of care for PDT and PBM requires novel dosimetric approaches that are bolstered with dynamic evidence and innovation. The complex tissues of the human dental-oral craniofacial complex demand innovative models to investigate light transmission and dosimetry. This series of porcine mandible cadaver experiments serves as a platform to investigate light dosimetry that can eventually be translated into human clinical care.

The broad variations of optical properties at the target site affect how PDT and PBM can achieve treatment endpoints. Irradiation parameters, including wavelength, power, fluence, irradiance, and the beam area spot size of the device, equally impact treatment efficacy. Dosing adjustments should be made while considering the varying absorption and scattering profiles of bone, soft tissue, dentin, and enamel.

The proof-of-concept investigation conducted in section 3.3 has yielded valuable insights into 661nm light transmission through different types of tissue. The results demonstrate that transmission is not uniform across different tissue types and is, in fact, modified as it passes through boundaries with different optical properties. Soft tissue regions were found to have higher transmission compared to those without. The regions containing dentin/enamel consistently reported lower rates. These conclusions suggest that the complex structures of bone, soft tissue, dentin, and enamel are responsible for these phenomena. These findings provide valuable insights into the transmission of light through different combinations of tissue and highlight the need for further investigation.

The experiments carried out in section 3.4 analyzed 661nmn transmission at fixed distances in six different regions across five specimens at both 500mW and 1W power outputs. The results obtained from this study indicated significant variations between the six regions, highlighting the differences in the structure of each group. Significant findings were reported between groups 1 and 2 at both power outputs and revealed a consistent difference between all pairs, irrespective of the power output.

171

The findings of section 3.4 provide insight into the behavior of the 661nm wavelength while transmitting light through soft tissue structures. This study determined impactful findings on the relationship of distance between measurements and the statistical significance in light transmission between regions. The negative correlation observed between light transmission and distance indicates that the intensity of light transmission decreases as the distance from the source of light increases. The positive correlation between light transmission and anatomical regions identified groups 3 and 5 with higher transmission rates than others, regardless of power output. These groups are also associated with the histology assessment in section 3.7, which reported G3 and G5 with higher amounts of adipose tissue and decreased amounts of muscle tissue. (See Figure 159 – 160)

Porcine, 661nm (500mW)

	Group	2mm	4mm	6mm	8mm	10mm	12mm	14mm
500mW; Mean VALUES	G1) Genioglossus Muscle	216.112	25.6032	5.776	0.874	0	0	0
	G2) Masseter Muscle	160.12	26.276	3.38	0	0	0	0
	G3) Sternohyoid Muscle	424.804	112.972	36.5	12.124	4.256	0	0
	G4) Buccinator Muscle	194.056	38.424	8.32	1.316	0	0	0
	G5) Cutaneous Fascia	500.772	301.16	63.228	23.292	9.476	1.456	0
	G6) Vestibule	191.608	29.172	3.66	0	0	0	0
	Placebo (Control), 500mW, In Air	215.02	56.6	25.26	14.88	9.34	6.46	4.525

Figure 159. Section 3.4 summary of findings, 661nm, 500mW.

172
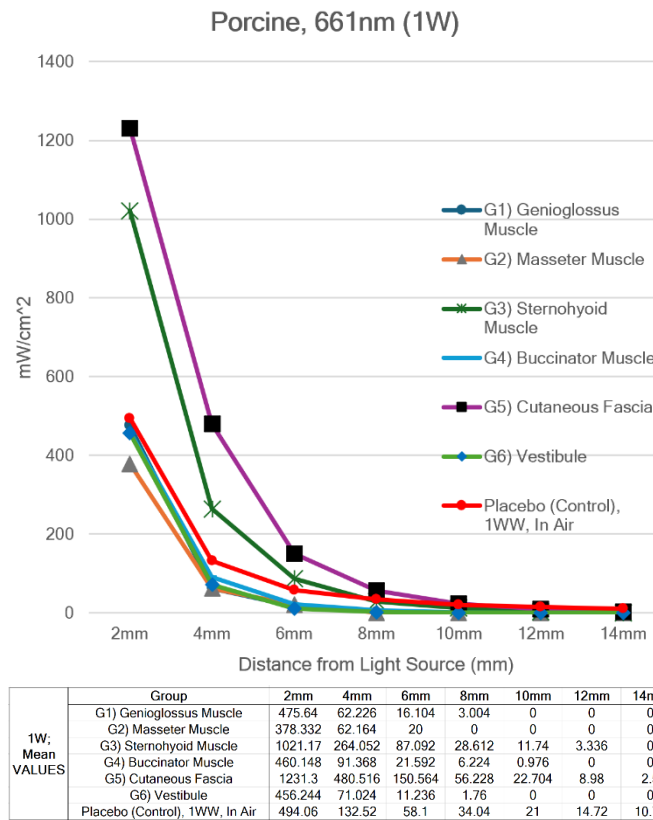
Figure 160. Section 3.4 summary of findings, 661nm, 1W.

Experimental series 3.5 assessed the differences between the 661nm red and 810nm near-infrared wavelengths at 500mW power outputs. This series determined that both wavelengths exhibited different characterizations within the same soft tissue regions. The data obtained suggests that the 810nm wavelength consistently reported higher levels of transmission than the 661nm wavelength. An inverse relationship was reported between light transmission and distance for both wavelengths, corroborating prior evidence that most light transmission occurs within the first few millimeters of tissue depth. (See Figure 161 – 166)

The findings of section 3.5 indicate that the absorption and scattering optical properties of each region in this model are different for the 661nm and 810nm wavelengths. Thus, highlighting the importance of considering wavelength-specific tissue responses while calculating dose for PDT and PBM dosimetry.
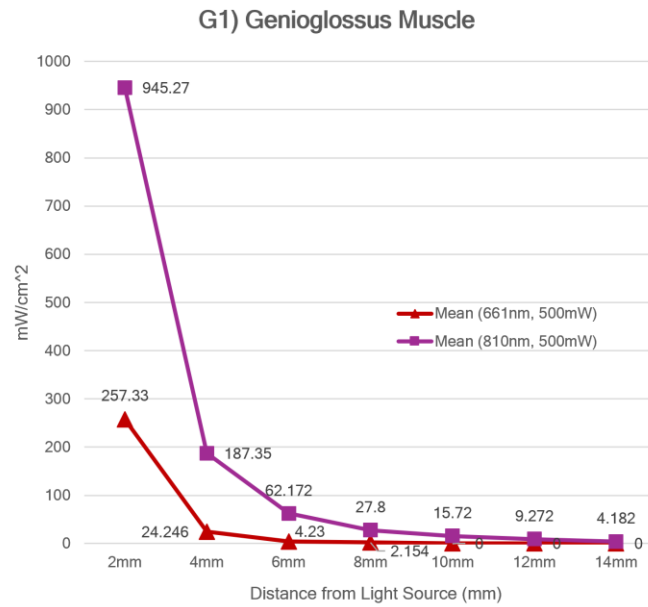
Figure 161. 661nm VS. 810nm, G1) Genioglossus Muscle.
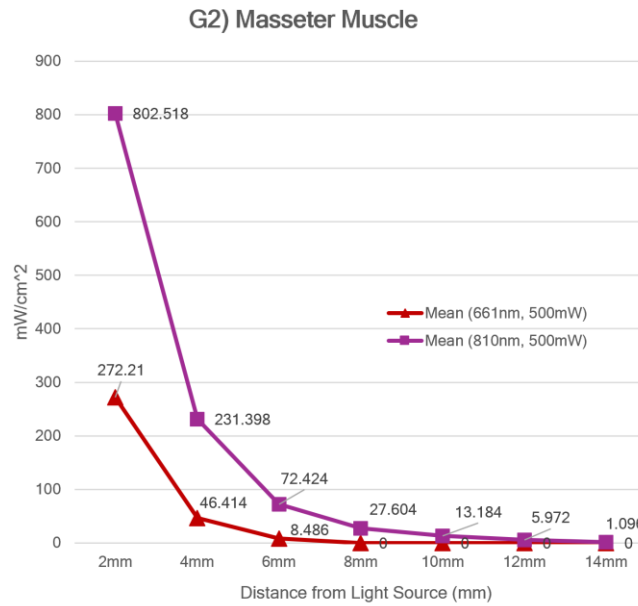
Figure 162. 661nm VS. 810nm, G2) Masseter Muscle.
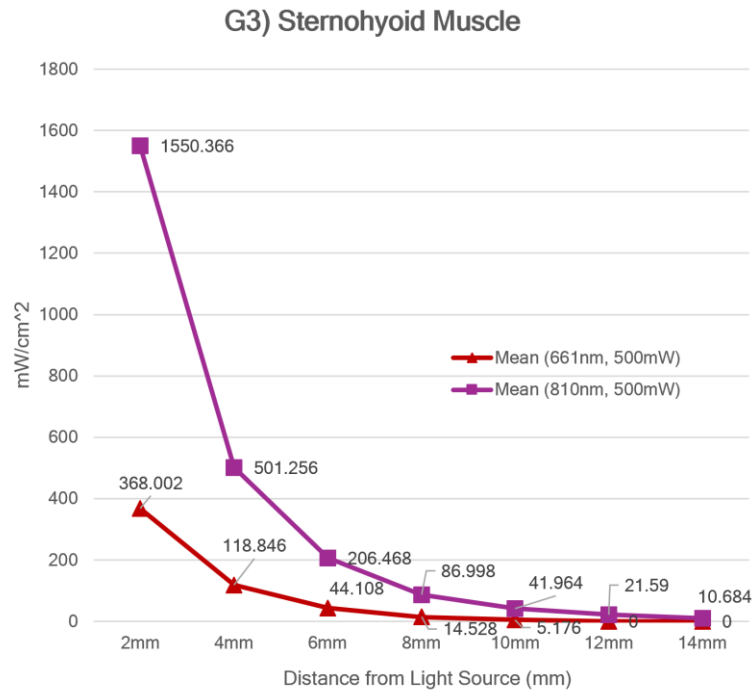
Figure 164. 661nm VS. 810nm, G3) Sternohyoid Muscle.
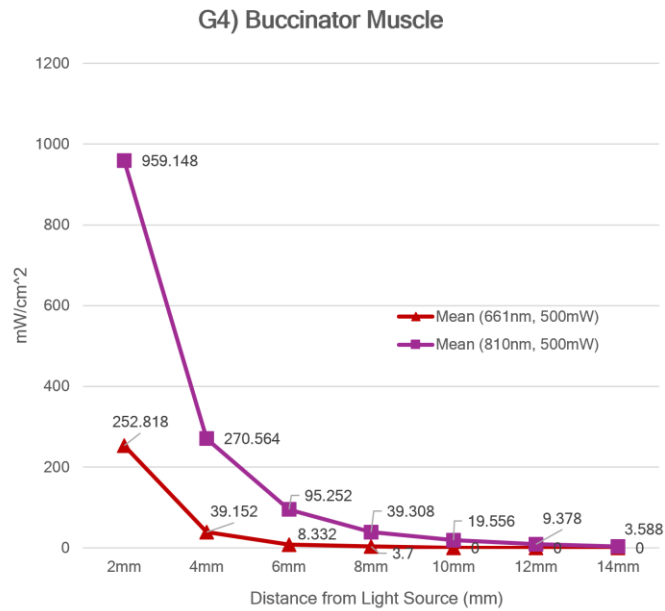
Figure 163. 661nm VS. 810nm, G4) Buccinator Muscle.

175

G5) Cutaneous Fascia
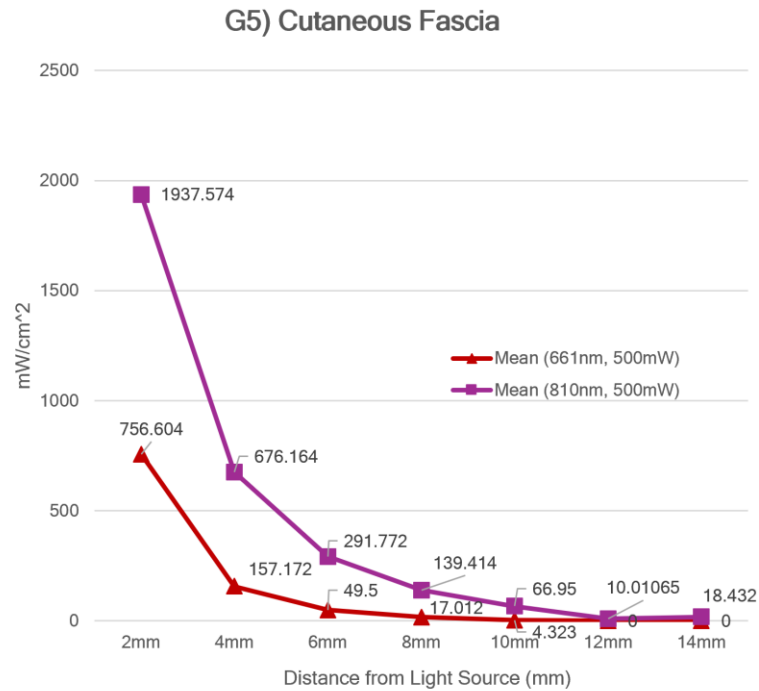
Figure 165. 661nm VS. 810nm, G5) Cutaneous Fascia.
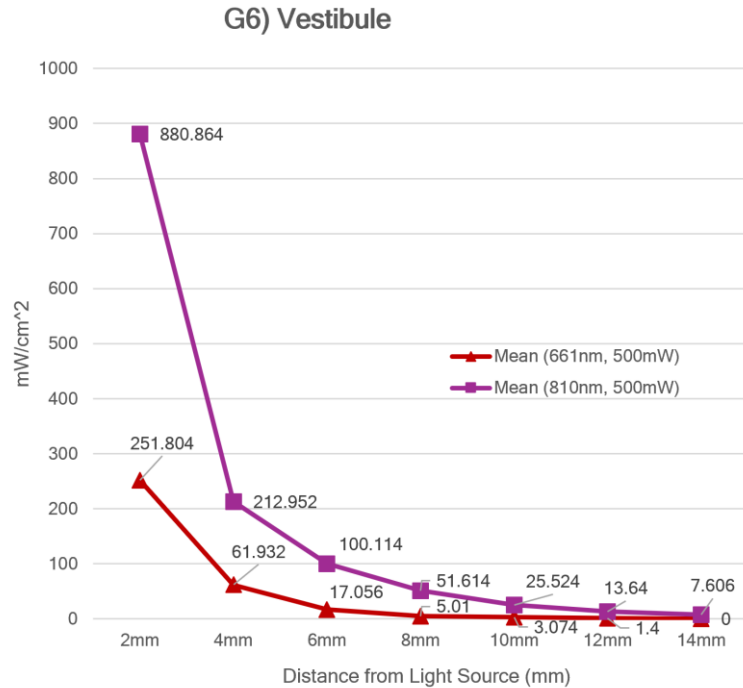
G6) Vestibule

Figure 166. 661nm VS. 810nm, G6) Vestibule.

176

The semi-infinite light transmission series described in series 3.6 served as a translational equivalent to the phantom model series described in section 2.5. There was extensive variability between all twenty-two regions of interest. The most prominent variability occurred in the vestibule and was likely due to underlying anatomic features like tissue type and mucosal glands present in the porcine model. Significant variations were also reported for the comparisons with soft tissue groups, indicating consistent differences in light transmission when compared to mixed tissues. The findings served to validate the medical dosimetry system across multiple diverse tissue regions and provided evidence that light dosimetry measurements can be standardized across complex 3-dimensional geometries, which can be implemented in human care for real-time dosimetry.

The semi-infinite light transmission experiments detailed in series 3.6 are an excellent translational component to the silicone phantom model series described in section 2.5. This investigation reported extensive variability among all twenty-two regions of interest. Notably, the vestibule exhibited the most prominent variability. This can be attributed to the underlying anatomic features, such as the tissue type and the presence of mucosal glands in the porcine model. (See Figure 167 – 168)
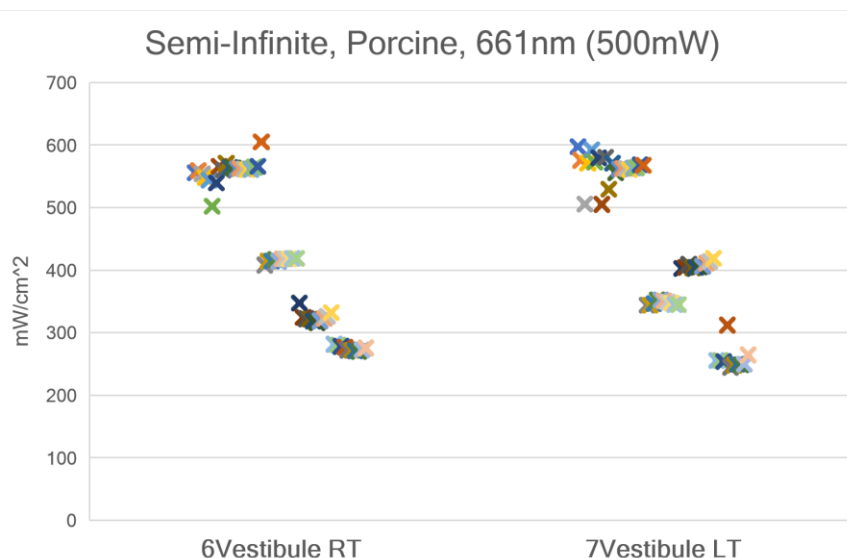
Figure 167. Semi-Infinite Light Transmission, Porcine. 661nm (500mW). Notating variability with groups 6 & 7 Vestibule Regions.

177
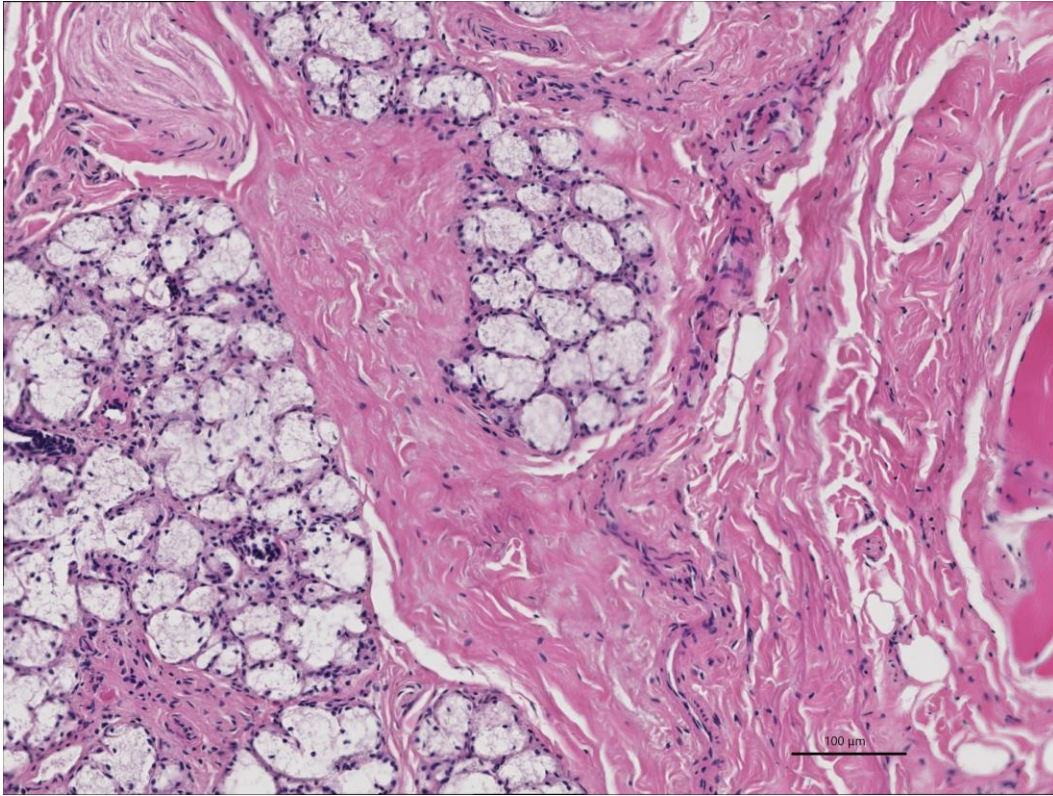
Figure 168. Histology, H&E, G6) Vestibular Region.

Significant variations were also reported for the comparisons with soft tissue groups. This finding indicates consistent differences in light transmission when compared to mixed tissues. These results validate the medical dosimetry system across multiple diverse tissue regions with substantial evidence that light dosimetry measurements can be standardized across complex 3-dimensional geometries. Given that the dosimetry system software is currently in use for ongoing human clinical trials, real-time dosimetric adjustments could potentially begin evaluating complex 3-dimensional structures.

In section 3.8 of this series, interstitial light dosimetry assessments were collected in standardized osteotomies in bone tissue across all five specimens. The results revealed significant variability in the absorption metrics, indicating that each specimen may have different optical properties. The scattering data was not statistically significant, which suggests that there were no differences between the specimens for

178

this optical property. Despite these findings in section 3.8, it is important to note that the sample size in this study was limited, and these results should be interpreted with caution. The discrepancies observed in the absorption metrics may be the result of inherent biological tissue differences that affect either absorption or scattering. Discrepancies can also be due to osteotomy proximity or the study design. Further research with a larger sample size and more controlled variables would be necessary to confirm these observations and provide more conclusive results. (See Figure 169)
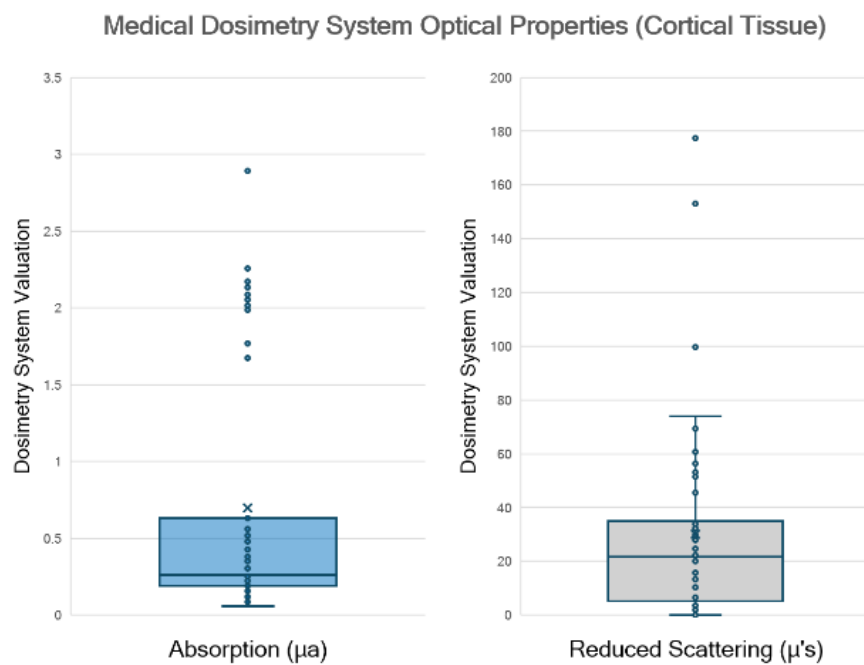
Figure 169. Bone Tissue Optical Property. Box Plot Visualization for all Five Specimens.

The porcine mandible cadaver series described in Chapter 3 represents the significant potential of an experimental platform for investigating the dosimetry of PDT and PBM in the dental-oral craniofacial complex. The complex 3-dimensional geometries, critical anatomical characteristics, and tissue optical properties all need to be considered when prescribing light therapy. This series of studies presents a comprehensive translational workflow that extends from interstitial to semi-infinite light transmission and is applicable to protocols currently in use for human care. This comprehensive series of observations reveals variability across different regions, power outputs, and wavelengths. Thus, providing insight for light-tissue interactions and improving dosimetry considerations. These findings can be leveraged to adjust light delivery parameters and optimize treatment outcomes to help achieve treatment endpoints for human clinical care.

4   CONCLUSION AND FUTURE OUTLOOK

This thesis research articulates multiple preclinical medical dosimetry experiments that are described in detail. I have described novel medical dosimetry translational science applications that can be used for PDT and PBM treatments. Additionally, I have provided a comprehensive set of data analytics to calibrate a medical dosimetry system to a broader spectrum of tissue optical properties (absorption and scattering).

This research is a contribution to a larger translational framework and will be correlated with findings from my prior publications and toward future human clinical care trials. By exploring these preclinical medical dosimetry experiments, we can understand the potential of this technology and its practical application in clinical care.

The impact of enhancing the standard of care for PDT and PBM cannot be overstated. It is now well established that PDT and PBM require innovative dosimetric approaches that are supported by dynamic evidence and technology. All experiments were conducted on a medical dosimetry system featuring proprietary algorithms, which have been implemented in human clinical care for over fifteen years. TAccess to this system has been critical with the ability to correlate the findings of this research with those from clinical care.

The first chapter of this thesis provides a comprehensive overview of the theoretical background, motivation, and preclinical experimental techniques involved with investigating the basic translational science components of PDT and PBM. The second chapter describes the phantom modeling fabrication process, which has undergone several improvements to eliminate microbubbles through the implementation of several techniques used to pour dental stone models. This resulted in a comprehensive multi-step protocol that is reproducible. This group of phantoms was replicated in the cylinder shape, which was traditionally used for breast and prostate cancer research. It was then expanded to a novel 3-dimensional shape replicating the human maxilla and a dental extraction socket. This involved the incorporation of several

181

advanced technologies, including 3-dimensional image manipulation, 3D printing, acquisition of 3D surface topography, and CBCT validations for homogeneity.

A medical dosimetry system is described in detail in section 2.3, which plays a critical role in accurately calculating the dose and quantifying optical properties during therapy. This system is used for interstitial light delivery, as detailed in section 2.4 with the cylinder phantom. This cylindrical shape has been the traditional gold standard for medical dosimetry with the Tim Zhu Laboratory at the Hospital of the University of Pennsylvania. By accurately quantifying absorption and scattering properties within each region of interest, this system facilitates the calculation of light delivery for various PDT therapeutic approaches. This medical dosimetry system is necessary to properly calculate dose during treatment, as optical properties have direct dosimetric effects on each other.

In section 2.5, the semi-infinite form of light transmission was introduced in the first known translation of the cylinder shape to a novel three-dimensional geometry of the human maxilla. Both shapes were produced in nine different categories of predetermined absorption and scattering variables. A standardized control was useful to assess complex convex and concave geometries between all nine groups. Statistical differences were revealed between the shapes and groups, thus implying that light transmission is affected by geometry. Pairwise comparisons were conducted between all nine groups and twenty-seven models. Despite multiple groups reporting significance, only one group remained significant after correction. These findings suggest that a wide variation in optical property differences can significantly impact how light is transmitted through complex geometries. These results highlight the need for the development of advanced computational models that can account for complex geometries and guide real-time dosimetry protocols to guide patient-specific treatment approaches.

Chapter three of this thesis focuses on a comprehensive investigation of a novel porcine mandible cadaver modeling system. The similarities between porcine and human dental-oral craniofacial tissues have

already been explored due to similar anatomical features and size ratios. Section 3.3 offers a proof-of-concept investigation of 661nm light transmission at the complex boundaries of bone, soft tissue, dentin, and enamel. This investigation concludes that transmission decreases through bone, dentin, and enamel with subsequent increases in soft tissues. However, tissue boundaries are more complex and involve multiple combinations of types. This notion provides a framework to characterize these distributions in future investigations.

Section 3.4 introduces an extended format of the porcine cadaver model that includes five specimens. The interstitial measurements were standardized in six distinct regions for 5mmW and 1W power configurations. The statistical significance reported in both power outputs supports the theory that tissue optical properties are not influenced by power output. When analyzing differences between the 661nm and 810nm wavelengths, it was determined that there are significant differences between all regions for both wavelengths. There were also wavelength-dependent characteristics that reported differences between groups. This was revealed through light transmission results in soft tissues where rates were higher for the 810nm compared to the 661nm. Another finding suggested that the 810nm wavelength is absorbed or scattered more effectively than the 661nm wavelength, with both demonstrating a depth-dependent relationship within the first 4-5mm of transmission.

The subsequent study conducted in section 3.6 served as a translational basis for the semi-infinite phantom modeling results of complex phantom geometries reported in section 2.5. This series investigated semi-infinite light transmission across twenty-two regions of interest. This cohort involved the soft tissue regions assessed in Chapter 3, along with regions that combined bone, soft tissue, dentin, and enamel. It was determined that this medical dosimetry system is properly calibrated and can differentiate variability between tissue-specific light interactions. Significant differences were observed in light transmission (mW/cm^2) for all regions. Sites involving mixed tissues exhibited more prominent transmission variations than those with a less complex architecture. These results not only validate the medical dosimetry system

183

using the semi-infinite technique but also emphasize the need for real-time dosimetry approaches to account for statistically significant variations in optical properties that are evident between tissues.

Section 3.7 provides a comprehensive histologic assessment of the six soft tissue regions of interest. The evaluation of images aimed to identify differences in muscle tissue as compared to adipose tissue. Adipose tissue is of great interest and is known to contain higher scattering properties. The assessment revealed that the masseter muscle and genioglossus muscle have the highest mean area of muscle tissue. The assessment of adipose tissue reported the sternohyoid muscle and cutaneous fascia groups to have higher means in comparison to the others. These findings are consistent with the earlier reported light transmission results, where the sternohyoid and cutaneous fascia groups both reported statistically significant higher rates of transmission in comparison to the others. Again, this is believed to be due to the increased scattering properties contained in adipose tissue.

A bone tissue optical property characterization was conducted in section 3.8. This experiment helped provide a more comprehensive understanding of bone tissue optical properties. It served as a direct translational component to the phantom model cylinder optical property assessments described in section 2.4. The absorption properties analysis revealed significant variability initially but was non-significant after correction. The scattering analysis reported non-significance for both. It was noted that the values of one of the specimens reported significant discrepancies in comparison to the others. This was likely due to a combination of factors, including osteotomy proximity and an underpowered study design.

The analyses conducted on both the silicone phantom and porcine cadaver modeling systems are the first component to a larger cascade of translational science. The most notable limitation of the silicone phantoms was the inconsistencies resulting from the fabrication process. Although these models were validated to be free of microbubbles, they were found to have inconsistencies in certain regions between the identical sets of dental molds. This could be attributed to the mixing and stirring process of the weighted

184

carbon and titanium oxide ratios. Regardless of this limitation, this model was successful in validating the dosimetry systems' ability to differentiate differences in light transmission between convex and concave geometric shapes.

The porcine cadaver system was limited in its ability to analyze the active chromophores that are present in vivo in non-cadaver (alive) test subjects. Nevertheless, we were able to quantify significant differences in tissue type. The tissues assessed are perceived to be scaffolds that would otherwise contain chromophores during active light transmission therapy.

Despite the comprehensive findings obtained for both models, there is still abundant data that needs to be analyzed for the dosimetry system from the perspective of medical physics. It is important to note that the semi-infinite silicone phantom model study only reported the pairwise results of each of the 22 regions with the control. Further analysis should investigate the reported significance of buccal and lingual regions for the osteotomy site, the anterior and posterior segments of each model. The dental arches were completed in duplicate, allowing for further calibration of the dosimetry system with complex geometries. The primary limitation of fabrication with the silicone model should be considered. To overcome this limitation, future investigations could assess the ability of 3D printing complex geometric shapes with built-in known optical properties with carbon (absorption) and titanium oxide (scattering).

The development of the porcine cadaver modeling system was consequential to this thesis research. This model is currently being utilized to analyze light transmission for the 661nm and 810nm wavelengths at multiple power outputs. This work will eventually compare both the point light sources described in this thesis along with FDA-approved clinical devices (where applicable).

The additional porcine cadaver experiments will aim to provide a more precise and quantitative understanding of the efficacy of PBM therapy after dental extraction. The ultimate goal is to optimize a protocol that will improve wound healing and reduce postoperative pain for dental patients. This preclinical

experimental series involves standardized osteotomies to evaluate the transmission of light within bone, and by external transmission through the boundary of soft tissue. To achieve a more precise assessment, the study will focus on regions containing dentin and enamel, with a large sample size. The upcoming project series will further investigate light transmission at a fixed distance in bone, with and without the superficial layer of soft tissue. Additional investigations will assess light transmission around dental implants. These experiments will provide insight into how light is absorbed and scattered as it reaches an anatomical region of interest.

In conclusion, the utilization of the silicon phantom and porcine cadaver model for studying PDT and PBM therapies has the potential to impact the field of medical physics. These modeling concepts provide an opportunity to analyze the complex interactions of different geometries, tissue types, and optical properties. The similarities between porcine and human tissues allow for a more accurate representation of the conditions that would be encountered during treatment. Analyzing the complex interactions of different tissue types, varied depths, and multiple tissue combinations provides an opportunity to investigate the underlying mechanisms of these therapies. As the pre-clinical translational model continues to be improved, it has the potential to lead to a more effective treatment strategy to advance the fields of medicine and dentistry.

BIBLIOGRAPHY

1.   Deng J, Lukens JN, Swisher-McClure S, Cohn JC, Spinelli BA, Quinn RJ, Chittams J, McMenamin E, Lin A. Photobiomodulation Therapy in Head and Neck Cancer-Related Lymphedema: A Pilot Feasibility Study. Integr Cancer Ther. 2021;20:15347354211037938. Epub 2021/08/14. doi: 10.1177/15347354211037938. PubMed PMID: 34387119; PMCID: PMC8366198.

2.   Berni M, Brancato AM, Torriani C, Bina V, Annunziata S, Cornella E, Trucchi M, Jannelli E, Mosconi M, Gastaldi G, Caliogna L, Grassi FA, Pasta G. The Role of Low-Level Laser Therapy in Bone Healing: Systematic Review. Int J Mol Sci. 2023;24(8). Epub 2023/04/28. doi: 10.3390/ijms24087094. PubMed PMID: 37108257; PMCID: PMC10139216.

3.   Courtois E, Bouleftour W, Guy JB, Louati S, Bensadoun RJ, Rodriguez-Lafrasse C, Magne N. Mechanisms of PhotoBioModulation (PBM) focused on oral mucositis prevention and treatment: a scoping review. Bmc Oral Health. 2021;21(1). doi: 10.1186/s12903-021-01574-4. PubMed PMID: WOS:000654880100002.

4.   de Carvalho ESRM, Mendes FM, Degasperi GR, Pinheiro SL. Photobiomodulation for the management of xerostomia and oral mucositis in patients with cancer: a randomized clinical trial. Lasers Med Sci. 2023;38(1):101. Epub 2023/04/16. doi: 10.1007/s10103-023-03760-y. PubMed PMID: 37060370.

5.   Alhumaidan AA, Alali Y, Ahmed S, Vohra F, Abduljabbar T. Effect of photobiomodulation after non-surgical mechanical debridement on cortisol levels in the peri-implant sulcular fluid among patients with peri-implant mucositis. Photodermatology Photoimmunology and Photomedicine. 2022. doi: 10.1111/phpp.12774.

6.   Schar D, Ramseier CA, Eick S, Arweiler NB, Sculean A, Salvi GE. Anti-infective therapy of peri-implantitis with adjunctive local drug delivery or photodynamic therapy: six-month outcomes of a prospective randomized clinical trial. Clinical Oral Implants Research. 2013;24(1):104-10. doi: 10.1111/j.1600-0501.2012.02494.x. PubMed PMID: WOS:000312814800016.

7.   Schär D, Ramseier CA, Eick S, Mettraux G, Salvi GE, Sculean A. Transgingival photodynamic therapy (tg-aPDT) adjunctive to subgingival mechanical instrumentation in supportive periodontal therapy. A randomized controlled clinical study. Photodiagnosis Photodyn Ther. 2020;32:101971. Epub 2020/08/25. doi: 10.1016/j.pdpdt.2020.101971. PubMed PMID: 32835882.

8.   Deluca MCD, Scarparo RK, Aspesi M, Matte BF, Brand LM, Grecca FS, Casagrande L, Kopper PMP. Cytotoxic, Migration, and Angiogenic Effects of Photodynamic Therapy and Photobiomodulation Associated with a Revascularization Protocol. Journal of Endodontics. 2021;47(1):69-77. doi: 10.1016/j.joen.2020.10.003. PubMed PMID: WOS:000602701600010.

9.   Zhao T, Song J, Ping Y, Li M. The Application of Antimicrobial Photodynamic Therapy (aPDT) in the Treatment of Peri-Implantitis. Comput Math Methods Med. 2022;2022:3547398. Epub 2022/05/24. doi: 10.1155/2022/3547398. PubMed PMID: 35602342; PMCID: PMC9119742.

10.   Zhu TC, Finlay JC. The role of photodynamic therapy (PDT) physics. Med Phys. 2008;35(7):3127-36. Epub 2008/08/14. doi: 10.1118/1.2937440. PubMed PMID: 18697538; PMCID: PMC2673560.

11.   Huang Z, Xu H, Meyers AD, Musani AI, Wang L, Tagg R, Barqawi AB, Chen YK. Photodynamic therapy for treatment of solid tumors--potential and technical challenges. Technol Cancer Res Treat. 2008;7(4):309-20. Epub 2008/07/23. doi: 10.1177/153303460800700405. PubMed PMID: 18642969; PMCID: PMC2593637.

12.   Wilson BC, Patterson MS. The physics, biophysics and technology of photodynamic therapy. Phys Med Biol. 2008;53(9):R61-109. Epub 2008/04/11. doi: 10.1088/0031-9155/53/9/r01. PubMed PMID: 18401068.

13.   Zhu TC. Dosimetry in pleural photodynamic therapy. J Natl Compr Canc Netw. 2012;10 Suppl 2:S60-4. Epub 2012/10/25. doi: 10.6004/jnccn.2012.0178. PubMed PMID: 23055219.

14.   Algorri JF, Ochoa M, Roldán-Varona P, Rodríguez-Cobo L, López-Higuera JM. Photodynamic Therapy: A Compendium of Latest Reviews. Cancers (Basel). 2021;13(17). Epub 2021/09/11. doi: 10.3390/cancers13174447. PubMed PMID: 34503255; PMCID: PMC8430498.

15.   Agostinis P, Berg K, Cengel KA, Foster TH, Girotti AW, Gollnick SO, Hahn SM, Hamblin MR, Juzeniene A, Kessel D, Korbelik M, Moan J, Mroz P, Nowis D, Piette J, Wilson BC, Golab J. Photodynamic therapy of cancer: an update. CA Cancer J Clin. 2011;61(4):250-81. Epub 2011/05/28. doi: 10.3322/caac.20114. PubMed PMID: 21617154; PMCID: PMC3209659.

16.   Plaetzer K, Krammer B, Berlanda J, Berr F, Kiesslich T. Photophysics and photochemistry of photodynamic therapy: fundamental aspects. Lasers Med Sci. 2009;24(2):259-68. Epub 2008/02/06. doi: 10.1007/s10103-008-0539-1. PubMed PMID: 18247081.

17.   Photodynamic Therapy to Treat Cancer [Website]. National Institute of Health Website2023 [cited 2023 October 9]. Available from: https://www.cancer.gov/about-cancer/treatment/types/photodynamic-therapy.

18.   Zhu TC, Finlay JC. Prostate PDT dosimetry. Photodiagnosis Photodyn Ther. 2006;3(4):234-46. Epub 2006/12/01. doi: 10.1016/j.pdpdt.2006.08.002. PubMed PMID: 25046988; PMCID: PMC4469490.

19.   Lilge L, Wu J, Xu Y, Manalac A, Molenhuis D, Schwiegelshohn F, Vesselov L, Embree W, Nesbitt M, Betz V, Mandel A, Jewett MA, Kulkarni G. Minimal required PDT light dosimetry for nonmuscle invasive bladder cancer (Erratum). J Biomed Opt. 2020;25(6):1. Epub 2020/06/28. doi: 10.1117/1.Jbo.25.6.069801. PubMed PMID: 32592341; PMCID: PMC7317183.

20.   Yassine AA, Lo WCY, Saeidi T, Ferguson D, Whyne CM, Akens MK, Betz V, Lilge L. Photodynamic therapy outcome modelling for patients with spinal metastases: a simulation-based study. Sci Rep. 2021;11(1):17871. Epub 2021/09/11. doi: 10.1038/s41598-021-97407-z. PubMed PMID: 34504208; PMCID: PMC8429418 Technologies Inc. Theralase Technologies Inc. has no interest in

commercializing the software tool, nor this particular indication. Hence, no conflict of interest is present. The remaining authors declare no competing interests.

21.   Dimofte A, Finlay JC, Sharikova AV, Cengel KA, Ahn P, Busch TM, Zhu TC. Determination of tissue optical properties in PDT treated Head & Neck patients. Proc SPIE Int Soc Opt Eng. 2014;8926. Epub 2014/02/01. doi: 10.1117/12.2037831. PubMed PMID: 25999648; PMCID: PMC4437641.

22.   Kim MM, Darafsheh A, Ahmad M, Finlay JC, Zhu TC. PDT Dose Dosimeter for Pleural Photodynamic Therapy. Proc SPIE Int Soc Opt Eng. 2016;9694:96940y. Epub 2016/04/08. doi: 10.1117/12.2213401. PubMed PMID: 27053825; PMCID: PMC4819254.

23.   Trindade AC, De Figueiredo JA, Steier L, Weber JB. Photodynamic therapy in endodontics: a literature review. Photomed Laser Surg. 2015;33(3):175-82. Epub 2015/02/27. doi: 10.1089/pho.2014.3776. PubMed PMID: 25719896.

24.   Kumar V, Sinha J, Verma N, Nayan K, Saimbi CS, Tripathi AK. Scope of photodynamic therapy in periodontics. Indian J Dent Res. 2015;26(4):439-42. Epub 2015/10/21. doi: 10.4103/0970-9290.167636. PubMed PMID: 26481895.

25.   Khammissa RA, Feller L, Meyerov R, Lemmer J. Peri-implant mucositis and peri-implantitis: bacterial infection. Sadj. 2012;67(2):70, 2-4. Epub 2012/11/30. PubMed PMID: 23189895.

26.   Freire MO, Sedghizadeh PP, Schaudinn C, Gorur A, Downey JS, Choi JH, Chen W, Kook JK, Chen C, Goodman SD, Zadeh HH. Development of an Animal Model for Aggregatibacter Actinomycetemcomitans Biofilm-Mediated Oral Osteolytic Infection: A Preliminary Study. Journal of Periodontology. 2011;82(5):778-89. doi: 10.1902/jop.2010.100263. PubMed PMID: WOS:000290414700017.

27.   Ricatto LGO, Conrado LAL, Turssi CP, França FMG, Basting RT, Amaral FLB. Comparative evaluation of photodynamic therapy using LASER or light emitting diode on cariogenic bacteria: An in vitro study. Eur J Dent. 2014;8(4):509-14. Epub 2014/12/17. doi: 10.4103/1305-7456.143634. PubMed PMID: 25512733; PMCID: PMC4253108.

28.   Zhu TC, Sun H, Ong YH, Morales RH, Dimofte A, Busch T, Singhal S, Cengel KA. Real-time PDT Dose Dosimetry for Pleural Photodynamic Therapy. Proc SPIE Int Soc Opt Eng. 2022;11940. Epub 2022/05/17. doi: 10.1117/12.2612188. PubMed PMID: 35573026; PMCID: PMC9104001.

29.   Ong YH, Zhu Y, Zhu TC. Validation of tissue optical properties measurement using diffuse reflectance spectroscopy (DRS). Proc SPIE Int Soc Opt Eng. 2019;10860. Epub 2019/05/07. doi: 10.1117/12.2513558. PubMed PMID: 31057197; PMCID: PMC6497391.

30.   Issa JPM, Trawitzki BF, Ervolino E, Macedo AP, Lilge L. Low-intensity laser therapy efficacy evaluation in FVB mice subjected to acute and chronic arthritis. Lasers Med Sci. 2017;32(6):1269-77. Epub 2017/06/01. doi: 10.1007/s10103-017-2235-5. PubMed PMID: 28560473.

31.   Moriyama Y, Moriyama EH, Blackmore K, Akens MK, Lilge L. In vivo study of the inflammatory modulating effects of low-level laser therapy on iNOS expression using bioluminescence imaging. Photochem Photobiol. 2005;81(6):1351-5. Epub 2005/08/04. doi: 10.1562/2005-02-28-ra-450. PubMed PMID: 16076245.

32.   Moriyama Y, Nguyen J, Akens M, Moriyama EH, Lilge L. In vivo effects of low level laser therapy on inducible nitric oxide synthase. Lasers Surg Med. 2009;41(3):227-31. Epub 2009/03/18. doi: 10.1002/lsm.20745. PubMed PMID: 19291752.

33.   Sourvanos D, Poon J, Lander B, Sarmiento H, Carroll J, Zhu TC, Fiorellini JP. Improving Titanium Implant Stability with Photobiomodulation: A Review and Meta-Analysis of Irradiation Parameters. Photobiomodul Photomed Laser Surg. 2023;41(3):93-103. Epub 2023/03/02. doi: 10.1089/photob.2022.0161. PubMed PMID: 36856530; PMCID: PMC10024586.

34.   Nussbaum EL, Heras FL, Pritzker KP, Mazzulli T, Lilge L. Effects of low intensity laser irradiation during healing of infected skin wounds in the rat. Photonics Lasers Med. 2014;3(1):23-36. Epub 2014/02/01. doi: 10.1515/plm-2013-0049. PubMed PMID: 26225295; PMCID: PMC4516410.

35. Trawitzki BF, Lilge L, de Figueiredo FAT, Macedo AP, Issa JPM. Low-intensity laser therapy efficacy evaluation in mice subjected to acute arthritis condition. J Photochem Photobiol B. 2017;174:126-32. Epub 2017/08/05. doi: 10.1016/j.jphotobiol.2017.07.028. PubMed PMID: 28772237.

36. Arany PR. Craniofacial Wound Healing with Photobiomodulation Therapy: New Insights and Current Challenges. Journal of Dental Research. 2016;95(9):977-84. doi: 10.1177/0022034516648939. PubMed PMID: WOS:000380815400002.

37. Arany PR, Cho A, Hunt TD, Sidhu G, Shin K, Hahm E, Huang GX, Weaver J, Chen AC, Padwa BL, Hamblin MR, Barcellos-Hoff MH, Kulkarni AB, D JM. Photoactivation of endogenous latent transforming growth factor-β1 directs dental stem cell differentiation for regeneration. Sci Transl Med. 2014;6(238):238ra69. Epub 2014/05/30. doi: 10.1126/scitranslmed.3008234. PubMed PMID: 24871130; PMCID: PMC4113395.

38. Arany PR, Nayak RS, Hallikerimath S, Limaye AM, Kale AD, Kondaiah P. Activation of latent TGF-beta1 by low-power laser in vitro correlates with increased TGF-beta1 levels in laser-enhanced oral wound healing. Wound Repair Regen. 2007;15(6):866-74. Epub 2007/11/22. doi: 10.1111/j.1524-475X.2007.00306.x. PubMed PMID: 18028135.

39. Arany PRC, A.C-H.; Hunt, T.H.; Mooney, D.J.; Hamblin, M. Role of ROS-mediated TGF beta activation in laser photobiomodulation,. Proc SPIE 7165, Mechanisms for Low-Light Therapy IV, 71650C (18 February 2009). 2009. doi: 10.1117/12.809839.

40. Finnson KW, Arany PR, Philip A. Transforming Growth Factor Beta Signaling in Cutaneous Wound Healing: Lessons Learned from Animal Studies. Adv Wound Care (New Rochelle). 2013;2(5):225-37. Epub 2014/04/25. doi: 10.1089/wound.2012.0419. PubMed PMID: 24761336; PMCID: PMC3676658.

41. Hosseinpour S, Fekrazad R, Arany PR, Ye Q. Molecular impacts of photobiomodulation on bone regeneration: A systematic review. Prog Biophys Mol Biol. 2019;149:147-59. Epub 2019/04/20. doi: 10.1016/j.pbiomolbio.2019.04.005. PubMed PMID: 31002851.

42.   Khan I, Rahman SU, Tang E, Engel K, Hall B, Kulkarni AB, Arany PR. Accelerated burn wound healing with photobiomodulation therapy involves activation of endogenous latent TGF-β1. Sci Rep. 2021;11(1):13371. Epub 2021/06/30. doi: 10.1038/s41598-021-92650-w. PubMed PMID: 34183697; PMCID: PMC8238984.

43.   Sourvanos D, Lander B, Sarmiento H, Carroll J, Hall RD, Zhu TC, Fiorellini JP. Photobiomodulation in dental extraction therapy: Postsurgical pain reduction and wound healing. J Am Dent Assoc. 2023;154(7):567-79. Epub 2023/05/19. doi: 10.1016/j.adaj.2023.03.004. PubMed PMID: 37204376.

44.   Rahman SU, Mosca RC, Govindool Reddy S, Nunez SC, Andreana S, Mang TS, Arany PR. Learning from clinical phenotypes: Low-dose biophotonics therapies in oral diseases. Oral Diseases. 2018;24(1-2):261-76. doi: 10.1111/odi.12796; PMCID: AxcanbiolitecDusaNovartisPharmacyclics Photocure.

45.   Silveira FM, Schmidt TR, Neumann B, Rosset C, Zanella VG, Maahs GS, Martins MAT, Arany P, Wagner VP, Lopes MA, Santos-Silva AR, Martins MD. Impact of photobiomodulation in a patient-derived xenograft model of oral squamous cell carcinoma. Oral Diseases. doi: 10.1111/odi.13967. PubMed PMID: WOS:000678192900001.

46.   Tang E, Arany P. Photobiomodulation and implants: implications for dentistry. Journal of Periodontal and Implant Science. 2013;43(6):262-8. doi: 10.5051/jpis.2013.43.6.262. PubMed PMID: WOS:000342344200003.

47.   Tang E, Khan I, Andreana S, Arany PR. Laser-activated transforming growth factor-β1 induces human β-defensin 2: implications for laser therapies for periodontitis and peri-implantitis. J Periodontal Res. 2017;52(3):360-7. Epub 2016/07/12. doi: 10.1111/jre.12399. PubMed PMID: 27396269; PMCID: PMC5226924.

48.   Hamblin MR. Mechanisms and applications of the anti-inflammatory effects of photobiomodulation. AIMS Biophys. 2017;4(3):337-61. Epub 2017/07/28. doi: 10.3934/biophy.2017.3.337. PubMed PMID: 28748217; PMCID: PMC5523874.

49.   Hamblin MR. Mechanisms and Mitochondrial Redox Signaling in Photobiomodulation. Photochem Photobiol. 2018;94(2):199-212. Epub 2017/11/23. doi: 10.1111/php.12864. PubMed PMID: 29164625; PMCID: PMC5844808.

50.   da Silva TG, Ribeiro RS, Mencalha AL, de Souza Fonseca A. Photobiomodulation at molecular, cellular, and systemic levels. Lasers Med Sci. 2023;38(1):136. Epub 2023/06/13. doi: 10.1007/s10103-023-03801-6. PubMed PMID: 37310556.

51.   Karu TI, Kolyakov SF. Exact action spectra for cellular responses relevant to phototherapy. Photomed Laser Surg. 2005;23(4):355-61. Epub 2005/09/08. doi: 10.1089/pho.2005.23.355. PubMed PMID: 16144476.

52.   Karu TI. Multiple roles of cytochrome c oxidase in mammalian cells under action of red and IR-A radiation. IUBMB Life. 2010;62(8):607-10. Epub 2010/08/04. doi: 10.1002/iub.359. PubMed PMID: 20681024.

53.   Zecha JA, Raber-Durlacher JE, Nair RG, Epstein JB, Sonis ST, Elad S, Hamblin MR, Barasch A, Migliorati CA, Milstein DM, Genot MT, Lansaat L, van der Brink R, Arnabat-Dominguez J, van der Molen L, Jacobi I, van Diessen J, de Lange J, Smeele LE, Schubert MM, Bensadoun RJ. Low level laser therapy/photobiomodulation in the management of side effects of chemoradiation therapy in head and neck cancer: part 1: mechanisms of action, dosimetric, and safety considerations. Support Care Cancer. 2016;24(6):2781-92. Epub 2016/03/18. doi: 10.1007/s00520-016-3152-z. PubMed PMID: 26984240; PMCID: PMC4846477.

54.   Wong-Riley MT, Liang HL, Eells JT, Chance B, Henry MM, Buchmann E, Kane M, Whelan HT. Photobiomodulation directly benefits primary neurons functionally inactivated by toxins: role of

cytochrome c oxidase. J Biol Chem. 2005;280(6):4761-71. Epub 2004/11/24. doi: 10.1074/jbc.M409650200. PubMed PMID: 15557336.

55.   Peplow PV, Chung TY, Baxter GD. Laser photostimulation (660 nm) of wound healing in diabetic mice is not brought about by ameliorating diabetes. Lasers Surg Med. 2012;44(1):26-9. Epub 2011/11/24. doi: 10.1002/lsm.21133. PubMed PMID: 22109569.

56.   Karu T. Mitochondrial mechanisms of photobiomodulation in context of new data about multiple roles of ATP. Photomed Laser Surg. 2010;28(2):159-60. Epub 2010/04/09. doi: 10.1089/pho.2010.2789. PubMed PMID: 20374017.

57.   Chellini F, Sassoli C, Nosi D, Deledda C, Tonelli P, Zecchi-Orlandini S, Formigli L, Giannelli M. Low pulse energy Nd:YAG laser irradiation exerts a biostimulative effect on different cells of the oral microenvironment: "an in vitro study". Lasers Surg Med. 2010;42(6):527-39. Epub 2010/07/28. doi: 10.1002/lsm.20861. PubMed PMID: 20662029.

58.   Ravera S, Ferrando S, Agas D, De Angelis N, Raffetto M, Sabbieti MG, Signore A, Benedicenti S, Amaroli A. 1064 nm Nd:YAG laser light affects transmembrane mitochondria respiratory chain complexes. J Biophotonics. 2019;12(9):e201900101. Epub 2019/04/30. doi: 10.1002/jbio.201900101. PubMed PMID: 31033186.

59.   Gokmenoglu C, Ozmeric N, Erguder I, Elgun S. The effect of light-emitting diode photobiomodulation on implant stability and biochemical markers in peri-implant crevicular fluid. Photomed Laser Surg. 2014;32(3):138-45. Epub 2014/02/21. doi: 10.1089/pho.2012.3473. PubMed PMID: 24552468.

60.   Brawn PR, Kwong-Hing A. Histologic comparison of light emitting diode phototherapy-treated hydroxyapatite-grafted extraction sockets: a same-mouth case study. Implant Dent. 2007;16(2):204-11. Epub 2007/06/15. doi: 10.1097/ID.0b013e318065a84c. PubMed PMID: 17563511.

61.   Pinheiro AL. Advances and perspectives on tissue repair and healing. Photomed Laser Surg. 2009;27(6):833-6. Epub 2009/12/29. doi: 10.1089/pho.2009.2716. PubMed PMID: 20035600.

62.	Huang YY, Sharma SK, Carroll J, Hamblin MR. Biphasic dose response in low level light therapy - an update. Dose Response. 2011;9(4):602-18. Epub 2011/01/01. doi: 10.2203/dose-response.11-009.Hamblin. PubMed PMID: 22461763; PMCID: PMC3315174.

63.	Rosso MPO, Buchaim DV, Pomini KT, Coletta BBD, Reis CHB, Pilon JPG, Duarte Júnior G, Buchaim RL. Photobiomodulation Therapy (PBMT) Applied in Bone Reconstructive Surgery Using Bovine Bone Grafts: A Systematic Review. Materials (Basel). 2019;12(24). Epub 2019/12/11. doi: 10.3390/ma12244051. PubMed PMID: 31817369; PMCID: PMC6947623.

64.	Zupin L, Ottaviani G, Rupel K, Biasotto M, Zacchigna S, Crovella S, Celsi F. Analgesic effect of Photobiomodulation Therapy: An in vitro and in vivo study. J Biophotonics. 2019;12(10):e201900043. Epub 2019/06/21. doi: 10.1002/jbio.201900043. PubMed PMID: 31219220.

65.	Tam SY, Tam VCW, Ramkumar S, Khaw ML, Law HKW, Lee SWY. Review on the Cellular Mechanisms of Low-Level Laser Therapy Use in Oncology. Front Oncol. 2020;10:1255. Epub 2020/08/15. doi: 10.3389/fonc.2020.01255. PubMed PMID: 32793501; PMCID: PMC7393265.

66.	Baldassarro VA, Alastra G, Lorenzini L, Giardino L, Calzà L. Photobiomodulation at Defined Wavelengths Regulates Mitochondrial Membrane Potential and Redox Balance in Skin Fibroblasts. Oxid Med Cell Longev. 2023;2023:7638223. Epub 2023/09/04. doi: 10.1155/2023/7638223. PubMed PMID: 37663921; PMCID: PMC10471456 publication of this paper.

67.	Suh S, Choi EH, Atanaskova Mesinkovska N. The expression of opsins in the human skin and its implications for photobiomodulation: A Systematic Review. Photodermatol Photoimmunol Photomed. 2020;36(5):329-38. Epub 2020/05/21. doi: 10.1111/phpp.12578. PubMed PMID: 32431001; PMCID: PMC7674233.

68.	Bonewald LF, Mundy GR. Role of transforming growth factor-beta in bone remodeling. Clin Orthop Relat Res. 1990(250):261-76. Epub 1990/01/01. PubMed PMID: 2403492.

69.   Janssens K, ten Dijke P, Janssens S, Van Hul W. Transforming growth factor-beta1 to the bone. Endocr Rev. 2005;26(6):743-74. Epub 2005/05/20. doi: 10.1210/er.2004-0001. PubMed PMID: 15901668.

70.   Ramirez H, Patel SB, Pastar I. The Role of TGFβ Signaling in Wound Epithelialization. Adv Wound Care (New Rochelle). 2014;3(7):482-91. Epub 2014/07/18. doi: 10.1089/wound.2013.0466. PubMed PMID: 25032068; PMCID: PMC4086377.

71.   Aimetti M, Mariani GM, Ferrarotti F, Ercoli E, Liu CC, Romano F. Adjunctive efficacy of diode laser in the treatment of peri-implant mucositis with mechanical therapy: A randomized clinical trial. Clin Oral Implants Res. 2019;30(5):429-38. Epub 2019/04/02. doi: 10.1111/clr.13428. PubMed PMID: 30933384.

72.   Marin-Conde F, Castellanos-Cosano L, Pachon-Ibanez J, Serrera-Figallo MA, Gutierrez-Perez JL, Torres-Lagares D. Photobiomodulation with low-level laser therapy reduces oral mucositis caused by head and neck radio-chemotherapy: prospective randomized controlled trial. International Journal of Oral and Maxillofacial Surgery. 2019;48(7):917-23. doi: 10.1016/j.ijom.2018.12.006. PubMed PMID: WOS:000474320000010.

73.   Miranda-Silva W, da Fonseca FP, Gomes AA, Mafra ABB, Rocha V, Fregnani ER. Oral mucositis in paediatric cancer patients undergoing allogeneic hematopoietic stem cell transplantation preventively treated with professional dental care and photobiomodulation: Incidence and risk factors. International Journal of Paediatric Dentistry. 2022;32(2):251-63. doi: 10.1111/ipd.12850. PubMed PMID: WOS:000675149500001.

74.   Baxter GD, Liu L, Petrich S, Gisselman AS, Chapple C, Anders JJ, Tumilty S. Low level laser therapy (Photobiomodulation therapy) for breast cancer-related lymphedema: a systematic review. BMC Cancer. 2017;17(1):833. Epub 2017/12/09. doi: 10.1186/s12885-017-3852-x. PubMed PMID: 29216916; PMCID: PMC5719569.

75.   Galiano-Castillo N, Liu LZ, Lozano-Lozano M, Tumilty S, Cantarero-Villanueva I, Baxter GD. Acute and cumulative benefits of Photobiomodulation for xerostomia: A systematic review and meta-analysis. Oral Diseases. 2021;27(5):1115-26. doi: 10.1111/odi.13648. PubMed PMID: WOS:000576539400001.

76.   Rosero KAV, Sampaio RMF, Deboni MCZ, Corrêa L, Marques MM, Ferraz EP, da Graça Naclério-Homem M. Photobiomodulation as an adjunctive therapy for alveolar socket preservation: a preliminary study in humans. Lasers Med Sci. 2020;35(8):1711-20. Epub 2020/01/24. doi: 10.1007/s10103-020-02962-y. PubMed PMID: 31970564.

77.   Hadad H, Santos AFP, de Jesus LK, Poli PP, Mariano RC, Theodoro LH, Maiorana C, Souza F. Photobiomodulation Therapy Improves Postoperative Pain and Edema in Third Molar Surgeries: A Randomized, Comparative, Double-Blind, and Prospective Clinical Trial. J Oral Maxillofac Surg. 2022;80(1):37.e1-.e12. Epub 2021/10/18. doi: 10.1016/j.joms.2021.08.267. PubMed PMID: 34656515.

78.   Le HT, Huynh NC, Nguyen-Ho QA, Nguyen TT, Le SH, Nguyen LT. Effect of Photobiomodulation Therapy on Reducing Acute Pain and Inflammation Following Surgical Removal of Impacted Mandibular Third Molars: A Randomized, Split-Mouth Clinical Trial. Photobiomodul Photomed Laser Surg. 2022;40(4):245-51. Epub 2022/03/31. doi: 10.1089/photob.2021.0110. PubMed PMID: 35353636.

79.   Vande A, Sanyal PK, Nilesh K. Effectiveness of the photobiomodulation therapy using low-level laser around dental implants: A systematic review and meta-analysis. Dental and medical problems. 2022. doi: 10.17219/dmp/143242.

80.   Hadad H, Santos AFP, de Jesus LK, Poli PP, Mariano RC, Theodoro LH, Maiorana C, Souza FÁ. Photobiomodulation Therapy Improves Postoperative Pain and Edema in Third Molar Surgeries: A Randomized, Comparative, Double-Blind, and Prospective Clinical Trial. Journal of Oral and Maxillofacial Surgery. 2022;80(1):37.e1-.e12. doi: 10.1016/j.joms.2021.08.267; PMCID: dfl ind com(Brazil)

mantecorp farmasa lab(Brazil).

81.   Al-Askar MH, Abdullatif FA, Alshihri AA, Ahmed A, Divakar DD, Almoharib H, Alzoman H. Comparison of photobiomodulation and photodynamic therapy as adjuncts to mechanical debridement for the treatment of peri-implantitis. Technology and Health Care. 2022;30(2):389-98. doi: 10.3233/THC-213062.

82.   Qu C, Luo F, Hong G, Wan Q. Effects of photobiomodulation therapy on implant stability and postoperative recovery: a systematic review and meta-analysis. British Journal of Oral and Maxillofacial Surgery. 2022. doi: 10.1016/j.bjoms.2022.01.014.

83.   Morshedzadeh G, Aslroosta H, Vafaei M. Effect of GaAlAs 940 nm Photobiomodulation on palatal wound healing after free gingival graft surgery: a split mouth randomized controlled clinical trial. Bmc Oral Health. 2022;22(1). doi: 10.1186/s12903-022-02229-8. PubMed PMID: WOS:000801183800001.

84.   da Silva TMV, Melo TS, de Alencar RC, Pereira JRD, Leão JC, Silva IHM, Gueiros LA. Photobiomodulation for mucosal repair in patients submitted to dental extraction after head and neck radiation therapy: a double-blind randomized pilot study. Support Care Cancer. 2021;29(3):1347-54. Epub 2020/07/10. doi: 10.1007/s00520-020-05608-5. PubMed PMID: 32642953.

85.   Isolan C, Kinalski MD, Leão OA, Post LK, Isolan TM, Dos Santos MB. Photobiomodulation therapy reduces postoperative pain after third molar extractions: A randomized clinical trial. Med Oral Patol Oral Cir Bucal. 2021;26(3):e341-e8. Epub 2020/12/20. doi: 10.4317/medoral.24228. PubMed PMID: 33340081; PMCID: PMC8141316 third parties (government, commercial, private foundation, etc.) were disclosed for any aspect of the submitted work (including but not limited to grants, data monitoring board, study design, manuscript preparation, statistical analysis, etc.).

86.   Soheilifar S, Fathi H, Naghdi N. Photobiomodulation therapy as a high potential treatment modality for COVID-19. Lasers in Medical Science. 2021;36(5):935-8. doi: 10.1007/s10103-020-03206-9.

87.   Scarano A, Lorusso F, Postiglione F, Mastrangelo F, Petrini M. Photobiomodulation Enhances the Healing of Postextraction Alveolar Sockets: A Randomized Clinical Trial With Histomorphometric Analysis and Immunohistochemistry. Journal of Oral and Maxillofacial Surgery. 2021;79(1):57.e1-.e12. doi: 10.1016/j.joms.2020.09.008.

88.   Zayed SM, Noureldin MG, Alshimy A, Hakim AAA. Outcomes of Mandibular Overdentures Supported by Four Short Implants Combined with Photobiomodulation Therapy. International Journal of Oral and Maxillofacial Implants. 2021;36(2):379-87. doi: 10.11607/jomi.8909.

89.   Lakshmi MR, Nvs Sruthima G, Penmetsa GS, Ramesh KSV, Mohan Kumar P, Bypalli V. Photobiomodulation in management of periodontitis and periimplantitis - a review. European Journal of Molecular and Clinical Medicine. 2021;8(3):3109-18.

90.   Salehpour F, Gholipour-Khalili S, Farajdokht F, Kamari F, Walski T, Hamblin MR, Diduro JO, Cassano P. Therapeutic potential of intranasal photobiomodulation therapy for neurological and neuropsychiatric disorders: A narrative review. Reviews in the Neurosciences. 2020;31(3):269-86. doi: 10.1515/revneuro-2019-0063.

91.   Zayed S, Hakim AA. Clinical efficacy of photobiomodulation on dental implant osseointegration: A systematic review. Saudi Journal of Medicine and Medical Sciences. 2020;8(2):80-6. doi: 10.4103/sjmms.sjmms_410-19.

92.   Hosseinpour S, Tunér J, Fekrazad R. Photobiomodulation in Oral Surgery: A Review. Photobiomodul Photomed Laser Surg. 2019;37(12):814-25. Epub 2019/11/22. doi: 10.1089/photob.2019.4712. PubMed PMID: 31750798.

93.   Bitencourt FV, Cardoso De David S, Schutz JDS, Otto Kirst Neto A, Visioli F, Fiorini T. Minimizing patient morbidity after free gingival graft harvesting:A triple-blind randomized-controlled clinical trial. Clin Oral Implants Res. 2022;33(6):622-33. Epub 2022/03/20. doi: 10.1111/clr.13923. PubMed PMID: 35305280.

94.	de Carvalho MM, Hidalgo MAR, Scarel-Caminaga RM, Ribeiro NV, Sperandio FF, Pigossi SC, de Carli ML. Photobiomodulation of gingival lesions resulting from autoimmune diseases: systematic review and meta-analysis. Clinical Oral Investigations. 2022;26(5):3949-64. doi: 10.1007/s00784-021-04362-0. PubMed PMID: WOS:000742257900001.

95.	Peron D, Bergamo A, Prates R, Vieira SS, de Tarso Camillo de Carvalho P, Serra AJ. Photodynamic antimicrobial chemotherapy has an overt killing effect on periodontal pathogens? A systematic review of experimental studies. Lasers Med Sci. 2019;34(8):1527-34. Epub 2019/05/22. doi: 10.1007/s10103-019-02806-4. PubMed PMID: 31111263.

96.	Ribeiro LN, de Lima M, Carvalho AT, de Albuquerque RF, Leao JC, Silva IHM. Evaluation of the salivary function of patients in treatment with radiotherapy for head and neck cancer submitted to photobiomodulation. Medicina Oral Patologia Oral Y Cirugia Bucal. 2021;26(1):E14-E20. doi: 10.4317/medoral.23912. PubMed PMID: WOS:000604964100002.

97.	Zayed SM, Hakim AAA. Clinical Efficacy of Photobiomodulation on Dental Implant Osseointegration: A Systematic Review. Saudi J Med Med Sci. 2020;8(2):80-6. Epub 2020/06/27. doi: 10.4103/sjmms.sjmms_410_19. PubMed PMID: 32587488; PMCID: PMC7305678.

98.	López-Ramírez M, Vílchez-Pérez MÁ, Gargallo-Albiol J, Arnabat-Domínguez J, Gay-Escoda C. Efficacy of low-level laser therapy in the management of pain, facial swelling, and postoperative trismus after a lower third molar extraction. A preliminary study. Lasers in Medical Science. 2012;27(3):559-66. doi: 10.1007/s10103-011-0936-8.

99.	Eshghpour M, Ahrari F, Takallu M. Is Low-Level Laser Therapy Effective in the Management of Pain and Swelling After Mandibular Third Molar Surgery? J Oral Maxillofac Surg. 2016;74(7):1322.e1-8. Epub 2016/04/08. doi: 10.1016/j.joms.2016.02.030. PubMed PMID: 27055228.

100.	Monea A, Beresescu G, Boeriu S, Tibor M, Popsor S, Antonescu DM. Erratum to: Bone healing after low-level laser application in extraction sockets grafted with allograft material and covered with a

resorbable collagen dressing: a pilot histological evaluation. BMC Oral Health. 2016;16:16. Epub 2016/02/11. doi: 10.1186/s12903-016-0173-4. PubMed PMID: 26860738; PMCID: PMC4748477.

101.   Nica DF, Heredea ER, Todea DCM. Alveolus soft and bone tissue regeneration after laser biomodulation - a histological study. Rom J Morphol Embryol. 2019;60(4):1269-73. Epub 2019/01/01. PubMed PMID: 32239104.

102.   Romão MM, Marques MM, Cortes AR, Horliana AC, Moreira MS, Lascala CA. Micro-computed tomography and histomorphometric analysis of human alveolar bone repair induced by laser phototherapy: a pilot study. Int J Oral Maxillofac Surg. 2015;44(12):1521-8. Epub 2015/09/19. doi: 10.1016/j.ijom.2015.08.989. PubMed PMID: 26381208.

103.   Abdel-Alim HM, Abdel-Dayem H, Mustafa ZA, Bayoumi A, Jan A, Jadu F. A Comparative Study of the Effectiveness of Immediate Versus Delayed Photobiomodulation Therapy in Reducing the Severity of Postoperative Inflammatory Complications. Photomed Laser Surg. 2015;33(9):447-51. Epub 2015/09/04. doi: 10.1089/pho.2015.3923. PubMed PMID: 26332915.

104.   Paschoal MA, Santos-Pinto L. Therapeutic effects of low-level laser therapy after premolar extraction in adolescents: a randomized double-blind clinical trial. Photomed Laser Surg. 2012;30(9):559-64. Epub 2012/08/09. doi: 10.1089/pho.2012.3243. PubMed PMID: 22870960.

105.   Landucci A, Wosny AC, Uetanabaro LC, Moro A, Araujo MR. Efficacy of a single dose of low-level laser therapy in reducing pain, swelling, and trismus following third molar extraction surgery. Int J Oral Maxillofac Surg. 2016;45(3):392-8. Epub 2015/12/23. doi: 10.1016/j.ijom.2015.10.023. PubMed PMID: 26691932.

106.   Sierra SO, Deana AM, Bussadori SK, da Mota AC, Ferrari RA, do Vale KL, Fernandes KP. Choosing between intraoral or extraoral, red or infrared laser irradiation after impacted third molar extraction. Lasers Surg Med. 2016;48(5):511-8. Epub 2016/02/13. doi: 10.1002/lsm.22488. PubMed PMID: 26868520.

107.	Sandell JL, Zhu TC. A review of in-vivo optical properties of human tissues and its impact on PDT. J Biophotonics. 2011;4(11-12):773-87. Epub 2011/12/15. doi: 10.1002/jbio.201100062. PubMed PMID: 22167862; PMCID: PMC3321368.

108.	Dimofte A, Finlay JC, Liang X, Zhu TC. Determination of optical properties in heterogeneous turbid media using a cylindrical diffusing fiber. Phys Med Biol. 2012;57(19):6025-46. Epub 2012/09/13. doi: 10.1088/0031-9155/57/19/6025. PubMed PMID: 22968172; PMCID: PMC3444568.

109.	Dimofte A, Finlay JC, Zhu TC. A method for determination of the absorption and scattering properties interstitially in turbid media. Phys Med Biol. 2005;50(10):2291-311. Epub 2005/05/07. doi: 10.1088/0031-9155/50/10/008. PubMed PMID: 15876668; PMCID: PMC4467592.

110.	Ong YH, Kim MM, Finlay JC, Dimofte A, Singhal S, Glatstein E, Cengel KA, Zhu TC. PDT dose dosimetry for Photofrin-mediated pleural photodynamic therapy (pPDT). Phys Med Biol. 2017;63(1):015031. Epub 2017/11/07. doi: 10.1088/1361-6560/aa9874. PubMed PMID: 29106380; PMCID: PMC5952607.

111.	Zhu TC, Finlay JC, Dimofte A, Hahn SM. Light Dosimetry at Tissue Surfaces for Oblique Incident Circular Fields. Proc SPIE Int Soc Opt Eng. 2004;5315:113-24. Epub 2004/01/01. doi: 10.1117/12.529827. PubMed PMID: 26139956; PMCID: PMC4485452.

112.	Dimofte A, Sharikova AV, Meo JL, Simone CB, 2nd, Friedberg JS, Zhu TC. Light dosimetry and dose verification for pleural PDT. Proc SPIE Int Soc Opt Eng. 2013;8568. Epub 2013/02/02. doi: 10.1117/12.2004941. PubMed PMID: 25999646; PMCID: PMC4437736.

113.	Morales RDH, Hong Ong Y, Finlay J, Dimofte A, Simone CB, Friedberg JS, Busch TM, Cengel KA, Zhu TC. In vivo spectroscopic evaluation of human tissue optical properties and hemodynamics during HPPH-mediated photodynamic therapy of pleural malignancies. J Biomed Opt. 2022;27(10). Epub 2022/11/02. doi: 10.1117/1.Jbo.27.10.105006. PubMed PMID: 36316298; PMCID: PMC9621284.

114.	Ong YH, Dimofte A, Kim MM, Finlay JC, Sheng T, Singhal S, Cengel KA, Yodh AG, Busch TM, Zhu TC. Reactive Oxygen Species Explicit Dosimetry for Photofrin-mediated Pleural Photodynamic

Therapy. Photochem Photobiol. 2020;96(2):340-8. Epub 2019/11/16. doi: 10.1111/php.13176. PubMed PMID: 31729774; PMCID: PMC7299188.

115.   Choe R. Diffuse optical tomography and spectroscopy of breast cancer and fetal brain. Medical physics. 2005;32(10):3230-. doi: 10.1118/1.2047847.

116.   Hu Y, Finlay JC, Zhu TC. The design of a robotic multichannel platform for photodynamic therapy. Proc SPIE Int Soc Opt Eng. 2009;7380:738049. Epub 2009/07/13. doi: 10.1117/12.823069. PubMed PMID: 25983368; PMCID: PMC4430865.

117.   Couso-Queiruga E, Weber HA, Garaicoa-Pazmino C, Barwacz C, Kalleme M, Galindo-Moreno P, Avila-Ortiz G. Influence of healing time on the outcomes of alveolar ridge preservation using a collagenated bovine bone xenograft: A randomized clinical trial. J Clin Periodontol. 2023;50(2):132-46. Epub 2022/11/09. doi: 10.1111/jcpe.13744. PubMed PMID: 36345818; PMCID: PMC10100450.

118.   Saleh MHA, Couso-Queiruga E, Ravidà A, Dukka H, Paiva De Andrade N, Ou A, Wang HL. Impact of the periodontal phenotype in premolar and molar sites on bone loss following full-thickness mucoperiosteal flap: A 1-year prospective clinical trial. J Periodontol. 2022;93(7):966-76. Epub 2022/02/10. doi: 10.1002/jper.21-0591. PubMed PMID: 35137413.

119.   González Rodríguez JL, Sánchez Tabernero A, Sánchez Hernando VJ, Vega Cruz MS. PBM in traumatologic surgery at Zamora Hospital, Spain: Future improvements. Transfusion Medicine. 2017;27:37-8. doi: 10.1111/tme.12417.

120.   González-Martín O, Veltri M. Cone beam analysis of the buccal bone associated with a dental implant: A tridimensional assessment case report. Quintessence Int. 2017;48(4):339-44. Epub 2017/03/16. doi: 10.3290/j.qi.a37798. PubMed PMID: 28294197.

121.   Couso-Queiruga E, Barboza EP, Avila-Ortiz G, Gonzalez-Martin O, Chambrone L, Rodrigues DM. Relationship between supracrestal soft tissue dimensions and other periodontal phenotypic features: A cross-sectional study. J Periodontol. 2023;94(8):944-55. Epub 2023/02/18. doi: 10.1002/jper.22-0434. PubMed PMID: 36797817.

122.   Couso-Queiruga E, Graham ZA, Peter T, Gonzalez-Martin O, Galindo-Moreno P, Avila-Ortiz G. Effect of periodontal phenotype characteristics on post-extraction dimensional changes of the alveolar ridge: A prospective case series. J Clin Periodontol. 2023;50(5):694-706. Epub 2023/01/17. doi: 10.1111/jcpe.13781. PubMed PMID: 36644815.

123.   Couso-Queiruga E, Tattan M, Ahmad U, Barwacz C, Gonzalez-Martin O, Avila-Ortiz G. Assessment of gingival thickness using digital file superimposition versus direct clinical measurements. Clin Oral Investig. 2021;25(4):2353-61. Epub 2020/09/01. doi: 10.1007/s00784-020-03558-0. PubMed PMID: 32865627.

124.   Jacques SL. Optical properties of biological tissues: a review. Phys Med Biol. 2013;58(11):R37-61. Epub 2013/05/15. doi: 10.1088/0031-9155/58/11/r37. PubMed PMID: 23666068.

125.   Kyllar M, Stembírek J, Putnová I, Stehlík L, Odehnalová S, Buchtová M. Radiography, computed tomography and magnetic resonance imaging of craniofacial structures in pig. Anat Histol Embryol. 2014;43(6):435-52. Epub 2013/11/23. doi: 10.1111/ahe.12095. PubMed PMID: 24261592.

126.   Mahdy MAA. Correlation between computed tomography, magnetic resonance imaging and cross-sectional anatomy of the head of the guinea pig (Cavia porcellus, Linnaeus 1758). Anat Histol Embryol. 2022;51(1):51-61. Epub 2021/11/03. doi: 10.1111/ahe.12752. PubMed PMID: 34726282.

127.   Robertson N, Schook LB, Schachtschneider KM. Porcine cancer models: potential tools to enhance cancer drug trials. Expert Opin Drug Discov. 2020;15(8):893-902. Epub 2020/05/08. doi: 10.1080/17460441.2020.1757644. PubMed PMID: 32378979.

128.   Saalfrank A, Janssen KP, Ravon M, Flisikowski K, Eser S, Steiger K, Flisikowska T, Müller-Fliedner P, Schulze É, Brönner C, Gnann A, Kappe E, Böhm B, Schade B, Certa U, Saur D, Esposito I, Kind A, Schnieke A. A porcine model of osteosarcoma. Oncogenesis. 2016;5(3):e210. Epub 2016/03/15. doi: 10.1038/oncsis.2016.19. PubMed PMID: 26974205; PMCID: PMC4815050.

129.   Sasaki R, Watanabe Y, Yamato M, Aoki S, Okano T, Ando T. Surgical anatomy of the swine face. Laboratory Animals. 2010;44(4):359-63. doi: 10.1258/la.2010.009127. PubMed PMID: 20696789.

130.	Schook LB, Collares TV, Hu W, Liang Y, Rodrigues FM, Rund LA, Schachtschneider KM, Seixas FK, Singh K, Wells KD, Walters EM, Prather RS, Counter CM. A Genetic Porcine Model of Cancer. PLoS One. 2015;10(7):e0128864. Epub 2015/07/02. doi: 10.1371/journal.pone.0128864. PubMed PMID: 26132737; PMCID: PMC4488487.

131.	Shen W, Teo KYC, Wood JPM, Vaze A, Chidlow G, Ao J, Lee SR, Yam MX, Cornish EE, Fraser-Bell S, Casson RJ, Gillies MC. Preclinical and clinical studies of photobiomodulation therapy for macular oedema. Diabetologia. 2020;63(9):1900-15. doi: 10.1007/s00125-020-05189-2.

132.	Štembírek J, Kyllar M, Putnová I, Stehlík L, Buchtová M. The pig as an experimental model for clinical craniofacial research. Lab Anim. 2012;46(4):269-79. Epub 2012/09/13. doi: 10.1258/la.2012.012062. PubMed PMID: 22969144.

133.	Swindle MM, Smith AC. Swine in the laboratory: surgery, anesthesia, imaging, and experimental techniques. Third ed: CRC Press; 2015.

134.	Verdonck HWD, Meijer GJ, Laurin T, Nieman FHM, Stoll C, Riediger D, Stoelinga PJW, de Baat C. Assessment of vascularity in irradiated and nonirradiated maxillary and mandibular minipig alveolar bone using laser Doppler Flowmetry. International Journal of Oral & Maxillofacial Implants. 2007;22(5):774-8. PubMed PMID: WOS:000250345600011.

135.	Xu C, Wu S, Schook LB, Schachtschneider KM. Translating Human Cancer Sequences Into Personalized Porcine Cancer Models. Front Oncol. 2019;9:105. Epub 2019/03/16. doi: 10.3389/fonc.2019.00105. PubMed PMID: 30873383; PMCID: PMC6401626.

136.	Araujo DV, Oliva M, Li K, Fazelzad R, Liu ZA, Siu LL. Contemporary dose-escalation methods for early phase studies in the immunotherapeutics era. Eur J Cancer. 2021;158:85-98. Epub 2021/10/18. doi: 10.1016/j.ejca.2021.09.016. PubMed PMID: 34656816.

137.	Hansen AR, Graham DM, Pond GR, Siu LL. Phase 1 trial design: is 3 + 3 the best? Cancer Control. 2014;21(3):200-8. Epub 2014/06/24. doi: 10.1177/107327481402100304. PubMed PMID: 24955703.

138.   Le Tourneau C, Lee JJ, Siu LL. Dose escalation methods in phase I cancer clinical trials. J Natl Cancer Inst. 2009;101(10):708-20. Epub 2009/05/14. doi: 10.1093/jnci/djp079. PubMed PMID: 19436029; PMCID: PMC2684552.

139.   Petrov D, Burrell JC, Browne KD, Laimo FA, Roberts SE, Ali ZS, Cullen DK. Neurorrhaphy in Presence of Polyethylene Glycol Enables Immediate Electrophysiological Conduction in Porcine Model of Facial Nerve Injury. Front Surg. 2022;9:811544. Epub 2022/03/29. doi: 10.3389/fsurg.2022.811544. PubMed PMID: 35341161; PMCID: PMC8948462.

140.   Burrell JC, Bhatnagar D, Brown DP, Murthy NS, Dutton J, Browne KD, Laimo FA, Ali ZS, Rosen JM, Kaplan HM, Kohn J, Cullen DK. Tyrosine-derived polycarbonate nerve guidance tubes elicit proregenerative extracellular matrix deposition when used to bridge segmental nerve defects in swine. J Biomed Mater Res A. 2021;109(7):1183-95. Epub 2020/09/29. doi: 10.1002/jbm.a.37110. PubMed PMID: 32985789.

141.   Sculean A, Gruber R, Bosshardt DD. Soft tissue wound healing around teeth and dental implants. Journal of Clinical Periodontology. 2014;41:S6-S22. doi: 10.1111/jcpe.12206. PubMed PMID: WOS:000332956100002.

142.   Burrell JC, Browne KD, Dutton JL, Laimo FA, Das S, Brown DP, Roberts S, Petrov D, Ali Z, Ledebur HC, Rosen JM, Kaplan HM, Wolf JA, Smith DH, Chen HI, Cullen DK. A Porcine Model of Peripheral Nerve Injury Enabling Ultra-Long Regenerative Distances: Surgical Approach, Recovery Kinetics, and Clinical Relevance. Neurosurgery. 2020;87(4):833-46. Epub 2020/05/12. doi: 10.1093/neuros/nyaa106. PubMed PMID: 32392341.

143.   Fuerst G, Gruber R, Tangl S, Sanroman F, Watzek G. Effects of fibrin sealant protein concentrate with and without platelet-released growth factors on bony healing of cortical mandibular defects. An experimental study in minipigs. Clin Oral Implants Res. 2004;15(3):301-7. Epub 2004/05/15. doi: 10.1046/j.1600-0501.2003.01007.x. PubMed PMID: 15142092.

144.   Saulacic N, Bosshardt DD, Jensen SS, Miron RJ, Gruber R, Buser D. Impact of bone graft harvesting techniques on bone formation and graft resorption: a histomorphometric study in the mandibles of minipigs. Clin Oral Implants Res. 2015;26(4):383-91. Epub 2014/02/20. doi: 10.1111/clr.12357. PubMed PMID: 24547966.

145.   Troeltzsch M, Zeiter S, Arens D, Nehrbass D, Probst FA, Liokatis P, Ehrenfeld M, Otto S. Chronic Periodontal Infection and Not Iatrogenic Interference Is the Trigger of Medication-Related Osteonecrosis of the Jaw: Insights from a Large Animal Study (PerioBRONJ Pig Model). Medicina (Kaunas). 2023;59(5). Epub 2023/05/27. doi: 10.3390/medicina59051000. PubMed PMID: 37241232; PMCID: PMC10222433.

146.   Wanasathop A, Zhong C, Nimmansophon P, Murawsky M, Li SK. Characterization of Porcine Gingiva for Drug Absorption. J Pharm Sci. 2023;112(4):1032-40. Epub 2022/11/24. doi: 10.1016/j.xphs.2022.11.016. PubMed PMID: 36417948; PMCID: PMC10033335.

147.   Ash C, Dubec M, Donne K, Bashford T. Effect of wavelength and beam width on penetration in light-tissue interaction using computational methods. Lasers Med Sci. 2017;32(8):1909-18. Epub 2017/09/14. doi: 10.1007/s10103-017-2317-4. PubMed PMID: 28900751; PMCID: PMC5653719.

148.   Chung H, Dai T, Sharma SK, Huang YY, Carroll JD, Hamblin MR. The nuts and bolts of low-level laser (light) therapy. Ann Biomed Eng. 2012;40(2):516-33. Epub 2011/11/03. doi: 10.1007/s10439-011-0454-7. PubMed PMID: 22045511; PMCID: PMC3288797.

149.   Zecha JAEM, Raber-Durlacher JE, Nair RG, Epstein JB, Sonis ST, Elad S, Hamblin MR, Barasch A, Migliorati CA, Milstein DMJ, Genot M-T, Lansaat L, van der Brink R, Arnabat-Dominguez J, van der Molen L, Jacobi I, van Diessen J, de Lange J, Smeele LE, Schubert MM, Bensadoun R-J. Low level laser therapy/photobiomodulation in the management of side effects of chemoradiation therapy in head and neck cancer: part 1: mechanisms of action, dosimetric, and safety considerations. Supportive care in cancer : official journal of the Multinational Association of Supportive Care in Cancer. 2016;24(6):2781-92. Epub 2016/03/16. doi: 10.1007/s00520-016-3152-z. PubMed PMID: 26984240.

150. de Souto Medeiros MR, da Silva Barros CC, de Macedo Andrade AC, de Lima KC, da Silveira É JD. Antimicrobial photodynamic therapy in the treatment of oral erythematous candidiasis: a controlled and randomized clinical trial. Clin Oral Investig. 2023. Epub 2023/09/18. doi: 10.1007/s00784-023-05252-3. PubMed PMID: 37718381.

151. Salem S. Consequences of 660 nm Diode Laser Following Postsurgical Exodontia in Patients under Contraceptive Pills: A Randomized Double-blinded Clinical Trial. J Contemp Dent Pract. 2020;21(1):2-10. Epub 2020/05/10. PubMed PMID: 32381793.

152. Farhadi F, Eslami H, Majidi A, Fakhrzadeh V, Ghanizadeh M, KhademNeghad S. Evaluation of adjunctive effect of low-level laser Therapy on pain, swelling and trismus after surgical removal of impacted lower third molar: A double blind randomized clinical trial. Laser Ther. 2017;26(3):181-7. Epub 2017/11/15. doi: 10.5978/islsm.17-OR-13. PubMed PMID: 29133965; PMCID: PMC5675908.

153. Neugebauer J, Jozsa M, Kübler A. [Antimicrobial photodynamic therapy for prevention of alveolar ostitis and post-extraction pain]. Mund Kiefer Gesichtschir. 2004;8(6):350-5. Epub 2004/12/08. doi: 10.1007/s10006-004-0572-6. PubMed PMID: 15583924.

154. Salmeron S, Rezende MLR, Consolaro A, Sant'Ana ACP, Damante CA, Greghi SLA, Passanezi E. Laser Therapy as an Effective Method for Implant Surface Decontamination: A Histomorphometric Study in Rats. Journal of Periodontology. 2013;84(5):641-9. doi: 10.1902/jop.2012.120166. PubMed PMID: WOS:000318753800009.

155. Shahnaz A, Jamali R, Mohammadi F, Khorsand A, Moslemi N, Fekrazad R. A preliminary randomized clinical trial comparing diode laser and scalpel periosteal incision during implant surgery: impact on postoperative morbidity and implant survival. Lasers Med Sci. 2018;33(1):19-25. Epub 2017/09/02. doi: 10.1007/s10103-017-2315-6. PubMed PMID: 28861729.

156. Star WM. Light dosimetry in vivo. Phys Med Biol. 1997;42(5):763-87. Epub 1997/05/01. doi: 10.1088/0031-9155/42/5/003. PubMed PMID: 9172258.

157.	Trombelli L, Farina R, Pollard A, Claydon N, Franceschetti G, Khan I, West N. Efficacy of alternative or additional methods to professional mechanical plaque removal during supportive periodontal therapy: A systematic review and meta-analysis. J Clin Periodontol. 2020;47 Suppl 22:144-54. Epub 2020/02/16. doi: 10.1111/jcpe.13269. PubMed PMID: 32060940.

158.	Vohra F, Al-Rifaiy MQ, Lillywhite G, Abu Hassan MI, Javed F. Efficacy of mechanical debridement with adjunct antimicrobial photodynamic therapy for the management of peri-implant diseases: a systematic review. Photochem Photobiol Sci. 2014;13(8):1160-8. Epub 2014/06/14. doi: 10.1039/c4pp00083h. PubMed PMID: 24924586.

159.	Wang HW, Zhu TC, Putt ME, Solonenko M, Metz J, Dimofte A, Miles J, Fraker DL, Glatstein E, Hahn SM, Yodh AG. Broadband reflectance measurements of light penetration, blood oxygenation, hemoglobin concentration, and drug concentration in human intraperitoneal tissues before and after photodynamic therapy. J Biomed Opt. 2005;10(1):14004. Epub 2005/04/26. doi: 10.1117/1.1854679. PubMed PMID: 15847585.

160.	Barbora A, Bohar O, Sivan AA, Magory E, Nause A, Minnes R. Higher pulse frequency of near-infrared laser irradiation increases penetration depth for novel biomedical applications. PLoS One. 2021;16(1):e0245350. Epub 2021/01/08. doi: 10.1371/journal.pone.0245350. PubMed PMID: 33411831; PMCID: PMC7790424 Scientific Innovations Ltd had no role in study design, data collection and analysis, decision to publish, or preparation of the manuscript. This does not alter our adherence to PLOS ONE policies on sharing data and materials.

161.	Minnes R, Weitman H, You Y, Detty MR, Ehrenberg B. Dithiaporphyrin derivatives as photosensitizers in membranes and cells. J Phys Chem B. 2008;112(10):3268-76. Epub 2008/02/19. doi: 10.1021/jp0768423. PubMed PMID: 18278897.

162.	Abrahamse H, Hamblin MR. New photosensitizers for photodynamic therapy. Biochem J. 2016;473(4):347-64. Epub 2016/02/11. doi: 10.1042/bj20150942. PubMed PMID: 26862179; PMCID: PMC4811612.

163.   Jacques SL. Light distributions from point, line and plane sources for photochemical reactions and fluorescence in turbid biological tissues. Photochem Photobiol. 1998;67(1):23-32. Epub 1998/04/04. PubMed PMID: 9477762.

164.   Ohshiro T, Ogata H, Yoshida M, Tanaka Y, Sasaki K, Yoshimi K. PENETRATION DEPTHS OF 830nm DIODE LASER IRRADIATION IN THE HEAD AND NECK ASSESSED USING A RADIOGRAPHIC PHANTOM MODEL AND WAVELENGTH-SPECIFIC IMAGING FILM. LASER THERAPY. 1996;8(3):197-203. doi: 10.5978/islsm.8.197.

165.   Fukui Y, Ajichi Y, Okada E. Monte Carlo prediction of near-infrared light propagation in realistic adult and neonatal head models. Appl Opt. 2003;42(16):2881-7. Epub 2003/06/07. doi: 10.1364/ao.42.002881. PubMed PMID: 12790436.

166.   Stolik S, Delgado JA, Pérez A, Anasagasti L. Measurement of the penetration depths of red and near infrared light in human "ex vivo" tissues. J Photochem Photobiol B. 2000;57(2-3):90-3. Epub 2001/01/12. doi: 10.1016/s1011-1344(00)00082-8. PubMed PMID: 11154088.

167.   Hayashi T, Kashio Y, Okada E. Hybrid Monte Carlo-diffusion method for light propagation in tissue with a low-scattering region. Appl Opt. 2003;42(16):2888-96. Epub 2003/06/07. doi: 10.1364/ao.42.002888. PubMed PMID: 12790437.

168.   Okada E, Delpy DT. Near-infrared light propagation in an adult head model. I. Modeling of low-level scattering in the cerebrospinal fluid layer. Appl Opt. 2003;42(16):2906-14. doi: 10.1364/AO.42.002906.

169.   Okada E, Delpy DT. Near-infrared light propagation in an adult head model. II. Effect of superficial tissue thickness on the sensitivity of the near-infrared spectroscopy signal. Appl Opt. 2003;42(16):2915-22. Epub 2003/06/07. doi: 10.1364/ao.42.002915. PubMed PMID: 12790440.

170.   Koyama T, Iwasaki A, Ogoshi Y, Okada E. Practical and adequate approach to modeling light propagation in an adult head with low-scattering regions by use of diffusion theory. Appl Opt. 2005;44(11):2094-103. Epub 2005/04/20. doi: 10.1364/ao.44.002094. PubMed PMID: 15835358.

171.   Barbosa RI, Guirro ECO, Bachmann L, Brandino HE, Guirro RRJ. Analysis of low-level laser transmission at wavelengths 660, 830 and 904 nm in biological tissue samples. J Photochem Photobiol B. 2020;209:111914. Epub 2020/06/10. doi: 10.1016/j.jphotobiol.2020.111914. PubMed PMID: 32516626.

172.   Maqbool M. An Introduction to Medical Physics. Cham, SWITZERLAND: Springer International Publishing AG; 2017.

173.   Braslavsky SE. Glossary of terms used in photochemistry, 3rd edition (IUPAC Recommendations 2006). Pure and Applied Chemistry. 2007;79(3):293-465. doi: doi:10.1351/pac200779030293.

174.   Antoni R. Applied Physics of External Radiation Exposure: Dosimetry and Radiation Protection. 1st 2017. ed. Bourgois L, editor. Cham: Springer Nature; 2016.

175.   Yadav RK. Definitions in laser technology. J Cutan Aesthet Surg. 2009;2(1):45-6. Epub 2009/01/01. doi: 10.4103/0974-2077.53103. PubMed PMID: 20300375; PMCID: PMC2840918.

176.   Salehpour F, Sadigh-Eteghad S, Mahmoudi J, Kamari F, Cassano P, Hamblin MR. Biphasic Dose–response in Photobiomodulation of Neuronal Cells and the Brain. In: Salehpour F, Sadigh-Eteghad S, Mahmoudi J, Kamari F, Cassano P, Hamblin MR, editors. Photobiomodulation for the Brain: Photobiomodulation Therapy in Neurology and Neuropsychiatry. Cham: Springer Nature Switzerland; 2023. p. 87-102.

177.   Hinds LM, O'Donnell CP, Akhter M, Tiwari BK. Principles and mechanisms of ultraviolet light emitting diode technology for food industry applications. Innovative Food Science & Emerging Technologies. 2019;56:102153. doi: https://doi.org/10.1016/j.ifset.2019.04.006.

178.   Dipalma G, Inchingolo AM, Patano A, Palumbo I, Guglielmo M, Trilli I, Netti A, Ferrara I, Viapiano F, Inchingolo AD, Favia G, Dongiovanni L, Palermo A, Inchingolo F, Limongelli L. Photobiomodulation and Growth Factors in Dentistry: A Systematic Review. Photonics [Internet]. 2023; 10 10.

179.   Schott P, Beaudoin L, editors. Different approximations to the computation of reflected and refracted angles thanks to snell-descartes laws and fresnel coefficients. Proceedings 2005 IEEE International Geoscience and Remote Sensing Symposium, 2005 IGARSS '05; 2005 29-29 July 2005.

180.   Keiser G. Biophotonics: Concepts to Applications: Springer Nature Singapore; 2016.

181.   Horn APDDa. The physics of laser radiation-matter interaction : fundamentals, and selected applications in metrology. The physics of laser radiation-matter interaction :. 2022. doi: 10.1007/978-3-031-15862-9.

182.   Prasad PN. Introduction to biophotonics: John Wiley & Sons; 2004.

183.   Lister T, Wright PA, Chappell PH. Optical properties of human skin. J Biomed Opt. 2012;17(9):90901-1. Epub 2012/10/23. doi: 10.1117/1.Jbo.17.9.090901. PubMed PMID: 23085902.

184.   Jacques SL. FRACTAL NATURE OF LIGHT SCATTERING IN TISSUES. Journal of Innovative Optical Health Sciences. 2011;04:1-7.

185.   Xu M, Alfano RR. Fractal mechanisms of light scattering in biological tissue and cells. Opt Lett. 2005;30(22):3051-3. Epub 2005/12/01. doi: 10.1364/ol.30.003051. PubMed PMID: 16315718.

186.   Choe R. Diffuse optical tomography & spectroscopy in breast cancer characterization & therapy monitoring at UPENN. Annu Int Conf IEEE Eng Med Biol Soc. 2009;2009:6335-7. Epub 2009/12/08. doi: 10.1109/iembs.2009.5333164. PubMed PMID: 19964156.

187.   Zhu TC, Kim MM, Padawer J, Dimofte A, Potasek M, Beeson K, Parilov E. Light Fluence Dosimetry in Lung-simulating Cavities. Proc SPIE Int Soc Opt Eng. 2018;10476. Epub 2018/05/22. doi: 10.1117/12.2291355. PubMed PMID: 29780196; PMCID: PMC5959279.

188.   Wang H-W, Zhu T, Solonenko M, Hahn S, Metz J, Dimofte A, Mile J, Yodh A. In-vivo measurements of penetration depth, oxygenation, and drug concentration using broadband absorption spectroscopy in human tissues before and after photodynamic therapy: SPIE; 2003.

189.   Ko KI, DerGarabedian BP, Chen Z, Debnath R, Ko A, Link BN, Korostoff JM, Graves DT. Distinct fibroblast progenitor subpopulation expedites regenerative mucosal healing by

immunomodulation. J Exp Med. 2023;220(3). Epub 2022/12/31. doi: 10.1084/jem.20221350. PubMed

PMID: 36584405; PMCID: PMC9827523.